Bridging intermittency with iron electrodes

Weninger, B.

DOI
10.4233/uuid:a3fb56dd-0f74-449f-8e85-2ffaeb63a65c

Publication date
2023

Document Version
Final published version

Citation (APA)
Weninger, B. (2023). *Bridging intermittency: with iron electrodes*. [Dissertation (TU Delft), Delft University of Technology]. https://doi.org/10.4233/uuid:a3fb56dd-0f74-449f-8e85-2ffaeb63a65c

Bridging intermittency with iron electrodes

Bernhard Weninger

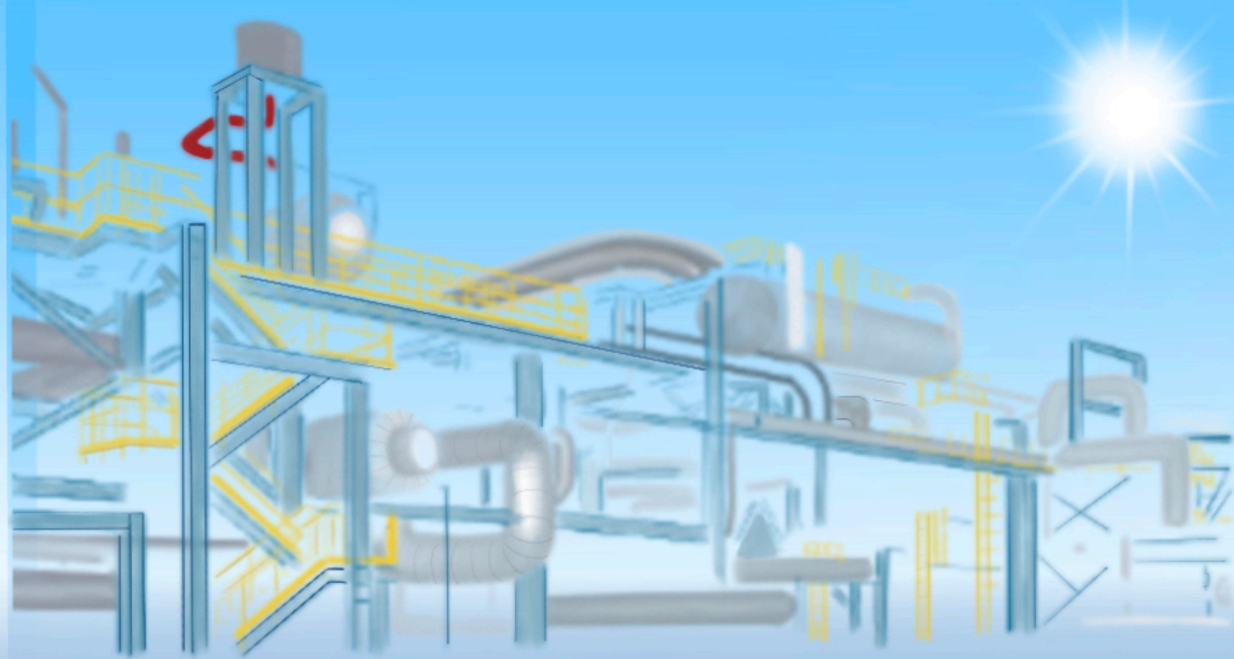

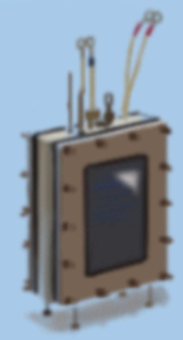

battery electrolyser

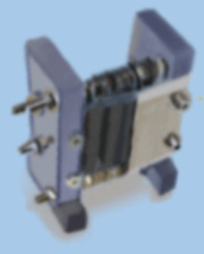

mc electrodes

hsp cell

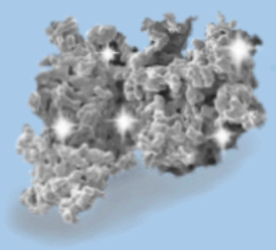

doped iron electrodes

Bridging intermittency

with iron electrodes

Bernhard Weninger

Bridging intermittency

with iron electrodes

Bernhard Weninger

Bridging intermittency

with iron electrodes

Dissertation

for the purpose of obtaining the degree of doctor
at Delft University of Technology,
by the authority of the Rector Magnificus prof. dr. ir. T.H.J.J. van der Hagen,
chair of the Board of Doctorates,
to be defended publicly on Tuesday, 16 May 2023 at 15:00 o'clock

by

Bernhard WENINGER

Master of Science in Sustainable Energy Technologies,
Delft University of Technology, The Netherlands,
Master of Science in Civil Engineering,
Vienna University of Technology, Austria,
born in Mistelbach, Austria.

This dissertation has been approved by the promotors.

Composition of the doctoral committee:

Rector Magnificus	chairperson
Prof. dr. F.M. Mulder	Delft University of Technology, promotor
Prof. dr. ir. J.R. van Ommen	Delft University of Technology, promotor
Independent members:	
Dr. ir. D.A. Vermaas	Delft University of Technology
Dr. A. Borgschulte	EMPA, Switzerland
Prof. dr. J.J.C. Geerlings	Delft University of Technology
Dr. E.M. Kelder	Delft University of Technology
Prof. dr. G. Mul	University of Twente, The Netherlands
Prof. dr. B. Dam	Delft University of Technology, reserve member

The work described in this thesis has been carried out in the Materials for Energy Conversion and Storage (MECS) group, Department of Chemical Engineering, Faculty of Applied Sciences, Delft University of Technology. This work is part of the Open Technology research program with Project Number 15169, which is (partly) financed by The Netherlands Organization for Scientific Research (NWO).

Keywords: battolyser, battolyzer, hydrogen storage, hydrogen production, multi-controlled electrodes, hsp-cell, iron electrode

Printed by: Ridderprint | www.ridderprint.nl

Cover artwork: Florine Weninger & Karin Nijman-Weninger

ISBN 978-94-6483-023-1

An electronic version of this dissertation is available at
http://repository.tudelft.nl/.

We most certainly need to embrace every bit of new clean technology.

Greta Thunberg

Brilliant Minds Conference

Stockholm, June13th 2019

Contents

Summary

We have to overcome the intermittent nature of renewables to master the energy transition. Harvesting renewable electricity is only part of the solution. Energy storage is another part and the main challenge of our time. Only with efficient storage solutions can big industries switch to renewables.

Electricity storage is most efficient with batteries while industrial sites and synthetic fuel production require a sustained hydrogen input to drive the processes. The aim of this thesis was the research and development of storage solutions mainly based on earth-abundant iron to bridge intermittency. The following scientific questions were at the basis of the conducted research:

1. Combined battery and electrolyser: is it possible and reasonable to develop a device that serves two purposes? Do the materials endure and support this double functionality?

2. Multiple electrodes: nickel is required for electricity and oxygen storage; iron is required for electricity and hydrogen storage. Is it possible to store electricity, oxygen and hydrogen in one electrochemical cell? Is it possible to decouple the electricity input from the oxygen and hydrogen output? Can a single electrode be used for two purposes simultaneously? Are configurations with multiple electrodes scalable to larger arrays?

3. Fundamentals of iron electrodes: Which phases occur for the first and second iron discharge plateau? And why are iron electrodes less responsive to higher discharge rates?

4. Sustained hydrogen from intermittent sources: Decoupling of the electricity input and the hydrogen output is possible with an electrochemical cell consisting of at least three electrodes. Is more sustained hydrogen from intermittent sources also feasible with a standard electrochemical cell with two electrodes?

5. Doped iron electrodes: Iron electrodes can have a limited rechargeability and can show gas accumulation inside the electrode. Does the addition of dopants enhance the ability of the iron electrode to recharge? Do these dopants enhance performance and the material utilisation?

Battolyser

NiFe batteries are known to be practically indestructible. However, these NiFe batteries have the disadvantages of hydrogen and oxygen production and self-discharge which makes them inefficient as a battery. In the battolyser we promote this "hydrogen-side-effect", and obtain an energy-efficient device that produces hydrogen with excess energy with the potential to reduce undesirable renewable electricity curtailments. Such a device can be operational around the clock: either the surplus of electricity is used to charge the battery and to produce hydrogen or electricity is provided to consumers.

The battolyser will supply hydrogen when overcharged, following an intermittent pattern of renewables availability. Therefore, downstream infrastructure needs the capability to handle an intermittent hydrogen input or requires a hydrogen storage infrastructure. Under these conditions the battolyser has the potential to become an essential single-combined tool for the energy transition since renewable electricity can be stored and excess electricity can be converted efficiently into hydrogen.

Multi-Controlled (MC-)electrodes

Then we demonstrated that we could supply a sustained hydrogen output from an intermittent energy input and that time shifting the hydrogen output comes at low energy costs. We accomplished that by creating electrochemical systems consisting of more than two electrodes within a single electrochemical cell. Here the storage electrodes can be charged/discharged while gas production, hydrogen and oxygen, can occur simultaneously and at independent rates. We also demonstrated that storage electrodes can serve two different processes at the same time. The proposed concept of MC-electrodes allows for controlling and scaling up multi-electrode configurations to larger arrays. Most importantly we used it for decoupling the electricity input from the hydrogen output by the combination of an iron storage electrode with two gas evolution electrodes, one for hydrogen evolution and one for oxygen evolution with two independent circuits. The position of the electrode phases in the Pourbaix diagram indicates that charging the iron electrode together with oxygen production requires most of the energy while little energy is required to generate hydrogen from previously charged iron electrodes. Independent operation of both circuits enables decoupling of the electricity input and the hydrogen output, and the iron storage electrode serves as an electrochemical storage reservoir.

Time-shifting 50% of the hydrogen production requires only 5% of the energy while 95% of the required energy can be fed through a main controller when electricity is cheap and abundant. Moreover, hydrogen can later be provided

from reduced iron electrodes with a substantial reduction of backup power. Compared to electrolysers, the electricity storage requirement is reduced by 85% to provide the same amount of hydrogen, using the previously reduced iron oxidation. In other words, seven times more hydrogen can now be provided from existing backup power, which can serve as a booster for delayed hydrogen generation.

Half-cell used as Hydrogen Storage and Production cell (HSP-cell)

We reduced the complexity of the system by combining the iron storage electrode with a bifunctional electrode for oxygen and hydrogen production which led to the concept of the HSP-cell. The HSP-cell is a simple half-cell, consisting of two electrodes which makes it easily scalable to larger bi-polar configurations. The HSP-cell can utilize the entire capacity of the iron electrode, comparable to the iron-air battery or battolyser, but delivers hydrogen instead of electricity. Both configurations can operate as a low-cost sink to store energy in reduced iron and both systems can use excess electricity for direct hydrogen generation to reduce undesirable curtailment of renewable power.

The replacement of the nickel hydroxide battery electrode by a thin bifunctional nickel metal electrode provides space and allows to increase the storage density. Considering only the iron electrode (and omitting counter electrode, electrolyte, casing, valves or other parts), a storage density of $0.78\,\mathrm{Ah/cm^3}$ is currently feasible, equivalent to $29\,\mathrm{kg\,H_2/m^3}$ or to a compressed hydrogen storage density of 500 bar. The stored hydrogen can be released easily and controlled by applying a current. This reduces the safety risk associated with the storage of compressed hydrogen gas. During electrochemical hydrogen release, only hydrogen is generated inside the cell, which offers an oxygen-free hydrogen gas output even at low discharge rates.

The HSP-cells can be configured in a self-sustaining manner and in a way to provide a sustained hydrogen output from an intermittent input by simultaneous and phase-shifted operation of several units. The concept can provide sustained hydrogen to industrial processes or synthetic fuel production with an overall efficiency including storage and production which exceeds 80% when operated at 40 °C. Therefore, the HSP-cell has the potential to become an essential device to boost the energy transition.

Doped Iron electrodes

The iron electrode is the common part of all previously discussed configurations. Having an optimal iron electrode is essential since the iron electrode determines the rate capabilities and the efficiencies. In the battolyser thin iron electrodes suffice because the nickel electrode is capacity limiting. Thicker iron electrodes can be used in the iron-air battery/battolyser, in the MC-cell and in the HSP-cell.

We developed a strategy to produce sintered iron electrodes to study the phase behaviour of the electrode in operando by means of neutron diffraction. The study revealed that substantial amounts of iron hydroxide were inside the bulk of the sample which could not be reduced back to metallic iron upon charging. We concluded that the electrochemical circuit within the electrode must be interrupted, and it is our hypothesis that gas accumulation within the cell negatively affected the ionic conductivity. We assume that gas accumulation within the electrode replaces electrolyte which increases the ionic resistance for phase transition. As a consequence, the inserted charge shifts from battery charging with phase transition to hydrogen evolution.

We wanted to improve the material utilization of the sintered iron electrodes and therefore needed to improve the ability of these electrodes to recharge. For this purpose, we added either zirconia oxide or alumina oxide to the electrodes. By adding metal-oxides to the electrode-composition we enhance the processability of the materials and the electrode performance.

With the new synthesis strategy, we produced thick sintered iron electrodes which show a volumetric storage density of up to $0.8\,\mathrm{Ah/cm^3}$ and reach areal storage densities of up to $160\,\mathrm{mAh/cm^2}$. These values are among the best reported values in literature for sintered iron electrodes. In the process we may create a sulphur free system which potentially reduces corrosion issues, and which potentially reduce the deterioration of air electrodes.

Bridging intermittency with iron electrodes

Summing up, the creation of an energy system based on renewables confronts us with the intermittent nature of renewable power generation. To bridge the intermittency we need storage solutions for electricity and hydrogen. With a sustained hydrogen output synthetic fuels based on renewables could be produced on a large scale. With the nickel-iron battolyser and the iron-air battolyser we can store electricity and we can convert excess electricity into hydrogen to overcome the curtailment-problem. With the concept of MC-electrodes and of the HSP-cell we can efficiently control, store, and postpone the hydrogen output, to provide a more sustained hydrogen output. The iron electrode is present in all

configurations and recharging was the main challenge. We addressed the issue of rechargeability with a modified synthesis strategy for sintered iron electrodes doped with Zr and Al instead of sulphur. Electrodes produced with this strategy may have the potential to perform as effective sintered iron electrodes.

With these new simple concepts and cost-efficient iron electrodes we offer new tools to support and accelerate the storage and conversion of renewable power, which is necessary for the energy transition and to overcome intermittency. We have to speed up the energy transition to limit the impact of climate change.

Samenvatting

In de energietransitie moeten we de schommelende aard van hernieuwbare energie overwinnen. Het genereren van hernieuwbare elektriciteit is slechts een deel van de oplossing. Energieopslag is een ander onderdeel en de belangrijkste uitdaging van onze tijd. Alleen met efficiënte opslagoplossingen kunnen grote industrieën overstappen op hernieuwbare energiebronnen.

Elektriciteitsopslag is het meest efficiënt met batterijen, terwijl industriële locaties en de productie van synthetische brandstof een aanhoudende waterstofinput nodig hebben om de processen aan te drijven. Het doel van dit proefschrift was het onderzoek naar en de ontwikkeling van opslagoplossingen, voornamelijk gebaseerd op het in de aarde overvloedig aanwezige ijzer om schommelingen in de aanvoer van energie te overbruggen. De volgende wetenschappelijke vragen stonden aan de basis van het uitgevoerde onderzoek:

1. Gecombineerde batterij en elektrolyser: is het mogelijk en rationeel om een apparaat te ontwikkelen dat twee doelen dient? Verdragen en ondersteunen de materialen deze dubbele functionaliteit?

2. Meerdere elektroden: nikkel is nodig voor de opslag van elektriciteit en zuurstof; ijzer is nodig voor de opslag van elektriciteit en waterstof. Is het mogelijk om elektriciteit, zuurstof en waterstof op te slaan in één elektrochemische cel? Is het mogelijk om de elektriciteitsinput los te koppelen van de zuurstof- en waterstofoutput? Kan een enkele elektrode tegelijkertijd voor twee doeleinden worden gebruikt? Zijn configuraties met meerdere elektroden schaalbaar naar grotere opstellingen?

3. Grondbeginselen van ijzerelektroden: welke fasen treden op voor het eerste en tweede ijzer-ontladingsplateau? En waarom reageren ijzerelektroden minder bij hogere ontladingssnelheden?

4. Voortdurende waterstof uit schommelende aanvoer vanuit hernieuwbare energiebronnen: ontkoppeling van de elektriciteitsinvoer en de waterstofoutput is mogelijk met een elektrochemische cel die uit minimaal drie elektroden bestaat. Is een aanhoudende waterstofoutput uit schommelende bronnen ook haalbaar met een standaard elektrochemische cel met twee elektroden?

5. Gedoopte ijzerelektroden: ijzerelektroden kunnen beperkt heroplaadbaar zijn en er kan gas ophopen in de elektrode. Verbetert de toevoeging van doteermiddelen het vermogen van de ijzerelektrode om op te laden? Verbeteren deze doteermiddelen de prestaties en het materiaalgebruik?

Battolyser

NiFe-batterijen staan erom bekend praktisch onverwoestbaar te zijn. Deze NiFe-batterijen hebben echter de nadelen van waterstof- en zuurstofproductie en zelfontlading, waardoor ze inefficiënt zijn als batterij. In de battolyser promoten we deze 'waterstof-neveneffect' en verkrijgen we een energie-efficiënt apparaat dat met overtollige energie waterstof produceert met het potentieel om ongewenste hernieuwbare elektriciteitsproductiebeperkingen te verminderen. Zo een apparaat kan 24 uur per dag operationeel zijn: ofwel wordt het overschot aan elektriciteit gebruikt om de batterij op te laden en waterstof te produceren, ofwel wordt elektriciteit geleverd aan de gebruikers .

De battolyser zal waterstof leveren wanneer hij volgeladen is. De waterstofproductie volgt het schommelende patroon van de beschikbaarheid van hernieuwbare energie. Daarom moet de erachter-liggende infrastructuur in staat zijn om een wisselende waterstoftoevoer te kunnen verwerken of er is infrastructuur voor waterstofopslag nodig. Onder deze omstandigheden heeft de battolyser het potentieel om een essentieel enkelvoudig-gecombineerd apparaat te worden voor de energietransitie, aangezien hernieuwbare elektriciteit kan worden opgeslagen en overtollige elektriciteit efficiënt kan worden omgezet in waterstof.

Meervoudig-gecontroleerde (MC-)elektroden

Vervolgens hebben we aangetoond dat we een aanhoudende waterstofoutput kunnen leveren met een schommelende energie-input en dat het verschuiven van de waterstofoutput naar een later moment, lage energiekosten meebrengt. Dat hebben we bereikt door elektrochemische systemen te creëren die uit meer dan twee elektroden in één elektrochemische cel bestaan. Hier kunnen de opslagelektroden worden geladen/ontladen terwijl de gasproductie van waterstof en zuurstof, gelijktijdig en met onafhankelijke snelheden kan plaatsvinden. We hebben ook aangetoond dat opslagelektroden twee doelen tegelijkertijd kunnen dienen. Het voorgestelde concept van MC-elektroden maakt het mogelijk configuraties met meerdere elektroden te controleren en op te schalen naar grotere systemen. Het belangrijkste was dat we het gebruikten voor het ontkoppelen van de elektriciteitsinvoer van de waterstofoutput door de combinatie van een ijzeropslagelektrode met twee elektroden voor de gasontwikkeling, één voor wa-

terstofontwikkeling en één voor zuurstofontwikkeling met twee onafhankelijke circuits. De positie van de elektrodefasen in het Pourbaix-diagram geeft aan dat het opladen van de ijzerelektrode samen met zuurstofproductie het meest energie vereist, terwijl er weinig energie nodig is om waterstof te genereren uit eerder geladen ijzerelektroden. Onafhankelijke werking van beide circuits maakt ontkoppeling van de elektriciteitsinvoer en de waterstofoutput mogelijk, en de ijzeropslagelektrode dient als een elektrochemisch opslagreservoir.

Time-shifting van 50% van de waterstofproductie vereist slechts 5% van de energie, terwijl 95% van de benodigde energie via een hoofdcontroller kan worden gevoed wanneer elektriciteit goedkoop en in overvloed aanwezig is. Bovendien kan later waterstof worden geleverd uit gereduceerd ijzerelektroden met een aanzienlijke vermindering van back-upvermogen. Vergeleken met elektrolysers wordt de behoefte aan elektriciteitsopslag met 85% verminderd om dezelfde hoeveelheid waterstof te leveren, met behulp van de eerder gereduceerde ijzeroxidatie. Met andere woorden, er kan nu zeven keer meer waterstof worden geleverd uit bestaande back-upcapaciteiten, wat kan dienen als aanjager voor vertraagde waterstofopwekking.

Halve cel gebruikt als waterstofopslag- en productiecel (HSP-cel)

We hebben het systeem vereenvoudigd door de ijzeropslagelektrode te combineren met een bifunctionele elektrode voor zuurstof- en waterstofproductie, wat leidde tot het concept van de HSP-cel. De HSP-cel is een eenvoudige halve cel, bestaande uit twee elektroden, waardoor hij eenvoudig schaalbaar is naar grotere bipolaire configuraties. De HSP-cel kan de volledige capaciteit van de ijzerelektrode benutten, vergelijkbaar met de ijzer-luchtbatterij of ijzer-lucht battolyser, maar levert waterstof in plaats van elektriciteit. Beide configuraties kunnen werken als een goedkope put om energie op te slaan in gereduceerd ijzer en beide systemen kunnen overtollige elektriciteit gebruiken voor directe waterstofopwekking het ongewenste beperken van hernieuwbare stroomproductie te verminderen.

De vervanging van de nikkelhydroxidebatterij-elektrode door een dunne bifunctionele nikkelmetaalelektrode biedt ruimte en maakt het mogelijk om de opslagdichtheid te verhogen. Als we alleen de ijzerelektrode beschouwen (en tegenelektrode, elektrolyt, behuizing, kleppen of andere onderdelen weglaten), is momenteel een opslagdichtheid van $0.78\,\mathrm{Ah/cm^3}$ haalbaar, wat overeenkomt met $29\,\mathrm{kg\,H_2/m^3}$ of een opslagdichtheid van gecomprimeerde waterstof van 500 bar. De opgeslagen waterstof kan eenvoudig gecontroleerd worden vrijgegeven door een stroom aan te leggen. Dit vermindert het veiligheidsrisico dat gepaard gaat

met de opslag van gecomprimeerd waterstofgas. Tijdens de elektrochemische waterstofafgifte wordt alleen waterstof gegenereerd in de cel, wat zelfs bij lage ontladingssnelheden een zuurstofvrije waterstofgasoutput biedt.

De HSP-cellen kunnen op een zelfvoorzienende manier worden geconfigureerd en op een manier om een aanhoudende waterstofoutput te leveren vanuit een intermitterende input door gelijktijdige en fase-verschoven werking van meerdere eenheden. Het concept kan voortdurende waterstof leveren voor industriële processen of voor de productie van synthetische brandstof met een algehele efficiëntie, inclusief opslag en productie, van meer dan 80% bij gebruik bij 40 °C. Daarom heeft de HSP-cel de potentie om een essentieel apparaat te worden in de energietransitie.

Gedoopte ijzerelektroden

De ijzerelektrode is het gemeenschappelijke onderdeel van alle eerder besproken configuraties. Het hebben van een optimale ijzerelektrode is essentieel omdat de ijzerelektrode de laadsnelheid en de efficiëntie bepaalt. In de battolyser volstaan dunne ijzerelektroden omdat de nikkelelektrode capaciteitsbeperkend is. In de ijzer-lucht batterij/battolyser, in de MC-cel en in de HSP-cel kunnen dikkere ijzerelektroden worden gebruikt. We ontwikkelden een strategie om gesinterde ijzerelektroden te produceren om het fasegedrag van de elektrode in operando te bestuderen door middel van neutronendiffractie. Uit het onderzoek bleek dat er aanzienlijke hoeveelheden ijzerhydroxide in het volume van het monster zaten, die door het opladen niet konden worden gereduceerd tot metallisch ijzer. We concludeerden dat het elektrochemische circuit in de elektrode onderbroken was, en het is onze hypothese dat gasophoping in de cel de ionische geleiding negatief beïnvloedde. We gaan ervan uit dat gasaccumulatie in de elektrode elektrolyt vervangt, wat de ionische weerstand voor faseovergang verhoogt. Als gevolg hiervan verschuift de ingebrachte lading van batterijlading met faseovergang naar waterstofontwikkeling. We wilden het materiaalgebruik van de gesinterde ijzerelektroden verbeteren en moesten daarvoor het oplaadvermogen van de elektroden verbeteren. Hiervoor hebben we zirkoniumoxide of aluminiumoxide aan de elektroden toegevoegd. Door deze metaaloxiden toe te voegen aan de elektrode-samenstelling verbeterden we de verwerkbaarheid van de materialen en de prestaties van de elektrode. Met de nieuwe synthesestrategie produceerden we dikke gesinterde ijzerelektroden die een volumetrische opslagdichtheid tot 0.8 Ah/cm^3 vertonen en een opslagdichtheid tot 160 mAh/cm^2 bereiken. Deze waarden behoren tot de best gerapporteerde waarden in de literatuur voor gesinterde ijzerelektroden. Door dit proces kunnen we een zwavelvrij systeem creëren dat mogelijk corrosieproblemen vermindert en mogelijk de ver-

slechtering van luchtelektroden vermindert.

Energieschommelingen overbruggen met ijzerelektroden

Samenvattend worden we bij groene energyoplossingen geconfronteerd met het schommelende karakter daarvan. Om deze schommelingen te overbruggen hebben we opslagoplossingen nodig voor elektriciteit en waterstof. Met een duurzame waterstofproductie zouden synthetische brandstoffen op basis van hernieuwbare energiebronnen op grote schaal kunnen worden geproduceerd. Met de nikkel-ijzer battolyser en de ijzer-lucht battolyser kunnen we elektriciteit opslaan en overtollige elektriciteit omzetten in waterstof om het probleem van het af laten vloeien van energie te ondervangen. Met het concept van MC-elektroden en de HSP-cel kunnen we de waterstofproductie efficiënt regelen, opslaan en uitstellen, om een voortdurende waterstofoutput te creëren. De ijzerelektrode is in alle configuraties aanwezig en het opladen was de grootste uitdaging. We zijn de kwestie van oplaadbaarheid aangevlogen met een aangepaste synthesestrategie voor gesinterde ijzerelektroden gedoopt met Zr en Al in plaats van zwavel. Elektroden die met deze strategie zijn geproduceerd, hebben het potentieel om te presteren als effectieve gesinterde ijzerelektroden.

Met deze nieuwe, eenvoudige concepten en kostenefficiënte ijzerelektroden bieden we nieuwe tools om de opslag en omzetting van hernieuwbare energie, die nodig is om de energietransitie te ondersteunen en te versnellen en om energieschommelingen te overwinnen. We moeten de energietransitie versnellen om de impact van klimaatverandering te beperken.

Zusammenfassung

Wir müssen lernen mit den natürlichen Schwankung erneuerbarer Energieträger umzugehen, um die Energiewende zu meistern. Die Produktion erneuerbaren Stroms ist nur ein Teil der Lösung. Energiespeicherung ist ein weiterer Teil und die große Herausforderung unserer Zeit. Nur mit effizienter Speicherung können industrielle Großverbraucher auf erneuerbare Energien umsteigen.

Stromspeicherung ist mit Batterien am effizientesten, während Industriestandorte und die Produktion synthetischer Kraftstoffe eine ununterbrochene Wasserstoffzufuhr benötigen, um die Prozesse anzutreiben. Das Ziel dieser Doktorarbeit war die Erforschung und Entwicklung von Speicherlösungen basiert auf Eisen, welches ausreichend verfügbar ist, zur Überbrückung der Intermittenz. Die folgende wissenschaftliche Fragen lagen der durchgeführten Forschung zugrunde:

1. Kombinierte Batterie und Elektrolyseur: Ist es möglich und sinnvoll, ein Gerät zu entwickeln, das zwei Zwecken dient? Haben die Materialien Bestand und unterstützen sie diesen doppelten Verwendungszweck?

2. Mehrere Elektroden: Nickel wird zur Strom- und Sauerstoffspeicherung benötigt; Eisen wird für die Strom- und Wasserstoffspeicherung benötigt. Ist es möglich um Strom, Sauerstoff und Wasserstoff in einer elektrochemischen Zelle speichern? Ist es möglich, den Strominput vom Sauerstoff- und Wasserstoffoutput zu entkoppeln? Kann eine einzelne Elektrode zur gleichen Zeit für zwei Aufgaben verwendet werden? Sind Konfigurationen mit mehreren Elektroden skalierbar für größere Anordnungen?

3. Grundlagen von Eisenelektroden: Welche Phasen formen das erste und zweite Entladungsplateau der Eisenelektroden? Und warum reagieren Eisenelektroden träge bei höhere Entladestrom?

4. Anhaltender Wasserstoff aus intermittierenden Quellen: Mit einer elektrochemischen Zelle, bestehend aus mindestens drei Elektroden, ist eine Entkopplung von Strominput und Wasserstoffoutput möglich. Ist fortwährender Wasserstoff aus intermittierenden Quellen auch realisierbar mit einer elektrochemischen Standardzelle bestehend aus zwei Elektroden?

5. Dotierte Eisenelektroden: Eisenelektroden können begrenzte aufladbar sein und eine Gasansammlung innerhalb der Elektrode aufweisen. Verbessert die Zugabe von Dotierstoffen die Fähigkeit der Eisenelektrode zum Wiederaufladen? Verbessern diese Dotierstoffe die Leistungsfähigkeit und die Materialausnutzung?

Battolyseur

NiFe-Akkus sind bekanntermaßen praktisch unzerstörbar. Diese NiFe-Batterien haben jedoch die Nachteile der Wasserstoff- und Sauerstofferzeugung und der Selbstentladung, was sie als Batterie ineffizient macht. Mit dem Battolyseur fördern wir diesen „Wasserstoff-Nebeneffekt“ und erhalten ein energieeffizientes Gerät, das aus überschüssigem Strom Wasserstoff produziert und dadurch das Potenzial hat, unerwünschte Beschränkungen bei erneuerbarer Stromerzeugung zu reduzieren. Ein solches Gerät kann rund um die Uhr eingesetzt werden: Entweder wird der überschüssige Strom zum Laden der Batterie und zur Produktion von Wasserstoff verwendet oder der gespeicherte Strom wird den Nutzern zur Verfügung gestellt.

Der Battolyseur produziert Wasserstoff, wenn er überladen wird. Die Wasserstoffproduktion folgt dem intermittierenden Muster der Verfügbarkeit des erneuerbaren Stroms. Daher muss die nachgelagerte Infrastruktur in der Lage sein, eine intermittierende Wasserstoffzufuhr zu verarbeiten, oder erfordert eine Infrastruktur zur Wasserstoffspeicherung. Unter diesen Voraussetzungen hat der Battolyseur das Potenzial, ein unverzichtbares einzel-kombiniertes Gerät für die Energiewende zu werden, da erneuerbarer Strom gespeichert und überschüssiger Strom effizient in Wasserstoff umgewandelt werden kann.

Mehrfach-kontrollierte (MC-)Elektroden

Weiters haben wir gezeigt, dass wir durchgehend Wasserstoff aus einer intermittierenden Energiezufuhr bereitstellen können und dass die Zeitverschiebung der Wasserstoffausgabe wenig Energie kostet. Wir haben das bewerkstelligt, indem wir elektrochemische Systeme geschaffen haben, die aus mehr dann zwei Elektroden innerhalb einer Zelle bestehen. Hier können die Speicherelektroden geladen/entladen werden, während die Gasproduktion, Wasserstoff und Sauerstoff, gleichzeitig und mit gesonderten Produktionsraten erfolgt. Wir haben auch gezeigt, dass Speicherelektroden zwei unterschiedlichen Prozessen gleichzeitig dienen können. Das vorgeschlagene Konzept von MC-Elektroden ermöglicht die Steuerung und Ausbreitung von MC-Elektrodenkonfigurationen auf größere Systeme. Wir haben es vor allem zur Entkopplung des Stromein-

gangs vom Wasserstoffausgang durch die Kombination einer Speicherelektrode aus Eisen mit zwei Elektroden zur Gasentwicklung, eine für Wasserstoff und eine für Sauerstoff, geschaltet mit zwei unabhängigen Stromkreisen, verwendet. Die Position der Elektrodenpotentiale im Pourbaix-Diagramm zeigt, dass das Laden der Eisenelektrode zusammen mit der Sauerstoffproduktion die meiste Energie erfordert, wenig Energie benötigt wird, um Wasserstoff aus zuvor geladenen Eisenelektroden zu erzeugen. Der unabhängige Betrieb beider Stromkreise ermöglicht die Entkopplung von Strominput und Wasserstoffoutput, die Eisenspeicherelektrode dient als elektrochemisches Speicherreservoir.

Das Zeitversetzten von 50% der Wasserstoffproduktion benötigen nur 5% der Energie, 95% der benötigten Energie werden über den zentralen Stromkreis eingespeist, wenn Strom günstig und reichlich vorhanden ist. Darüber hinaus kann Wasserstoff später aus reduzierten Eisenelektroden mit einem erheblichen reduziertem Energiebedarf generiert werden. Im Vergleich zu Elektrolyseuren wird der Stromspeicherbedarf um 85% reduziert, um die gleiche Menge an Wasserstoff zu generieren, indem die zuvor reduzierte Eisenoxidation genutzt wird. Mit anderen Worten, es könnte jetzt sieben Mal mehr Wasserstoff aus vorhandener Stromquellen generiert werden, was eine zeitversetzte Wasserstofferzeugung begünstigen kann.

Halbzelle als Wasserstoffspeicher- und Produktionszelle (HSP-Zelle)

Wir haben die Komplexität des Systems reduziert, indem wir die Eisenspeicherelektrode mit einer bifunktionellen Elektrode für die Sauerstoff- und Wasserstofferzeugung kombiniert haben, was zum Konzept der HSP-Zelle führte. Die HSP-Zelle ist eine einfache Halbzelle, bestehend aus zwei Elektroden, wodurch sie leicht ausbaubar ist zu größere bipolare Konfigurationen. Die HSP-Zelle kann die gesamte Kapazität der Eisenelektrode nutzen, vergleichbar mit der Eisen-Luft-Batterie oder dem Eisen-Luft Battolyseur, liefert aber Wasserstoff statt Strom. Beide Konfigurationen können als kostengünstige Energiesenke genützt werden, um Energie in reduziertem Eisen zu speichern, und beide Systeme können überschüssigen Strom direkt zur Wasserstoffproduktion nutzen, um unerwünschte Beschränkungen bei der erneuerbarer Stromerzeugung zu reduzieren.

Der Ersatz der Nickelhydroxid-Batterieelektrode durch eine dünne bifunktionelle Nickelmetallelektrode schafft Platz und ermöglicht eine Erhöhung der Speicherdichte. Betrachtet man nur die Eisenelektrode (und lässt Gegenelektrode, Elektrolyt, Gehäuse, Ventile und andere Teile weg), ist derzeit eine Speicherdichte von $0.78\,\mathrm{Ah/cm^3}$ realisierbar, äquivalent zu $29\,\mathrm{kg\,H_2/m^3}$ oder einer

Speicherdichte von komprimiertem Wasserstoff von 500 bar. Der gespeicherte Wasserstoff kann einfach und kontrolliert durch Anlegen eines Stroms freigesetzt werden. Dies verringert das Sicherheitsrisiko, das mit der Speicherung von komprimiertem Wasserstoffgas verbunden ist. Bei der elektrochemischen Wasserstofffreisetzung wird innerhalb der Zelle nur Wasserstoff erzeugt, was eine sauerstofffreie Wasserstoffabgabe ermöglicht, selbst bei niedrigen Entladungsraten.

Die HSP-Zellen können autark betrieben und so konfiguriert werden, dass sie durch gleichzeitigen und phasenverschobenen Betrieb mehrerer Einheiten an durchgehend Wasserstoff aus einer intermittierenden Stromzufuhr generieren. Das Konzept kann industrielle Prozesse oder die Produktion synthetischer Kraftstoffe nachhaltig mit Wasserstoff versorgen mit einem Effizienz von über 80%, einschließlich Lagerung und Produktion, wenn es bei 40 °C betrieben wird. Daher hat die HSP-Zelle das Potenzial, ein entscheidender Bestandteil zu werden, um die Energiewende voranzutreiben.

Dotierte Eisenelektroden

Die Eisenelektrode ist der verbindende Teil aller zuvor diskutierten Konfigurationen. Eine optimale Eisenelektrode ist unerlässlich, da die Eisenelektrode die verwendbare Stromstärke und die Effizienz bestimmt. Im Battolyseur genügt dünne Eisenelektroden, da hier die Nickelelektrode kapazitätsbegrenzend ist. Dickere Eisenelektroden können in der Eisen-Luft-Batterie/Battolyseur, in der MC-Konfiguration oder in der HSP-Zelle verwendet werden.

Wir haben eine Strategie zur Herstellung von Sintereisenelektroden entwickelt, um das Phasenverhalten der Elektrode in operando mittels Neutronendiffraktion zu untersuchen. Die Studie ergab, dass sich beträchtliche Mengen an Eisenhydroxid in der Masse der Probe befanden, die beim Laden nicht wieder zu metallischem Eisen reduziert werden konnten. Wir kamen zu dem Schluss, dass der elektrochemische Kreislauf innerhalb der Elektrode unterbrochen wurde, und es ist unsere Hypothese, dass eine Gasansammlung innerhalb der Zelle die Ionenleitfähigkeit negativ beeinflusst. Wir nehmen an, dass die Gasansammlung innerhalb der Elektrode den Elektrolyten verdrängt, was den ionischen Widerstand für den Phasenübergang erhöht. Als Konsequenz verschiebt sich die Verwendung der zugeführte Ladung von Batterieladung mit Phasenübergang zu Wasserstoffentwicklung.

Wir wollten die Materialausnutzung der Sintereisenelektroden verbessern und mussten daher die Fähigkeit der Elektroden zum Wiederaufladen erhöhen. Zu diesem Zweck haben wir den Elektroden entweder Zirconiumoxid oder Aluminiumoxid dotiert. Durch die Zugabe dieser Metalloxide zur Elektrodenformulierung verbessert sich die einerseits die Verarbeitbarkeit der Materialien und

andererseits die Elektrodenleistung.

Mit der neuen Synthesestrategie haben wir dicke Sintereisenelektroden hergestellt, die eine volumetrische Speicherdichte von bis zu $0.8\,\mathrm{Ah/cm^3}$ aufweisen und bezogen auf die Fläche eine Speicherdichte von bis zu $160\,\mathrm{mAh/cm^2}$ erreichen. Diese Werte gehören zu den am besten in der Literatur angegebenen Werten für Sintereisenelektroden. Dabei können wir ein schwefelfreies System schaffen, das potenziell Korrosionsprobleme und die Degradierung von Luftelektroden reduziert.

Überbrückung der Intermittenz mit Eisenelektroden

Zusammengefasst konfrontiert uns die Schaffung eines auf erneuerbaren Energien basierenden Energiesystems mit der intermittierenden Natur der erneuerbaren Stromerzeugung. Zur Überbrückung der Unbeständigkeit benötigen wir Speicherlösungen für Strom und Wasserstoff. Mit einer durchgehenden Wasserstoffversorgung könnten synthetische Kraftstoffe auf Basis erneuerbarer Energien in großem Maßstab hergestellt werden. Mit dem Nickel-Eisen-Battolyseur und dem Eisen-Luft-Battolyseur kann Strom gespeichert werden und überschüssigen Strom in Wasserstoff umgewandelt werden, um der zwangsweisen Abschalten von Strom aus Erneuerbare Energien entgegenzuwirken. Mit dem Konzept der MC-Elektroden und der HSP-Zelle kann die Wasserstoffproduktion effizient gesteuert, gespeichert und kontrolliert werden, um eine durchgängige Wasserstoffproduktion bereitzustellen. Die Eisenelektrode ist präsent in allen Konfigurationen und das Wiederaufladen war die größte Herausforderung. Wir gingen das Problem Wiederaufladbarkeit an mit einer modifizierten Synthesestrategie für gesinterte Eisenelektroden, die jetzt mit Zirconiumoxide und Aluminiumoxide dotiert sind, statt mit Schwefel. Elektroden, hergestellt mit dieser Strategie, können das Potenzial haben, als effektive Sintereisenelektroden zu fungieren.

Mit diesen neuen einfachen Konzepten und kostengünstigen Eisenelektroden bieten wir neue Mittel zur Unterstützung und Beschleunigung der Speicherung und Umwandlung von erneuerbarer Energie, die für die Energiewende und zur Überwindung der Intermittenz erforderlich sind. Wir müssen die Energiewende beschleunigen, um die Auswirkungen des Klimawandels zu begrenzen.

1

Introduction

1

1.1. Broader context

Without rigorously cutting CO_2 emissions global warming will exceed the intended limit of 1.5 °C defined in the 2015 Paris Agreement. Every tonne CO_2 emitted contributes to global warming [1]. In the last decades mankind developed and implemented new technologies to harvest renewable energy and replace fossil fuel usage. These new technologies mainly provide electricity with a projected market share of almost 30% for 2021 [2]. Although it is important to transform the electricity generation from fossil fuels to renewables, it is only one part of our global challenge. Other sectors such as transportation and industry also have to shift to a green feedstock, hydrogen, or synthetic fuels, to reduce their CO_2 emissions and limit global warming.

Figure 1.1 shows the – still representative - global energy-related CO_2 emissions by sector and indicates that approximately 1/3 of these emissions have no economically viable option for decarbonisation [3]. Among these sectors are the cement industry and the iron and steel industry which heavily rely on fossil fuels, such as coal, for the generation of high temperature heat. Substituting coal is essential for reaching the climate targets. For example, by electrification or by using hydrogen or other synthetic fuels, based on renewables.

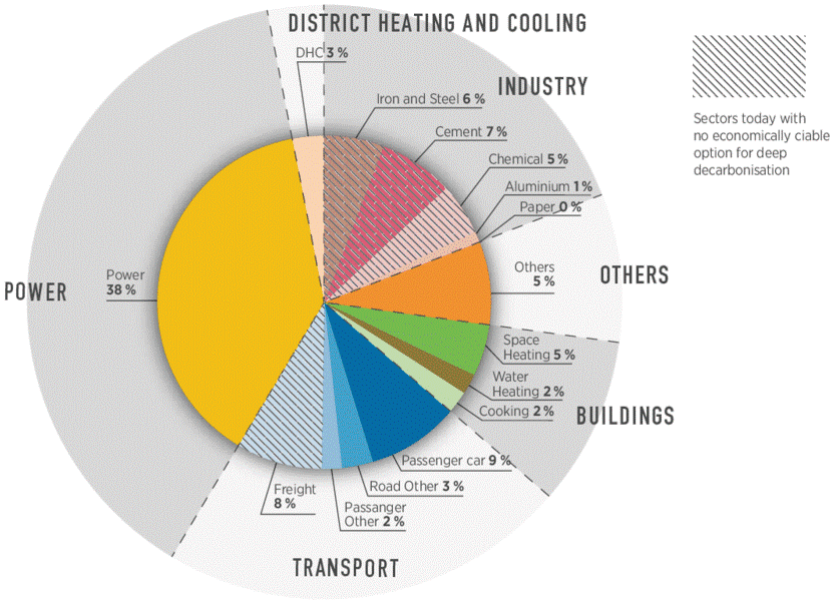

Figure 1.1: Breakdown of global energy-related CO_2 emissions by sector in 2015. Reprinted from ref. [3].

The challenges we face are multilateral; With the projected market share of 30%, renewable electricity is developing in the right direction, but not fast enough to meet the Paris-goals. And with no effective possibility of storing renewable electricity, at times when there is much sun or wind, there is more renewable electricity available than can be used and the power grid can handle. The only current option is that installed capacities with the potential to produce excess electricity, are turned off because the grid cannot handle it and the electricity cannot be stored. To avoid this so called 'curtailment', the intermittent nature of renewables has to be handled by demand response on the one hand and when that is insufficient by cost-efficient storage solutions [4]. But even if we manage that, we would only have solved the electricity part of the energy-puzzle.

How will the mentioned other sectors such as transportation and industry contribute to reduce their CO_2 emissions. Currently hydrogen production is essentially based on fossil fuels and caused nearly 900 Mt CO_2 emissions in 2020, about 3% of the total energy-related CO_2 emissions [5]. An entire new infrastructure has to be created for the production of green hydrogen. Not only do we have to replace the existing fossil fuels based hydrogen production, but the energy and fuel-demand for all the other sectors has to be produced too. Adding complexity to this puzzle is the requirement that the green synthetic fuels must be as easily stored and transported as oil or coal because the production and the usage will be separated in time and place. The scale is enormous which also means that the so needed novel concepts should be cost-efficient and based on abundant materials.

With a 72% application in stainless steel and 7% usage in batteries, nickel is an important element in the current sustainable developments [6]. In Li-ion batteries nickel is one of the crucial elements which forms the cathode. With increasing demand of electric vehicles, the demand in nickel increases too, nonetheless, that nickel does not meet the given requirements of low prize and earth abundance. It is foreseen for the EU, that a suitable feedstock supply for high quality nickel, necessary for lithium batteries, will be a "bottleneck" with a potentially structural deficit post 2027 [7].

This is why we should use nickel as efficient as possible and implement alternative materials. Figure 1.2 displays a chart which indicates abundant elements and iron is such an alternative. The metal abundance of iron is about 2000 times higher than that of nickel. Iron is a widely used non-toxic element. Iron is the cheapest transition metal which is broadly available in the earth crust, and about 40 times cheaper than nickel [9]. Iron is used in omnipresent products and can also be used as a negative electrode in alkaline batteries, best-known from the Ni-Fe batteries. This makes iron an essential material for the

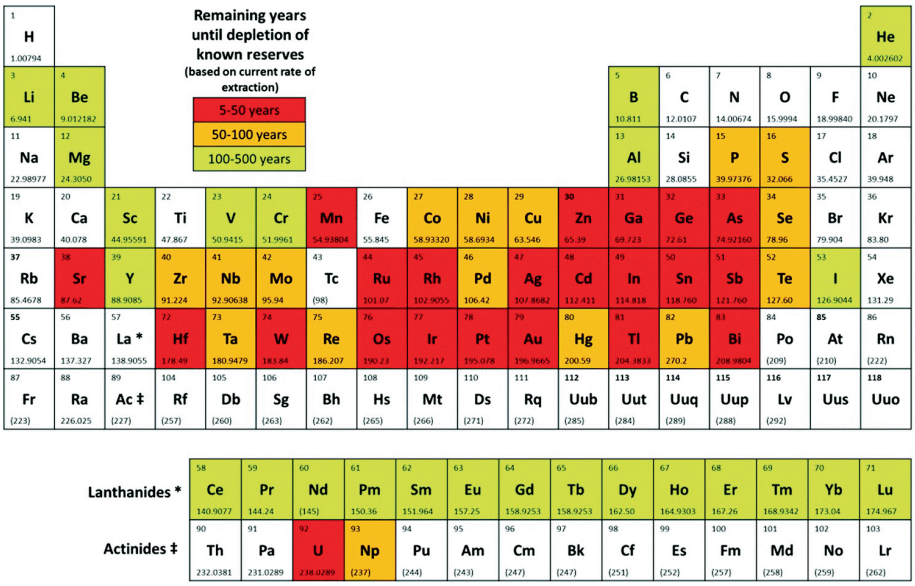

Figure 1.2: Number of years of rare and precious metal reserves if consumption continues at present rate, reprinted from ref. [8].

energy transition.

When we bring all these requirements together, we need concepts based on earth abundant, cheap materials, that can both provide renewable electricity and renewable fuel and that can overcome the intermittent nature of the renewable sources.

1.2. Scientific background

Electrochemistry will be a cornerstone of the future energy system, the link between renewable electricity generation, for instance wind and solar, on the one hand and electricity storage and conversion on the other hand. Batteries and electrolysers, both are electrochemical devices, batteries store electricity while electrolysers convert an electricity input into useful products. This section provides a brief introduction of the scientific background.

In electrochemistry, the most commonly used reference voltage is that of the 'Standard Hydrogen Electrode' or SHE. The chemical reactions at a single electrode are called 'half reactions', as they do not balance the number of electrons in the battery. The energy level of the electrons in a half reaction is specified as the voltage relative to an SHE.

To describe the chemistry of a whole battery, the half reactions at both

electrodes are described, with associated voltages. So, in the NiFe battery, the transition metals in the electrodes change their oxidation state. Iron gains two electrons (is 'reduced') on charging and changes its oxidation state from +2 to 0. Nickel loses one electron (is 'oxidised') and changes its oxidation state from +2 to +3 on charging. In a balanced system both electrodes provide the same storage capacity. To balance both electrodes of a NiFe battery, this requires twice as many atoms of nickel as of iron, as an atom of nickel can only store one electron, and an atom of iron can store two.

The following equations show the half reactions for iron electrode (1.1) (−0.88 V vs SHE) and the nickel electrode (1.2) (0.49 V vs SHE). Reaction (1.3) shows the cell reaction and its equilibrium potential of 1.37 V (=0.49-(-0.88)), the difference of their relative potentials. The left side of the reactions shows the discharged state and the right side the charged state.

$$Fe^{2+}(OH^-)_2 + 2e^- \rightleftharpoons Fe^0 + 2OH^- \tag{1.1}$$

$$Ni^{2+}(OH^-)_2 + OH^- \rightleftharpoons Ni^{3+}O^{2-}(OH^-) + H_2O + e^- \tag{1.2}$$

$$Fe(OH)_2 + 2Ni(OH)_2 \rightleftharpoons Fe + 2NiOOH + 2H_2O \tag{1.3}$$

$$H^+ + OH^- \rightleftharpoons H_2O \tag{1.4}$$

Reaction (1.4) shows dissociation and recombination of water, which occurs during operation to compensate for the change in oxidation state of nickel and iron, both electrodes have to remain charge neutral. In the discharged state the nickel electrode stores additional protons and electrons and the iron electrode hydroxyl ions and electron holes. Upon charging water is formed at the nickel electrode.

Electrodes for electrolysers are designed to perform a reaction during operation while the electrodes themselves remain unchanged. Reaction (1.5) (+0.40 V vs SHE) shows oxygen production at the nickel electrode, reaction (1.6) (−0.83 V vs SHE) shows hydrogen generation at the iron electrode and reaction (1.7) the overall reaction for the electrolysis of water with a potential of 1.23 V. The potential of 1.23 V can be derived from the Gibbs free energy which represents the required chemical energy for electrolysis. Additional energy is needed to turn a liquid into more gas molecules, because the gas has a higher entropy than the liquid. When this energy is included, 1.48 V (the thermo-neutral potential) is needed.

$$4OH^- \rightarrow O_2 + 2H_2O + 4e^- \tag{1.5}$$

$$2H_2O + 2e^- \rightarrow H_2 + 2OH^- \tag{1.6}$$

$$2H_2O \rightarrow 2H_2 + O_2 \tag{1.7}$$

When multiple reactions are possible in a battery, the reactions with the lowest potential are most likely to take place. In a NiFe battery, possible reactions include those of iron (1.1), nickel (1.2), oxygen (1.5), and hydrogen (1.6). To help visualise the different reactions, their relative potentials, and how those change when concentrations (including pH, which determines the concentrations of OH^- and H^+) change, Pourbaix diagrams are used. Pourbaix diagrams indicate the stability of compounds in aqueous (watery) systems. The y-axis in the Pourbaix diagram indicates the potential and the potential difference indicates the energy gain/cost per electron and the x-axis the concentration.

Figure 1.3 shows the Pourbaix diagram of the NiFe battery together with the stability window of water which is located between the (a) and (b) line. Within the stability window no gas formation is expected and water is stable. Above the (b) line oxygen evolution can occur and below the (a) line hydrogen evolution. Figure 1.3 also indicates the lines for the phase transitions associated with the iron electrode (c) and the nickel electrode (d) and the equilibrium potential for the nickel-iron battery. The numbers (1), (2), (5), and (6) in Figure 1.3 refer to the reactions above. Due to resistances the observed voltage will exceed the equilibrium potential during charging and overcharging and will fall below the equilibrium potential during discharging.

The deviation of the observed voltage during operation from the equilibrium potential depends on (1) the applied rates during (dis)charging and on (2) the state of charge (SoC). Higher rates enable faster charging and discharging and lead to higher currents and higher losses. Consequently the deviation from the equilibrium voltage will increase. The state of charge describes the ratio of the available discharge capacity to the full discharge capacity, 0% for a discharged battery and 100% for a completely charged battery. At the beginning of the charging process (SoC=0%) and at the beginning of the discharge process (SoC=100%) all most favourable sites are available for phase conversion. These sites can be converted with little resistances, the observed potential will deviate little from the equilibrium voltages. At the end of the charging process (SoC close to 100%) and at the end of the discharge process (SoC close to 0%) only unfavourable sites will remain for phase conversion. These sites are more difficult to reach and therefore the cell resistance will be higher and with it the deviation of the observed voltage from the equilibrium voltage. More energy will be lost.

The position of the equilibrium potentials and the potential for oxygen evolution and hydrogen evolution in the Pourbaix diagram will be of utmost importance for the following sections. Electrodes with different functionalities will be introduced and recombined in novel configurations. However, their positions for the specific functions as depicted in the Pourbaix diagram will not change.

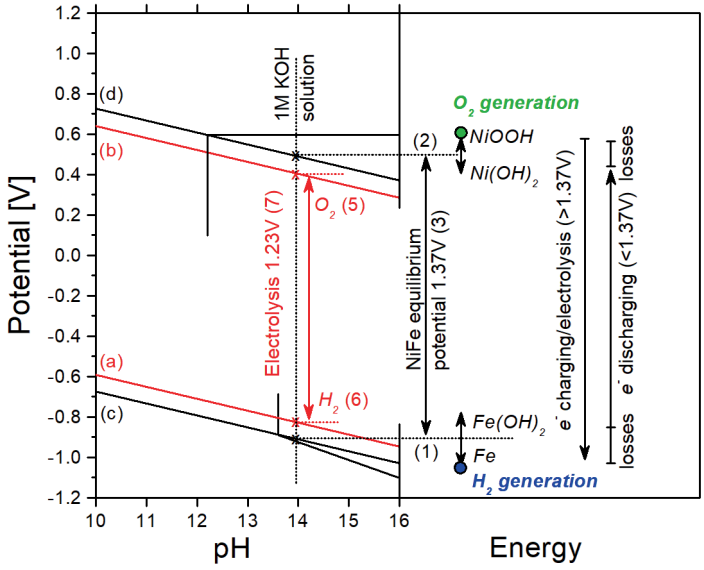

Figure 1.3: (left) Simplified Pourbaix diagram. Above the top red line (b) oxygen production is possible and below the bottom red line (a) hydrogen production is possible. The black line (c) indicates the phase equilibrium between Fe and $Fe(OH)_2$ and the black line (d) the phase equilibrium between $Ni(OH)_2$ and NiOOH. All four lines shift with the pH, the concentration of hydroxide ions. The vertical dotted line shows a 1M KOH solution, in line with the equations above. Their intersections with lines (a-d) represent the reported potential vs SHE. (right) The arrows indicate the equilibrium potential for the NiFe battery and the operational range for the nickel and for the iron electrode. Upon charging and electrolysis electrons travel from the nickel electrode to the iron electrode. The observed potential will be larger than the equilibrium potential because of resistances. Upon discharging electrons travel from the iron to the nickel electrode and the observed potential will be smaller than the equilibrium potential because of resistances.

In the end, it is their position in the Pourbaix diagram which defines the energy requirement for all combinations.

1.3. Research questions and outline of the thesis

The aim of this thesis is the research and development of storage solutions mainly based on iron and to bridge intermittency. The following scientific questions are the basis of the conducted research:

1. Combined battery and electrolyser: is it possible and reasonable to develop a device that serves two purposes? Do the materials endure and support this double functionality? (Chapter 2, ref. [10])

2. Multiple electrodes: nickel is required for electricity and oxygen storage; iron is required for electricity and hydrogen storage. Is it possible to store electricity, oxygen and hydrogen in one electrochemical cell? Is it possible to decouple the electricity input from the oxygen and hydrogen output? Can a single electrode be used for two purposes simultaneously? Are such configurations with multiple electrodes scalable to larger arrays? (Chapter 3, ref. [11])

3. Fundamentals of iron electrodes: Which phases occur for the first and second iron discharge plateau? And why are iron electrodes less responsive to higher discharge rates? (Chapter 4, ref. [12])

4. Sustained hydrogen from intermittent sources: Chapter 3 shows that decoupling of the electricity input and the hydrogen output is possible with an electrochemical cell consisting of at least three electrodes. Is sustained hydrogen from intermittent sources also feasible with a standard electrochemical cell with two electrodes? (Chapter 5)

5. Doped iron electrodes: Chapter 4 shows that iron electrodes have a limited rechargeability and in addition can have gas accumulation inside the electrode. Does the addition of dopants enhance the ability of the iron electrode to recharge? Do these dopants enhance performance and the material utilisation? (Chapter 5)

After this introduction and theoretical background, Chapter 2 discusses the combined BATTery and electrOLYSER [10, 13]. The battolyser-concept is based on the NiFe battery as developed by Jungner and Edison in 1901 and alkaline electrolysis. Two features make the NiFe battery attractive as combined battery and electrolyser: first, the active catalysts, which can reform with every battery-cycle and second, the overlap of the position of the electrodes with the stability

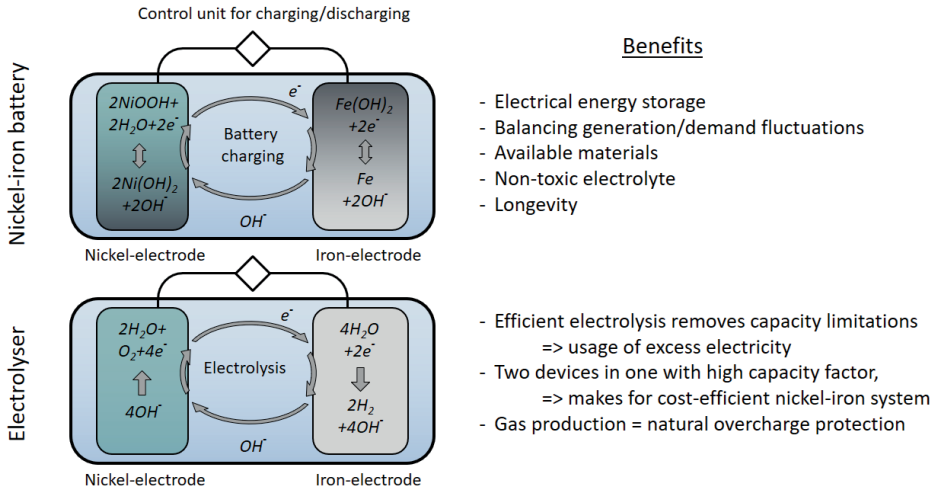

Figure 1.4: Benefits originating from the nickel-iron battery and the integrated electrolysis function.

window of water in the Pourbaix diagram, see figure 1.3. Charging automatically drives the electrodes to a potential where electrolysis occurs, and the catalysts are formed and reformed naturally. Figure 1.4 depicts the benefits of a combined nickel-iron battery.

Chapter 3 describes how the electricity input can be decoupled from the hydrogen output by adding additional electrodes to the electrochemical system. A sustained hydrogen output can now be realised efficiently since an iron storage electrode can be charged when electricity is cheap and abundant while only a fraction of the electricity is required to generate hydrogen at times when the renewables are scarce. Figure 1.5 schematically illustrates a cell with three electrodes which can simultaneously provide hydrogen and electricity from an iron storage electrode. Additionally, impressions from a multi-cell arrangement, demonstrated during the NWO Teknowlogy day on November 7$^{\text{th}}$, 2019 are compiled in Appendix A.

Chapter 4 investigates the phase behaviour of an iron electrode in operando. The applied technique, neutron diffraction, allows to determine what is happening in the bulk of the electrode. We could determine the phases for the first and the second iron discharge-plateau and from the observed fractional changes we concluded that substantial amounts of iron are present in an amorphous phase as they were not detectable in diffraction peaks. Moreover, we detected substantial amounts of iron hydroxide inside the electrode in the charge state which suggests that the iron electrode in this case lacks the ability to recharge.

1

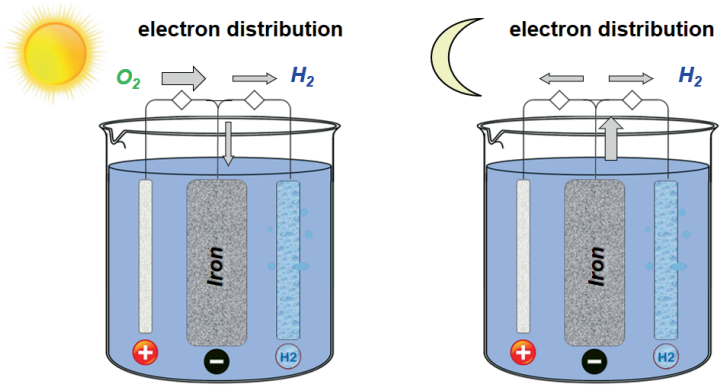

Figure 1.5: Three electrode arrangement with a central iron storage electrode and two controllers to distribute the currents (grey arrows) among the electrodes. The iron electrode is charged when the charging current exceeds the current for hydrogen production (left) and discharge to provide electricity and delayed hydrogen generation simultaneously (right).

Recharging is essential for proper full capacity operation of the electrode. Figure 1.6 displays the outcome which illustrates the perhaps unexpected high amount of amorphous iron phases.

Chapter 5 introduces two concepts: the hydrogen storage and production (HSP-)cell and a synthesis strategy for doped sintered iron electrodes.

- The HSP-cell is a combination of a bifunctional electrode for hydrogen and oxygen generation with an iron storage electrode, and as such similar to a half cell for testing iron electrodes but with a different application. This configuration allows to enhance the system specific storage capacity by

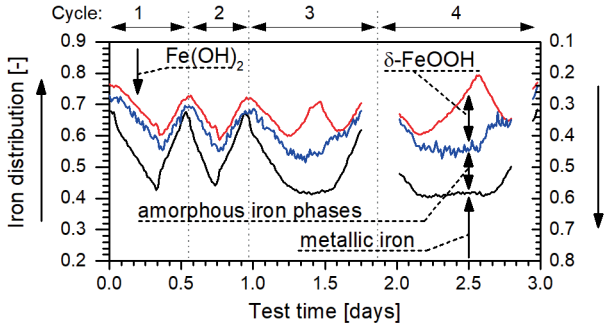

Figure 1.6: Observed iron distribution during operation. From top to bottom: $Fe(OH)_2$, $\delta-FeOOH$, amorphous iron phases and metallic iron. Reprinted from ref. [12].

utilizing the entire iron storage capacity, comparable to an iron-air battery but delivers hydrogen instead of electricity. Phase-shifted operation of HSP-cells has the potential to provide a more sustained hydrogen output from intermittent electricity by splitting up to different HSP-cells.

- Having a proper iron electrode is the central part for all previously discussed configurations. In Chapter 4 we described that our thicker sintered iron electrodes lack the ability to recharge. We addressed this issue by adding as dopants zirconia oxide and alumina oxide to our synthesis strategy. The produced electrodes show good rate performance and a high volumetric storage density even without intentionally adding sulphur additives. Apart from that, the devised strategy offers several other advantages for the production process, see Chapter 5.

Providing potential new solutions to address the intermittency issue associated with renewables is key for the electricity storage and conversion within the energy transition. The work presented in this thesis offers not only new electrochemical concepts to overcome intermittency, but also points out, that highly needed electrochemical storage and conversion can be realised with earth-abundant iron.

References

[1] V. Masson-Delmotte, P. Zhai, A. Pirani, S. L. Connors, C. Péan, S. Berger, N. Caud, Y. Chen, L. Goldfarb, M. I. Gomis, , M. Huang, K. Leitzell, E. Lonnoy, J. B. R. Matthews, T. K. Maycock, T. Waterfield, O. Yelekçi, R. Yu, and B. Zhou (eds.), *Climate change 2021: The physical science basis. contribution of working group I to the sixth assessment report of the intergovernmental panel on climate change,* IPCC, Cambridge University Press, In Press (2021).

[2] IEA, *Global Energy Review 2021,* IEA, Paris (2021).

[3] IRENA, *Hydrogen from renewable power: Technology outlook for the energy transition,* International Renewable Energy Agency, Abu Dhabi (2018).

[4] B. Frew, B. Sergi, P. Denholm, W. Cole, N. Gates, D. Levie, and R. Margolis, *The curtailment paradox in the transition to high solar power systems,* Joule **5**, 1143 (2021).

[5] IEA, *Hydrogen,* IEA, Paris (2021).

[6] First use of Nickel, https://nickelinstitute.org/about-nickel-and-its-applications/#04-first-use-nickel, (Accessed January 15, 2022).

[7] J. Fraser, J. Anderson, J. Lazuen, Y. Lu, O. Heathman, N. Brewster, J. Bedder, and O. Masson, *Study on future demand and supply security of nickel for electric vehicle batteries,* Publication Office of the European Union: Luxembourg (2021).

[8] A. J. Hunt, T. J. Farmer, and J. H. Clark, *CHAPTER 1. elemental sustainability and the importance of scarce element recovery,* in *Element Recovery and Sustainability* (Royal Society of Chemistry, 2013) pp. 1–28.

[9] M. Chen, Q. Liu, S.-W. Wang, E. Wang, X. Guo, and S.-L. Chou, *High-abundance and low-cost metal-based cathode materials for sodium-ion batteries: Problems, progress, and key technologies,* Advanced Energy Materials **9**, 1803609 (2019).

[10] F. M. Mulder, B. M. H. Weninger, J. Middelkoop, F. G. B. Ooms, and H. Schreuders, *Efficient electricity storage with a battolyser, an integrated Ni–Fe battery and electrolyser,* Energy & Environmental Science **10**, 756 (2017).

[11] B. M. H. Weninger and F. M. Mulder, *Renewable hydrogen and electricity dispatch with multiple Ni–Fe electrode storage,* ACS Energy Letters **4**, 567 (2019).

[12] B. M. H. Weninger, M. A. Thijs, J. A. C. Nijman, L. van Eijck, and F. M. Mulder, *Neutron diffraction study of a sintered iron electrode in operando,* The Journal of Physical Chemistry C **125**, 16391 (2021).

[13] B. M. H. Weninger, *The battolyzer - Combined short- and long-term energy storage*, Master's thesis, TU Delft (2016).

2

Efficient electricity storage with the battolyser, an integrated Ni-Fe battery and electrolyser

Grid scale electricity storage on daily and seasonal time scales is required to accommodate increasing amounts of renewable electricity from wind and solar power. We have developed for the first time an integrated battery-electrolyser ('battolyser') that efficiently stores electricity as a nickel-iron battery and can split water in hydrogen and oxygen as an alkaline electrolyser. During charge insertion the $Ni(OH)_2$ and $Fe(OH)_2$ electrodes form nanostructured NiOOH and reduced Fe, which act as efficient oxygen and hydrogen evolution catalysts respectively. The charged electrodes use all excess electricity for efficient electrolysis, while they can be discharged at any time to provide electricity when needed. Our results demonstrate a remarkable constant and high overall energy efficiency (80-90%), enhanced electrode storage density, fast current switching capabilities, and a general stable performance. The battolyser may enable efficient and robust short-term electricity storage and long-term electricity storage through production of hydrogen as fuel and feedstock within a single, scalable, abundant element based device.

This chapter has been published as "Efficient electricity storage with a battolyser, an integrated Ni–Fe battery and electrolyser" by F.M. Mulder, B.M.H. Weninger, J. Middelkoop, F.G.B. Ooms and H. Schreuders. Energy Environ. Sci., 2017,10, 756-764. (Supporting Information see appendix B)

2.1. Broader context

Electricity storage in batteries and artificial hydrogen fuels is key to enable the implementation of renewable energy from intermittent solar and wind power. This calls for both environmentally sound and durable batteries and electrolysers. Here, we design an integrated battery and electrolyser in one novel device based on electrodes that contain the abundant elements Ni and Fe as active elements. The battery – electrolyser operates efficiently as a battery and when fully charged as an electrolyser. It is remarkable that the electrodes form and reform the active battery materials $Ni(OH)_2$ and $Fe(OH)_2$ during discharge even after long term electrolysis. The oxygen evolution catalyst NiOOH and the hydrogen evolution catalyst of reduced Fe are formed automatically during charge. The operation is shown to be up to 90% energy efficient, highly durable and flexible, where the electrolysis also protects intrinsic battery overcharge. The flexibility is such that it enables storing electricity for the short term, therefore circumventing conversions to fuel and back, while also enabling conversion to fuel for long term storage. The materials efficiency of integrating two applications in one is high, which is an additional environmental benefit.

2.2. Introduction

In a renewable energy future the storage of electricity in batteries [1, 2] and in the production of hydrogen fuels [3, 4] will be required [5, 6]. Together they should provide adequate energy availability on both daily and seasonal timescales at the times when renewable sources have too low production. Batteries will be used for short-term energy efficient storage while long-term storage requires hydrogen fuels at the expense of conversion losses when generating electricity afterwards. The typical volume of energy stored on the various days in a year may range from equal amounts of battery storage and fuel generation (summer), to the whole capacity only as battery storage (autumn - spring) [6]. The storage infrastructure should provide for these different requirements throughout the year, and support the 'storage merit order' of first efficient battery storage, and second less efficient fuel production, storage and conversion. The battolyser presented here integrates the functionality of the Ni-Fe battery [7, 8] and the alkaline electrolyser [9–12] in one flexible, switchable and efficient solution. Most remarkably the battery electrodes and the hydrogen and oxygen evolution catalysts are formed and reformed over many charge and discharge cycles while there is excellent battery reversibility after prolonged charge insertion and electrolysis. It may provide an optimal utilisation factor throughout the year, by storing and providing electricity, and converting excess electricity far beyond the

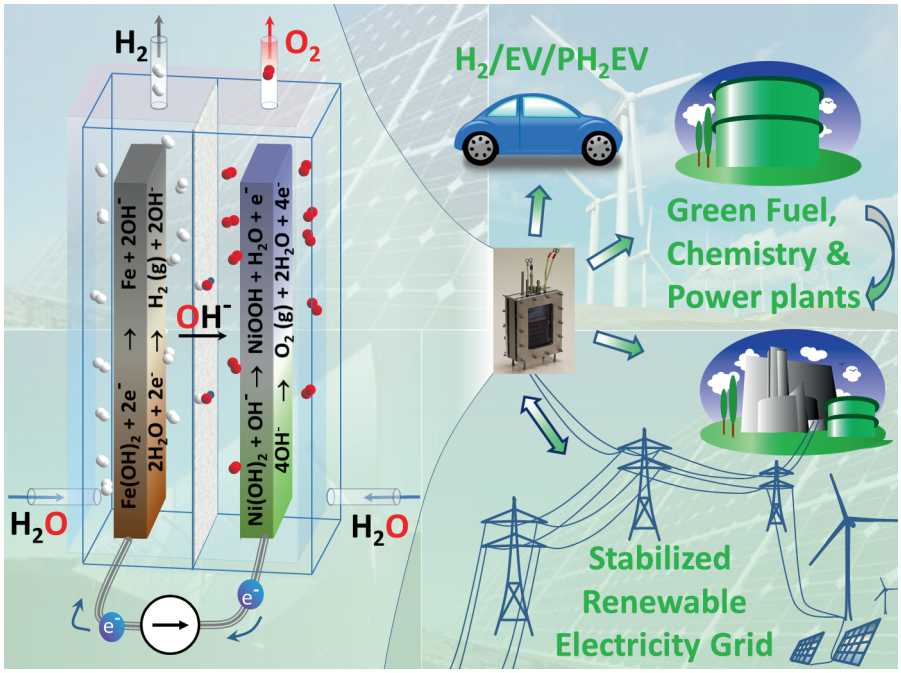

Figure 2.1: Battolyser functionality and application areas. (Left) Integrated electrochemical battery and electrolyser (*battolyser*) layout. During charge the Ni-Fe electrodes store electricity from the electricity source, converting the electrode materials as indicated. When fully charged hydrogen and oxygen are formed by splitting water. The grey diaphragm transmits OH^- and separates O_2 and H_2. (Right) Potential applications of the battolyser: as sink and source for stabilising the electricity grid, for supplying electricity as well as H_2 as fuel for e.g. plug-in hybrid electric and hydrogen vehicles (PH_2EV), and for H_2 as chemical feedstock.

battery capacity to hydrogen. The hydrogen production may enable long-term energy storage in (effectively carbon neutral) fuels and feedstock via chemical processes such as the Sabatier (methane from H_2 and CO_2), Haber-Bosch (ammonia synthesis from clean H_2 and N_2, which has current industrial efficiencies above 90% [13] and provides high energy density liquid storage at room temperature (RT) and ~ 8.5 *Bar*), and Fischer- Tropsch (alkanes from CO/CO_2 and H_2) process.

Figure 2.1 illustrates the battolyser and the function it can provide in several potential application areas. The device has a negative electrode in which $Fe(OH)_2$ is reduced to Fe upon charge:

$$Fe(OH)_2 + 2e^- \xrightarrow{\text{charge}} Fe + 2OH^- \tag{2.1}$$

(-0.88V relative to the standard hydrogen electrode (SHE)), considering only the Fe/Fe^{2+} discharge plateau. The positive electrode contains $Ni(OH)_2$ that upon charge releases a proton:

$$Ni(OH)_2 + OH^- \xrightarrow{\text{charge}} NiOOH + H_2O + e^- \tag{2.2}$$

(+0.49V vs SHE). An alkaline KOH electrolyte conducts the OH^- ions. These electrode materials are known from the robust Ni-Fe battery introduced by Jungner and Edison which has also a track record of extreme longevity [7, 8]. When becoming fully charged the formed Fe and NiOOH electrodes become increasingly active as efficient hydrogen (HER) and oxygen evolution reaction (OER) catalysts at increased cell potential. Then at the positive electrode the oxygen evolution takes place:

$$4OH^- \xrightarrow{\text{overcharging}} O_2(g) + 2H_2O + 4e^- \tag{2.3}$$

(1.23 - 0.059 x pH vs SHE) and at the negative electrode hydrogen evolution:

$$2H_2O + 2e^- \xrightarrow{\text{overcharging}} H_2(g) + 2OH^- \tag{2.4}$$

(0.00 – 0.059 x pH vs SHE). It is known in literature that the HER and OER catalysts are efficient in alkaline environment indeed [14], but here it will be shown that they are formed and reformed spontaneously during many charge, electrolysis and full discharge cycles, without apparent loss of functionality. Cyclic voltammograms for both electrodes (see appendix Figure B.7) are in agreement with literature [15, 16] and ascertain the reaction mechanism. A ceramic polymer composite diaphragm [11, 17] separates hydrogen and oxygen gas while permitting the flow of OH^- ions between the electrodes. For construction see appendix Figure B.1.

2.3. Concept of the battolyser

The integrated battery and electrolyser concept works as follows: the battery functionality provides electricity storage capacity, which is charged when a surplus of renewable electricity is available and discharged when there is an electricity deficiency. The battery functionality stores electricity directly with high power-to-power efficiency. When the battery is reaching its designed capacity, production of hydrogen from the excess electricity larger than the battery capacity takes place, i.e. the combination of battery and electrolyser has no capacity restriction. Utilising hydrogen as storage requires a hydrogen storage method and back conversion from hydrogen to power (not considered here), which lower

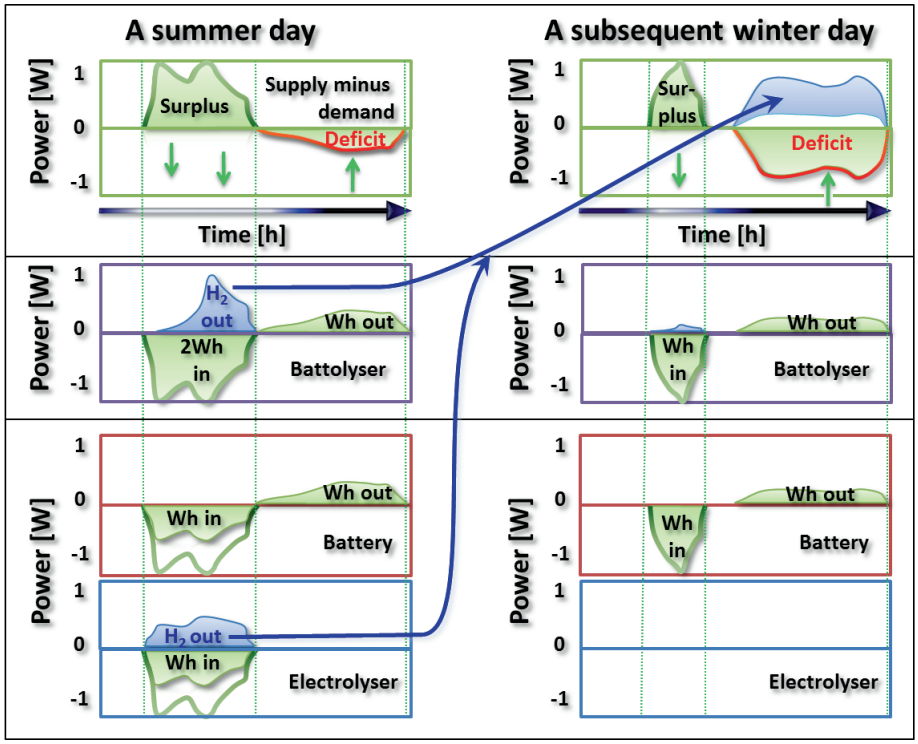

Figure 2.2: Battolyser utilisation. Illustration of storage of a surplus of renewable power (top) using the battolyser (middle) or in a separate battery and electrolyser (bottom). The full power (indicated by W) and energy (W h) capacities are a hardware choice that needs to provide the necessary power and energy storage handling capabilities during the different days throughout the year. On the left summer day there is both short-term (green area) and long-term (blue H_2 area) storage; in autumn, winter or spring, the full surplus energy and power may go into short term storage only because one requires the power a few hours later (and one prevents conversion to fuel since conversion means higher energy losses) [6]. The indicated daily deficits are compensated by short-term battery capacity (on this summer day) and by the battery plus hydrogen derived electricity (the winter day)

the overall power-to-power efficiency considerably compared to battery storage. However, hydrogen or its derived fuels are needed for seasonal energy storage since batteries are too costly to utilise only once in a season and also have much lower energy density than liquid hydrogen fuels like e.g. liquid ammonia or alkanes. The optimisation of the overall energy efficiency thus provides a rationale for combining efficient short term battery storage and long term hydrogen fuel storage.

The battolyser has the capability to follow electricity fluctuations caused by renewable generation or consumers demand as it allows for various charge and discharge rates. The device can operate essentially around the clock, leading to a high degree of utilization: either the electricity surplus is stored in electrical storage capacity and hydrogen or electricity is provided from the storage when there is a deficit. An illustration of potential battolyser use throughout characteristic days of the year is given in Figure 2.2 in a comparison with an independent battery and electrolyser next to each other. Hydrogen will be produced at times when renewable electricity is that highly available that the battery capacity is already reached and electricity prices are therefore low because of abundant supply. The battolyser will be used almost continuously while the individual battery and electrolyser will have a significantly lower utilisation or capacity factor; the electrolyser has no use hours in large periods of the year because the electricity surpluses are not larger than the battery capacity. Low utilisation factors are generally from the economical and materials use standpoint unfavourable. In principle the battolyser uses a single system instead of two separate ones which is also highly important for economic considerations.

2.4. Results

2.4.1. Functionality of the battolyser

The battolyser provides a flexible storage capacity for increasing charge insertion with full intermediate discharge, see Figure 2.3. Increasing electrical current insertion results in increasing battery electrode charging, and when charged, increasing electrolytic gas production. Increasing electrical current insertion far beyond the nominal cell capacity not only enables electrolytic gas production but also allows for usage of electrode material normally not employable for battery operation, and thus yielding higher discharge capacities. Hydrogen evolution starts at small rates immediately, whereas initially no oxygen evolution is detected. This is because the Ni electrode is the limiting electrode in the battolyser cell, which means that after discharge there is almost no NiOOH available to catalyse O_2 evolution, while there is still some unreduced Fe allow-

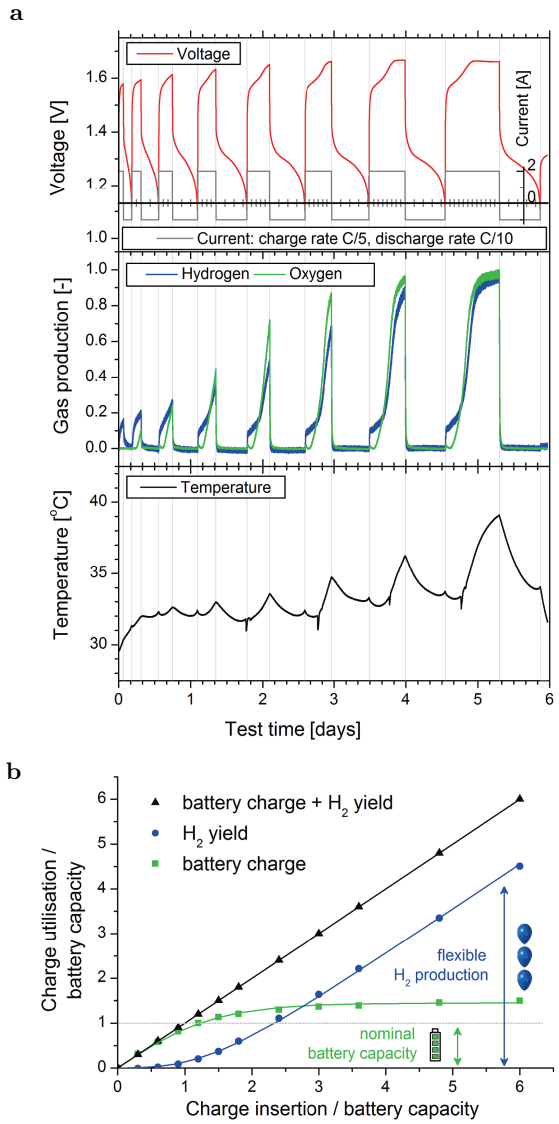

Figure 2.3: Battery and electrolysis yield. (a) Top: Observed potential during constant current insertion over increasing durations, followed by full discharges to 1.1 V. (The horizontal axis includes additional grey tick-marks for charge or discharge, step size ±0.3 C) Middle: Resulting normalised hydrogen and oxygen evolution. Bottom: Temperature development for the thermally insulated cell (detailed information see appendix Table B.2 and appendix Figure B.9). (b) Battolyser utilisation of charge in the battery and the H_2 production divided by the nominal battery discharge capacity of C=10 A h (now measured at constant regulated temperature of 30 °C). The drawn lines are fits with equation (2.9) and (2.10), see Experimental section. (Detailed information see appendix Table B.3.)

ing for hydrogen evolution. The normalised oxygen evolution catches up later and surpasses hydrogen evolution at about 80% of the nominal discharge capacity of the battery (C), 4 h after the start of each charge insertion. The highest gas evolution starts after the battery is charged to the nominal reversible battery discharge capacity of 10 A h (see also Experimental section and appendix Figure B.2b). Overall, stoichiometric gas evolution takes place. During discharge a fast decrease of gas evolution towards zero is observed. This is in line with earlier gas measurements of Ni-Fe batteries that were performed to characterise the occurring gas compositions in relation to explosion risks [18]. During battery (dis-)charge or electrolysis the temperature increases when the overpotentials increase compared to the battery open circuit potential (OCV) or the thermoneutral water splitting potential respectively (Setup with thermally insulated cell, see Experimental section). Interestingly the gas evolution is not constant during electrolysis. We attribute this to the increasing device temperature which promotes electrolysis, leading to increased gas yield at the expense of slower battery charge.

We designed a test-series to simulate various real-life renewable electricity supply and demand situations with partial and full (dis)charging, rapid charge-discharge switching, continuous or intermittent overcharging, as well as the around the clock cycling for months. The results are shown in Figure 2.4 and in appendix Figure B.4. Experiments were performed in four separate cells and proved to be fully reproducible between cells. The remarkable findings in Figure 2.4 are the overall stability of the energetic efficiency at 80-90% over many different types of cycles (see appendix Figure B.3 for selection of performed cycles), and the stability of the reversible discharge capacities of the battery even after more than 500 deep discharges and (over-)charges to more than 1000 times the nominal capacity. On average more than 40% of the total inserted charge was used for performing electrolysis. Energetic efficiency is calculated from the sum of the energy retrieved during the cell discharge and the chemical energy from hydrogen that was produced (see Experimental section and appendix Figure B.2a). Neither the battery capacity nor the electrolysis are harmed by the many cycles that included battery overcharges up to 10 times the nominal capacity, rapid current reversals and deep discharges for each cycle. Such finding illustrates the viability for operation as integrated battery and electrolyser. During the test period of 18 months a single cell consumed 1451.4 g of water, where 1409.7 g (97.1%) is expected due to electrolysis, the remainder is lost via the humidification of the released gas. Other side reactions leading to more weight loss or to H_2O_2 formation are not observed in trace gas analysis; the total faradaic efficiency of battery charge plus water splitting is 100% within experimental accuracy (±0.5%, see Experimental section). The cells still

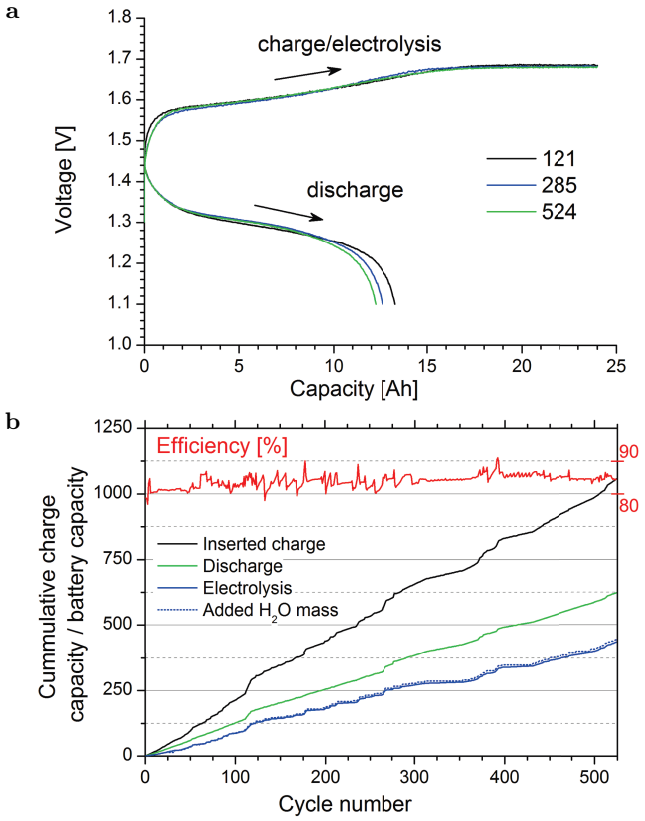

Figure 2.4: Long term cycling stability and efficiencies. (a) Voltage response of a battolyser cell being charged to 24.0 A h with subsequent discharge during the indicated cycle numbers. Changes over time are a slight ~ 7 mV decrease of the required potential during electrolysis (increases efficiency) which causes a slightly larger fraction of the 24.0 A h to be spent on electrolysis in these cycles, and equally less on battery charge. (b) The overall energy efficiency for a large number of different experimental cycles. A cycle is counted from full discharge to full discharge with various full or partial (over/dis)charge programs in between. Consistently the overall cycle energy efficiency adds up to above 80 to 90%. (see Experimental section and appendix Figures B.2,B.3 and B.4 for detail information). Also plotted is the cumulative inserted charge and breakdown in battery charge and electrolysis, and the required cumulative H_2O mass to replenish the electrolyte expressed with respect to the battery capacity.

operate with the initial electrolyte, only demineralised water was added.

The discharge capacity at an equal inserted charge of 24.0 A h is shown in Figure 2.4a. during the indicated cycles numbers. The slight reduction of the electrolysis potential (−7 mV) at the same applied current will cause that a larger amount of current is spent on electrolysis (see below). The change of the electrode occurs mainly the first 285 cycles and becomes less later on; it appears to be accompanied by a slight increase of total energy efficiency with progressing cycle number as well (Figure 2.4b). The reason may be that the large gas evolution modifies the internal electrolyte transport pathways or changes the accessibility of the catalytically active surfaces in the electrode.

As a further test of the operation of the battolyser we applied various rapidly changing charge - discharge cycles (Figure 2.5 and appendix Figure B.3). Such test may mimic the application as a peak shaving battery and electrolyser that experiences a high renewable electricity input (charge/electrolysis peak) interspaced with high electricity demand when the renewable electricity has shortages (discharge peak). As can be seen in Figure 2.5, the battery and gas production functionalities of the cell follow the applied currents directly without delay, which is an asset compared to e.g. conventional electrolysers. Most remarkably in appendix Figure B.3 the average potentials during fast charge and discharge switching come closer together, which means a higher electrical efficiency $\eta_{battery}$ during these rapidly varying currents; i.e. no adverse effects of switching but rather a positive effect.

The electrolysis potential as a function of current and temperature of a charged battolyser is shown in Figure 2.6. Higher temperatures lead to lower ionic resistance and lower cell potential, increasing efficiency. When the applied current is increased a factor 10 the required potential increases about 160 mV. This is a similar potential increase as observed for alkaline electrolysers at ~20 mA/cm^2 current densities [19]. We limited the test temperature to 40 °C preventing potential long term reduced stability issues of the iron electrode [20]. At the lowest currents, potentials below the thermoneutral potential of 1.48 V, but above the OCV of 1.37 V of the Ni-Fe battery are reached. Such electrolysis below the thermoneutral potential is possible because additional heat comes from the environment. In the normal electrolyser hydrogen production temperatures of 65 −150 °C [11, 21] are required and currents up to 400 mA/cm^2 electrode surface area are applied in a compromise between investment costs and operating efficiency (typically 71% [9]). The battolyser is operated with currents matching the normal (dis)charge rates of the battery active electrode mass and surface area, now reaching up to 20 mA/cm^2 (Figure 2.6). These same moderate currents split water efficiently at higher states of charge near room temperature, without any precious metal catalysts. These relatively moderate

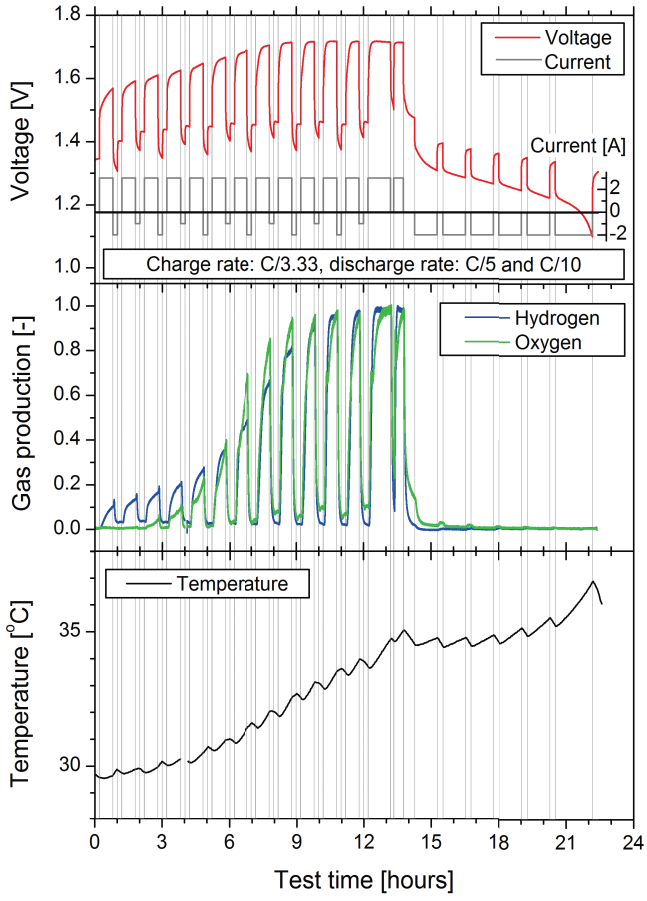

Figure 2.5: Intermittent battolyser use. (top) Sequence of intermittent charge, discharge and rest steps that shows the switching capabilities of current insertion followed by immediate current withdrawal, rests and electrolytic gas evolution. (middle) The measured hydrogen and oxygen yields. (bottom) The temperature of the insulated cell following the instantaneous heating from residual overpotential losses due to Ohmic resistances.

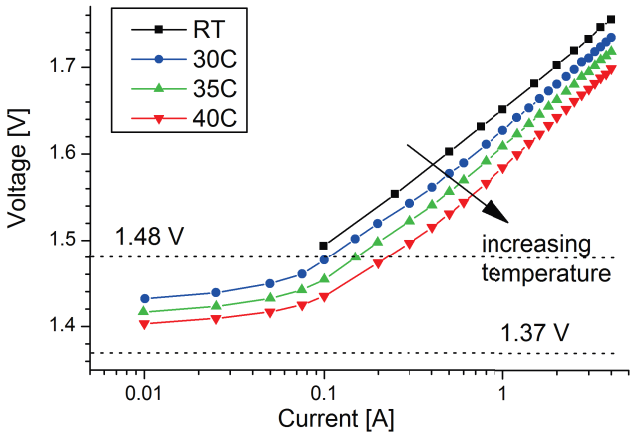

Figure 2.6: Electrolysis full cell potential. Electrolysis potential dependence on applied current for several temperatures. The total external electrode surface area is 216 mA/cm^2 and current densities up to 20 mA/cm^2 are reached.

conditions mean prolonged lifetime for all components. The operational flexibility exceeds these current limit, however: tests have been performed up to 100 mA/cm^2 with an efficiency close to 80% at a device temperature well below 40 °C (see appendix Figure B.6). Such efficiency is thus high compared to alkaline electrolysers.

Coming back to the small 7 mV reduction of the electrolysis potential observed in Figure 2.4a. we can now estimate that at a certain state of charge about 11% more current will be spent on electrolysis than on battery charging due to this 7 mV reduction. This is in line with the magnitude of the change of the battery discharge capacity after a fixed 24.0 A h charge insertion in Figure 2.4a. The way in which the current is divided over battery and electrolysis (Figure 2.3 and appendix Figure B.2b) is thus slightly changed.

2.4.2. Energy density

The volumetric energy density in Wh/L is relevant for the footprint that is occupied by an energy storage technology for stationary storage [22]. For the Ni-Fe based battery capabilities of the battolyser one can calculate the energy density of the cell, including the electrode materials but excluding external components such as electronics, water and gas treatment facilities (which are similar to an alkaline electrolyser). The theoretical energy density of the $Ni(OH)_2$ and $Fe(OH)_2$ electrode materials equals 1031 Wh/L when using only the densities of the materials and the OCV of 1.37 V. An energy density of around 130-250 Wh/L

can be estimated as a practical limit taking into account that possibly a maximum of 20-30% of the cell volume may be occupied with active materials and the rest by the conductive construction and electrolyte and gas flow areas, and also by taking into account the overpotentials for battery charge and discharge. The current experimental cell already reaches ~100 Wh/L. Such energy density may be compared with liquid sodium-sulphur batteries (150-250 Wh/L), lead-acid batteries (50-80 Wh/L Wh/L), lithium ion batteries (200 – 600 Wh/L), or vanadium redox-flow batteries (16-33 Wh/L) [23]. In addition to the battery capabilities, however, the battolyser has the electrolyser capabilities that enable an unlimited additional W h to be stored in the form of hydrogen based fuels.

2.4.3. Stability

The findings of durability and flexibility are impressive since modern batteries will be rapidly destroyed by overcharging and/or deep discharging, as well as loose the overcharge energy. Lithium ion batteries suffer from electrolyte decomposition during overcharging [24], while nickel-metal hydride and lead-acid batteries suffer mainly from detrimental corrosion effects during overcharge and deep discharge [25, 26]. The exceptional stability here will be related to the fact that the Ni and Fe based electrodes are operating between the thermodynamically stable phases in their Pourbaix diagrams [8, 27]. Apparently during the electrolysis mode at the negative electrode one can only reduce water to H_2 or reactivate iron hydroxides and oxides (when formed during deep discharge) to become Fe. The internal surface area of the electrode is sufficient for efficient HER and for reforming the $Fe(OH)_2$ during discharge. At the positive electrode any $Ni(OH)_2$ which is oxidised to NiOOH or overcharged to γ-NiOOH [28–30] will readily revert to $Ni(OH)_2$ during the discharge. Such intrinsic stable points of return during charge (Fe) or discharge ($Ni(OH)_2$, $Fe(OH)_2$) will enhance the stability of the electrodes during prolonged electrolysis operation and deep discharge. The switching tests in Figure 2.5 and appendix Figure B.3 indicate that the cell potential rapidly relaxes to around the OCV of 1.37 V. Such finding indicates that the active electrode materials are still showing the potentials corresponding to discharging NiOOH and Fe. The prolonged electrolysis does not lead to e.g. further oxidation of the Ni electrode to e.g. NiO_2.

The natural position of the electrode materials in their Pourbaix diagrams also account for the high efficiency of water splitting since the individual electrode potentials are close to the potentials for water splitting and the overall full cell potential (OCV = 1.37 V) is very close to 1.48 V, the thermoneutral potential required for water splitting.

2.5. Concluding remarks

The integration of Ni-Fe battery and alkaline electrolyser in one single device reaches high energy efficiencies of 80-90%, high compared to the individual Ni-Fe battery (~60-70% [7, 31]) and alkaline electrolysis (typically up to 71% with respect to HHV [4, 9]), and up to ~50% higher utilisation of the active battery material. The energy density of the battery capacity may reach values up to 250 Wh/L after optimisation. When only looking to the battery round trip efficiency in cycles without significant overcharging one sees efficiencies of ~80-83% (plus an additional percentage H_2, Figure 2.3, appendix Figure B.4), which may be compared to lithium ion batteries that are considered to have the highest efficiency, 90-94%, vanadium redox batteries 65-70%, and liquid sodium-sulphur batteries 75-80% [2, 10]. Since the device can charge, perform electrolysis, discharge, and efficiently switch between those, it will have a very high utilisation degree and excellent flexibility that can be matched to demand. The combination of earth abundant Ni-Fe elements store electricity as a battery, and split water without noble metal catalysts which are in use in alkaline and PEM electrolysers [12, 32]. The operation appears to be extremely durable, and due to the position of the battery potentials close to the potentials needed for thermoneutral water splitting, and uniquely efficient. In this way heat losses in the battolyser charging are used partially for electrolysis, enhancing efficiency especially for the part of the hydrogen produced while the potential is close to the thermoneutral potential. The battolyser enables high power-to-power battery efficiency and can provide high power-to-fuel efficiency as well: battolyser electrolysis efficiency of up to 90% combined with industrial ammonia synthesis [13] may enable up to 80% (0.9x0.9) power to carbon neutral liquid fuel efficiency. The battolyser requires an amount of about 0.868 kg active Fe and 1.825 kg active Ni electrode material for storing 1 kWh of electricity in the battery functionality and the capability for unlimited hydrogen generation, which is not prohibitively expensive (< 20\$ raw materials cost). Also a low cost water based electrolyte is used. We believe that these advantages of the integrated device will lead to reduced cost and a long lifetime compared to solutions using separate batteries and electrolysers, while the complexity of the infrastructure is essentially similar to an alkaline electrolyser, i.e. requires investments and operation similar to an electrolyser alone but with the double functionality.

2.6. Experimental section

2.6.1. Battolyser

A picture of the integrated battery electrolyser or the battolyser is shown in the appendix, Figure B.1. The electrodes are produced using the technology description in [31, 33]. $Ni(OH)_2$ is precipitated from a nickel sulfate solution, using concentrated NaOH. The $Ni(OH)_2$ precipitate is filtered, washed and dried at 120 °C. The dry hydroxide is ground with a 13 wt.% graphitic carbon conductive additive, compacted and collected in perforated pockets of nickel coated steel. The iron electrode is produced from finely ground magnetite (Fe_3O_4), pure iron and 2 wt.% of graphitic carbon conductive additive plus 10 wt.% NaCl pore former. After compaction and sintering at 700 °C the pore former is dissolved and the electrode material is collected in perforated pockets of nickel coated steel. X-ray diffraction characterisation of the initial and activated material is shown in the appendix, Figure B.8. The electrodes are separated from each other using state of the art gas separation membranes (Zirfon-Perl-UTP500 from Agfa Specialty Products). These membranes are known for their low resistance for ionic transport and stability up to 110 °C (Zirfon [17]). A 4.5 molar potassium hydroxide electrolyte with 1.5 molar sodium hydroxide and 0.05 molar lithium hydroxide is utilised as described in [31, 33]. Some tests were performed to observe if large effects of LiOH in the electrolyte on the potentials during electrolysis would be present (Appendix Figure B.5)

2.6.2. Galvanostatic cycling

Various charge insertion and withdrawal experiments were programmed on a multichannel Maccor 2000 battery cycling system for in total 7 different cells. The experiments leading to Figure 2.4 were performed independently in four different cells to check reproducibility and long term performance.

A cycle is counted from full discharge to full discharge. Figure 2.4 and appendix Figure B.4 depict the chronological record of a cell. Various partial (over/dis)charge programs in between full discharges add up, so when there are many partial discharges and recharges before a final full discharge the aggregated (dis)charge in that cycle can be much larger than the nominal capacity (see appendix Figure B.3 for a selection of performed cycles and appendix Table B.1 for additional data to these cycles). The graphs of Figure 2.4 and appendix Figure B.4 may seem spiky. This appearance originates in the diversity of tests applied to check the applicability of the battolyser as a renewable energy storage solution.

The charge rates that are often mentioned for battery charging are defined

as follows: a charge rate of C/x means that the applied current corresponds to the insertion of the full nominal capacity in x hours.

2.6.3. Energy efficiency of battolyser discharge plus gas generation

The energy efficiency η_{total} for each charge and electrolysis and subsequent discharge cycle is calculated from the equations:

$$\eta_{total} = \eta_{battery} + \eta_{electrolyser} \tag{2.5}$$

$$\eta_{battery} = \frac{\int_{t_c}^{t_c+t_{dc}} V_{dc} I_{dc} dt}{\int_0^{t_c} V_c I_c dt} \tag{2.6}$$

$$\eta_{electrolyser} = \frac{\int_0^{t_c+t_{dc}} H_{el} I_{el} dt}{\int_0^{t_c} V_c I_c dt} \tag{2.7}$$

V_c and I_c are the applied experimental cell voltage and current during the charge and electrolysis cycle with duration t_c, V_{dc} and I_{dc} are the experimental discharge voltage and current during the discharge time t_{dc}, I_{el} the current for electrolysis (and hydrogen evolution induced battery self-discharge) with an energy yield corresponding to the thermo neutral potential H_{el}. The H_{el} equals 1.48 V at RT while $2eH_{el}$ equals the higher heating value (HHV) of hydrogen of $-286\,\mathrm{kJ/mol}$ H_2.

In appendix Figure B.2a an illustration of the energy efficiency is shown graphically. In appendix Table B.1-B.3 explicit numeric examples are given of experimental energy efficiencies of several experiments. Of further interest for the temperature of the cell is the power generated as heat due to the losses. This power is the sum of ohmic losses in the battery function, which equals the absolute value $|\mathrm{V} - 1.37| I_{dc}$, and the resulting losses in electrolysis, which equals $(\mathrm{V} - 1.48) \times I_{el}$. The electrolysis losses can be positive or negative at very low currents (see remarks in relation to Figure 2.6).

Below we show that the faradaic (or coulombic) equals 100% within the experimental accuracy of 0.5%. At this 100% faradaic efficiency the total charge $\mathrm{C_c}$ inserted in the battery electrolyser equals the charge used for electrolysis $\mathrm{C_{el}}$ plus the integrated current discharge $\mathrm{C_{dc}}$:

$$C_c = \int_0^{t_c} I_c dt = \int_0^{t_c+t_{dc}} I_{el} dt + \int_{t_c}^{t_c+t_{dc}} I_{dc} dt = C_{el} + C_{dc} \tag{2.8}$$

Note that the electrolysis yield $\mathrm{C_{el}}$ also includes the gas production during (self) discharge (if any).

The ionic resistance of the gas separation diaphragm was determined by measuring in a battolyser with and without the diaphragm in place. At the highest

current density used an additional potential of ~10 mV was recorded, which corresponds to an energy efficiency loss of less than ~1%. Such small additional overpotential can be mitigated by a small change in operation temperature.

Figure 2.3b shows the measured discharge capacity and electrolysis yield as a function of the total charge insertion. The curves are the result of fitting with the following equations for C_{dc} and C_{el}, where the battery capacity saturates at C_{cap}:

$$C_{dc}(C) = C_{cap}(\frac{2}{1+exp(-2\frac{C}{C_{cap}})} - 1) \tag{2.9}$$

$$C_{el}(C) = C - C_{cap}(\frac{2}{1+exp(-2\frac{C}{C_{cap}})} - 1) \tag{2.10}$$

The charge is expressed in the unit [Coulomb] or [A h]. The function (2.9) above is a logistic function used more often for reactions where one of the reactants is limited (in this case the Ni electrode is limiting) [34]. The fits in figure 2.3b describe the experimental data accurately. The instantaneous charge insertion in the two processes – either battery charging or electrolysis- at a certain moment, when a total charge current $I = dC/dt$ is applied, can be calculated from the derivatives of the equations for C_{dc} and C_{el} with respect to time:

$$\frac{dC_{dc}(C)}{dt} = I_{dc}(C) = (\frac{4exp(-2\frac{C}{C_{cap}})I}{(1+exp(-2\frac{C}{C_{cap}}))^2}) \tag{2.11}$$

and

$$\frac{dC_{el}(C)}{dt} = I_{el}(C) = I - (\frac{4exp(-2\frac{C}{C_{cap}})I}{(1+exp(-2\frac{C}{C_{cap}}))^2}) \tag{2.12}$$

$$\frac{dC_{dc}(C)}{dt} + \frac{dC_{el}(C)}{dt} = I_{dc}(C) + I_{el}(C) = I \tag{2.13}$$

Equations (2.11) and (2.12) give the yield for either battery charge or electrolysis at a total applied charge current I, depending on the state of charge C/C_{cap} of the battery. Appendix Figure B.2b shows the resulting curves for I_{dc}/I and I_{el}/I as a function of the total inserted charge. The saturation capacity C_{cap}, which is dependent on the available electrode material, is with 14.5 A h significantly larger than what we consider the nominal capacity of 10 A h of the battery. This is because the battery is normally considered to be full when the evolved gas is still small (Figure 2.3b) and then does not use the available electrode material as fully as the battolyser does; C_{cap} is significantly larger than the so defined nominal capacity therefore.

2.6.4. Water refilling, quantitative gas evolution, and faradaic efficiency

Demineralised water from a Merck Milli-Q Plus 185 water purification system was used for replenishing the electrolyte. The actual water loss was determined by weight after - on average - five individual completed cycles. In Figure 2.4b the total inserted charge C_c minus the battery discharge C_{dc} is used to determine the amounts of electrolysis C_{el}, assuming 100% faradaic (or coulombic) efficiency. The result is compared with the actual lost (and subsequently replenished) amounts of demineralised water that are expressed in a capacity as well (1 g of water corresponds to $2F/(18.02x3600)$ A h where F is the Faraday constant of 96 485 sA/mol and the molar mass of water equals 18.02 g/mol). This already gives for all cycles together that the faradaic efficiency is close to 100%.

As a second independent verification of the faradaic efficiency the rate of the gas evolution was determined volumetrically for the charged battolyser at several constant applied currents using calibrated gas syringes (Poulten-Graf, Fortuna 100 mL). The volumes of gas measured in mL/s are within 0.5% agreement with corresponding theoretical values for the ambient temperature and pressure. Combining the charge insertion with the discharge capacity and the water loss and gas volume evolutions we come to the conclusion that the faradaic efficiency is $100 \pm 0.5\%$ based on the experimental accuracies. With this outcome it is justified to use 100% faradaic efficiency in our energy efficiency calculations.

2.6.5. Gas characterisation and separation

The separate channels of hydrogen and oxygen were analysed during operation using a calibrated quantitative gas analysis system with a sensitive Hiden 3F-PIC series Quadrupolar Mass Spectrometer for detection. During these gas measurements an argon carrier gas flow was administered over the exit of cell gas. There is hardly any detectible O_2 in the hydrogen channel and hardly any detectible H_2 in the oxygen channel.

2.6.6. Thermally insulated cell

The battolyser was insulated as far as possible by using styrofoam insulation. Still the electronic leads and also the argon gas flow for the gas measurements cause heat flows between cells and the environment. Temperature changes in Figures 2.3a and 2.5 are the resultant of the overpotentials and the thermal losses through the insulation. Measurements were also performed on uninsulated cells in temperature regulated ovens with temperature regulation to $\pm 0.1\,^{\circ}C$.

2.6.7. Lithium in the electrolyte

Lithium hydroxide (LiOH) is normally not utilised in alkaline electrolysis, but it is used in Ni-Fe batteries. To observe if detrimental effects on the electrolysis efficiency may be present we varied the LiOH concentration which was added to a 21 wt.% KOH solution from 0 (pure KOH) to 0.5 and 1.0 mol/L. In the appendix Figure B.5 results for a large range of current insertions (in A h) are shown. Although the efficiency of electrolysis increases about 0.5% without addition of LiOH, such an increase is less than for instance the effects of temperature variation (~4%). In view of this limited impact and the low 0.05 molar LiOH concentration applied for battery operation this concentration was maintained throughout the experiments.

Author contributions

F. M. devised the research project, B. W. worked out the research methodology and performed the experiments, B. W., H. S., J. M. and F. M. designed the experimental setup, H. S., J. M. and F. O. gave experimental support, B. W. and F. M. analysed the data, F.M. and B.W. wrote the manuscript, F. M. supervised the project.

References

[1] M. Armand and J.-M. Tarascon, *Building better batteries,* Nature **451**, 652 (2008).

[2] B. Dunn, H. Kamath, and J.-M. Tarascon, *Electrical energy storage for the grid: A battery of choices,* Science **334**, 928 (2011).

[3] A. Züttel, A. Remhof, A. Borgschulte, and O. Friedrichs, *Hydrogen: the future energy carrier,* Philosophical Transactions of the Royal Society A: Mathematical, Physical and Engineering Sciences **368**, 3329 (2010).

[4] J. Holladay, J. Hu, D. King, and Y. Wang, *An overview of hydrogen production technologies,* Catalysis Today **139**, 244 (2009).

[5] N. Armaroli and V. Balzani, *Towards an electricity-powered world,* Energy & Environmental Science **4**, 3193 (2011).

[6] F. M. Mulder, *Implications of diurnal and seasonal variations in renewable energy generation for large scale energy storage,* Journal of Renewable and Sustainable Energy **6**, 033105 (2014).

[7] D. Linden and T. B. Reddy, *Handbook of batteries Third Edition* (McGraw-Hill, 2001).

[8] K. Vijayamohanan, T. S. Balasubramanian, and A. K. Shukla, *Rechargeable alkaline iron electrodes,* Journal of Power Sources **34**, 269 (1991).

[9] K. Zeng and D. Zhang, *Recent progress in alkaline water electrolysis for hydrogen production and applications,* Progress in Energy and Combustion Science **36**, 307 (2010).

[10] M. A. Pellow, C. J. M. Emmott, C. J. Barnhart, and S. M. Benson, *Hydrogen or batteries for grid storage? a net energy analysis,* Energy & Environmental Science **8**, 1938 (2015).

[11] A. Ursua, L. M. Gandia, and P. Sanchis, *Hydrogen production from water electrolysis: Current status and future trends,* Proceedings of the IEEE **100**, 410 (2012).

[12] J. A. Herron, J. Kim, A. A. Upadhye, G. W. Huber, and C. T. Maravelias, *A general framework for the assessment of solar fuel technologies,* Energy & Environmental Science **8**, 126 (2015).

[13] J. R. Jennings, *Catalytic ammonia synthesis: fundamentals and practice.* (Springer Science & Business Media, 2013).

[14] C. C. L. McCrory, S. Jung, I. M. Ferrer, S. M. Chatman, J. C. Peters, and T. F. Jaramillo, *Benchmarking hydrogen evolving reaction and oxygen evolving reaction electrocatalysts for solar water splitting devices,* Journal of the American Chemical Society **137**, 4347 (2015).

[15] G. A. Snook, N. W. Duffy, and A. G. Pandolfo, *Evaluation of the effects of oxygen evolution on the capacity and cycle life of nickel hydroxide electrode materials,* Journal of power sources **168**, 513 (2007).

[16] M. K. Ravikumar, T. S. Balasubramanian, A. K. Shukla, and S. Venugopalan, *A cyclic voltammetric study on the electrocatalysis of alkaline iron-electrode reactions,* Journal of applied electrochemistry **26**, 1111 (1996).

[17] P. Vermeiren, J. P. Moreels, A. Claes, and H. Beckers, *Electrode diaphragm electrode assembly for alkaline water electrolysers,* International journal of hydrogen energy **34**, 9305 (2009).

[18] R. C. Saltat, *Nickel-iron battery system safety. Final report*, Tech. Rep. (Eagle-Picher Industries, Inc., Joplin, MO (USA). Electronics Div., 1984).

[19] S. Marini, P. Salvi, P. Nelli, R. Pesenti, M. Villa, M. Berrettoni, G. Zangari, and Y. Kiros, *Advanced alkaline water electrolysis,* Electrochimica Acta **82**, 384 (2012).

[20] L. Öjefors, *Temperature dependence of iron and cadmium alkaline electrodes,* Journal of The Electrochemical Society **123**, 1139.

[21] D. Pletcher and X. Li, *Prospects for alkaline zero gap water electrolysers for hydrogen production,* International Journal of Hydrogen Energy **36**, 15089 (2011).

[22] Y. Gogotsi and P. Simon, *True performance metrics in electrochemical energy storage,* science **334**, 917 (2011).

[23] H. Chen, T. N. Cong, W. Yang, C. Tan, Y. Li, and Y. Ding, *Progress in electrical energy storage system: A critical review,* Progress in natural science **19**, 291 (2009).

[24] N.-S. Choi, Z. Chen, S. A. Freunberger, X. Ji, Y.-K. Sun, K. Amine, G. Yushin, L. F. Nazar, J. Cho, and P. G. Bruce, *Challenges facing lithium batteries and electrical double-layer capacitors,* Angewandte Chemie International Edition **51**, 9994 (2012).

[25] F. Feng, M. Geng, and D. O. Northwood, *Electrochemical behaviour of intermetallic-based metal hydrides used in Ni/metal hydride (MH) batteries: a review,* International Journal of Hydrogen Energy **26**, 725 (2001).

[26] F. Cheng, J. Liang, Z. Tao, and J. Chen, *Functional materials for rechargeable batteries,* Advanced Materials **23**, 1695 (2011).

[27] A. I. Demidov and E. N. Volkova, *Potential-pH diagram for the nickel-water system containing nickel(III) metahydroxide,* Russian Journal of Applied Chemistry **82**, 1498 (2009).

[28] J. Desilvestro, D. A. Corrigan, and M. J. Weaver, *Characterization of redox states of nickel hydroxide film electrodes by in situ surface raman spectroscopy,* Journal of The Electrochemical Society **135**, 885 (1988).

[29] D. A. Corrigan and S. L. Knight, *Electrochemical and spectroscopic evidence on the participation of quadrivalent nickel in the nickel hydroxide redox reaction,* Journal of the Electrochemical Society **136**, 613 (1989).

[30] A. Van der Ven, D. Morgan, Y. S. Meng, and G. Ceder, *Phase stability of nickel hydroxides and oxyhydroxides,* Journal of The Electrochemical Society **153**, A210 (2006).

[31] S. U. Falk and A. J. Salkind, *Alkaline Storage Batteries* (John Wiley & Sons, 1969).

[32] D. Stolten and B. Emonts, *Hydrogen Science and Engineering, 2 Volume Set: Materials, Processes, Systems, and Technology*, Vol. 1 (John Wiley & Sons, 2016).

[33] R. Kinzelbach, *Stahlakkumulatoren* (VARTA Battery AG, 1974).

[34] N. W. Loney, *Applied mathematical methods for chemical engineers* (CRC Press, 2015).

3

Renewable Hydrogen and Electricity Dispatch With Multiple Ni-Fe Electrode Storage

This chapter has been published as "Renewable Hydrogen and Electricity Dispatch with Multiple Ni-Fe Electrode Storage" by B.M.H. Weninger and F.M. Mulder. ACS Energy Lett. 2019, 4, 2, 567–571. (Supporting Information see appendix C)

Synthetic fuel production from renewable power or power to "X", e.g. ammonia, methane, methanol, is considered a key component for long-term energy storage [1–7]. At industrial scale, the synthesis of these would start from hydrogen, N_2, and CO_2, where the currently available chemical processes are designed for steady-state full power operation [8]. In a renewable powered future, intermittent solar and wind power will become prominent. Dynamic plant operation is possible but complex and costly. Flexible operation necessitates high turn-down ratios and/or shorter shut-down times. Moreover, capacities for dynamic operation may increase in size, as the maximum production capacity needs to be increased to compensate production loss from frequent shut-down/stand-by periods.

Hydrogen production from a conventional electrolyser is coupled to the energy input. Continuous hydrogen supply from intermittent renewable sources can be achieved with two strategies [3]: (1) electricity storage (e.g., batteries) to provide continuous power to an electrolyser for steady-state operation or (2) hydrogen storage subsequent to an electrolyser with the capability to follow intermittent electricity input, see Figure 3.1. Intermittent hydrogen storage together with a defined allowance for dynamic operation is the indicated solution for "power to X" concepts [8, 9]. Hydrogen storage is also utilized in a state of the art system for the conversion of renewable energy to synthetic fuels as suggested by Gallandat et al. [10]. The combination of electricity storage and hydrogen production in an integrated battery-electrolyser ('battolyser') was recently reported [6].

A key challenge is to decouple the electricity input from the hydrogen output to minimize storage requirements. Different solutions have been suggested for decoupling, for example, Shabangoli et al. propose a system consisting of three electrodes for switchable operation between water splitting and charging [11]. Chen et al. demonstrate a switchable three-electrode setup that allows for time-shifting of hydrogen evolution and oxygen evolution [12]. Jin, Li, and Xiao demonstrate another three-electrode concept in a photoelectrochemical cell for optional photoelectrochemical charging with addition of a bipolar membrane [13]. All these concepts introduce additional electrodes to facilitate decoupling of electricity input and hydrogen production. Amstutz et al. present a different approach for decoupling hydrogen and oxygen production. They built a redox-flow battery and added catalytic reactors for hydrogen and oxygen production [14, 15]. Finally, Symes and Cronin present an approach that uses an electron-coupled-proton buffer for decoupling [16]. Key to all these innovative approaches is the introduction of a mediator to facilitate storage inside the device. However, all these approaches lack controllability and operational flexibility necessary for a better controlled hydrogen output.

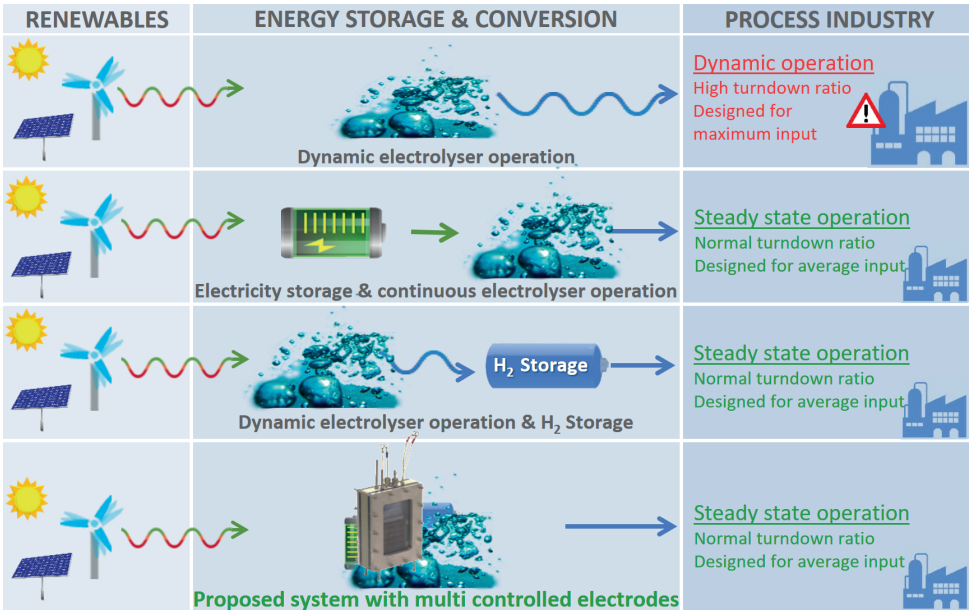

Figure 3.1: Intermittent renewable electricity as source for hydrogen in the process industry. Top to bottom: Following intermittent hydrogen production requires scale up of processing capacities to reach -on average- sufficient production. Using storage of either electricity or hydrogen facilitates steady-state hydrogen supply for process industry scaled to match the average continuous production level. The proposed system integrates hydrogen production and electrochemical storage to provide a controllable hydrogen output from intermittent renewable electricity sources, enabling, for example, dispatchable or continuous hydrogen release for process industry.

Here we introduce a hybrid hydrogen – electrical energy storage concept that provides the flexibility to follow and balance fluctuations in electrical supply as battery, while providing hydrogen and oxygen output on demand. The proposed configuration consists of multiple electrodes based on nickel and iron, having different functions, and thus permits to decouple material usage for the battery and for the hydrogen storage. Simultaneous operation of more than one working electrode within one electrochemical cell is well known from scientific research, e.g. bipotentiostat operation, but to our knowledge it has not yet been used for electrochemical storage and conversion systems [17–19].

3.1. Delayed gas production from storage electrodes

Delayed oxygen and hydrogen production comprises two storage electrodes (SEs, nickel and iron serve as base materials) and two gas production electrodes, the

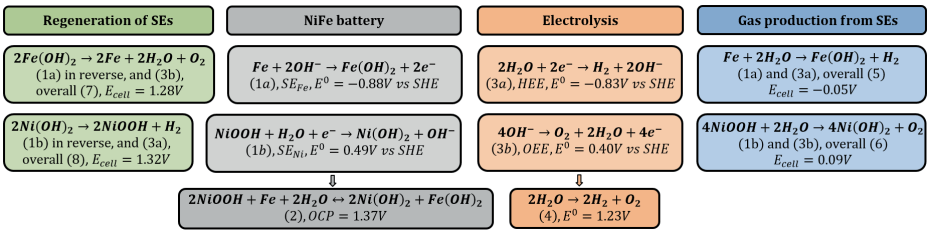

Scheme 1.: Half reaction at the storage (1a and 1b) and gas evolution (3a and 3b) electrodes with combinations (a) for battery (2, gray) and electrolysis (4, orange) operation, (b) for gas production from the storage electrodes (blue) and (c) for regeneration of the storage electrodes (green).

hydrogen evolution electrode (HEE), which facilitates the hydrogen evolution reaction (Scheme 1, reaction 3a, HER) and the oxygen evolution electrode (OEE), which facilitate the oxygen evolution reaction (Scheme 1, reaction 3b, OER) within one electrochemical cell. Scheme 1 depicts the half-reactions associated with all electrodes and combinations thereof, for example, for battery operation with an open cell potential (OCP) of 1.37 V.

We now want to promote controlled hydrogen evolution by combining reaction (1a) at the iron electrode (SE_{Fe}) and reaction (3a) at the HEE resulting in overall reaction (5) and controlled oxygen evolution by combining reaction (1b) at the nickel electrode (SE_{Ni}) and reaction (3b) at the OEE resulting in overall reaction (6) (see appendix section C.1 for visualisation of operation modes). From the potential difference between reactions 1a and 3a and between 1b and 3b, +0.05 V and -0.09 V, respectively, the electrochemical reactions are expected to be spontaneous. Note that the battery OCP of 1.37 V is higher than the 1.23 V necessary for spontaneous water splitting; however, it is lower than the thermoneutral potential of 1.48 V which is required to produce the additional heat to compensate the entropy change when evolving the gases.

Figure 3.2 provides the voltage response for oxygen and hydrogen production from SEs at varying rates; the electrodes serve as storage and gas evolution electrode [6]. The storage capacity of the used iron electrode exceeds the storage capacity of the nickel electrode by a factor of 1.6. Both storage capacities can be fully utilized.

To force running the reaction at moderate rates, a current needs to be applied at some overpotential because of kinetic barriers and to produce the required heat in view of the entropy change during gas evolution. The cell potential for discharging the iron or nickel electrode for hydrogen or oxygen production, respectively, at a continuous rate of C/10 appears to equal around 0.2 V (see Fig-

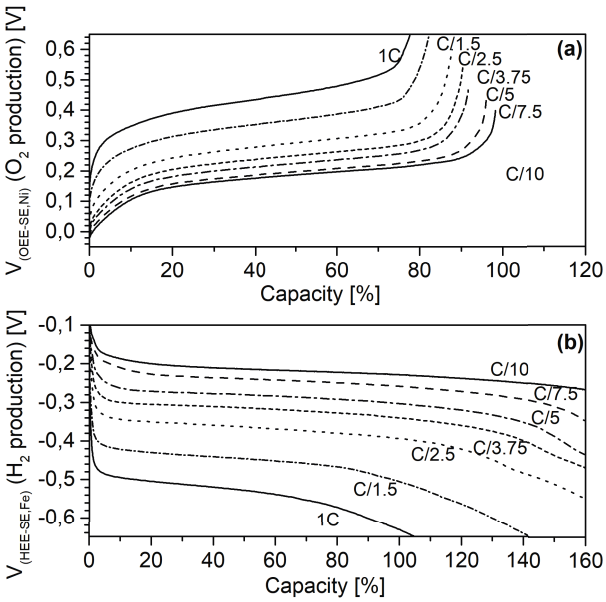

Figure 3.2: Cell potentials for simultaneous oxygen and hydrogen production from storage electrodes at constant and equal production rates. 100% capacity is defined as the discharge capacity of the smallest capacity electrode (nickel electrode) at a discharge rate of C/10. In normal Ni-Fe battery operation the Ni electrode is thus limiting. (a) Observed cell potential for oxygen production by discharging the nickel electrode at constant rates ranging from C/10 to C/1. (b) Observed cell potential for hydrogen production by discharging the iron electrode at constant rates ranging from C/10 to C/1. Note: "x" in the expressing C/"x" stands for discharge time in hours for the full capacity C. Gas production rates at the OEE and HEE can vary independently; however, for testing, simultaneous operation with gas production at constant and equal rates is programmed.

ure 3.2). The cell potential for a high rate of 1C is around 0.52 V (HEE − SE_{Fe}) and 0.42 V (OEE − SE_{Ni}), indicating that gas production at high rates is feasible at the expense of increased overpotentials (see appendix section C.3 for detailed results).

Returning both SEs to the initial state of charge (SoC) requires rearranging the electrical wiring. It results in overall stoichiometric gas production as charging the iron electrode (reaction 1a) is coupled with oxygen production (reaction 3b) combining to reaction 7 and charging the nickel electrode (reaction 1b) with hydrogen production (reaction 3a) combining to reaction 8.

3.2. Concept of multi-controlled electrodes

Gas production from storage electrodes works as intended and shows little overpotentials at moderate rates. The next step is providing the flexibility to respond to intermittent electricity fluctuations while providing a controlled gas output.

The key approach for multi-controlled electrodes is (1) that an assembly of electrodes forms the positive electrode, and/or (2) an assembly of electrodes forms the negative electrode, and (3) that all electrodes may be operational at the same time while (4) currents can be distributed in a controlled way within these assemblies of electrodes. The main electrode configuration is explained using the system depicted in Figure 3.3. This configuration offers not only electricity storage combined with independent and controllable hydrogen and oxygen storage and production inside one electrochemical cell but also scalability to multi-cell systems. The storage electrodes can be charged when electricity is cheap and abundant while only a fraction of the electricity is required to generate hydrogen and oxygen at times when the renewables are scarce, caused by the natural position of the required potentials (see Figure 3.3 left).

Each cell has one connection to the positive (SE_{Ni}+OEE) and one connection to the negative assembly (SE_{Fe}+HEE) of electrodes. The current i_{TSC} (total stack current) passing the array of electrochemical cells determines whether these cells operate as electricity sink or electricity source. The HEE and OEE are connected via a side line from the main line. The electron flow from the main line to the HEE is the current for hydrogen evolution (i_{HE}), whereas the flow of electrons from the OEE to the main line is the current for oxygen evolution (i_{OE}). Both currents are independently controllable and determine the gas output at the respective electrodes. When turned off, no gas production takes place at the gas evolution electrodes (OEE and HEE). The SEs provide battery functionality and facilitate effectively independent electrochemical storage of hydrogen (SE_{Fe}) and oxygen (SE_{Ni}).

Following Kirchhoff's current law, all currents in the system are defined by i_{TSC}, i_{HE}, and i_{OE}. The conservation of charge implies that the difference between i_{TSC} and i_{HE} respectively i_{OE}, defines the current flows from/to the storage electrodes (SE), i_{Fe} and i_{Ni}. The current flows at the SEs are the result of two superimposed currents; they are therefore 'multi-controlled'. The subset-electrodes operate at floating potentials resulting from the controlled current to their storage electrodes.

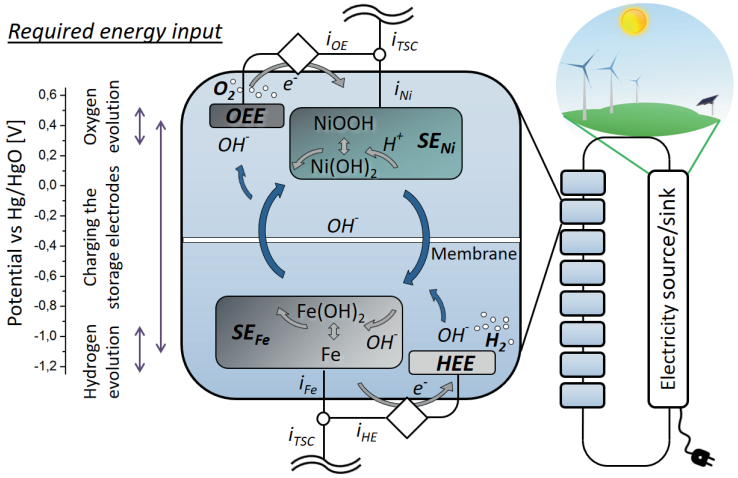

Figure 3.3: The concept of multi-controlled electrodes. The electrochemical cell consists of four electrodes in a multi-cell series, capable of operating as electricity source or sink. The OEE and the nickel electrode form the positive electrode, the HEE and the iron electrode the negative electrode. The currents i_{TSC}, i_{HE}, and i_{OE} are controlled currents and define the current flow to the individual electrodes. I_{TSC} is the array current defining the operation mode of the system. Blue arrows indicate the hydroxyl-ion flow in the cell. The HEE produces hydroxyl ions while the OEE consumes them. The SEs can either produce or consume the ions, dependent on their operation mode (charging/discharging). (The H_2O and water feed system not depicted). (Left) Energy requirement for charging the SEs, H_2 production, and O_2 production from the SE. (Right) Scalability to extended series arrays.

3.3. Testing multi-controlled electrochemical systems

A single-cell setup according to Figure 3.3 was assembled and tested as proof of concept (see appendix section C.4). The expandability of the concept to a multi-cell system with integrated hydrogen storage is tested and verified with a two-cell system in series connection (see appendix section C.5).

The test program consisted of 16 sequences with varying test currents i_{TSC}, i_{HE}, and i_{OE} to mimic an alkaline electrolyser with alternating energy input (i_{TSC} on/off) and with controlled hydrogen (i_{HE} = on) and/or oxygen production (i_{OE} = on). The operation status of the main channel (i_{TSC}) and of the auxiliary channels (i_{HE} and i_{OE}) is indicated in Figure 3.4.

The measured gas output and voltage response is in line with expectations; the gas output follows the main electricity input when the individual H_2 or O_2 evolution electrodes are turned off, while a more continuous gas-production is recognizable when turned on separately or both capabilities together, demon-

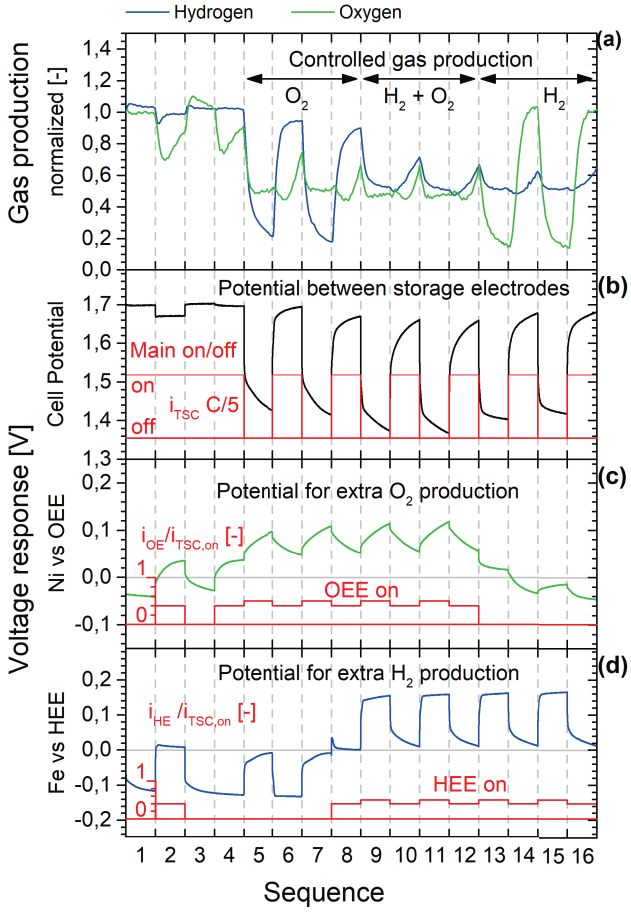

Figure 3.4: Gas production and voltage response for a single-cell test setup consisting of SEs, OEE, and HEE. (a) Normalised hydrogen and oxygen production. (b) Main channel for controlling current i_{TSC} between iron and nickel electrode with schematic operation status on/off for electrolyser operation (rate C/5 when on, red line). (c) Channel for controlling test current i_{OE} between nickel electrode and OEE for controlled oxygen production with schematic operation status on/off. (red line, ratio i_{OE}/i_{TSC} C/5) (d) Channel for controlling test current i_{HE} between iron electrode and HEE for controlled hydrogen production with schematic operation status on/off. (red line, ratio i_{HE}/i_{TSC} C/5)

strating independent and stable operation of the assembly with a controlled current distribution. Again, low potentials for gas production at gas evolution electrodes using energy stored in SEs can be observed, resulting in a low share of energy input compared to the total cycle energy input (for methodology see appendix section C.6, for detailed results see appendix section C.4). The total cycle energy input increases with about 2% for delayed oxygen release, and about 3% for controlled hydrogen release. Most of the energy input is required at electrode charge time (e.g. daytime for solar driven systems), oxygen production requires about 2.5% of the total energy input while hydrogen production about 4.5% indicating little electricity storage needs for enabling delayed (e.g. night time) gas release.

3.4. Iron-water hydrogen storage

The suggested iron - water hydrogen storage system can be characterised as hydrogen storage via chemical reactions [20]. The currently applied iron electrodes possess a volumetric storage density of 0.5 Ah/cm^3, equivalent to 18.5 kg H_2/m^3 or a compressed hydrogen storage density of 300 bar [20], not considering space for different electrodes, electrolyte and gas transport space. Iron-water hydrogen storage may offer the following additional advantages:

- Easy and instantaneous control with electrochemical charging-discharging;
- Reducing the safety risks associated with the storage of compressed hydrogen gas;
- Output hydrogen pressure equivalent to cell pressure, adjustable to match consumer needs (up to 30 bar, operation pressure of commercial alkaline electrolysers [21]).

3.5. System integration

This iron-water hydrogen storage solution can be integrated into a battolyser or an alkaline electrolyser (see appendix, section C.2) with the main advantage of substantially reduced backup power requirements for sustained hydrogen output. Moreover, system integration enables adjustment of material usage to the individual storage needs for hydrogen (iron), oxygen (nickel), and electricity (iron and nickel).

A Ni-Fe system with self-sustaining electricity for hydrogen storage and release would require a storage ratio of 1 to 6 for electricity to hydrogen storage in which the ratio of storage capacity of the nickel electrode to the iron electrode would be 1 to (1+6=) 7. Hence, the amount of nickel for sustained hydrogen

production is reduced by 86% (6/7) for the Ni-Fe system. One should, however, factor in additional electronic components and regulation.

Compared to an alkaline electrolyser with other types of back-up power (e.g., batteries, pumped hydro storage, or compressed air storage), sustained hydrogen production can now be realised electrochemically with substantial reduced back-up power capacity: not 100%, but $\sim 1/7^{th} = 14\%$.

3.6. Summary

In this study we have introduced a hydrogen storage or delayed hydrogen generation concept together with a new control concept for electrochemical cells: multi-controlled electrodes in electrochemical systems. The novel approach allows for current control and distribution among a number of electrodes with dedicated purposes. The concept is not only applicable to one single-electrochemical cell but scalable to multi-cell arrangements and may be of interest to other electrochemical fields in addition to the system proposed here. The fundamental novelty and advantage of this configuration is that both storage electrodes can be charged when electricity is cheap and abundant and only a fraction of the electricity is required to release the stored hydrogen and oxygen at times when the renewables are scarce, e.g., to serve subsequent industrial use. Here, hydrogen storage requires earth-abundant iron-based electrodes and provides a significant effective storage density.

Supporting Information

The Supporting Information is available in appendix C and contains:

(C.1) Operation modes for hybrid–electrical storage system,

(C.2) Integration of hydrogen storage in the battolyser and an alkaline electrolyser,

(C.3) Additional results for gas production from storage electrodes,

(C.4) Additional results for testing a single-cell with simultaneous operation of four electrodes,

(C.5) Additional results for testing a two-cell system in series connection with simultaneous operation of 2 × 3 electrodes, and

(C.6) Experimental methods.

References

[1] W. AVERY, *A role for ammonia in the hydrogen economy,* International Journal of Hydrogen Energy **13**, 761 (1988).

[2] A. Züttel, A. Remhof, A. Borgschulte, and O. Friedrichs, *Hydrogen: the future energy carrier,* Philosophical Transactions of the Royal Society A: Mathematical, Physical and Engineering Sciences **368**, 3329 (2010).

[3] G. Gahleitner, *Hydrogen from renewable electricity: An international review of power-to-gas pilot plants for stationary applications,* International Journal of Hydrogen Energy **38**, 2039 (2013).

[4] B. Decourt, B. Lajoie, R. Debarre, and O. Soupa, *The hydrogen-based energy conversion factbook,* The SBC Energy Institute (2014).

[5] F. M. Mulder, *Implications of diurnal and seasonal variations in renewable energy generation for large scale energy storage,* Journal of Renewable and Sustainable Energy **6**, 033105 (2014).

[6] F. M. Mulder, B. M. H. Weninger, J. Middelkoop, F. G. B. Ooms, and H. Schreuders, *Efficient electricity storage with a battolyser, an integrated Ni–Fe battery and electrolyser,* Energy & Environmental Science **10**, 756 (2017).

[7] C. Philibert, *Renewable energy for industry,* Paris: International Energy Agency (2017).

[8] M. Götz, J. Lefebvre, F. Mörs, A. McDaniel Koch, F. Graf, S. Bajohr, R. Reimert, and T. Kolb, *Renewable power-to-gas: A technological and economic review,* Renewable Energy **85**, 1371 (2016).

[9] R. A. Verzijlbergh, L. J. De Vries, G. P. J. Dijkema, and P. M. Herder, *Institutional challenges caused by the integration of renewable energy sources in the european electricity sector,* Renewable and Sustainable Energy Reviews **75**, 660 (2017).

[10] N. Gallandat, J. Bérard, F. Abbet, and A. Züttel, *Small-scale demonstration of the conversion of renewable energy to synthetic hydrocarbons,* Sustainable Energy & Fuels **1**, 1748 (2017).

[11] Y. Shabangoli, M. S. Rahmanifar, M. F. El-Kady, A. Noori, M. F. Mousavi, and R. B. Kaner, *An integrated electrochemical device based on earth-abundant metals for both energy storage and conversion,* Energy Storage Materials **11**, 282 (2018).

[12] L. Chen, X. Dong, Y. Wang, and Y. Xia, *Separating hydrogen and oxygen evolution in alkaline water electrolysis using nickel hydroxide,* Nature Communications **7**, 11741 (2016).

[13] Z. Jin, P. Li, and D. Xiao, *A hydrogen-evolving hybrid-electrolyte battery with electrochemical/photoelectrochemical charging from water oxidation,* ChemSusChem **10**, 483 (2017).

[14] V. Amstutz, K. E. Toghill, F. Powlesland, H. Vrubel, C. Comninellis, X. Hu, and H. H. Girault, *Renewable hydrogen generation from a dual-circuit redox flow battery,* Energy Environ. Sci. **7**, 2350 (2014).

[15] V. Amstutz, K. E. Toghill, C. Comninellis, and H. H. Girault, *Redox flow battery for hydrogen generation,* (2017), US Patent 9,543,609.

[16] M. D. Symes and L. Cronin, *Decoupling hydrogen and oxygen evolution during electrolytic water splitting using an electron-coupled-proton buffer,* Nature Chemistry **5**, 403 (2013).

[17] A. J. Bard, L. R. Faulkner, J. Leddy, and C. G. Zoski, *Electrochemical methods: fundamentals and applications, vol 2* (Wiley, 1980).

[18] J. Newman and K. E. Thomas-Alyea, *Electrochemical systems* (John Wiley & Sons, 2012).

[19] H. Vogt, G. Kreysa, S. Vasudevan, R. Wüthrich, J. D. Abou Ziki, and R. El-Haddad, *Electrochemical reactors,* (2014).

[20] A. Züttel, *Materials for hydrogen storage,* Materials Today **6**, 24 (2003).

[21] N. Guillet and P. Millet, *Alkaline water electrolysis. in Hydrogen production by electrolysis* (Wiley-VCH Verlag GmbH & Co.KGaA, 2015) pp. 117–166.

4

Neutron Diffraction Study of a Sintered Iron Electrode In Operando

Iron is a promising, earth-abundant material for future energy applications. In this study, we use a neutron diffractometer to investigate the properties of an iron electrode in an alkaline environment. As neutrons penetrate deeply into materials, neutron scattering gives us a unique insight into what is happening inside the electrode. We made our measurements while the electrode was charging or discharging. Our key questions are: Which phases occur for the first and second discharge plateau? And why are iron electrodes less responsive at higher discharge rates? We conclude that metallic iron and iron hydroxide form the redox pair for the first discharge plateau. For the second discharge plateau, we found a phase similar to feroxyhyte but with symmetrical and equally spaced arrangement of hydrogen atoms. The data suggest that no other iron oxide or iron (oxy)hydroxide formed. Remarkable findings include: (1) substantial amounts of iron hydroxide are always present inside the electrode. (2) Passivation is mostly caused by iron hydroxide that is unable to recharge. (3) Iron fractions change as expected, while iron hydroxide fractions are delayed, resulting in substantial amounts of amorphous, undetectable iron phases. About 40% of the participating iron of the first plateau and about 55% of the participating iron for the second plateau are undetectable. (4) Massive and unexpected precipitation of iron hydroxide occurs in the transition from discharging to charging.(2), (3), and (4) together cause accumulation of iron hydroxide inside the electrode.

This chapter has been published as "Neutron Diffraction Study of a Sintered Iron Electrode In Operando" by B.M.H. Weninger, M.A. Thijs, J.A.C. Nijman, L. van Eijck, and F.M. Mulder, J. Phys. Chem. C 2021, 125, 16391-16402. (Supporting Information see appendix D)

4.1. Introduction

The development and implementation of renewable electricity generation increasingly asks for electrochemical energy storage and conversion based on earth-abundant materials. Iron is a low-cost and earth-abundant material, which can be used for energy storage and conversion. Here, we use a neutron diffractometer to study an iron electrode in operando.

As an energy storage material, iron works as a negative electrode. At high pH, metallic iron and iron hydroxide can be in a reversible phase equilibrium at a potential that is slightly more negative than the potential of the reversible hydrogen electrode. The nickel-iron battery as invented by Jungner and Edison combines iron anodes with nickel cathodes. When such batteries are overcharged, they electrolyse the water in the electrolyte to form hydrogen and oxygen. In a battolyser [1, 2], the hydrogen is collected, combining the storage and conversion function in one device. Replacing the positive nickel electrode with a reversible oxygen electrode creates the iron-air battery. Recently, there has been a renewed interest in iron-air batteries as they promise high energy density combined with reduced nickel content [3–6]. Iron electrodes have recently been proposed as means to decouple oxygen and hydrogen generation [7–10]. To do so, the iron electrode is located in between the cathode and the anode to delay hydrogen generation. The resulting system can release its stored energy electrically or as hydrogen. This versatility makes iron electrodes promising for future energy applications.

Iron electrodes have two discharge plateaus. The first plateau is the two-electron transition from Fe^0 to Fe^{2+}. The second plateau is the one-electron transition from Fe^{2+} to Fe^{3+}. Battery operation is usually restricted to the first plateau due to limited reversibility of the second plateau. The first plateau is a dissolution-precipitation reaction. The dissolution process is strongly dependent on pH, potential, and temperature [11, 12]. Reaction (4.1) (−0.88 V relative to standard hydrogen electrode, SHE) provides the overall reaction scheme for the first plateau. Reaction (4.1) is composed of the reaction steps for dissolution (4.2) and precipitation (4.3):

$$Fe^0 + 2OH^- \rightleftharpoons Fe^{2+}(OH)_2 + 2e^- \tag{4.1}$$

$$Fe^0 + 3OH^- \rightleftharpoons [HFe^{2+}(O)_2]^- + H_2O + 2e^- \tag{4.2}$$

$$[HFe^{2+}O_2]^- + H_2O \rightleftharpoons Fe^{2+}(OH)_2 + OH^- \tag{4.3}$$

The dissolution process (4.2) can be further split up into [13]:

$$\mathrm{F}\, e^0 + OH^- \rightleftharpoons Fe^0(OH)_{ads} + e^- \tag{4.4a}$$

$$Fe^0(OH)_{ads} + OH^- \rightleftharpoons [Fe^0(OH)_2]_{ads} + e^- \tag{4.4b}$$

$$[Fe^0(OH)_2]_{ads} + OH^- \rightleftharpoons [HFe^{2+}O_2]^- + H_2O \tag{4.4c}$$

Note that reaction (4.3) and reaction (4.4c) are not electrochemical reactions but regular chemical reactions with pH and temperature dependent equilibria.

Some of these iron species are soluble. For Fe^{2+} this is $HFeO_2^-$ (hydrated as $Fe(OH)_3^-$). Soluble Fe^{3+} is FeO_2^- (hydrated as $Fe(OH)_4^-$). Fe^{2+} and Fe^{3+} are in equilibrium in highly alkaline solutions. During battery operation, the dissolution from Fe to Fe^{2+} is likely the rate limiting step for discharging. Equilibration between soluble Fe^{2+} and Fe^{3+} species appears to be fast [14].

Recent work [15] suggests an oxidation path from iron to magnetite (Fe_3O_4) via a soluble intermediate. In this case, reaction (4.3) would be replaced by reaction (4.5). The net overall reaction then becomes reaction (4.6) ($-0.91\,V$ vs. SHE):

$$3HFeO_2^- + H^+ \rightarrow Fe_3O_4 + 2H_2O + 2e^- \tag{4.5}$$

$$3Fe + 8OH^- \rightarrow Fe_3O_4 + 4H_2O + 8e^- \tag{4.6}$$

Such a more direct oxidation from iron to magnetite, without intermediate iron hydroxide, is also observed for systems with nanosized iron particles [16]. Thermodynamically, both reactions are possible. The equilibrium potential for the reactions from iron to iron hydroxide and from iron to magnetite is close to each other [17]. Dehydrated iron compounds are slightly more stable than hydrated compounds. Iron hydroxide can be oxidized to magnetite according to the Schikorr reaction (4.7). This reaction is slow at room temperature but faster at higher temperatures [18]:

$$3Fe(OH)_2 \rightarrow Fe_3O_4 + 2H_2O + H_2 \tag{4.7}$$

Metallic iron is not stable under highly alkaline conditions. The corrosion process produces hydrogen through reaction (4.8):

$$Fe + 2H_2O \rightarrow Fe(OH)_2 + H_2 \tag{4.8}$$

Iron hydroxide can be oxidized to any iron oxide or (oxy)hydroxide, except γ-FeOOH. All other iron oxide/(oxy)hydroxides should be evaluated as possible reaction products of the second discharge plateau. The structure of $Fe(OH)_2$ is stable until the Fe^{3+} content reaches 10% of the total iron content. In strongly alkaline solutions, like our electrolyte, $Fe(OH)_2$ is oxidized to $Fe(OH)_3$ first and then dehydrated to FeOOH [19]. The second discharge reaction can be written

as reaction (4.9) (−0.56 V relative to SHE) [20], considering iron hydroxide and iron oxyhydroxide:

$$Fe^{2+}(OH)_2 + OH^- \rightleftharpoons Fe^{3+}OOH + H_2O + e^- \tag{4.9}$$

δ-FeOOH and/or Fe_3O_4 are the discharge products most commonly identified for the second discharge plateau. Higher temperatures and continuous cycling favour the formation of Fe_3O_4. Moreover, Fe_3O_4 is always found when the electrolyte contains LiOH, a common electrolyte additive [21–23]. In situ Mössbauer spectroscopy supports this finding, Fe_3O_4 is the discharge product of the second discharge plateau in an electrolyte containing lithium hydroxide, whereas pure KOH electrolyte leads to the formation of β-FeOOH [24]. A recent in situ X-ray diffraction (XRD) study links the presence of δ-FeOOH to the oxidation of iron hydroxide but points out that δ-FeOOH is only an intermediate towards the formation of Fe_3O_4 upon dehydration, and Fe_3O_4 is identified as the main product of the second discharge step [15]. Here, electrodes were prepared with and without BiS_2 additive. Interestingly, iron hydroxide and δ-FeOOH were only detected with samples containing BiS_2. Otherwise, only Fe_3O_4 was detected as the crystalline phase for the first and second discharge plateaus. According to the authors, iron hydroxide may be present, but undetectable, in an amorphous phase. Additionally, γ-Fe_2O_3 was recently identified by Raman spectroscopy as the discharge product of the second discharge stage where it forms large crystals [25]. Note that γ-Fe_2O_3 (maghemite) and Fe_3O_4 (magnetite) are isostructural and can hardly be distinguished in XRD patterns.

The operating conditions (e.g., charge/discharge rates) and/or additives determine which discharge products are formed [15, 22]. To exclude these effects, we study the iron-water system without any additives to either electrode or electrolyte. Our electrolyte was a 25% KOH solution by weight, and our electrodes were made of pure, sintered iron. In this study, we conducted neutron diffraction measurements while the electrode was charging, overcharging (electrolysing), or discharging. This allowed us to observe the different crystallographic phases that are present. Hydrogen causes incoherent neutron scattering increasing the background signal level. This allows us to see the hydrogen and electrolyte content inside the sample. As neutrons penetrate deeply into materials, neutron scattering gives us a unique insight into what is occurring inside of the electrode, rather than on the surface.

4.2. Experimental Section

4.2.1. Electrode Production

In this study, sintered iron electrodes are investigated. The production is based on the process as described by Falk and Salkind [26]. This is the classical route for the production of iron oxides for pocket electrodes. The synthesis starts with iron (II) sulphate heptahydrate (VWR chemicals, ≥98%, GPR Rectapur). First, the iron sulphate was dried to monohydrate at 100 °C. Then, the powder was oxidized to hematite (Fe_2O_3) at 800 °C. Energy-dispersive X-ray spectroscopy (EDX) was used to confirm that no sulphur remained after oxidation. Reduction took place in a flow-through reactor at 550 °C with hydrogen as the reducing agent. This temperature avoids sintering of the reduced iron powder during this stage of synthesis. The sintering threshold temperature, or Tamann temperature, of a solid is roughly half the melting temperature in K. For iron, this is 906 K (633 °C) [27]. The reactor was left to cool to room temperature in a reducing Ar/H_2 atmosphere. After cooling, the reactor was moved into an argon filled glovebox. The reduced iron was carefully ground inside a glovebox. The resulting powder was pressed into tube shapes at a pressure of 300 kg/cm^2. These tube sections were sintered at 750 °C under an Ar/H_2 atmosphere. Reduced iron powders and iron electrodes remained inside the argon-filled glovebox where possible to limit oxidation. The active electrode material was only exposed to air during pressing and cell assembly. Exposure to air causes the formation of a passivation layer on the surface of the electrode. This passivation layer was removed electrochemically.

In total, 12 electrode sections were produced with the following dimensions: total weight: 6.58 g Fe, average porosity 64.3%, average inner diameter: 3.23 mm, average outer diameter: 7.53 mm, and total height: 64.5 mm. These dimensions were chosen to maximize the iron content inside the sample holder for neutron diffraction experiments. A porosity of 64.3% should provide a stable iron electrode with a reasonable material utilization. Higher porosities may yield a higher material utilization, but a higher conversion may cause disintegration of the sintered iron body together with a loss of essential electrical conductivity [6]. Figure D.1 of appendix D provides additional characterization for the iron powder.

Electrodes produced in this way work right away as they consist of porous iron. Initial charging of about 15 minutes is sufficient to remove the passivation layer from the surface. The electrode can then be discharged.

4.2.2. Cell Assembly

To assemble the cell, the 12 tube sections were mounted in a quartz tube sample holder. The nickel-wire counter electrode, necessary for cell operation during the diffraction measurements, was placed in the center of the tube sections.

In the head space above the iron electrode, an Hg/HgO reference electrode was inserted. This electrode provided the voltage reference for the measurement of the iron electrode potential. The head space remained outside of the neutron beam. Figure 4.1 shows the used setup during preliminary testing. The insert shows one of the tube sections after pressing. Appendix D Figure D.2 shows additional pictures of the setup that was used.

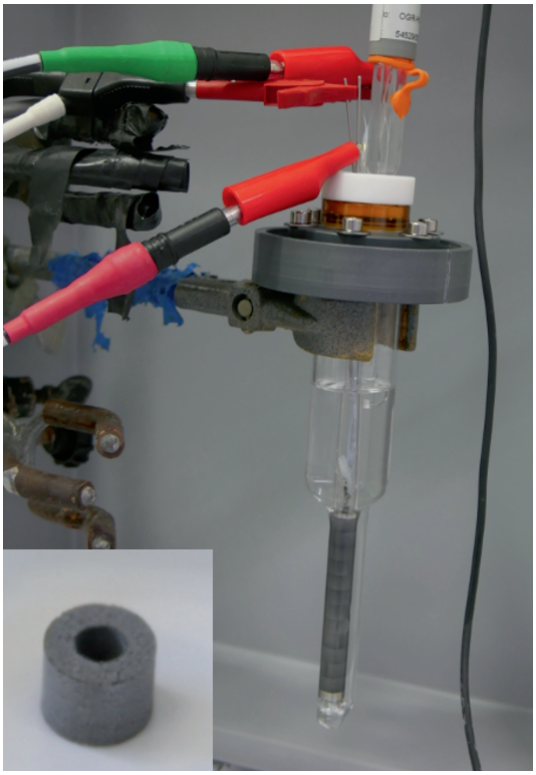

Figure 4.1: Preliminary testing of the electrode. The setup comprises the tubular iron electrode, the centered nickel counter electrode, and a Hg/HgO reference electrode, which senses the headspace. A capillary in the back connects the headspace with the bottom of the cell to provide electrolyte. Insert: one tube section after pressing.

Initial considerations led to the conclusion that water (H_2O) should be used for the tests rather than of heavy water (D_2O). Deuterium hardly causes any incoherent scattering. This would reduce the background intensity. Normally,

hydrogen does cause a substantial background. This allowed us to investigate the hydrogen-related densities inside the system by analyzing variations of the background signal during operation. Previous experience in hydrogen storage materials also indicates that protonated samples still give good signal-to-noise ratios in modern diffractometers [28]. The use of H_2O left us enough diffraction signal intensity above background to be able to identify the phases quantitatively.

When a cell is discharged to the first discharge plateau for the first time, it shows a higher capacity than on subsequent discharges. In this study, we found about 0.40 Ah/g_{Fe} for the first discharge. Subsequent cycles yield lower capacities of about 0.15 Ah/g_{Fe}. To condition the electrode before measurement, it was cycled eight times and then fully charged. Prior to measurement, the electrode was set on an additional floating charge (30 mA) for 24 hours.

The sintered iron electrode we produced was discharged to a capacity of 0.21 Ah/g_{Fe} to study the first discharge plateau. To study the second discharge plateau, it was discharged to a capacity of 0.42 Ah/g_{Fe}. Geometric factors play an important role, in determining material utilization. Thinner electrodes have advantages and show a higher utilization (see e.g., [6]). For a proper comparison of geometric factors like thickness, counter electrode position, and current density, information about electrode and electrolyte additives need to be reported and considered [5]. Here, we produced a pure iron electrode with tubular shape and a wall thickness of 2.15 mm with neither electrode additives nor electrolyte additives, and a Ni-wire counter electrode in the center. The volumetric energy density for the first discharge plateau results in 0.59 Ah/cm^3 excluding the space for the counter electrode and to 0.48 Ah/cm^3 including that space.

4.2.3. In Operando Neutron Diffraction

In operando neutron diffraction data was collected with the Pearl instrument at the Reactor Institute Delft [29]. This instrument uses thermal neutrons. A monochromator allows the selection of four different wavelengths of neutrons. For this study, we used the wavelength of 1.667 Å. The setup has a fixed multi-pixel detector with a 2 Θ_M range of 150° over 1408 pixels. The recording time of each neutron diffraction pattern was set to 15 minutes. 247 diffractograms were collected in three sessions: (1) pattern 0-167, (2) pattern 192-266, and (3) pattern 281-284.

This study contains four electrochemical cycles of discharging and then recharging. In the first two cycles, we investigate the phase changes for the first iron discharge plateau. In the first cycle, we used a moderate discharge rate of 200 mA. In the second cycle, we used a 50% higher discharge rate of

300 mA. Sluggish discharge characteristics are a downside of iron electrodes. In cycles 3 and 4, we investigate the phase changes for extended discharging. Our aim is to identify the iron phase of the second iron discharge plateau. Session one consists of:

- Cycle 1: discharge to 0.214 Ah/g_{Fe} at a rate of 200 mA with subsequent recharge
- Cycle 2: discharge to 0.192 Ah/g_{Fe} at a rate of 300 mA with a subsequent recharge
- Cycle 3: discharge to 0.320 Ah/g_{Fe} at rates of 200 mA first, later 100 mA with partial subsequent recharge.

Session two consists of:

- Cycle 4: discharge from 0.156 Ah/g_{Fe} to 0.423 Ah/g_{Fe} executed with decreasing rates from 200 mA through 150 mA to finally 100 mA with a partial recharge to 0.262 Ah/g_{Fe}

The third session consists of the recharge for cycle 4 from 0.406 to 0.454 Ah/g_{Fe}. All (re)charges were programmed to slightly overcharge the electrode at a rate of 300 mA. A charge rate of 300 mA is equivalent to 46.6 mA/g_{Fe} or to a current density of 46.3 mA/cm^2 at the inner circumference of the iron electrode. The corresponding current density at the outer circumference of the counter electrode is twice as high, 92.6 mA/cm^2. Table D.1 of the appendix provides the executed electrochemical program. Figure D.3 shows the neutron diffraction pattern together with the observed electrochemical data. (Re)charging includes (1) a phase transition and (2) a hydrogen production period at the iron electrode and oxygen production at the counter electrode (Ni-wire). During discharging, the iron electrode is oxidized, while the nickel counter electrode now produces hydrogen. Equations (4.10-4.12) [7] provide the overall system equations for the first discharge plateau of iron and the nickel wire counter electrode. The half reactions for discharging (4.10, $E_{cell} = -0.05$ V), recharging (4.11, $E_{cell} = 1.28$ V), and overcharging (4.12, E^0=1.23 V) combined give the cell reactions:

$$Fe + 2H_2O \rightarrow Fe(OH)_2 + H_2 \tag{4.10}$$

$$2Fe(OH)_2 \rightarrow 2Fe + 2H_2O + O_2 \tag{4.11}$$

$$2H_2O \rightarrow 2H_2 + O_2 \tag{4.12}$$

Galvanostatic electrochemical experiments were executed with a Parstat MC 2000 A Module. The test currents were programmed on this module. A voltmeter was used to measure the cell voltage. A second voltmeter was used to measure the voltage of the iron electrode relative to the voltage of a Hg/HgO reference electrode.

4.2.4. Data Processing

This study uses the GSAS-II software package for data processing [30]. For the determination of the unit cell parameters, three consecutive patterns were combined to improve counting statistics. These unit cell parameters were then used to calculate the phase fraction of the individual patterns.

It is common practice to fit phase fraction and the histogram scale factor to reach unity within one data set. Here, we follow a different approach. We fixed the histogram scale factors for all patterns. This approach allows us to track the crystalline phase fractions during operation and to estimate how much iron-containing material is missing. For other sample parameters, the Pearl setup can be characterized as a Debye-Scherrer-type diffractometer.

Parameters for instrumental resolution were used as determined in [29]. Initial tests indicated that the fitting quality did not improve upon fitting the instrumental parameters (U, V, and W for Gaussian and X and Y for Lorentzian part). As these parameters remained close to the instrumental line shape, no further broadening was assumed.

4.2.5. Background Measurement

The individual components, sample holder, electrolyte, and counter electrode, contribute to the background in distinct ways. The quartz (SiO_2) sample holder contributes the "wavy" shape to the background signal. The pattern of the amorphous quartz has three broad peaks, at 2Θ positions 24, 44, and 88 degrees, as shown in Figure 4.2. We modelled the background shape by inserting these three peaks into the background function of the GSAS-II software.

After final charging, the iron electrode was removed. This left the sample holder with the counter electrode and electrolyte (60% filled). The diffraction pattern of this background sample was measured. The overall intensity increases, relative to the measurement of the quartz tube alone. The shape and the wavy pattern of the quartz are still recognizable. Additional reflection peaks from the nickel counter electrode are clearly visible. This background signal is present in all measurements. All additional peaks observed in measurements with the iron electrode present would then be caused by the electrode under investigation.

4.2.6. Characterization of the Second Fe Discharge Phase

Iron (α-Fe) has a body-centered cubic (BCC, space group $Im\overline{3}m$, a=2.866 Å) unit cell containing two Fe atoms. Nickel has a face-centered cubic (FCC, space group $Fm\overline{3}m$, a=3.526 Å) unit cell containing four Ni atoms per unit cell. Iron

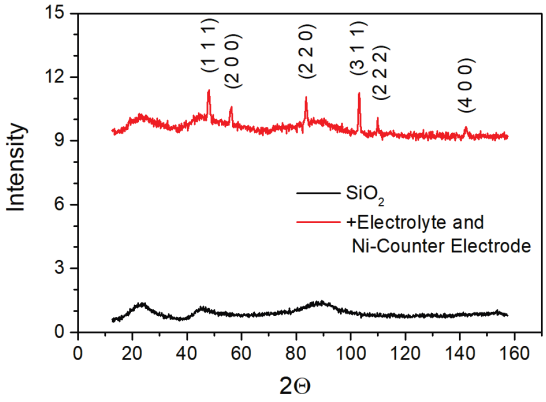

Figure 4.2: Intensities measured for a quartz tube (black line) and the quartz sample holder filled with 60% electrolyte (25wt% KOH solution) together with the Ni-wire counter electrode (red line).

hydroxide has a hexagonal unit cell with the space group $P\bar{3}m1$ containing one Fe atom per unit cell. Here, refinement makes use of the CIF file number COD ID 9002261 from the Crystallography Open Database (COD) [31–36]. This file is based on neutron powder diffraction data collected at 300 K to study the nuclear and magnetic structure of iron hydroxide [37].

The diffraction patterns of the most charged and the most discharged states, after subtraction of the background, are combined in Figure 4.3. We observed, as expected, a decrease in the diffraction intensities for iron in the discharged state. Remarkably, we found substantial and equal intensities for iron hydroxide in both states. Additional reflections, indicated with blue arrows, appear on deep discharging.

From the known iron oxides and (oxy)hydroxides (α-, β-, γ-, δ-FeOOH, α-, γ-, ϵ-Fe_2O_3, Fe_3O_4, FeO, and $Fe(OH)_3$) only the formation of δ-FeOOH was detectable during second plateau discharging. So, we focused our further work on δ-FeOOH (for simulations of the diffraction patterns of iron oxides and (oxy)hydroxides see appendix, Figure D.4 and Table D.2). Other authors identified various other iron oxides/(oxy)hydroxides with their measurements[15, 23–25, 38–44]. However, as many analytical methods require dry samples, it is entirely conceivable that some of these substances only precipitate, or even form, when drying the material. Additionally, the presence of additives affects the product that forms.

δ-FeOOH is a synthetic material. The related natural compound, feroxyhyte, is also named δ'-FeOOH. They consist of a hexagonal unit cell, where the oxygen is in a similar positions as in $Fe(OH)_2$. However, iron and hydrogen have

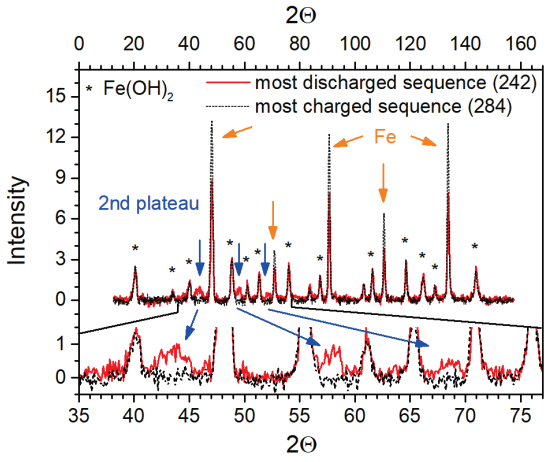

Figure 4.3: Top: intensities measured for the most charged pattern (284) and the most discharged pattern (242) with the background subtracted. Blue arrows indicate reflections belonging to the second Fe plateau. Orange arrows indicate varying intensities for iron. Ni is not indicated. Bottom: magnification for a 2Θ range from 35 to 77 degrees.

additional allowed positions, doubling the number of sites in a doubled number of layers in the crystal, see Figure 4.4. The Fe^{3+} cations are distributed in an ordered manner in the synthetic compound. In the natural compound, Fe^{3+} is randomly distributed. Feroxyhyte has a slightly larger unit cell (c dimensions 0.456 nm vs. 0.449 nm) [45].

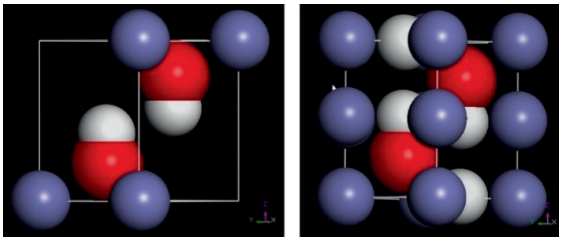

Figure 4.4: Left: The $Fe(OH)_2$ structure (purple: Fe, red: O, white: H). The layers between the oxygen atoms are alternatingly filled with iron and hydrogen atoms. Right: δ-FeOOH structure with additional Fe and H sites that are partially occupied.

To perform Rietveld refinement on neutron diffraction data, we use a symmetrical hexagonal unit ($P\bar{3}m1$) with a random distribution of the Fe ions in the octahedral sites [46]. When we investigated distorted oxygen lattices [47], the position of the oxygen atom always converged towards symmetric spacing between the oxygen layers. When we studied displacement of the Fe ions from

their octahedral site [48], the ions also converged towards the center of the octahedron from their distorted position upon refinement. Little is known about the position of the hydrogen atom in the structure. The authors of the CIF file COD ID 1008762 [47] suggest its positions is 0.120 nm above the oxygen atom in the direction of the C-axis. This leads to asymmetry in the structure, as only one layer of oxygen atoms is filled with hydrogen atoms, while the next layer is empty. The 0.120 nm O-H distance is unusually big, and the distance in a hydroxide ion is generally close to 0.096 nm (e.g., $Fe(OH)_2$: 0.094 nm). Symmetrical arrangement of the hydrogen atoms in the suggested position inside the unit cell improved the fitting quality. Placing the hydrogen atoms closer to the oxygen atom at a distance of 0.096 nm, or putting the hydrogen atoms into the tetrahedral positions worsened the fitting quality. Interestingly, distributing the hydrogen atoms symmetrically and equally between the tetrahedral sites and sites at a distance of 0.096 nm to the oxygen atom provided the same fit quality as the symmetrically rearranged hydrogen position mentioned above. Figure 4.5 provides the final fit for the most discharged stage (averaged data from pattern 240-242), with unweighted phase residuals RF of 1.560% for iron, 1.972% for iron hydroxide, and 3.571% for δ-FeOOH. For this δ-FeOOH, the refinement yielded a characteristic crystal size of 23 nm with microstrain of 42000.

Note that we focused on minimizing the unweighted phase fraction with fitting due to the background. The data residuals wR result in 0.910% on 1366 observations, and $\chi^2 = 1.6$.

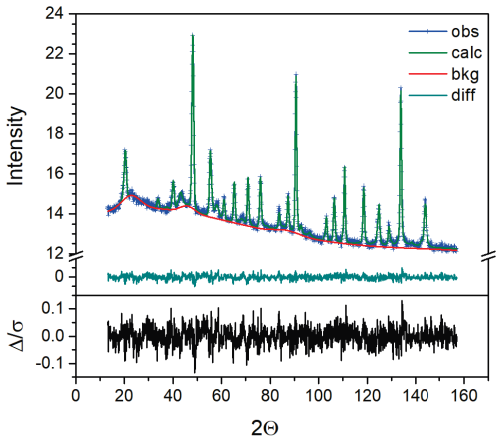

Figure 4.5: Top: observed intensities for the combined, most discharged pattern, 240-242 (obs), together with calculated intensities (calc), background (bkg) and difference (diff) curve. Bottom: difference curve divided by the estimated standard deviation for the data points (GSAS-II output).

Iron hydroxide and iron oxyhydroxide have the same space group, no. 164, with different a dimension and a similar c dimension. However the transition is more than a simple (de)protonation with additional iron and hydrogen layers occurring with partial occupation. This changes the interlayer spacing between Fe-layers and H-layers from one c-axis length to half of that and also causes fractional occupation of the sites. This has a large effect on the (001) diffraction peak at 2Θ position 20 degrees when comparing $Fe(OH)_2$ and FeOOH. For the $Fe(OH)_2$ pattern at this position, no large change is observed when comparing the most charged and the most discharged measurements, see Figure 4.4. As can be observed in the appendix, Figure D.5 for the FeOOH phase, this peak disappears due to the shorter c/2 repetition of the partially occupied iron and hydrogen layers. Not only is hydrogen extracted during the transition but apparently also Fe-ions and the remaining hydrogen shift in the unit cell. The oxygen atoms remain relatively unaffected. Such a relocation of transition-metal ions within the unit cell upon ions being removed from the structure is reminiscent of what happens to Ni and Mn ion redistribution within the unit cell of ordered $LiNi_{0.5}Mn_{1.5}O_4$ upon lithium insertion into the structure; apparently such mobility and transition-metal valence changes can induce such mobility [49]. A deconvolution of the pattern shown in Figure 4.5 into the individual contributions of the present phases is added to the appendix, Figure D.5. The derived structural parameters of all refined phases are depicted in Table D.3 of the appendix.

4.2.7. Data Interpretation

The iron electrode contains 6.58 g (0.118 mol) of Fe. One Ah of charge is equivalent to 0.0373 moles of electrons. Assuming that 100% of the iron is available for a lossless two-electron process, this results in a theoretical capacity of 6.33 A h. So, a hypothetical two-electron exchange process at a (dis)charging rate of 100 mA for an hour results in fractional change of 0.0158 or 1.58% of the iron atoms in the electrode. Table 4.1 shows the theoretical fractional changes for the applied rates for one-, two- and three-electron exchange processes.

electron exchange/ charge rate	$1e^-/Fe$	$2e^-/Fe$	$3e^-/Fe$
100 mA h	0.0317	0.0158	0.0106
150 mA h	0.0475	0.0237	0.0158
200 mA h	0.0633	0.0317	0.0211
300 mA h	0.095	0.0475	0.0317

Table 4.1: Expected fractions of affected iron atoms as a function of the inserted charge and iron valence change.

Each diffraction pattern was corrected for the efficiency of the 1408 pixels of the detector. The intensity of each of the collected patterns was corrected for the variation in neutron beam intensity over the 70 h instrumental time.

Compared to hydrogen, the elements iron, oxygen, and potassium have a negligible incoherent scattering length contributing to the background. So, changes in background levels reflect the hydrogen content of sample and electrolyte in the beam. Gas bubbles replacing liquid electrolyte are to be expected. The electrolyte has a hydrogen content of 0.108 mol H/cm^3, iron hydroxide has 0.0756 mol H/cm^3, and the same sample converted completely to Fe and electrolyte inside the created free space has 0.079 mol H/cm^3. Consequently, the hydrogen content should hardly change during a steady first plateau transition if the gas content in the electrolyte is stable; however, it is known that gas evolution occurs readily during charging. This can alter the condensed (solid or liquid) hydrogen density in the beam. For calculations concerning the hydrogen content see appendix D (Table D.4, D.5 and D.6).

4.2.8. First-Principles Calculations on δ-FeOOH

The nuclear density distribution in time of the ions in the various FeOOH structures, as well as their ground-state energies, were modelled using density functional theory (DFT) in the generalized gradient approximation (GGA), as implemented in the VASP plane-wave pseudopotential code [50]. Molecular dynamics was used at different decreasing temperatures to reach a starting structure that was subsequently minimized in a minimum energy calculation. Typically, a $2 \times 2 \times 2$ (8 unit cells) primitive cell having 32 atoms was applied starting from several initial structures: a) δ-FeOOH, with the appropriate randomized occupation of sites to fill the different planes for Fe and H with an average composition; b) a structure derived from $Fe(OH)_2$ with a composition corresponding to FeOOH (so one H removed) and lattice parameters of the δ-FeOOH.

The resulting structures are consistent with the δ-FeOOH structure, in that they have additional H planes compared to $Fe(OH)_2$, but only the structure resulting from an initial δ-FeOOH has the additional Fe plane positions. The positions of Fe and O were stable during lengthy MD simulations at 600 K and during subsequent minimization. The energies of the models are remarkably close at to each other. The more random δ-FeOOH structure is only 4.8 kJ/mol lower in energy. This small difference, approximately two times k_BT, may explain a low driving force for crystallization into the δ-FeOOH form, where Fe and H form additional different planes when transforming between a H-extracted $Fe(OH_{0.5})_2$ and FeOOH, going in either direction.

It appears from these calculations that δ-FeOOH can indeed be formed in

a solid-state reaction in which $Fe(OH)_2$ is dehydrogenated according to reaction (4.9), and where the $Fe^{3+}(OH_{0.5})_2$ subsequently partially transforms to an amorphous $Fe^{3+}OOH$ and more crystalline δ-$Fe^{3+}OOH$. The driving force to crystallize δ-FeOOH is low, which apparently makes the characteristic diffraction peak of (001) of $Fe(OH)_2$ easily disappear. Further factors leading to apparent amorphization could be the layer thickness of the materials formed upon (de-)intercalation of H; nanoscopic layer thicknesses will deform the lattice by strains in view of the different a and c parameters of the otherwise isomorphic phases [51].

4.3. Results and Discussion

Figure 4.6 depicts the parameters extracted from the neutron diffraction Rietveld refinements. The top insert shows the total detector counts as fraction of the highest detector count we measured. The inserts in the center show, in descending order, the total amount of Fe and the calculated molar fractions for Fe, $Fe(OH)_2$, and FeOOH. The detector counts and the weight fractions are normalized to the maximum detector counts (pattern 146) and the maximum total Fe content (pattern 89), respectively. The bottom-middle insert shows the iron electrode potential relative to the Hg/HgO reference electrode. The bottom insert depicts the cycle number and the programmed current to indicate the mode of operation (charging or discharging). A detailed analysis of the results is added to the appendix, clustered into: (1) start of discharging from a charged electrode, (2) steady-state discharging at the first plateau, (3) charging a discharged electrode from the first discharge plateau, and (4) the second iron discharge-plateau. The following text presents and discusses the main results.

The processed results show a variation of molar iron content between 40% and 70% for the iron metal phase and between 20% and 41% for the iron hydroxide phase. FeOOH is present from pattern 120 to 150 and from pattern 200 to 260 and reaches a molar content of 24%.

The high content of iron hydroxide is the first remarkable finding from the current work. Before testing, the cell was fully charged, followed by a floating charge for 24 hours. Even so, at the start of testing, the fraction of iron hydroxide was still at 24%. So, a large fraction of the iron mass remained inactive as iron hydroxide. Literature [20, 25] suggests that the passivation of iron limits the material utilization. Our data suggests that the iron electrode passivation is mostly a result of $Fe(OH)_2$ that cannot be reduced by recharging.

Figure 4.7 shows the derived iron content in a stacked graph with $Fe(OH)_2$, δ-FeOOH, amorphous iron phases, and metallic iron from top to bottom. We consider parts of Fe^{2+}/Fe^{3+} (oxy)hydroxides as amorphous iron-containing phases,

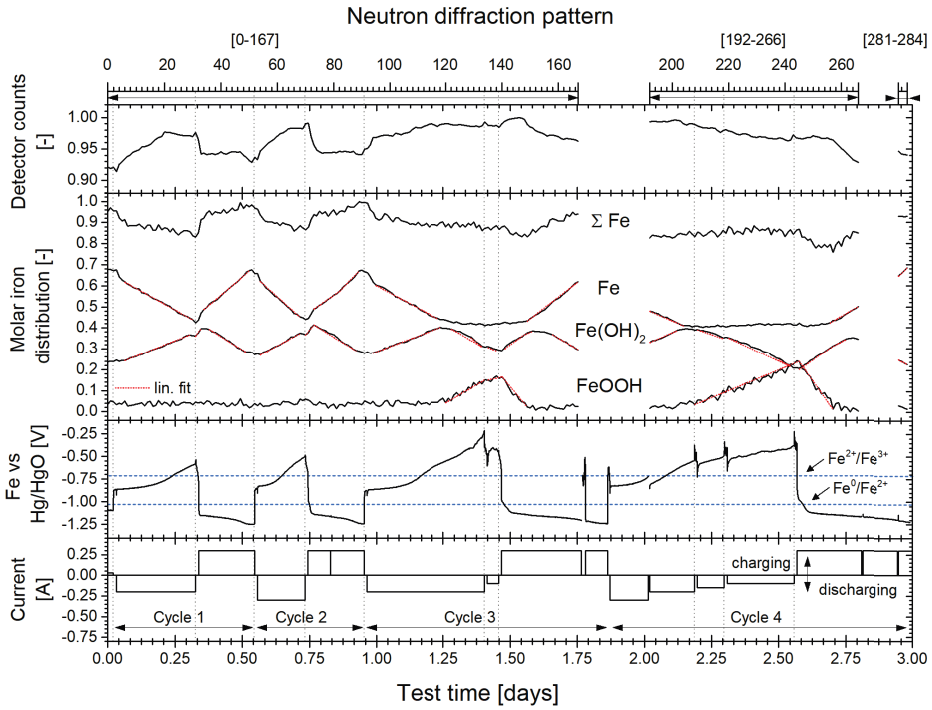

Figure 4.6: Detector counts, derived normalized molar iron fractions from the neutron diffraction pattern for Fe, $Fe(OH)_2$ and FeOOH with their sum, the voltage of iron electrode relative to the Hg/HgO reference electrode, and applied current. The red dotted lines indicate the linear fits depicted in the appendix D section results, Tables D.6-D.10. Note: the vertical grey dotted lines depict the rest periods between different experimental stages; the horizontal dashed lines depict the $Fe^{2+}(OH)_2/Fe^{3+}OOH$ and the $Fe^0/Fe^{2+}(OH)_2$ equilibrium potentials.

not Fe^0. About 40% of the total iron content participates in the observed phase transitions, 20% remains inactive as iron hydroxide, and 40% remains inactive as iron. It was expected that a substantial fraction of the iron will remain inactive as iron is necessary to provide a stable physical structure and electrical conductivity. The sum of the detectable iron phases (metallic iron, $Fe(OH)_2$, and δ-FeOOH) varies upon operation and is assumed to be 100% at the observed maximum of the molar amounts of iron in the combined phase fractions. The subtraction of the iron in the combined crystalline phase fractions yields the fraction of the iron that is present in an amorphous phase. Note that it cannot be excluded that there is more amorphous material that never crystallizes. The top of Figure 4.7 shows the ratio of the calculated amorphous iron phase to the

participating, detectable iron content. For first plateau operation (cycle 1 and cycle 2), the amorphous iron content shows maxima of 40% at the end of the discharge. For second plateau operation (cycle 3 and cycle 4), when δ-FeOOH disappears during recharging, the maxima were found around the 55% point. The high content of amorphous iron, at 22% of the sample (=0.4*0.55), is the second remarkable finding from the current work.

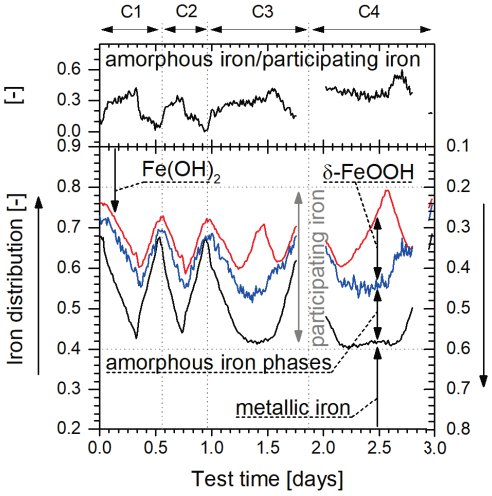

Figure 4.7: Top: ratio of amorphous iron (Fe^{2+}/Fe^{3+}) phases to participating iron. Bottom: stacked and normalized iron distribution: from top to bottom: $Fe(OH)_2$, δ-FeOOH, amorphous iron phases, and metallic iron.

The increase and decrease of crystalline iron show a steep change in the transition period immediately after rest. A third of the reduction of detectable iron phases happens in this period. This is followed by a steady rate of change for two-third of the reduction of detectable iron phases. Figure 4.8 shows the progress in molar amounts of iron phases during discharging of cycles 1-3 (first plateau only). Metallic iron shows steady changes in the fractional iron content that are close to the expected changes for a two-electron exchange process. The fractional changes in iron hydroxide are delayed (~35%) relative to the expected changes.

The discharge of C2 (1.5 times higher discharge rate than C1 and C3; delay of iron hydroxide formation with ~40% slightly higher) follows the pattern of C1 and C3. However, the same amount of undetectable amorphous iron phases (0.012 mol) forms after 10% less charge withdrawn (at 0.045 mol e^- rather than at 0.05 mol e^-).

Figure 4.9 shows the variation of metallic iron (Fe), iron (II) hydroxide, and

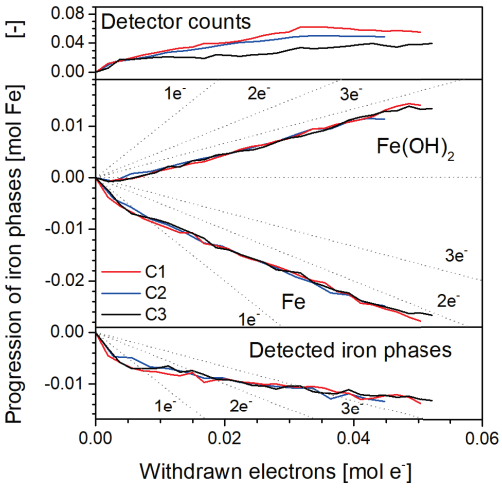

Figure 4.8: Progress in detector counts and molar iron amount during discharging of cycle 1 (C1, measurement 3-30), cycle 2 (C2, measurement 53-69), and cycle 3 (C3, only first plateau, measurements 92-120) vs inserted electrons. Top: detector counts; middle: decreasing iron amount and increasing iron hydroxide amount; and bottom: variation in detectable molar iron amount. Grey dotted lines indicate expected molar changes for a one-, two-, and three-electron process.

detectable iron during charging. The amounts of metallic iron and detectable iron phases increase with charging. The ratio of both at the end of charging exceeds 50%, supporting the finding that a substantial amount of iron phases must be present in amorphous form when discharged to the first plateau. This amorphous iron phase is then reduced back to metallic iron upon charging, as is iron hydroxide. The delayed reduction of iron hydroxide alone cannot provide enough iron to cause the observed increase in metallic iron.

Interestingly, the amount of iron hydroxide first increases upon recharging before it starts decreasing. Figure 4.9 indicates a one-electron process for the increase in iron hydroxide phase. We speculate that amorphous iron is present as Fe(II) and Fe(III) and that the unexpected steep increase of the iron hydroxide phase during recharging is caused by the reduction of amorphous iron (III) to crystalline iron (II) hydroxide at a higher rate than the reduction of Fe(II) hydroxide to Fe metal. It is likely that an increased discharge rate (C2) causes a larger fraction of (amorphous) Fe(III) since the sloppy kinetics of the iron electrode cannot keep up. The increase in the iron hydroxide fraction in the transition following the discharge at higher rates is about 40% higher than in the previous transition, 4.8% compared to 3.4%, see appendix Figure D.7. The in-

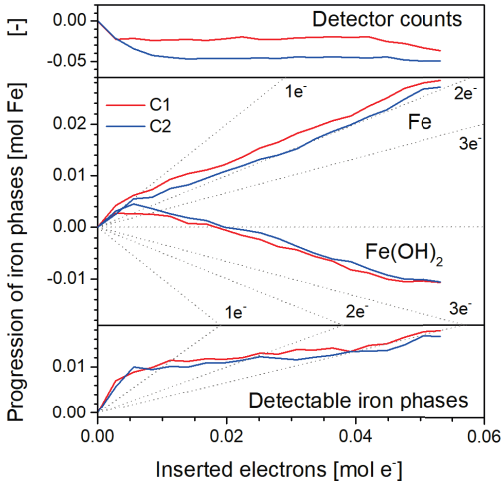

Figure 4.9: Detector counts and amount of iron phases during charging of cycle 1 (C1, measurement 32-51) and cycle 2 (C2, measurement 71-90) vs inserted electrons. Top: detector counts; middle: increasing metallic iron amount and decreasing iron hydroxide amount; and bottom: variation in detectable molar iron amount. Grey dotted lines indicate the expected molar changes for a one-, two-, and three-electron process.

creased amorphous Fe(III) content would cause more crystalline iron hydroxide formation from the amorphous Fe(III) phase.

Both the delayed rates for iron hydroxide and the iron hydroxide formation at the start of the charging period contribute to an accumulation of iron hydroxide inside the electrode. The iron hydroxide content increased from 24% to 27% after the first recharge, and to 28% after the second recharge. The initial discharge after production has a material utilization of about $0.4\,\mathrm{Ah/g_{Fe}}$. Subsequent discharges have a utilization of about $0.15\,\mathrm{Ah/g_{Fe}}$. This suggests that the first discharge already causes accumulation within the electrode of iron hydroxide, which cannot be fully reactivated. Discharging to the second plateau may help in reactivating iron hydroxide. The derived iron hydroxide content at the broad peaks before and after the second plateau discharge shows a reduction of 2% of the iron hydroxide content for the first shorter discharge and a reduction of 4% for the second longer discharge. In addition, the minimum iron hydroxide content at the charged state can be found at the end of our experiments, even without completed recharging.

We see a stable iron content in the different crystalline phases when iron oxyhydroxide is present in detectable amounts. When iron oxyhydroxide is no longer detectable, the phase fraction from iron metal starts increasing. From

this, we conclude that no direct reduction from detected $Fe^{3+}OOH$ to Fe^0 occurs. $Fe(OH)_2$ shows broad maxima in the detected intensity before and after the transition to the second discharge plateau, see Figure 4.6 and 4.10. This smooth transition suggests that a smooth solid state reaction with Fe^{2+} going to Fe^{3+} by dehydrogenation. Moreover, it suggests that the internal charge rearrangement occurs, up to the stability limit of 10% Fe^{3+}. At higher Fe^{3+} saturation, change rates for $Fe(OH)_2$ are increasing, supporting this conclusion. The transition from second plateau discharging to charging shows an immediate response to the current input, as can be seen from the sharp peaks for both phases. Figure 4.10 shows the further recharging of cycle 4.

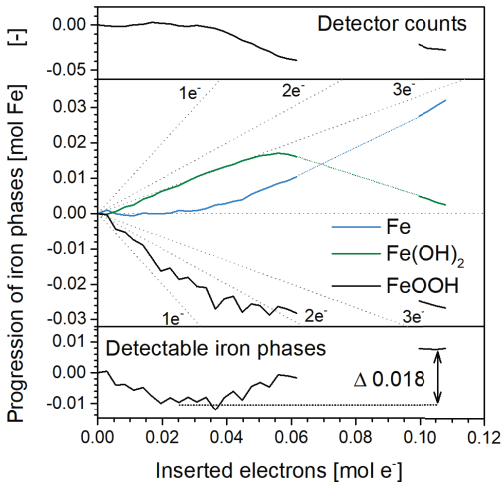

Figure 4.10: Progress in detector counts and amount of iron phases during recharging of cycle 4 (starting from the second discharge plateau, measurements 244-266 and 281-284) vs inserted electrons. Top: detector counts; middle: increasing metallic iron amount, decreasing iron oxyhydroxide amount, and first increasing, later decreasing iron hydroxide amount; and bottom: variation in the amount of detectable iron phases. Blue and green dotted lines indicate interpolated Fe and $Fe(OH)_2$ amount, and grey dotted lines indicate expected molar changes for a one-, two-, and three-electron process.

FeOOH decreases faster than the increase seen in $Fe(OH)_2$, and the detectable crystalline iron content reaches a minimum when FeOOH has vanished, as seen in pattern 257. Then, suprisingly, both iron and iron hydroxide phases increase simultaneously. So, the reduction of amorphous Fe^{2+} to Fe^0 again takes place alongside the reduction of amorphous Fe^{3+} to $Fe^{2+}(OH)_2$. Notably, during patterns 258 and 262 we have close to perfect agreement between the measured fractional change and electrochemical charge input when assigning 66% of the

charge, which contributes to the formation of Fe^0 in a two-electron process and 29% of the charge to the formation of $Fe^{2+}(OH)_2$ in a one-electron process. So here, amorphous iron phases are not produced but only consumed to serve the formation of the detected crystalline phases.

Figure 4.11 depicts a contour plot of the all recorded neutron diffraction patterns. This plot shows that reflections indicate constant lattice parameters while the patterns vary in intensity. Changing intensities reflect the varying observable phase content, as described earlier. In Figure 4.11, the incoherent background can be seen in between the horizontal lines of the coherent reflections.

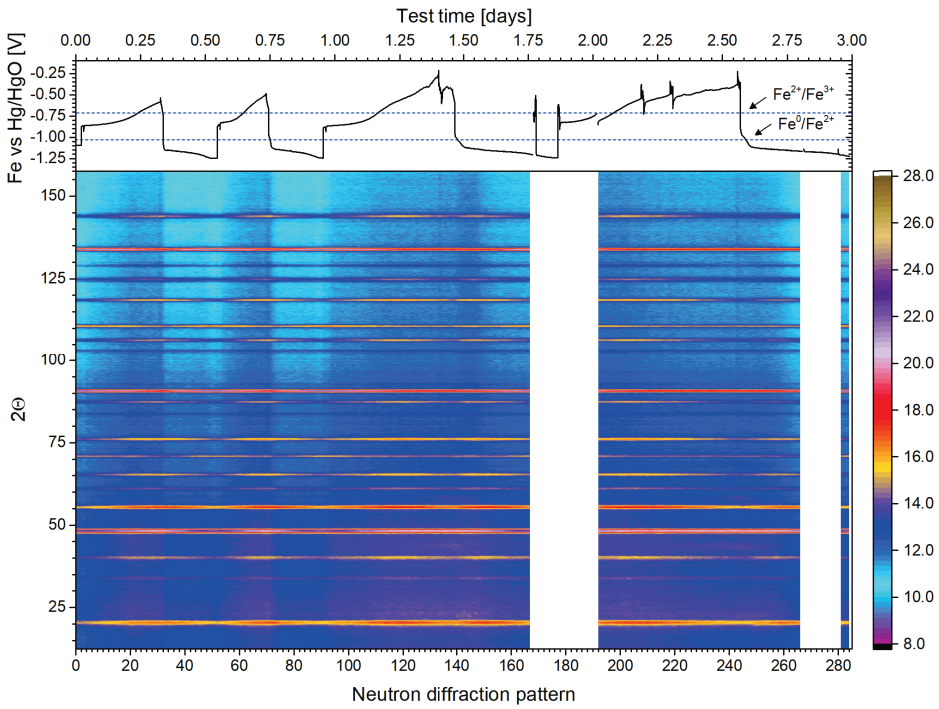

Figure 4.11: Contour plot of observed neutron diffraction patterns, with as a reference at the top the observed potentials of the iron electrode relative to the reference electrode (Hg/HgO) that result from the discharging, charging and waiting periods.

The background counts are linked to incoherent scattering caused by the hydrogen content inside the cell. Variations correspond with the electrolyte content as the electrolyte has the highest volumetric hydrogen density. Most significant variations are recognizable in the transition zones from charging to discharging and vice versa.

In our point of view, two mechanisms cause background variation: (1) gas production/accumulation/release, and (2) material precipitation/dissolution; both result in changes of the electrolyte content.

The first mechanism can be observed, e.g., when the system is at rest. The space between iron electrode and counter electrode is filled with gas bubbles and/or electrolyte. During operation, gas leaves the system via this gap. At rest, no gas is produced and the gap is refilled with electrolyte. Because of this, maxima in the total detector counts at rest are visible in their pattern (increased electrolyte background). When the cell is turned on again, these maxima vanish (gas replaces some electrolyte). Furthermore, hydrogen gas production also inside the electrode is indicated by the decrease in detector counts at the end of the charging step pattern 47-51 and 87-90. Note that the hydrogen evolution potential is that close to the Fe^0/Fe^{2+} equilibrium potential that the overpotential makes that hydrogen evolution can occur already from the start of charging. Here steadily increasing (1) porosity, due to phase changes, (2) metallic iron content, and (3) cell voltage would favour hydrogen production and accumulation. However, the stable detector counts depicted in Figure 4.9 indicate that in the period after the transition until the end of charging no gas accumulates within the electrode, so any produced gas can leave, keeping the content nearly constant. After prolonged charging, the voltage reaches a stable plateau, indicating that the inserted charge contributes to only hydrogen production. This is further supported by the fact that the increase in iron phase flattens out and the decrease of the iron hydroxide phase stops. Gas production is also likely to occur during the final measurement session, pattern 281-284. In these measurements, the voltage curve is already bent and close to stabilization. At this time, the detector counts are decreasing while the amount of iron is still increasing.

Gas may disappear from inside the electrode during the first two discharges (since production ceases). Here the detector counts first increase as accumulated gas is released and then stabilize, see Figure 4.8. Iron and iron hydroxide show here steady gradients, suggesting no correlation between the detector counts and the phase change rates. (A discussion of a possible correlation between incoherent background affecting the screening of the samples and observed diffraction intensities is added to the appendix.)

The second mechanism for changes in detector counts may be the different hydrogen contents in the solid phase precipitates. Metallic iron has no hydrogen content, and the hydrogen content of iron (II) hydroxide is lower than that of the electrolyte. At the start of the charging of C1 and C2 (see Figure 4.9) a substantial amount of iron and iron hydroxide forms. Also during recharging of C3 and C4, we observe a simultaneous increase of these phases but with a

wider spread. The speed of change for the detector counts is correlated with the speed of phase precipitation. This correlation supports the idea that electrolyte displacement by changing precipitates occurs.

In commercial nickel-iron batteries, it is common knowledge that electrolyte levels increase during charging and decease during discharging. This characteristic can be explained by both mechanisms described, although the $Ni(OH)_2$ / NiOOH phase changes play a role.

A factor of importance appears to be the gas evolution that interferes with the electrolyte content of the electrodes: gas inside the electrode may replace electrolyte, reducing the ionic conductivity, consistent with the observed increase in overpotentials. Moreover, the process of iron hydroxide reduction starts slowing down at the same time as the start of decrease of the detector counts that indicate gas evolution. This hydrogen can further hinder electrolyte access to any remaining iron hydroxide inside the porous structure. This would limit further $Fe(OH)_2$ dissolution necessary for iron hydroxide reduction.

Interestingly, the iron fraction increases while gas evolution takes place, so amorphous iron hydroxide still has contact with the electrolyte and can be reduced. It may be limited by poor electrolyte access as well, as the soluble intermediate Fe species requires the electrolyte, although these intermediates are reported to disappear before hydrogen evolution starts [11, 14].

Changes in the neutron screening of the sample likely affect the fractional changes in the transitions from discharging to charging. This makes both rates appear faster than they are. We observed high fractional changes of metallic iron in the transition from charging to discharging. We relate this to the start of the corrosion process of the iron electrode in the waiting period before discharging. The corrosion process is comparable to the discharge process and could provide adsorbed hydroxyl groups. With available adsorbed hydroxyl ions, fractional changes may occur at rates higher than those expected on the start of discharging.

Iron hydroxide precipitation starts with a delay after some iron is transformed into an amorphous state and iron hydroxide reduction stops when the amorphous iron has vanished. We speculate that the presence of amorphous phases is essential for a proper operation of the electrode since changes in the solid iron hydroxide phase only occur in the presence of amorphous iron phases.

4.4. Conclusion

In this study, we use neutron diffraction combined with Rietveld refinement to investigate the phase transitions of a sintered iron electrode in operando. This technique enables to probe the bulk of the sample without interference.

Iron and iron (II) hydroxide are the phases forming the first discharge plateau of the iron electrode. We found that a substantial inactive amount of iron hydroxide is always present. This finding indicates that the reduction from iron hydroxide to iron needs to be improved for increased material utilization. We ascertained that crystalline iron disappears and forms as expected during operation, while iron hydroxide reacts slowly, via an intermediate amorphous phase.

The structure of δ-FeOOH fits the phase occurring at the second discharge plateau. This structure differs from that of δ-FeOOH in that it has equal spacing between the oxygen layers and symmetric distribution of the iron and hydrogen atoms. We can confirm that iron is passivated when δ-FeOOH is present and that no direct reduction from crystalline Fe^{3+} to Fe^0 occurs.

As much as 40% of the participating iron can be in an amorphous Fe(II)/Fe(III) containing phase. As such, it is undetectable in the diffraction during first plateau operation. The amount of detectable crystalline iron phases reaches an absolute minimum upon recharging when FeOOH disappears and as much as 55% of the total participating iron content is amorphous.

References

[1] F. M. Mulder, B. M. H. Weninger, J. Middelkoop, F. G. B. Ooms, and H. Schreuders, *Efficient electricity storage with a battolyser, an integrated Ni–Fe battery and electrolyser,* Energy & Environmental Science **10**, 756 (2017).

[2] J. P. Barton, R. J. L. Gammon, and A. Rahil, *Characterisation of a nickel-iron battolyser, an integrated battery and electrolyser,* Frontiers in Energy Research , 318 (2020).

[3] L. Öjefors and L. Carlsson, *An iron—air vehicle battery,* Journal of Power Sources **2**, 287 (1978).

[4] R. D. McKerracher, C. Ponce de Leon, R. G. A. Wills, A. A. Shah, and F. C. Walsh, *A review of the iron–air secondary battery for energy storage,* ChemPlusChem **80**, 323 (2015).

[5] H. Weinrich, M. Gehring, H. Tempel, H. Kungl, and R.-A. Eichel, *Electrode thickness-dependent formation of porous iron electrodes for secondary alkaline iron-air batteries,* Electrochimica acta **314**, 61 (2019).

[6] C. Yang, A. K. Manohar, and S. Narayanan, *A high-performance sintered*

iron electrode for rechargeable alkaline batteries to enable large-scale energy storage, Journal of The Electrochemical Society **164**, A418 (2017).

[7] B. M. H. Weninger and F. M. Mulder, *Renewable hydrogen and electricity dispatch with multiple Ni–Fe electrode storage,* ACS Energy Letters **4**, 567 (2019).

[8] M. F. Lagadec and A. Grimaud, *Water electrolysers with closed and open electrochemical systems,* Nature Materials **19**, 1140 (2020).

[9] J. Huang and Y. Wang, *Efficient renewable-to-hydrogen conversion via decoupled electrochemical water splitting,* Cell Reports Physical Science , 100138 (2020).

[10] Z. Jin, P. Li, and D. Xiao, *A hydrogen-evolving hybrid-electrolyte battery with electrochemical/photoelectrochemical charging from water oxidation,* ChemSusChem **10**, 483 (2017).

[11] R. D. Armstrong and I. Baurhoo, *Solution soluble species in the operation of the iron electrode in alkaline solution,* Journal of Electroanalytical Chemistry and Interfacial Electrochemistry **34**, 41 (1972).

[12] L. Öjefors, *Temperature dependence of iron and cadmium alkaline electrodes,* Journal of The Electrochemical Society **123**, 1139.

[13] M. K. Ravikumar, T. S. Balasubramanian, A. K. Shukla, and S. Venugopalan, *A cyclic voltammetric study on the electrocatalysis of alkaline iron-electrode reactions,* Journal of applied electrochemistry **26**, 1111 (1996).

[14] R. D. Armstrong and I. Baurhoo, *The dissolution of iron in concentrated alkali,* Journal of Electroanalytical Chemistry and Interfacial Electrochemistry **40**, 325 (1972).

[15] M. K. Ravikumar, A. S. Rajan, S. Sampath, K. R. Priolkar, and A. K. Shukla, *In situ crystallographic probing on ameliorating effect of sulfide additives and carbon grafting in iron electrodes,* Journal of The Electrochemical Society **162**, A2339 (2015).

[16] H. Wang, Y. Liang, M. Gong, Y. Li, W. Chang, T. Mefford, J. Zhou, J. Wang, T. Regier, F. Wei, and H. Dai, *An ultrafast nickel–iron battery from strongly coupled inorganic nanoparticle/nanocarbon hybrid materials,* Nature communications **3**, 917 (2012).

[17] M. Pourbaix, *Atlas of electrochemical equilibria in aqueous solution,* NACE **307** (1974).

[18] B. Beverskog and I. Puigdomenech, *Revised pourbaix diagrams for iron at 25–300 °C,* Corrosion Science **38**, 2121 (1996).

[19] J. Bernal, D. Dasgupta, and A. Mackay, *The oxides and hydroxides of iron and their structural inter-relationships,* Clay Minerals Bulletin **4**, 15 (1959).

[20] A. K. Shukla and B. Hariprakash, *Secondary batteries–nickel systems/ electrodes: iron. In Encyclopedia of Electrochemical Power Sources; J. Garche, Ed.* (Elsevier Science Publishing Co. Inc, 2009).

[21] L. Öjefors, *SEM studies of discharge products from alkaline iron electrodes,* Journal of The Electrochemical Society **123**, 1691 (1976).

[22] K. Micka and I. Roušar, *Theory of porous electrodes—XVIII. the iron electrode,* Electrochimica acta **29**, 1411 (1984).

[23] H. G. Silver and E. Lekas, *The products of the anodic oxidation of an iron electrode in alkaline solution,* Journal of The Electrochemical Society **117**, 5 (1970).

[24] Y. Geronov, T. Tomov, and S. Georgiev, *Mössbauer spectroscopy investigation of the iron electrode during cycling in alkaline solution,* Journal of Applied Electrochemistry **5**, 351 (1975).

[25] D.-C. Lee, D. Lei, and G. Yushin, *Morphology and phase changes in iron anodes affecting their capacity and stability in rechargeable alkaline batteries,* ACS Energy Letters **3**, 794 (2018).

[26] S. U. Falk and A. J. Salkind, *Alkaline storage batteries* (John Wiley & Sons, 1969).

[27] P. R. Vassie and A. C. C. Tseung, *High performance, rechargeable sintered iron electrodes—i: The effect of preparative methods and additives on the structure and performance of sintered iron electrodes,* Electrochimica Acta **21**, 299 (1976).

[28] H. G. Schimmel, J. Huot, L. C. Chapon, F. D. Tichelaar, and F. M. Mulder, *Hydrogen cycling of niobium and vanadium catalyzed nanostructured magnesium,* Journal of the American Chemical Society **127**, 14348 (2005).

[29] L. Van Eijck, L. Cussen, G. Sykora, E. Schooneveld, N. Rhodes, A. Van Well, and C. Pappas, *Design and performance of a novel neutron powder diffractometer: PEARL at TU Delft,* Journal of Applied Crystallography **49**, 1398 (2016).

[30] B. H. Toby and R. B. Von Dreele, *GSAS-II: the genesis of a modern open-source all purpose crystallography software package,* Journal of Applied Crystallography **46**, 544 (2013).

[31] M. Quirós, S. Gražulis, S. Girdzijauskaitė, A. Merkys, and A. Vaitkus, *Using SMILES strings for the description of chemical connectivity in the Crystallography Open Database,* Journal of Cheminformatics **10**, 23 (2018).

[32] A. Merkys, A. Vaitkus, J. Butkus, M. Okulič-Kazarinas, V. Kairys, and S. Gražulis, *COD:: CIF:: Parser: an error-correcting CIF parser for the Perl language,* Journal of Applied Crystallography **49**, 292 (2016).

[33] S. Gražulis, A. Merkys, A. Vaitkus, and M. Okulič-Kazarinas, *Computing stoichiometric molecular composition from crystal structures,* Journal of Applied Crystallography **48**, 85 (2015).

[34] S. Gražulis, A. Daškevič, A. Merkys, D. Chateigner, L. Lutterotti, M. Quiros, N. R. Serebryanaya, P. Moeck, R. T. Downs, and A. Le Bail, *Crystallography Open Database (COD): an open-access collection of crystal structures and platform for world-wide collaboration,* Nucleic acids research **40**, D420 (2012).

[35] S. Gražulis, D. Chateigner, R. T. Downs, A. F. T. Yokochi, M. Quirós, L. Lutterotti, E. Manakova, J. Butkus, P. Moeck, and A. Le Bail, *Crystallography open database–an open-access collection of crystal structures,* Journal of applied crystallography **42**, 726 (2009).

[36] R. T. Downs and M. Hall-Wallace, *The American Mineralogist crystal structure database,* American Mineralogist **88**, 247 (2003).

[37] J. B. Parise, W. G. Marshall, R. I. Smith, H. Lutz, and H. Möller, *The nuclear and magnetic structure of "white rust"—Fe (OH0. 86D0. 14) 2,* American Mineralogist **85**, 189 (2000).

[38] J. O. G. Posada and P. J. Hall, *Towards the development of safe and commercially viable nickel–iron batteries: improvements to Coulombic efficiency at high iron sulphide electrode formulations,* Journal of Applied Electrochemistry **46**, 451 (2016).

[39] A. J. Salkind, C. J. Venuto, and S. U. Falk, *The reaction at the iron alkaline electrode,* Journal of The Electrochemical Society **111**, 493 (1964).

[40] U. Casellato, N. Comisso, and G. Mengoli, *Effect of Li ions on reduction of Fe oxides in aqueous alkaline medium,* Electrochimica Acta **51**, 5669 (2006).

[41] D. Lei, D.-C. Lee, A. Magasinski, E. Zhao, D. Steingart, and G. Yushin, *Performance enhancement and side reactions in rechargeable nickel–iron batteries with nanostructured electrodes,* ACS Applied Materials & Interfaces **8**, 2088 (2016).

[42] W. Jiang, F. Liang, J. Wang, L. Su, Y. Wu, and L. Wang, *Enhanced electrochemical performances of FeO x–graphene nanocomposites as anode materials for alkaline nickel–iron batteries,* RSC Advances **4**, 15394 (2014).

[43] H. A. Figueredo Rodríguez, R. D. McKerracher, C. Ponce de León, and F. C. Walsh, *Improvement of negative electrodes for iron-air batteries: comparison of different iron compounds as active materials,* Journal of the Electrochemical Society **166**, A107 (2019).

[44] A. K. Manohar, S. Malkhandi, B. Yang, C. Yang, G. K. S. Prakash, and S. R. Narayanan, *A high-performance rechargeable iron electrode for large-scale battery-based energy storage,* Journal of The Electrochemical Society **159**, A1209 (2012).

[45] R. M. Cornell and U. Schwertmann, *The iron oxides: structure, properties, reactions, occurrences and uses* (John Wiley & Sons, 2003).

[46] S. Okamoto, *Structure of δ-FeOOH,* Journal of the American Ceramic Society **51**, 594 (1968).

[47] G. Patrat, F. De Bergevin, M. Pernet, and J. C. Joubert, *Structure locale de δ-FeOOH,* Acta Crystallographica Section B: Structural Science **39**, 165 (1983).

[48] V. A. Drits, B. A. Sakharov, and A. Manceau, *Structure of feroxyhite as determined by simulation of X-ray diffraction curves,* Clay Minerals **28**, 209 (1993).

[49] M. Wagemaker, F. G. B. Ooms, E. M. Kelder, J. Schoonman, and F. M. Mulder, *Extensive migration of Ni and Mn by lithiation of ordered LiMg0. 1Ni0. 4Mn1. 5O4 spinel,* Journal of the American Chemical Society **126**, 13526 (2004).

[50] G. Kresse and J. Furthmüller, *Efficiency of ab-initio total energy calculations for metals and semiconductors using a plane-wave basis set,* Computational Materials Science **6**, 15 (1996).

[51] M. Wagemaker, D. P. Singh, W. J. H. Borghols, U. Lafont, L. Haverkate, V. K. Peterson, and F. M. Mulder, *Dynamic solubility limits in nanosized*

olivine LiFePO4, Journal of the American Chemical Society **133**, 10222 (2011).

5

Iron electrodes with Al/Zr doping for large- and small-scale energy storage and hydrogen production

The implementation of renewables allows for the reduction of fossil-fuel based carbon emissions of the global energy system. Fossil fuels are easy to store whereas renewables are intermittent in their nature. In this study we introduce the hydrogen storage and production (HSP-)cell, which is related to a so-called iron half cell, operated for hydrogen and oxygen evolution. This HSP-cell is energy efficient and based on earth abundant iron and alkaline water based electrolyte, that on purpose only generates hydrogen and oxygen from water. We also developed a new synthesis strategy for producing fine reduced iron powders, based on iron sulfate, a cost-efficient iron source. The synthesis strategy includes the addition of the dopants zirconium oxide or aluminum oxide. These dopants improve the ability of the iron electrode to recharge and allow for operation at higher discharge rates when compared to similar dimensioned electrodes without them. We produced 2 mm thick iron electrodes, accessible only from one side, with an areal storage density of 161 mAh/cm^2 when discharged at 10 mA/cm^2 and of 149 mAh/cm^2 when discharged at 25 mA/cm^2. The reported volumetric storage density of 0.76 mAh/cm^3 at 40 °C, compares favorable with the undoped ones. Such performance suggests that often applied additives, such as sulphur, can be circumvented by this approach. The proposed storage concept together with the presented iron electrodes brings us closer to overcome the renewable energy intermittency challenge.

(Supporting Information see appendix E)

5.1. Introduction

Without rigorously cutting CO_2 emissions global warming will exceed the intended limit of 1.5 °C defined in the 2015 Paris Agreement. Every tonne CO_2 emitted contributes to global warming [1]. Renewables can replace fossil fuel usage and successive installations of renewables resulted in a projected market share of electricity generation of almost 30% for 2021 [2]. However, electricity generation is only one sector. Other sectors such as transportation and industry have to shift to a green feedstock, likely in the form of hydrogen or derived synthetic fuels, to reduce their CO_2 emissions and hence limit global warming.

The required scale is enormous and solutions to address these issues should preferably be based on abundant materials. Iron is a widely-used non-toxic element. According to Chen et al.[3] iron is the cheapest transition metal which is broadly available in the earth crust. Iron is used in omnipresent products and can also be used as a negative electrode in alkaline batteries, best-known from the Ni-Fe batteries. These Ni-Fe batteries are robust and overcharging only causes water decomposition into H_2 and O_2, the same electrochemistry which can be applied in electrolysis. During electrolysis the iron electrode operates as the cathode for hydrogen generation. Hence, the iron electrode can have a double functionality: It can be used as a battery electrode for energy storage and as an electrolyser electrode for energy conversion as described in the previous chapters and in reference [4].

Iron electrodes utilized in nickel-iron and iron-air batteries provide electricity storage. Recently iron electrodes have been suggested as an indirect means to store hydrogen by delaying the hydrogen output [5–8]. Such systems work with a switchable auxiliary electrode [9] or with the concept of multi-controlled electrodes [10] which distributes currents among electrodes and thereby allows to convert an intermittent electricity input into a preferably sustained hydrogen output for industrial applications, overcoming the intermittency problem [11]. Thus, iron electrodes can serve electricity storage, indirect hydrogen storage and hydrogen generation, and its optimization should take into account all possible applications.

Iron electrodes have been developed and optimized for over a 100 years. It started with Jungner and Edison who constructed the first iron pocket electrodes. There exist different types of commercial electrodes that can have different characteristics. We tested commercially available pocket electrodes from Changhong (NF10-S, thickness 3.2mm). These electrodes show a storage density of up to 186 mAh/cm^2 and 0.58 Ah/cm^3 when discharged at a current density of 10 mA/cm^2 from one side. In general, pocket electrodes show a low charging efficiency [12] because the higher internal resistance [13] causes earlier hydrogen

evolution. We also had to insert 480 mAh/cm^2 to reach this storage density, see table 5.1. Currently, commercially available pocket electrodes are designed to operate at moderate rates for bridging daily fluctuations in renewable electricity generation and demand.

Alternative types of iron electrodes were successfully developed after the first oil crises 1973 for the propulsion of electric vehicles. Siemens developed plastic-bond iron electrodes for iron-air batteries, the Westinghouse Electric Corporation (WEC) and the Swedish National Development Corporation (SNDC) developed sintered iron electrodes for nickel-iron batteries and for iron-air batteries. Nickel-iron batteries are limited by the capacity of the more expensive nickel electrode, thin iron electrodes, about half the thickness of the nickel-electrode, suffice. Iron-air batteries overcome this capacity restriction, thicker iron electrodes can be used, since an infinite amount of air can be supplied to an air electrode. However, the lower voltaic efficiency due to higher overpotentials for thermodynamic and kinetic reasons is a drawback of the iron-air battery.

Concerning iron-air battery development, all companies, Siemens, WEC and SNDC developed iron-air batteries where the iron electrode is sandwiched between two air electrodes. WEC and SNDC also developed nickel-iron batteries for traction purposes. In these batteries many alternating electrodes form a cell and the electrodes are accessible for both sides. The test setups of WEC and SNDC are a reproduction of these configurations. Counter-electrodes are placed on both sides of the iron electrode [14–16], in order to achieve the best performance possible, profiting from lower effective resistances (Note: Confirmed by Lars Öjefors, (co-)author of [17–21]). Their reported current density relates to the size of the iron electrode (lxb) and not to the exchange current density between the iron electrode and the counter electrodes. Operation from both sides creates a symmetry plane in the centre of the electrode [22] and the applied current distributes equally over both accessible surfaces. For instance, a reported current density of 50 mA/cm^2 for the iron electrode corresponds to a current density of 25 mA/cm^2 for the air electrode, which represents the exchange current density at each side of the iron electrode.

For clarity we report in the benchmark table the total electrode current density (TCD), the total electrode thickness (d), the surface related exchange current density (ECD) and the surface related electrode thickness (d_s). These values define the conditions under which a key parameter for comparison in the benchmark table - the reported volumetric storage density - is determined.

Figure 5.1 shows a simplified cross section of an electrode for one-sided testing and for an electrode for two-sided testing and defines the characteristics denoted in the benchmark table (TCD, ECD, d and d_s). The simplified representation relates to the fact that the volumetric conversion rate (i_v) throughout

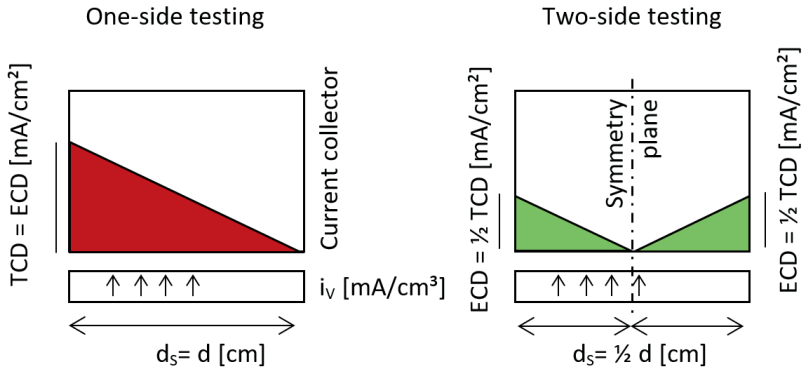

Figure 5.1: Simplified cross section with ion-current distribution within an electrode for one-sided testing (left, with exchange surface left and current collector at the right side) and two-sided testing (right, with symmetry plane in the centre of the electrode [22]).

5

the electrode is assumed to be uniform. Yet, the difference between one-sided testing and two-sided testing is recognizable. Under the same test conditions (same TCD and d), the exchange current density at the exchange surface (ECD) is two times lower in case of two-sided testing when the same current is applied. Also is the surface related electrode thickness (d_s), the path the ions need to travel within the electrode, is two times shorter.

The plastic bond iron electrodes from Siemens were 10 mm thick and are to our knowledge the thickest iron electrodes reported. They consist of a mixture of iron powder, acetylene black, and binder as active mass, which is embedded in between iron fibers which are enclosed with expanded metal. The electrode is structured perpendicular to the surface in alternating coarse and fine layers. The coarse layers (iron fibers without active mass) provided ionic and electrical conductivity and the iron fibers together with the acetylene black provided electric conductivity for the active mass. The electrode showed a capacity of 320 mAh/cm^2 when discharged in between two air electrodes at a current density of 40 mA/cm^2. This discharge capacity included both iron discharge plateaus, approximately 2/3 belonging to the 1st plateau and 1/3 to the 2nd plateau leading to a first plateau volumetric discharge capacity of 0.43 Ah/cm^3. Limiting discharging to the 1st plateau caused capacity fading, here 2nd plateau discharging was required to stabilize the discharge capacity. Back then in 1980, this system was not considered as suitable for large-scale energy storage due to the low total efficiency of 35%, including voltaic losses and 20% faradaic loss through overcharging [23, 24].

WEC and SNDC developed sintered iron electrodes. Both synthesis strate-

gies were alike and start with the reduction of iron-oxide powders to iron by hydrogen. The reduced iron powder was further pressed on current collectors and then sintered together, resulting in highly porous iron electrodes with densities of 20-25%, relative to the theoretical density of iron [16].

The projected development goal of the Westinghouse iron-air battery was an areal storage capacity of 100 mAh/cm^2 per side of the iron electrode, defined by a current density of 25 mA/cm^2 for the air electrodes for a discharge time of four hours. The cell voltage for this conditions is projected as 0.89 V [25]. The reported total electrode discharge capacity of 170 mAh/cm^2 (corresponding to 0.68 Ah/cm^3) for this current density comes close to the project goal. However, the cycle history is with 8 cycles very limited which does not allow for statements concerning the long-term cycling stability of the iron storage electrodes [16].

SNDC produced thin electrodes for nickel-iron batteries and thicker electrodes for iron-air batteries [20]. Their 0.8 mm thick electrode had a volumetric storage density of 0.85 Ah/cm^3 and a material utilization of 0.27 Ah/g when discharged in between two nickel electrodes with an exchange discharge current density (ECD) of 6.67 mA/cm^2 [26]. Their 3.2 mm thick electrodes possessed a storage density of 0.51 Ah/cm^3 when discharged at an exchange current density of 25 mA/cm^2 [19]. Also the performance of a 2.1 mm thick electrode is reported [19, 20]. This electrode showed a performance of 0.95 Ah/cm^3 when discharged at an exchange current density of 25 mA/cm^2 at room temperature. This value seems to be slightly higher, compared to the other reported values but it cannot be verified by examining the belonging voltage curves. It appears that they did not reach these storage densities for their thicker iron electrodes used in the iron-air cell which are relevant for comparison with our sintered electrodes.

The latest publication concerning the SNDC 30 kWh iron-air battery system [20] reports an energy density of 80 Wh/kg for a 5-h discharge rate and specifies the system weight to 393 kg and the number of iron electrodes to 760, together yielding a storage capacity of 41.37 Wh/electrode, or 172.5 mWh/cm^2 taking the provided electrode dimensions (117 x 205 mm) into account. The achieved volumetric storage capacity can be estimated by division of the value with the discharge voltage and cell thickness (3.2 mm). Assuming a conservative average discharge voltage of 0.8 V yields a volumetric storage capacity of 0.67 Ah/cm^3 with a resultant exchange current density of 21.56 mA/cm^2 between the iron electrode and the belonging air electrodes. The SNDC iron-air battery had an overall efficiency of about 40%. About 70% of the losses are caused by the voltaic losses of the air electrode.

In recent years several papers covered iron electrodes and collected performance parameters [27–30]. Research mainly focused on a high material utilization (Ah/g$_{Fe}$) in combination with high discharge rates (C-Rate and A/g) which

can be achieved with thin electrodes. For instance, one referenced work showed novel and promising processing techniques which enabled discharge rates of up to 32 A/g, equivalent to about 110 mA/cm^2 [31]. However, the areal storage capacity was only 0.7 mAh/cm^2, measured at 1 A/g. Bulk energy storage rather asks for higher storage densities, preferably reported in Ah/cm^3 or in mAh/cm^2 for the estimation of the energy and power density. Table 5.1 lists electrodes with higher areal storage capacity produced in recent years, together with the electrodes of Siemens, SNDC and WEC. It can be recognized that the electrode of Siemens still has the highest areal storage capacity, while the sintered electrodes from SNDC had the highest volumetric storage capacity.

The here reported electrodes have the second highest areal storage density, while being 2.4 times thinner than the Siemens electrodes. At a discharge rate of 25 mA/cm^2, we report a capacity of 150 mAh/cm^2. This value exceeds the set development goal of 100 mAh/cm^2 (at a C/4 rate) for the Westinghouse iron-air battery by 50% [25]. Moreover, we report a volumetric storage density of 0.76 mAh/cm^3 for the electrode with Zr-doping. This value is 12% higher than the value of Westinghouse iron electrode (0.68 mAh/cm^3), 13% higher than the SNDC iron electrode (0.67 mAh/cm^3) while the surface related electrode thickness (d_s) of the Zr-doped electrode of 2.07 mm exceeds the values from WEC (1.25 mm) / SNDC (1.6 mm) by 66% / 29%. The reported electrodes have a theoretical density of about 34% while the optimal theoretical density is about 22% [16], indicating the potential for further performance improvements.

From our previous work with sintered iron electrodes [36] we know that our pure iron electrodes lack the capability to completely recharge, substantial amounts of iron hydroxide were detected in the charged state, 22-28% of the total iron fraction. Initially the electrode had an iron hydroxide content of 24% where a fully charged electrode could have been expected considering the preconditioning that consisted of a full charge plus an extra floating charge for 24 h. At the end of the charging process decreasing detector counts were measured indicating gas increasingly accumulates inside the electrode, replacing part of the strongly incoherently scattering electrolyte. It seems obviously that gas accumulation inside the electrode acts as a resistor by replacing electrolyte and thereby reducing the ionic conduction. Therefore the inserted current shifts from phase conversion inside the electrode to gas production at the surface of the electrode. To address this issue we tried to improve the ionic conduction within the electrode during gas production by the addition of dopants.

With our strategy, applying zirconia and alumina as dopants, we could produce 2 mm thick iron electrodes with sizable areal and volumetric storage capacities compared to our undoped material. Furthermore we propose the utilization of iron electrodes in a low-cost application for hydrogen storage and production,

Electrode construction type	Iron source	Thickness d/d_s [mm]	sides [#]	Discharge conditions ins. capacity [mAh/cm^2]	TCD/ECD [mA/cm^2]	1^{st} plateau capacity areal T/ES [mAh/cm^2]	volumetric [Ah/cm^3]	Ref.
Pocket	Commercial electrode (Changhong)	3.2	1	480	10	186	0.58	this work
			1	300	10	167	0.52	
			1	300	25	119	0.37	
Plastic bond (organic)	Commercial electrode (Siemens)	10/5	2	-	80/40	∼426/213	∼0.43	[24]
Sintered	Commercial electrode (SNDC)	0.8/0.4	2	-	13.34/6.67	68/34	0.85	[26]
	(SNDC)	2.1/1.05	2	-	50/25	200/100	0.95	[19, 20]
	(SNDC)	3.2/1.6	2	-	50/25	162/81	0.51	[19]
	(SNDC)	3.2/1.6	2	-	43.2/21.6	215.6/107.8	0.67	[20]
Sintered	Commercial electrode (WEC) project goal	2.5/1.25	2	-	50/25	170/85	0.68	[16], 44 °C
		-	1	-	25	100	-	[25]
Plastic bond (PFTE)	Carbonyl iron	-	2	36	14.4/7.2	57.6/28.8	-	[32]
Plastic bond (PFTE)	Carbon-grafted iron	-	2	28.8	11.6/5.8	46/23	-	[33]
Plastic bond (PFTE)	Fe/C composite	1.5/0.75	2	-	5/2.5	60/30	0.4	[34]
Plastic bond (PE)	Carbonyl iron	0.6/0.3	2	14.7	8.8/4.4	26.4/13.2	0.44	[35]
Sintered	Fe with Zr-doping	2.07	1*)	206	10	161	0.78	this work
				206	25	149	0.72	
				206	20	158	0.76	40 °C
Sintered	Fe with Al-doping	2.05	1*)	210	10	138	0.68	this work
				210	25	128	0.62	
				210	20	147	0.72	40 °C

*) We enclosed the side face and the backside of the electrodes to allow electrolyte exchange only via the front side, detailed cell description and note to table 5.1 see appendix E.

Table 5.1: 1^{st} plateau volumetric storage densities of iron electrodes with belonging test-conditions; d/d_s: total/surface related electrode thickness; TCD/ECD: total electrode/surface related exchange current density; T/ES: total/exchange surface related capacity. Note: With a given electrode thickness two-sided testing provides the best electrolyte accessibility into an electrode volume and therefore the highest volumetric storage density. If such an electrode would be tested with the same exchange current density from one side only, one can assume an increase of the areal exchange-surface related storage capacity (more volume accessible from this side) while the volumetric storage capacity can, depending on the internal ionic and electronic conductivities, decrease. In the case of high porosities ionic conductivities will be high, while iron provides high electronic conductivity. The actual porosity varies and depends on initial porosity, state of charge and rechargeability.

the HSP-cell. The utilization of the iron capacity allows to convert renewable electricity into a sustained green hydrogen output.

5.2. Production process for doped sintered iron electrodes

Figure 5.2 illustrates the process we have developed for the production of sintered iron electrodes. It shows the classical route for the production of iron active material for pocket electrodes as described by Falk and Salkind [37] together with proposed modifications:

1. Synthesis starts with the vacuum drying of iron (II) sulfate heptahydrate to monohydrate at 100 °C.

2. Dried iron sulfate monohydrate is a loose, easily grindable powder. We grind the powder together with the dopants in a ball mill. The purpose of ball milling is rather mixing than milling.

3. Then the powder is oxidized to doped iron oxide at 800 °C.

4. Reduction takes place in a flow-through reactor at 550 °C with hydrogen as the reducing agent. The reactor is left to cool to room temperature in a reducing Ar/H_2 atmosphere.

5. After cooling, the reactor is moved into an argon filled glovebox.

6. The resulting powder is inserted into combustion boats for an additional stabilization step inside a tube furnace at 650 °C in a reducing Ar/H_2 atmosphere. The stabilization step reduces the shrinkage of the samples during sintering. The observed weight of the sample remains stable during the stabilization step confirming that the conversion process has been completed during the reduction step.

7. The powders are mixed with pore former (ammonium carbonate) and pressed into tube shapes and cylinders at a pressure of 300 kg/cm^2. Then these electrodes are sintered under an Ar/H_2 atmosphere at various temperatures: pure iron samples at 750 °C; Zr doped iron samples at 800 °C; and Al doped iron samples at 850 °C.

Reduced iron powders and iron electrodes remain inside the argon filled glovebox where possible, to limit oxidation. The active electrode material is only exposed to air during pressing and cell assembly. Exposure to air causes the formation of a passivation layer on the surface of the electrode. This passivation layer is removed electrochemically. Electrodes produced in this way work right

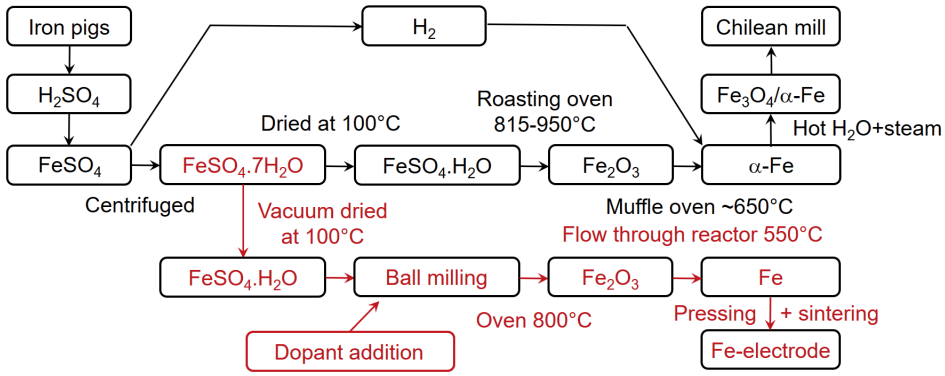

Figure 5.2: Proposed production process for iron electrodes (bottom, red) compared to the classical route for the production of iron active material for pocket electrodes as described by Falk and Salkind (top, black) [37].

away as they consist of porous iron. Initial charging of about 15 minutes is sufficient to remove the passivation layer from the surface. The electrode can then be discharged.

5.3. Dopants

Zirconium disulfate tetrahydrate and aluminium sulfate octadecahydrate in a concentration of three percent on a molar base were used as dopants. Note, we also studied bulk doping of these metals in a concentration of one percent and bulk doping with copper (II) sulfate pentahydrate and nickel (II) sulfate. We limit this paper to the samples with three percent Al and Zr doping as these two dopants outperform all other samples.

We use Al and Zr for structural improvement of the electrode. Zr- and Al- oxides are neither electrically conductive nor do they have catalytic activity for hydrogen evolution, these dopants have an impact on the electrode (re)chargeability when present. Zirconium oxide is a material which is stable in an alkaline environment and which is used as a wetting agent in Zirfon, the state of the art membrane for alkaline electrolysis [38]. As wetting agent it provides the ionic conductivity through the membrane. Alumina is a highly wettable oxide, but it can dissolve in alkaline electrolyte [39]. XRD measurements after cycling and charge indicate the absence of crystalline iron hydroxide in the doped material, see Figure 5.3. In the Zr- and Al-doped samples only reduced iron is observable in diffraction in the charged state whereas pure iron samples always show iron and iron hydroxide. So in terms of the discharge product $Fe(OH)_2$ and/or the rechargeability of the $Fe(OH)_2$ the doping has had an

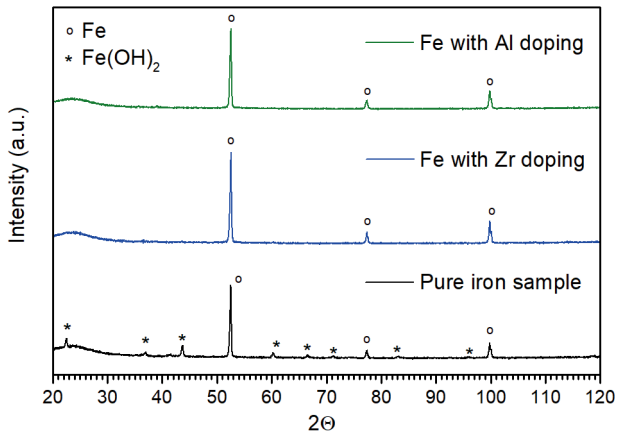

Figure 5.3: XRD measurements of pure and doped iron electrodes in the charged state. The electrodes were fully charged, followed by a floating charge for 12 h, in line with the preconditioning procedure for the neutron data [36] were initially 24% of the iron fraction were identified to be iron hydroxide.

influence. A number of factors may be responsible for the effect, including for instance ionic and/or electronic conduction parameters, structural/morphological features of the sample and overpotentials for charging and hydrogen evolution. These factors will be of interest to study in future research.

Figure 5.4 shows XRD data and EDX data of the doped materials gathered during the production process. The top insert of the XRD-data confirms that iron oxide has formed after oxidation which is later reduced to iron by hydrogen, bottom insert. The XRD-data further confirms the presence of zirconia oxide. Zirconia oxide is formed during the oxidation process and remains during the reduction process, only iron is reduced. The right side of Figure 5.4 shows EDS results of the fabricated doped iron electrodes which confirm the presence of iron, oxygen and the dopants zirconium and aluminum.

Figure 5.5 shows magnifications of the doped and pure iron electrodes, on top with aluminum, in the middle with zirconium and on the bottom pure iron. All pictures indicate a highly porous surface of the electrode and a small particle size. For comparison, carbonyl iron powder, SM grade, has a d50 value (50% of the particles are larger than that threshold) of 3.5 µm. All samples have a particle size below 3.5 µm, the pure iron sample and the iron sample with Al doping in the micron range, the iron sample with Zr doping in the sub-micron range (additional pictures and the mapping results see appendix E).

Iron electrodes require sufficient porosity to accommodate the molar volume expansion of 3.73 associated with the transition from iron to iron hydroxide [40],

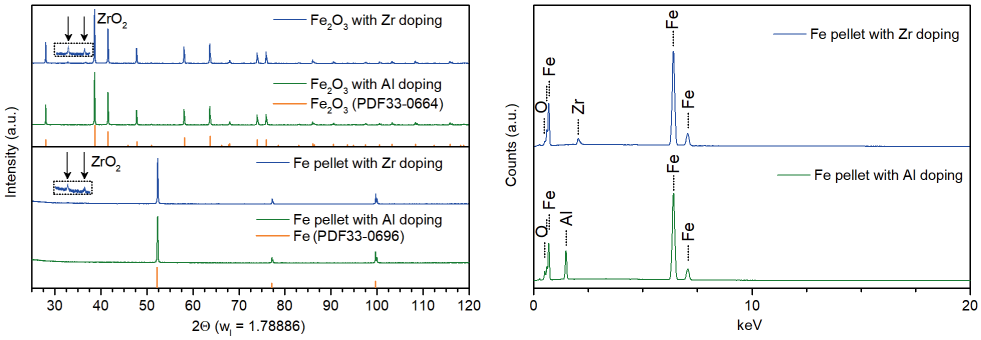

Figure 5.4: Material characterization. Left: XRD-data of sample material after oxidation (top) and after reduction (bottom). Right: EDS results of Fe electrodes with Zr- and Al-doping.

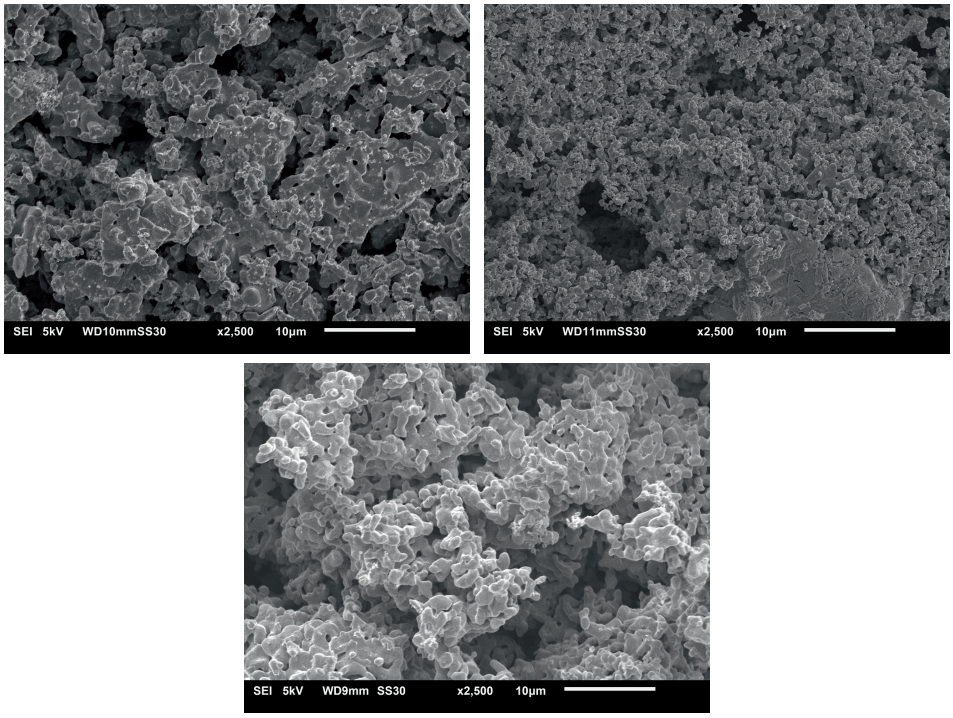

Figure 5.5: SEM images of the surfaces of doped and pure iron electrodes. (Left) electrode with Al-doping, (right) electrode with Zr-doping and (bottom) pure iron electrode with pore former.

and to provide pathways for the electrolyte to increase the material utilization [41]. Theoretically, all iron could be converted with a porosity of 73% or higher. Below this threshold utilization is limited due to volumetric restraints. The synthesis strategy resulted in a porosity of 58.1% for pure iron samples without pore former and in 66.8% for samples with pore former (ammonium carbonate, $(NH_4)_2CO_3$). Doped samples were produced with pore former, the resultant porosities of the doped samples were 65.7% for the Al and 65.9% for Zr. All produced electrodes are derived from the iron sulfate route, as described earlier.

The devised production process for doped sintered iron electrodes offers extra advantages:

1. Cheap iron source, compared to often used expensive carbonyl iron;
2. Doping and mixing can easily be done at an early stage with little energy;
3. The resulting iron oxide with doped alumina or zirconia oxide remain loose powders during oxidation while pure iron powders form larger agglomerates;
4. The iron powders with these dopants remain loose powders after reduction while pure iron powders tend to sinter together even at 550 °C;
5. The BET surface area of the doped iron materials is significantly higher than the BET surface area of the pure iron powder: 0.65 m^2/g for pure iron, 2.5 m^2/g for Zr-doped iron and 5 m^2/g for Al–doped iron, measured after the stabilization step.

Sulfide containing compounds improve the performance of the iron electrode and these additives are generally used [42]. However, we want to avoid sulfur additives as even traces of sulfur cause corrosion of air-electrodes [21]. Moreover, we intend to use the iron electrode not only for energy storage but also for hydrogen production. We want efficient electrolysis and sulfur increases the overpotential for hydrogen production [17]. That is why we prefer a sulfur free system for our cells and we use a 25wt% KOH solution without additives for our test cells.

5.4. Delayed hydrogen generation with an iron electrode

The position of the potential of an iron electrode in the Pourbaix diagram is close to the potential for hydrogen evolution. Because of that, hydrogen evolution occurs readily at the iron electrode, a feature we also used in the battolyser concept [4].

The iron electrode has two discharge plateaus, here we consider only the first iron discharge plateau, the two-electron transition from Fe^0 to Fe^{2+}, see reaction (5.1) (−0.88 V relative to standard hydrogen electrode, SHE). Reaction (5.2) (−0.83 V vs SHE) shows the hydrogen evolution reaction and reaction (5.3) (0.40 V vs SHE) the oxygen evolution reaction. 1st plateau operation offers more attractive potentials for storage applications then 2nd plateau operation.

$$Fe + 2OH^- \rightleftharpoons Fe(OH)_2 + 2e^- \tag{5.1}$$

$$2H_2O + 2e^- \rightarrow H_2 + 2OH^- \tag{5.2}$$

$$4OH^- \rightarrow O_2 + 2H_2O + 4e^- \tag{5.3}$$

In our previous work [10] we indicated that hydrogen production from iron electrodes could be expected to be spontaneous since the potential of the iron electrode is slightly more negative than the potential for hydrogen generation. Reaction (5.4) indicates the hydrogen production process which occurs either spontaneously during self-discharge at the iron electrode, or non-spontaneously driven by a current between two electrodes, the electrode for hydrogen evolution (reaction (5.2)) and the iron electrode (reaction (5.1)). In the latter case the hydrogen production rate can be controlled by the applied current settings.

$$Fe + 2H_2O \rightarrow Fe(OH)_2 + H_2 \tag{5.4}$$

Now we want to introduce the following concept, the hydrogen storage and production (HSP-)cell [43]. The HSP-cell makes use of a bifunctional electrode for time separated oxygen and hydrogen production at one electrode. This electrode produces oxygen upon current insertion while the iron electrode first charges and later facilitates hydrogen production, see reaction (5.5) and (5.6) respectively. Figure 5.6 illustrates a HSP-cell and indicates the reactions taking place during delayed hydrogen release and recharging.

$$2Fe(OH)_2 \rightarrow 2Fe + 2H_2O + O_2 \tag{5.5}$$

$$2H_2O \rightarrow 2H_2 + O_2 \tag{5.6}$$

Here the iron electrode acts as an electrochemical storage system in which the storage potential is naturally located close to the hydrogen evolution reaction. The electrochemical storage system can be charged with renewable electricity and discharged with H_2 evolution if necessary, overcoming the intermittency problem associated with renewable electricity generation. The storage system is mainly based on iron and water, both cheap and earth abundant, allowing upscaling to large installations.

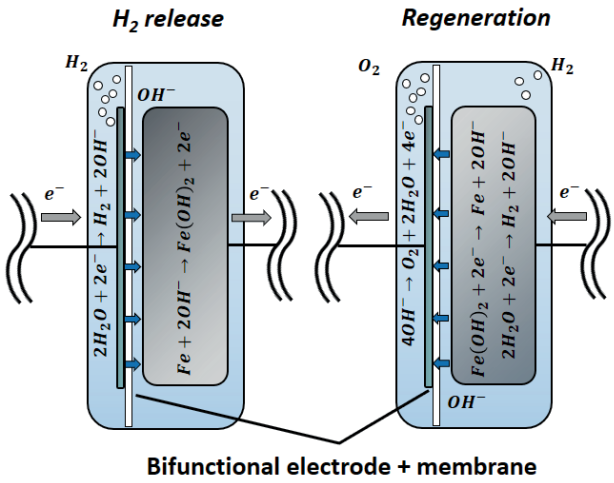

5

Figure 5.6: HSP-cell during hydrogen release and regeneration. We used an expanded Ni-mesh as bifunctional electrode.

Note that the HSP-cell can use the entire available capacity of the iron electrode like the iron-air battery and is not limited by the capacity of the nickel electrode. The iron-air battery provides electricity while the HSP-cell provides hydrogen, both products are important for the energy transition. Both systems can operate as an electrolyser with prolonged charging. Both systems will have a substantial increase in volumetric storage density compared to the integrated nickel-iron battery and electrolyser, also indicated as battolyser, where the nickel electrode occupies about twice the volume of the iron electrode while being the limiting electrode [44]. Compared to a setup with a nickel electrode, their removal allows to (1) double the areal storage capacity and to (2) use the obtained space for additional cells (increase of about 50%). The same volume will facilitate three times more storage capacity and 1.5 times more surface area. What is missing, however, is the capability to discharge as a battery; this becomes rather a hydrogen (delayed) production method.

All efficiencies we report for the HSP-cell are related to the higher heating value of hydrogen. We used the following equations to calculate characteristic numbers - the cycle efficiency, the charge efficiency, the storage efficiency, and the electrolysis efficiently:

$$\eta_{cycle} = \frac{E_{output}}{E_{input}} = \frac{H_{el} \cdot C_c}{\overline{V_c} \cdot C_c + \overline{V_{dc}} \cdot C_{dc}} = \frac{H_{el}}{\overline{V_c} + \overline{V_{dc}} \cdot \eta_{charge}} \tag{5.7}$$

$$\eta_{charge} = \frac{C_{dc}}{C_c} \tag{5.8}$$

$$\eta_{storage} = \frac{H_{el}}{\overline{V_{pc}} + \overline{V_{dc}}} \tag{5.9}$$

$$\eta_{electrolysis} = \frac{H_{el}}{\overline{V_{el}}} \tag{5.10}$$

The cycle efficiency is the ratio of the energy output to the energy input of one cycle, and the charge efficiency the ratio of the discharge capacity to the inserted capacity, a measure of how much hydrogen is produced directly/delayed during one cycle. Since the HSP-cell can be used to store hydrogen and to produce hydrogen we also calculate the storage efficiency and the electrolysis efficiency. Therefore the charging process is split up into two sections. The first part, up to a charge insertion equal to the discharge capacity, relates to phase conversion (V_{pc}) and the second part relates to electrolysis (V_{el}). The energy input for storage is the average charging potential for phase conversion ($\overline{V_{pc}}$) plus the average discharge potential ($\overline{V_{dc}}$), the energy required to release the stored hydrogen (equations see appendix E).

5.5. Results and discussion

We tested our electrodes at various charging and discharging rates to study their applicability for high performance operation. We were especially interested in:

1. The charge retention with increasing current insertion;
2. The capability to handle higher discharge rates;
3. The charging efficiency of the electrodes at higher charging rates,
4. The efficiency at elevated temperatures, and
5. The long-term stability of the electrodes.

Figure 5.7 shows the charge retention, the progress in measured discharge capacity versus inserted capacity, of our electrodes. The pure iron sample without pore former has the lowest areal storage capacity with 96 mAh/cm^2 (=0.59 Ah/cm^3), followed by the pure iron sample with pore former with 126 mAh/cm^2 (=0.62 Ah/cm^3). The increase in areal storage density goes together with an increase in material utilization, from 0.18 to 0.23 Ah/g, since all samples have approximately the same areal material loading. The results also demonstrate that the sample porosity has a major impact on the material utilization as reported earlier [16, 40, 41]. However, the results also indicate that porosity is not the only parameter necessary to consider. Both samples

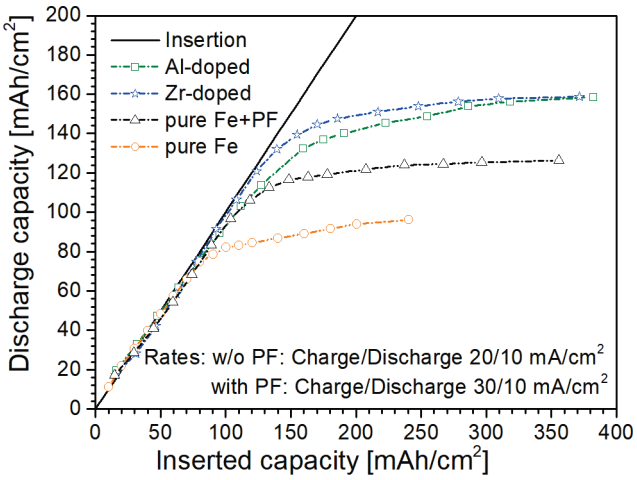

Figure 5.7: Progress in discharge capacity with increasing charge insertion. (Note, all samples have about the same amount of active material per cm^2.)

with dopants have a porosity comparable to the pure iron sample with pore former but show a 26% increased storage density. They possess a storage density of 159 mAh/cm^2 (=0.77 Ah/cm^3) and a material utilization of 0.29 Ah/g when fully charged.

The ratio of discharge capacity to charge capacity represents the efficiency towards the charging process, recognizable in the deviation of the depicted lines in Figure 5.7 from the line for insertion. Noteworthy is especially the high charging efficiency of the sample with Zr-doping of 95% for a current insertion of 139 mAh/cm^2 (=0.68 Ah/cm^3) and higher at lower current insertions. The pure iron samples also show a high charging efficiency while the sample with Al-doping deviates slightly, indicating parallel ongoing hydrogen production.

Figure 5.8 shows the capability of the electrodes to handle higher discharge rates. We charged the doped electrodes at a fixed rate of 30 mA/cm^2 to a capacity of 200 mAh/cm^2, the pure iron sample with pore former to a capacity of 160 mAh/cm^2, with subsequent discharges at discharge rates of 10, 15, 20 and 25 mA/cm^2. We repeated each discharge current density five times before increasing the discharge current density to the next set-point. Stable discharge capacities and voltage curves (see appendix E) for each set of five subsequent cycles indicate a stable performance for the doped samples, see Figure 5.8. As expected, the discharge capacities of the electrodes decrease slightly with increasing discharge rates from 0.68 Ah/cm^3 to 0.62 Ah/cm^3 for the Al-doped sample and from 0.78 Ah/cm^3 to 0.72 Ah/cm^3 for the Zr-doped sample, see

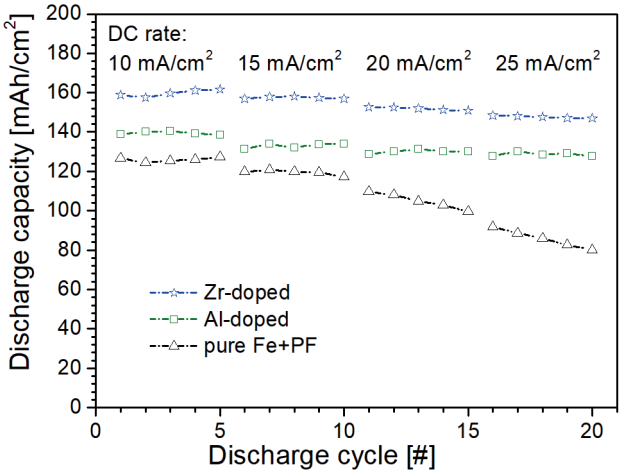

Figure 5.8: Discharge capacity for increasing discharge rate. Cycle 1-5: DC rate $10\,\mathrm{mA/cm^2}$; cycle 6-10: $15\,\mathrm{mA/cm^2}$; cycle 11-15: $20\,\mathrm{mA/cm^2}$ and cycle 16-20: $25\,\mathrm{mA/cm^2}$; charge rate: $30\,\mathrm{mA/cm^2}$.

table E.1. Both samples provide a stable discharge capacity when discharging at higher rates. In comparison, the pure iron sample with pore former provides only stable discharge capacities for discharge rates of 10 and $15\,\mathrm{mA/cm^2}$. At higher discharge rates the measured discharge capacity decreases with each cycle. We assume that the mechanisms [36], of accumulation of iron hydroxide at high discharge rates together with the limited ability to recharge, cause the decline in discharge capacity. Note, we restricted discharging to the first iron discharge plateau.

To evaluate the charging efficiency of the electrodes at higher charging rates ($10-60\,\mathrm{mA/cm^2}$) we inserted the same amount of charge of $160\,\mathrm{mAh/cm^2}$ with increasing charge rate into the electrodes with subsequent discharges at $10\,\mathrm{mA/cm^2}$. Figure 5.9 displays the observed discharge capacity and charging efficiency for various charging rates. Charging at a low rate provides the highest discharge capacity, $0.71\,\mathrm{Ah/cm^3}$ for the Zr-doped sample and $0.66\,\mathrm{Ah/cm^3}$ for the Al-doped sample. The observed discharge capacity decreases slightly with increasing the charge rate. The ratio of discharge capacities of the highest to the lowest charge rate is 0.935 for both samples which shows high charging efficiencies, also at higher charging rates.

For further electrochemical characterization we performed cycle-voltaic scans, see Figure 5.10. The left side shows the pure iron samples with and without pore former and the right side the Al- and the Zr- doped samples. Peak (I), iron oxidation, and peak (III), iron reduction, are the couple for the 1st plateau

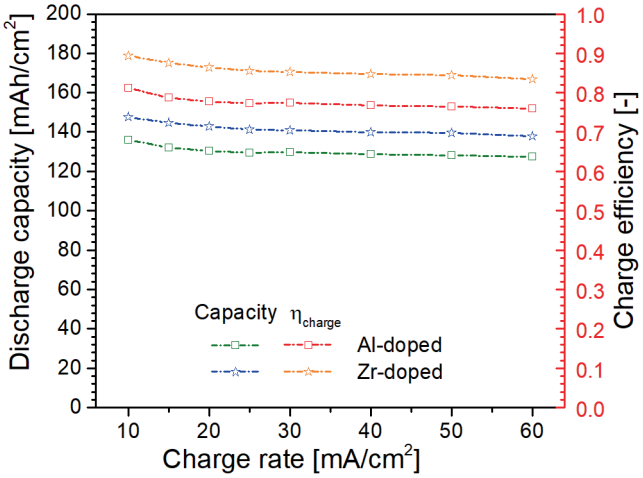

Figure 5.9: Observed discharge capacities and charging efficiencies for a discharge rate of 10 mA/cm^2 subsequent to a constant charge insertion (exact values: Al-sample 168 mAh/cm^2; Zr-sample 165 mAh/cm^2, see note appendix E) at various, increasing charging rates.

transition between iron and iron hydroxide, see reaction (5.1). Peak (II) shows the 2nd plateau transition from Fe (III), iron oxyhydroxide, to Fe (II) iron hydroxide, indicating that little Fe (III) has formed during the scans.

The cycling experiments already indicated that the samples with dopants have a higher storage capacity and a better high discharge-rate performance than the pure iron samples and the CV scan confirm this observation. The comparison between the pure iron samples shows the higher storage capacity of the sample with pore former, indicated by the increased area at peak (I) during the anodic sweep. Both samples show a similar shape and most prominent is the saturation or apparent passivation of the electrodes after peak (III) before H_2 evolution starts. Interestingly, both doped samples show similar shapes too, but different than the pure iron samples, with much less saturation / passivation. Here both scans merge smoothly with H_2 evolution and the Al-doped sample shows the highest activity for H_2 evolution. Both doped samples outperform the pure iron samples as they reach higher currents at the same applied potential, which makes them especially interesting for combined devices, including hydrogen production. The same is true for the discharge capacity, indicated by the larger currents and area of peak (I). In addition, the gradient of peak (I) of the doped samples is 10% steeper than the gradient of the pure iron samples, confirming an enhancement of discharge-capability. It should be noticed that the doped samples continue discharging at substantial rates during the cathodic sweep up to peak (II). No

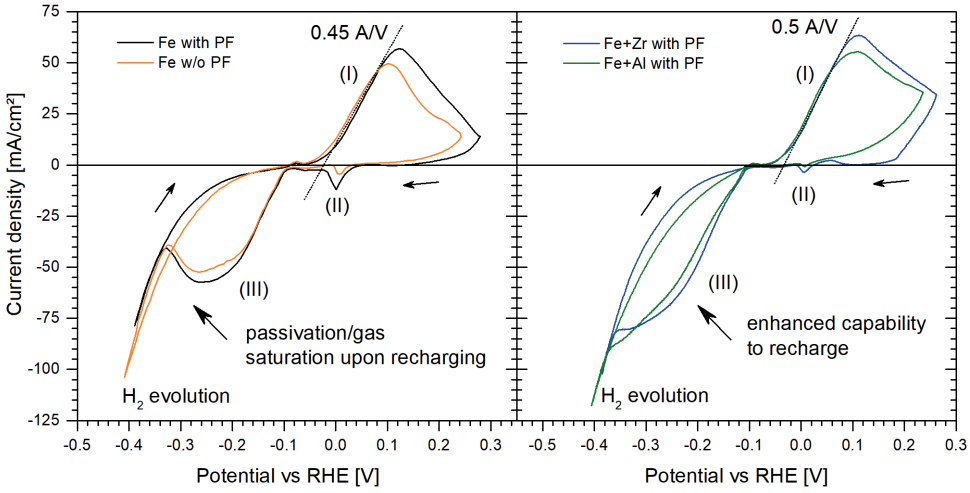

Figure 5.10: CV scans vs H_2 reference electrode, scan speed 0.025 mV/s. (left) Pure iron samples with and without pore former, (right) Al and Zr doped iron samples with pore former. Peak (I) iron oxidation and peak (III) iron reduction form together the 1st plateau transition from iron to iron hydroxide, see reaction (5.1), peak (II) 2nd plateau reaction, reduction of iron oxyhydroxide. (Appendix Figure E.9 shows both panels plotted on top of each other.)

peak (II) can be observed for the Al-doped sample and hardly any for the Zr-doped sample.

Figure 5.3 indicates that plenty of iron hydroxide is available in pure iron electrodes and it can be excluded that lack of iron hydroxide causes their passivation. It is not clear what induces the apparent improvement in electrochemical performance of the doped electrodes. We assume that the changes in morphology and/or in hydrophilicity suppress gas accumulation and facilitate gas release. As a consequence, more ionic pathways remain inside the electrode which prevents ionic isolation and the creation of inactive areas. Increased ability to recharge also explains the observed capacity increase. With dopants present the fraction of inactive iron hydroxide will likely be lower and more volume is available to accommodate the volumetric changes associated with the 1st plateau iron phase transition.

Energy storage and conversion systems need to be efficient to be attractive for future applications. Therefore we evaluated the characteristic numbers - the cycle efficiency, the H_2 storage efficiency and the electrolysis efficiency - for the system and the storage costs related to the iron electrode. Note, these iron electrode storage costs represent the voltage requirement for the iron phase

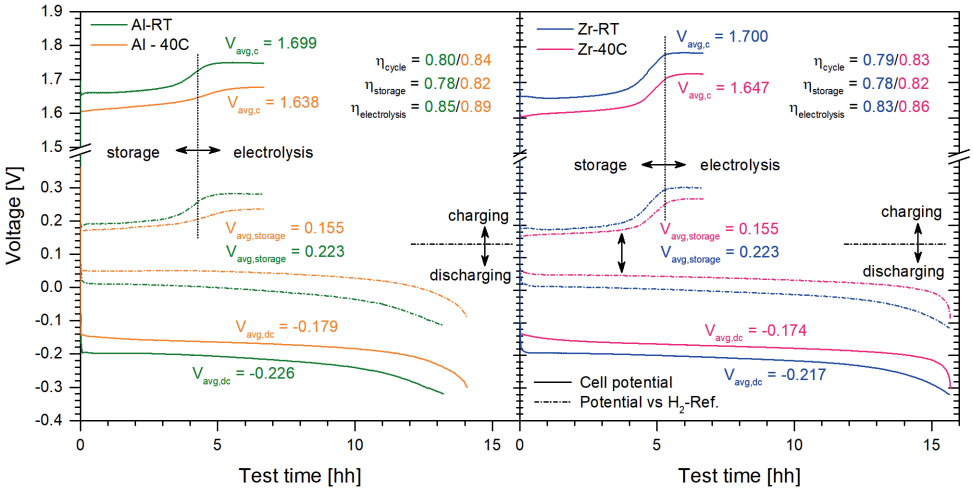

Figure 5.11: Cell potentials (solid lines) and potential of the iron electrode vs H_2 reference electrode (dash-dotted lines) for room temperature tests and tests at 40 °C. Charge insertion 200 mAh/cm^2, charge rate 30 mA/cm^2, discharge rate 10 mA/cm^2. Left: Al-doped sample, right: Zr-doped sample.

conversion at defined rates and may also be used to evaluate characteristics for nickel-iron or iron air systems. We evaluated the performance characteristics at room temperature and at 40 °C, the temperature at which iron-air systems in the 1980s were also operated.

Figure 5.11 contains cell potentials (solid lines) and iron electrode potentials vs H_2 reference electrode (dash-dotted lines), both at room temperature and at elevated temperature, left the Al-doped electrode and right the Zr-doped electrode. These are exemplary voltage curves for charging the cells at a current density of 30 mA/cm^2 to a storage capacity of 200 mAh/cm^2 with subsequent discharge at 10 mA/cm^2. Moreover, Figure 5.11 includes the average potentials under these conditions together with the characteristic numbers.

The number displayed in Figure 5.11 show that both samples have similar storage efficiencies, and confirms that the Al-doped sample produces hydrogen more efficiently. Also the cycle efficiency of the Al-doped sample is slightly above the cycle efficiency of the Zr-doped sample. This fact is partly caused by the higher discharge capacity of the Zr-doped sample, more delayed hydrogen generation requires more energy to release the hydrogen.

Test were conducted at various charge and discharge rates and Figure 5.11 shows one specific operation case. Figure 5.12 depicts the calculated efficiencies for charge rates from 10 to 60 mA/cm^2 and Figure 5.13 depicts the average cell

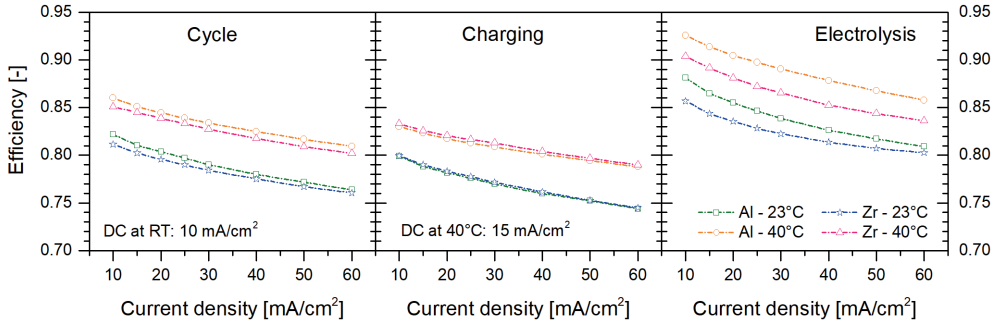

Figure 5.12: Efficiencies vs charge current density for Al- and Zr-doped samples evaluated at room temperature (discharge current density 10 mA/cm^2) and at 40 °C (discharge current density 15 mA/cm^2). Left: cycle efficiency; middle: charging efficiency; right: electrolysis efficiency.

potentials for discharge rates from 10 to 25 mA/cm^2.

The left part of Figure 5.12 shows the cycle efficiencies of the Al- doped and the Zr- doped samples. The Al-doped samples performs about 1% point better than the Zr-doped sample when operated at the same temperature. At room temperature the efficiencies are in a range between 82% at low rates and 76% at high rates, at 40 °C between 86% and 80%. The efficiency gain associated with temperature increase is about 4%.

The middle part of Figure 5.12 depicts the charging efficiencies of the Al-doped and the Zr- doped samples. The charging efficiencies are almost identical for both samples when operated at the same temperature. The efficiencies range from 80% to 74% at room temperature and from 83% to 79% at 40 °C. The temperature related efficiency increase is remarkable, considering that the discharge current increased too, from 10 mA/cm^2 at RT to 15 mA/cm^2 at 40 °C. Note, the Zr-doped sample provides about 15% more storage capacity than the Al-doped sample.

The right part of Figure 5.12 shows the electrolysis efficiency of the Al- doped and the Zr- doped samples. The Al-doped sample has an efficiency between 88% and 81% at RT and between 93% and 86% at 40 °C and performs about 2% better than the Zr-doped sample. Increasing the temperature increase the electrolysis efficiency by 5%.

Figure 5.13 depicts the calculated average cell voltages for releasing the hydrogen at the reversible electrode and while forming $Fe(OH)_2$ during discharging the cells at various discharge rates. The cell voltage times the current is equivalent to the backup-power requirement for delayed hydrogen release. At low discharge current densities both samples have a comparable average discharge

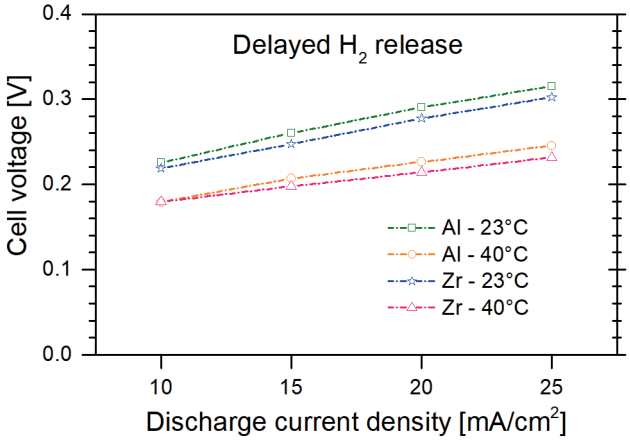

Figure 5.13: Average cell voltage for delayed hydrogen generation evaluated at various discharge rates at room temperature and at 40 °C.

voltage. With increasing discharge rate, the Zr-doped sample performs slightly better. The average potentials range between 0.17 V and 0.25 V at 40 °C and between 0.22 V and 0.32 V at room temperature.

Towards the end of the testing, a continuous cycling experiment (about 100 cycles) consisting of a 5h charge at 40 mA/cm^2 combined with a discharge at 20 mA/cm^2, all at 40 °C was programmed. Stable discharge capacities can be be observed for these challenging conditions, 147 mAh/cm^2 for the Al-doped sample (cycle 445-552) and 158 mAh/cm^2 for the Zr-doped sample (cycle 443-543).

In total, 567 cycles for iron electrode with Zr-doping and 577 cycles for the iron electrode with Al-doping were conducted, see Figure 5.14. These cycles include varying rates for charging and discharging and cell operation at RT and at 40 °C. Throughout the 63 test weeks (including 6 weeks of shut down) we observed solid results which make these electrode compositions promising for future applications.

5.6. System integration for sustained hydrogen generation

In our previous work [10] we suggest a configuration consisting of four electrodes within one electrochemical cell for electricity, hydrogen and oxygen storage and generation. We proved that this configuration provides, among other functionalities, a continuous hydrogen output from intermittent energy input by distributing the currents between the individual electrodes with their designated functions. With the proposed HSP-cell we can provide the same functionality but then within a simplified cell. This cell consists of only two electrodes which

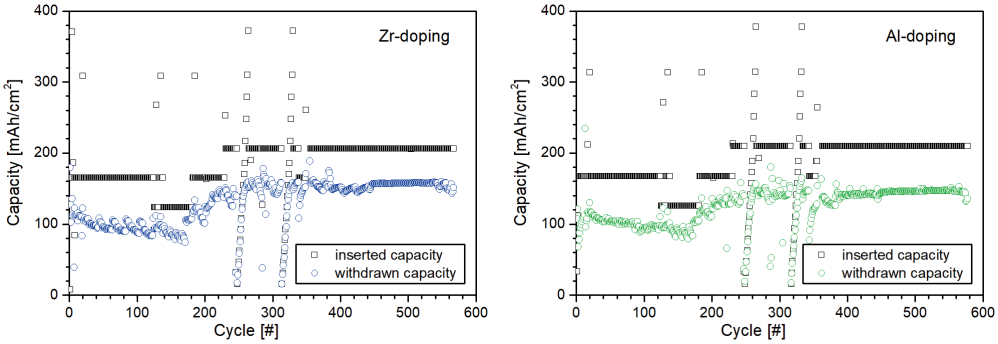

Figure 5.14: Cycle history of the doped iron electrodes, capacity [mAh/cm^2] vs cycle number for varying test conditions (charging rates $10-60\,\mathrm{mA/cm^2}$; discharging rates $10-25\,\mathrm{mA/cm^2}$; and test temperature: RT and 40 °C. Left: Iron pellet with Zr-doping. Right: Iron pellet with Al-doping.

makes for easy upscaling to larger multi-cell bi-polar units. For sustained hydrogen generation we now distribute the current not between electrodes within a electrochemical cell but between these larger units having always units available which absorb energy and/or which provide hydrogen. We envision that, for instance, a configuration of three multi-cell units can balance day-night energy fluctuation as illustrated in Figure 5.15. It is important to realize that the operation pattern of these units is now phase-shifted. During night-time two of these units serve hydrogen generation at the bifunctional electrode when discharging the iron electrode while the third one remains standby. The discharge is driven by a small overpotential, i.e. requires a reduced amount of stored electrical energy. With renewable electricity coming available with the next sunrise the stand-by unit can take over the hydrogen production at the iron electrode while the other two units will recharge. Phase-shifting of these sequences ensures routinely overcharging of all units which prolongs the lifetime of the iron electrodes.

The distribution of the currents among the units controls how much of the available energy goes to hydrogen production and to hydrogen storage. With this system hydrogen production is effectively shiftable from daytime to night-time reducing the daytime-production peaks and providing easily accessible hydrogen for sustained night-time production.

Iron-water hydrogen storage can be characterized as hydrogen storage via electrochemical reactions and may offer the following potential advantages [10]:

- Relatively easy and instantaneous control with electrochemical charging–discharging

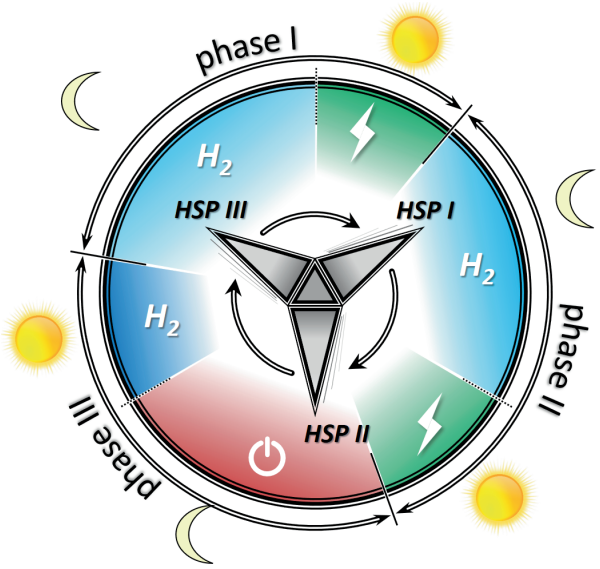

Figure 5.15: Illustration of time-shifted operation of three bipolar multi-cell HSP-units (I, II, and III).

- Reducing the safety risks associated with the storage of compressed hydrogen gas

- Output hydrogen pressure equivalent to cell pressure, adjustable to match consumer needs (up to 30 bar, operation pressure of commercial alkaline electrolyzers [38])

These iron storage electrodes possesses a volumetric storage density of 0.78 Ah/cm^3, equivalent to 29 $kg\,H_2/m^3$ or to a compressed hydrogen storage density of 500 bar [45], not considering the space for the bifunctional electrode, electrolyte and gas transport space. When taking that into account the practical density may go to ~200 or 300 bar effectively. We expect an oxygen-free hydrogen gas output during delayed hydrogen release even at low current densities since no oxygen may be present then.

We anticipate that our HSP-cell will be used for the production of synthetic fuels such as ammonia or hydrocarbons since we can provide a sustained hydrogen output from an intermittent input. Especially useful is the concept at locations with high renewable energy potential. H_2 buffer storage for a continuous production from intermittent sources is expensive [46], here an alternative option is provided to stabilise hydrogen production based on iron and water. We expect a combination with hydro-power as valuable. Such sites could ac-

commodate substantial additional renewable installations to charge HSP-units. At times without renewables, hydro-power could then act as a booster to release hydrogen, about 10 times more compared to direct electricity usage in combination with an electrolyzer. A combination with a battery, gas-turbine or a fuel-cell system is another possibility. The related conversion efficiency from hydrogen to electricity $\eta_{conversion}$ only affects the energy requirement to release hydrogen, characterized by the average discharge voltage $\overline{V_{dc}}$, not the energy requirement for charging, see equations 5.11 and 5.12. Hence, the cycle efficiency and the storage efficiency will remain attractive.

$$\eta_{cycle} = \frac{H_{el}}{\overline{V_c} + \frac{\overline{V_{dc}} \cdot \eta_{charge}}{\eta_{conversion}}} \tag{5.11}$$

$$\eta_{storage} = \frac{H_{el}}{\overline{V_{pc}} + \frac{\overline{V_{dc}}}{\eta_{conversion}}} \tag{5.12}$$

It is also noteworthy, that the average voltage for charging is lower than the average voltage for electrolysis and that energy is saved when no compression for storage is required and the end user does not need compressed hydrogen. Consequently, with the same amount of energy and on an A h basis, the iron-water storage cell should be designed about 25% larger than a compressed storage tank because of the ratio of electrolysis potential times compression costs (about 10% of HHV) to charging potential. Hence, it seems reasonable to consider the utilization of parts of the stored hydrogen in fuel-cells or gas-turbines to create self-sustaining systems. A combination with a nickel-iron battery-electrolyser would be able to provide the electricity required for sustained hydrogen production as well.

The work presented may serve as a starting point for HSP–cells. The focus was on the iron electrode and we only used an expanded nickel mesh as bifunctional electrode. Promising bifunctional electrodes are already under investigation for high pH environment, see for instance Fang Yu et al. [47], and it is likely that the efficiencies will increase in optimized systems.

5.7. Conclusion

In this paper we presented a novel approach for the synthesis of doped iron electrodes. Synthesis starts with cost-effective iron sulfate, the same iron source which is used for cheap iron pocket electrodes. Our synthesis strategy with the early addition of the dopants yields fine reduced iron powders with a high surface area which can be used to produce sintered iron electrodes.

We use aluminum sulfate and zirconium sulfate as dopants, both materials are oxides after synthesis. Our electrodes with dopants, 2 mm thick and accessible only from one side, show a high volumetric storage densities of up to 0.78 Ah/cm^3, equivalent in theory to 500 bar compressed hydrogen in the electrode volume, and allow for stable operation at higher discharge rates. Our study reveals, that these dopants increase (1) the ability to recharge and (2) the ability to discharge at higher rates when compared to similar synthesized electrodes without the dopants.

Comparing both dopants it can be concluded that Zr-doping results in a higher charging efficiency and a higher storage density and that Al-doping results in more efficient hydrogen production. Dependent on the intended use, Zr-doping can be recommended for applications where the focus is on storage while Al-doping can be recommended for application where the focus is on electrolysis.

We also introduced the HSP-cell or half cell as a means of utilization for the iron electrodes. The HSP-configuration utilizes the entire capacity of the iron electrode for hydrogen storage and delayed production with a cycle efficiency over 80%, when operational at 40 °C and at a charging rate of 60 mA/cm^2 combined with a discharge rate of 15 mA/cm^2. The good high rate performance together with the high volumetric storage density makes this concept, based on earth abundant water and iron, promising for large- and small-scale hydrogen based storage solutions.

References

[1] V. Masson-Delmotte, P. Zhai, A. Pirani, S. L. Connors, C. Péan, S. Berger, N. Caud, Y. Chen, L. Goldfarb, M. I. Gomis, , M. Huang, K. Leitzell, E. Lonnoy, J. B. R. Matthews, T. K. Maycock, T. Waterfield, O. Yelekçi, R. Yu, and B. Zhou (eds.), *Climate change 2021: The physical science basis. contribution of working group I to the sixth assessment report of the intergovernmental panel on climate change,* IPCC, Cambridge University Press, In Press (2021).

[2] IEA (2021), *Global Energy Review 2021,* https://www.iea.org/reports/global-energy-review-2021.

[3] M. Chen, Q. Liu, S.-W. Wang, E. Wang, X. Guo, and S.-L. Chou, *High-abundance and low-cost metal-based cathode materials for sodium-ion batteries: Problems, progress, and key technologies,* Advanced Energy Materials **9**, 1803609 (2019).

[4] F. M. Mulder, B. M. H. Weninger, J. Middelkoop, F. G. B. Ooms, and H. Schreuders, *Efficient electricity storage with a battolyser, an integrated*

Ni–Fe battery and electrolyser, Energy & Environmental Science **10**, 756 (2017).

[5] J. Huang and Y. Wang, *Efficient renewable-to-hydrogen conversion via decoupled electrochemical water splitting,* Cell Reports Physical Science **1**, 100138 (2020).

[6] M. F. Lagadec and A. Grimaud, *Water electrolysers with closed and open electrochemical systems,* Nature Materials **19**, 1140 (2020).

[7] Z. P. Ifkovits, J. M. Evans, M. C. Meier, K. M. Papadantonakis, and N. S. Lewis, *Decoupled electrochemical water-splitting systems: a review and perspective,* Energy & Environmental Science **14**, 4740 (2021).

[8] F. Zhang and Q. Wang, *Redox-mediated water splitting for decoupled h2 production,* ACS Materials Letters **3**, 641 (2021).

[9] Z. Jin, P. Li, and D. Xiao, *A hydrogen-evolving hybrid-electrolyte battery with electrochemical/photoelectrochemical charging from water oxidation,* ChemSusChem **10**, 483 (2017).

[10] B. M. H. Weninger and F. M. Mulder, *Renewable hydrogen and electricity dispatch with multiple Ni–Fe electrode storage,* ACS Energy Letters **4**, 567 (2019).

[11] G. Gahleitner, *Hydrogen from renewable electricity: An international review of power-to-gas pilot plants for stationary applications,* International Journal of Hydrogen Energy **38**, 2039 (2013).

[12] A. K. Manohar, C. Yang, S. Malkhandi, G. K. S. Prakash, and S. R. Narayanan, *Enhancing the performance of the rechargeable iron electrode in alkaline batteries with bismuth oxide and iron sulfide additives,* Journal of The Electrochemical Society **160**, A2078 (2013).

[13] R. Kinzelbach, *Stahlakkumulatoren* (VARTA Battery AG, 1974).

[14] J. D. Birge, J. T. Brown, W. Feduska, C. C. Hardman, W. Pollack, R. Rosey, and J. Seidel, *Performance characteristics of a new iron-nickel cell and battery for electric vehicles,* Power Sources **6**, 111 (1976).

[15] E. S. Buzzelli and G. R. Folser, *Method of producing self-supporting fully activated iron electrodes by thermal reduction-sintering,* (1979), US Patent 4,132,547.

[16] W. Bryant, *The structure and performance of sintered iron electrodes,* Electrochimica Acta **24**, 1057 (1979).

[17] L. Öjefors, *Self-discharge of the alkaline iron electrode,* Electrochimica Acta **21**, 263 (1976).

[18] B. Andersson and L. Öjefors, *Slow potentiodynamic studies of porous alkaline iron electrodes,* Journal of The Electrochemical Society **123**, 824 (1976).

[19] L. Öjefors and L. Carlsson, *An iron—air vehicle battery,* Journal of Power Sources **2**, 287 (1978).

[20] B. Andersson and L. Öjefors, *Optimization of iron-air and nickel oxide-iron traction batteries,* Power Sources **7**, 329 (1979).

[21] L. Carlsson and L. Öjefors, *Bifunctional air electrode for metal-air batteries,* Journal of The Electrochemical Society **127**, 525 (1980).

[22] K. Micka and I. Roušar, *Theory of porous electrodes—XVIII. the iron electrode,* Electrochimica acta **29**, 1411 (1984).

[23] H. Cnobloch, D. Gröppel, W. Nippe, and F. von Sturm, *Eisen-Elektroden für Metall/Luft-Zellen,* Chemie Ingenieur Technik - CIT **45**, 203 (1973).

[24] H. Cnobloch, *Fuel cells and metal-air batteries as electrochemical energy storage systems,* in *Energy Storage* (Elsevier, 1980) pp. 172–184.

[25] A. Gibney and D. Zuckerbrod, *Fe-air secondary battery: Improvements in the air electrode,* Power Sources **9**, 143 (1983).

[26] J. Černý, J. Jindra, and K. Micka, *Comparative study of porous iron electrodes,* Journal of Power Sources **45**, 267 (1993).

[27] R. D. McKerracher, C. Ponce de Leon, R. G. A. Wills, A. A. Shah, and F. C. Walsh, *A review of the iron-air secondary battery for energy storage,* ChemPlusChem **80**, 323 (2014).

[28] Z. He, F. Xiong, S. Tan, X. Yao, C. Zhang, and Q. An, *Iron metal anode for aqueous rechargeable batteries,* Materials Today Advances **11**, 100156 (2021).

[29] W. K. Tan, G. Kawamura, H. Muto, and A. Matsuda, *Current progress in the development of Fe-air batteries and their prospects for next-generation batteries,* in *Sustainable Materials for Next Generation Energy Devices* (Elsevier, 2021) pp. 59–83.

[30] J. Yang, J. Chen, Z. Wang, Z. Wang, Q. Zhang, B. He, T. Zhang, W. Gong, M. Chen, M. Qi, P. Coquet, P. Shum, and L. Wei, *High-capacity iron-based anodes for aqueous secondary nickel-iron batteries: Recent progress and prospects,* ChemElectroChem **8**, 274 (2020).

[31] X. Wu, H. Zhang, K.-J. Huang, and Z. Chen, *Stabilizing metallic iron nanoparticles by conformal graphitic carbon coating for high-rate anode in Ni–Fe batteries,* Nano Letters **20**, 1700 (2020).

[32] A. Sundar Rajan, M. K. Ravikumar, K. R. Priolkar, S. Sampath, and A. K. Shukla, *Carbonyl-iron electrodes for rechargeable-iron batteries,* Electrochemical Energy Technology **1** (2015), 10.2478/eetech-2014-0002.

[33] A. Sundar Rajan, S. Sampath, and A. K. Shukla, *An in situ carbon-grafted alkaline iron electrode for iron-based accumulators,* Energy & Environmental Science **7**, 1110 (2014).

[34] H. A. Figueredo-Rodríguez, R. D. McKerracher, M. Insausti, A. Garcia Luis, C. Ponce de León, C. Alegre, V. Baglio, A. S. Aricò, and F. C. Walsh, *A rechargeable, aqueous iron air battery with nanostructured electrodes capable of high energy density operation,* Journal of The Electrochemical Society **164**, A1148 (2017).

[35] H. Weinrich, M. Gehring, H. Tempel, H. Kungl, and R.-A. Eichel, *Electrode thickness-dependent formation of porous iron electrodes for secondary alkaline iron-air batteries,* Electrochimica Acta **314**, 61 (2019).

[36] B. M. H. Weninger, M. A. Thijs, J. A. C. Nijman, L. van Eijck, and F. M. Mulder, *Neutron diffraction study of a sintered iron electrode in operando,* The Journal of Physical Chemistry C **125**, 16391 (2021).

[37] S. U. Falk and A. J. Salkind, *Alkaline storage batteries,* (1969).

[38] N. Guillet and P. Millet, *Alkaline water electrolysis,* in *Hydrogen Production* (Wiley-VCH Verlag GmbH & Co. KGaA, 2015) pp. 117–166.

[39] G. Carchini, M. García-Melchor, Z. Łodziana, and N. López, *Understanding and tuning the intrinsic hydrophobicity of rare-earth oxides: A DFT+U study,* ACS Applied Materials & Interfaces **8**, 152 (2015).

[40] C. S. Tong, S. D. Wang, Y. Y. Wang, and C. C. Wan, *A study of the iron electrode structure of Ni-Fe cell,* Journal of the Electrochemical Society **129**, 1173 (1982).

[41] C. Yang, A. K. Manohar, and S. R. Narayanan, *A high-performance sintered iron electrode for rechargeable alkaline batteries to enable large-scale energy storage,* Journal of The Electrochemical Society **164**, A418 (2017).

[42] H. A. Figueredo Rodríguez, R. D. McKerracher, C. Ponce de León, and F. C. Walsh, *Improvement of negative electrodes for iron-air batteries: Comparison of different iron compounds as active materials,* Journal of The Electrochemical Society **166**, A107 (2019).

[43] B. Weninger and F. M. Mulder, *Electrolytic cell for H2 generation,* (2018), Dutch Patent App. 2022332.

[44] A. M. Raventos, G. Kluivers, J. W. Haverkort, W. de Jong, F. M. Mulder, and R. Kortlever, *Modeling the performance of an integrated battery and electrolyzer system,* Industrial & Engineering Chemistry Research **60**, 10988 (2021).

[45] A. Züttel, *Materials for hydrogen storage,* Materials Today **6**, 24 (2003).

[46] J. Armijo and C. Philibert, *Flexible production of green hydrogen and ammonia from variable solar and wind energy: Case study of chile and argentina,* International Journal of Hydrogen Energy **45**, 1541 (2020).

[47] F. Yu, H. Zhou, Y. Huang, J. Sun, F. Qin, J. Bao, W. A. Goddard III, S. Chen, and Z. Ren, *High-performance bifunctional porous non-noble metal phosphide catalyst for overall water splitting,* Nature Communications **9** (2018), 10.1038/s41467-018-04746-z.

6

Conclusion and outlook

We have to create an energy system based on renewables and low greenhouse gas emissions to prevent a severe change of the climate of our planet. This means, we have to overcome and learn to work with the intermittent nature of renewables. Tremendous amounts of storage – electricity, hydrogen, synthetic fuels, all of it – will be required. Likely, synthetic fuels will be produced at sites with a high renewable potential and these synthetic fuels will be used and stored as well as shipped in tankers like oil tankers around the globe to the energy consumers. Consumers will be, for instance, Northern Europe and Japan which do not have enough renewable potential to create a fully self-sustaining energy system.

The energy transition is complex and every region has its own challenges. With the battolyser (Chapter 2) we provided a new concept that can store electricity as a battery and that converts excess electricity into hydrogen. With the expansion of renewable electricity generation curtailment will increase if insufficient direct use, storage and conversion are available. The battolyser can solve this problem, because it can store electricity and can use excess electricity to generate hydrogen. Therefore, the installations of battolysers can foster further implementation of renewables. It is important to realise that the battolyser is not a stand-alone technology. For electricity it is evident that an electricity infrastructure is out there. For hydrogen a similar infrastructure is required. The battolyser will supply hydrogen when overcharged, in an intermittent pattern. Therefore, downstream infrastructure needs the capability to handle an intermittent hydrogen input and/or requires a hydrogen storage infrastructure. At locations with a hydrogen infrastructure or the direct need of hydrogen, the battolyser has the potential to become an essential tool for the energy transition since renewable electricity can be stored and excess electricity can be converted efficiently into hydrogen in a combined device.

Green hydrogen can replace fossil fuels in industrial processes and green hydrogen is the key building block for synthetic fuel production. It does not matter if it concerns nitrogen-based ammonia or carbon-based methane or methanol synthesis. It is the production of hydrogen that costs energy while the synthesis of a nitrogen- or carbon-based fuel itself is exothermic (releases energy). In the case of ammonia, the hydrogen bound to nitrogen carries the energy, in the case of methane and methanol, carbon and hydrogen carry the energy. However, these carbon-based fuels need extra hydrogen for the conversion of CO_2, one H_2 molecule per oxygen atom that needs to be removed. Currently, all these processes are designed to run continuously at a large scale. Thus, green hydrogen has to be supplied continuously to these synthesis units to provide the required uninterrupted energy input.

We demonstrated that we can supply a sustained hydrogen output from an intermittent energy input and that time shifting the hydrogen output comes at low energy costs (Chapter 3). We accomplished that by adding electrodes to the electrochemical cell, a combination of storage electrodes and electrodes for gas production. By doing so, we created electrochemical systems with more than two electrodes where all electrodes can be operational simultaneously and at independent rates. The proposed concept of what we called 'multi-controlled (MC-)electrodes' in electrochemical systems provides a systematic approach for controlling and scaling up multi-electrode configurations. We used it for electricity, oxygen and hydrogen storage, all in one cell, where the storage electrode can serve two purposes simultaneously. Most importantly we used it for decoupling the electricity input from the hydrogen output by combining an iron storage electrode with two gas evolution electrodes, one for hydrogen evolution and one for oxygen evolution. This implies that abundant renewable electricity can be used to charge the iron electrode, charging the iron electrode in combination with oxygen production costs most of the energy. Independently hydrogen can be generated from the iron electrodes, a process which costs little energy when we look at the position of the electrodes in the Pourbaix diagram. Having two independent circuits enables decoupling electricity input and hydrogen output and the iron electrode serves as electrochemical storage reservoir.

It is like in a large reservoir of water which is filled with rain or meltwater from snow and ice. This reservoir can be used for electricity generation as long as there is water available. This reservoir is charged and discharged independently. We do the same, but electrochemically. The iron electrode is the reservoir, charging occurs together with oxygen production and discharging together with hydrogen production.

The concept of MC-electrodes allows for the scaling up of single electrochemical cells consisting of more than two electrodes to larger arrays of cells

where the operation status of an entire array can be controlled by a single controller, as demonstrated during the NWO teknowlogy day (see Appendix A). We demonstrated in our publication that most of the energy (95%), in the future preferably with abundant renewable electricity, will be fed through the main controller to the system and that only as little as 5% of the energy is required for time-shifting 50% of the hydrogen production (Chapter 3). Additionally, a hydrogen output from reduced iron electrodes can be supplied with substantially reduced backup power (-85% compared to conventional electrolysis) at times with little available renewable electricity.

But still, the system is complex, and complexity does not foster the energy transition. With the proposed concept of the hydrogen storage and production (HSP-)cell we reduced complexity through merging the separated electrodes for oxygen and hydrogen evolution into one bifunctional electrode, which provides both functionalities, dependent on the current flow. The iron-storage electrode can be charged and overcharged together with oxygen production at the bifunctional electrode and discharged together with hydrogen production at the same bifunctional electrode. This HSP-cell also has similarities to the iron-air battolyser but provides hydrogen as an output. This configuration can be used as a sink to store excess electricity. The energy is stored in reduced iron and the energy can be released as hydrogen at times when hydrogen is needed. This means that the cell can be used for hydrogen storage and for hydrogen production. The HSP-concept can also provide a sustained hydrogen output from intermittent sources. For this purpose, several units should be operational simultaneously, but then in a phase-shifted pattern.

Intermittency is one of the main challenges associated with the transition of fossil fuel based industrial processes or synthetic fuel production to renewables. The HSP-cell is a simple, cost-efficient concept based on earth-abundant iron that provides a potential solution to overcome intermittency. The HSP-concept can be located in regions with a high renewable potential, can be configured in a self-sustaining manner and can provide a sustained hydrogen output from intermittent sources. And, the overall efficiency including storage and production exceeds 80% when operated at 40 °C (Chapter 5). Therefore, the HSP-cell has the potential to become an additional option for handling intermittency and to boost the energy transition.

The iron electrode is at the core of all presented configurations. Therefore we studied a sintered iron electrode with neutron diffraction to investigate the phases inside the iron electrode during operation (Chapter 4). Neutron diffraction in combination with Rietveld refinement enabled us to probe the bulk of the sample without interference because neutrons penetrate deeply into materials. We concluded that crystalline metallic iron and iron hydroxide phases form

during the first discharge plateau and that iron oxyhydroxide forms the second plateau discharge product. We determined that crystalline iron disappears and forms as expected during an operation, while iron hydroxide reacts slowly via intermediate amorphous phases. As much as 40% of the participating iron can be in amorphous phases for first plateau operation and up to 55% while recharging from the second plateau. Moreover, and maybe most importantly the data revealed that substantial amounts of inactive iron hydroxide are always present inside the electrode. This unexpected finding indicated that the reduction from iron hydroxide to iron needs to be improved to increase material utilization of iron electrodes.

Usually sulphur is added to the electrode or the electrolyte to stabilize the discharge capacity and to improve the discharge performance of iron electrodes. But sulphur additives increase the overpotential for hydrogen production, which lowers the efficiency. Moreover, sulphur compounds can cause corrosion in the system. We aimed to create a sulphur free system to improve the electrolysis efficiency and to avoid corrosion issues. Alternatively we produced sintered iron electrodes with the dopant's zirconia oxide (Zr) and alumina oxide (Al) which showed promising performance without sulphur additives (Chapter 5).

The production process starts with the same base chemical as cheap iron pocket electrodes and the early addition of the dopants. As indicated in chapter 5 good storage capacities are obtained. The proposed process yields several advantages for processing such as (a) a good dopant distribution within the sample, (b) iron powders with a high BET-surface area and (c) iron oxides as well as reduced iron powders which remain loose powders during all synthesis stages without forming agglomerates. Currently the produced cells have a theoretical density of 33%, while the optimal theoretical density would be between 20-25% for sintered iron electrodes. Therefore, the reported values of these sintered iron electrodes with Zr and Al doping can be considered as a starting point for further improvement. Such electrodes with an optimized theoretical density have the potential to yield even higher storage densities.

Summing up, the creation of an energy system based on renewables confronts us with intermittency of these energy sources and raises new challenges as the undesirable curtailment of renewables. Storage solutions for electricity and hydrogen are highly needed. With a sustained hydrogen output synthetic fuels based on renewables could be produced on a large scale. With the nickel-iron battolyser and the iron-air battolyser we can store electricity and we can convert excess electricity into hydrogen to overcome such curtailment-problems. With the concept of MC-electrodes and the HSP-cell we can efficiently store and delay the hydrogen output, to provide a more sustained hydrogen output to industrial sites. The iron electrode is at the centrepiece of all configurations and

recharging was the main challenge. We addressed the issue of rechargeability with a new synthesis strategy for sintered iron electrodes doped with Zr and Al instead of sulphur. Electrodes produced with this strategy have the potential to become the new benchmark for sintered iron electrodes. With these concepts we offer new tools to support and accelerate electricity storage and conversion within the energy transition. We have to speed up with all what we do to limit the impact of climate change.

A

NWO Teknowlogy Day

A

Doing research includes making the research accessible to a broader public. I had the opportunity to present the battolyser [1] and an alkaline electrolyser with postponed hydrogen output [2] to a broader public during the NWO Teknowlogy day on November 7th, 2019.

Figure A.1 shows the battolyser and figures A.2 and A.3 show such a prototype and the demonstration of an alkaline electrolyser with the capability to delay the hydrogen output.

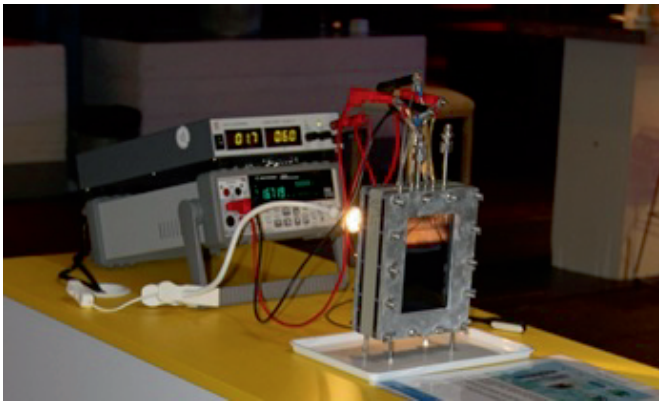

Figure A.1: Battolyser. At the time the photo is taken the battolyser electrolyses water at a low voltage

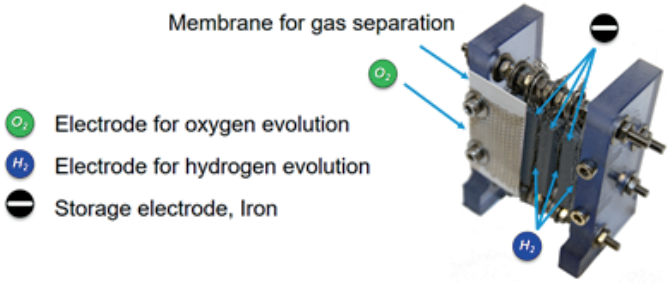

Figure A.2: Prototyp of an alkaline electrolyser with integrated hydrogen storage

The prototype of the electrolyser concept consists of an electrode for oxygen generation on one side of the membrane, and alternating electrodes for hydrogen production and storage at the other side of the membrane. The main idea is that the iron electrodes (negative terminal, black) can be charged together with oxygen production when electricity is abundant while the electrodes for hydrogen evolution provide a continuous hydrogen supply. The iron electrode is the main storage which buffers the fluctuations between electricity supply

and hydrogen output. This is possible because the potential of the iron storage electrode is naturally located close to potential for hydrogen evolution, see Figure 1.3 Simplified Pourbaix diagram. The decoupling of the electricity input from the hydrogen output is realized by two controllers which are operational simultaneously and which distribute the currents within the cell.

We also demonstrated the novel storage concept based on multi-controlled electrodes in operation, see figure A.3. Three cells in series were connected in an array, always connecting the iron storage electrode with the oxygen evolution electrode of the next cell. Little controllers with small batteries, one for each cell, connect the iron storage electrodes with the electrodes for hydrogen evolution. These controllers regulated the constant hydrogen output while the entire assembly was controlled by a delta unit which could be turned on and off at will, as unpredictable as renewables are. The little controllers with additional batteries are isolated systems. Such an approach provides a cost-efficient alternative compared to the test setup used for the publication [2]. There we used a Parstat Multi-channel potentiostat in floating operation to control the hydrogen evolution in each cell.

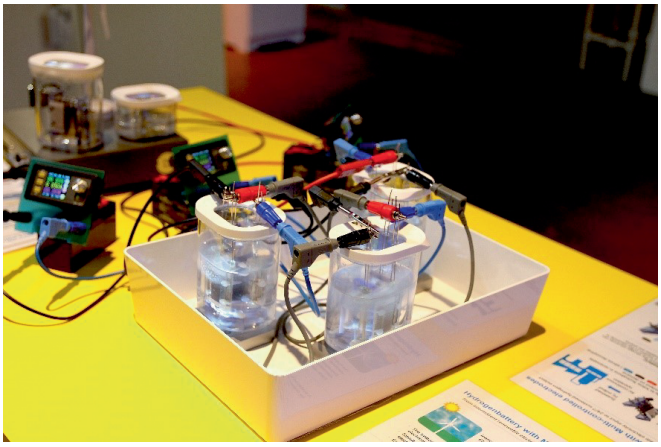

Figure A.3: Demonstration of an alkaline electrolyser with sustained hydrogen output. Three cells in a series connection.

Public support is important for the energy transition and the public is interested in the energy transition and in hydrogen developments. However, many people relate the use of hydrogen only to cars and transportation, and not to the potential green hydrogen has to reduce the enormous CO_2 footprint of the industry. We need hydrogen or synthetic fuels to replace fossil fuel usage for the industry. That was an eye-opener for many visitors to the NWO Teknowlogy day on November 7^{th}, 2019.

A

References

[1] F. M. Mulder, B. M. H. Weninger, J. Middelkoop, F. G. B. Ooms, and H. Schreuders, *Efficient electricity storage with a battolyser, an integrated Ni–Fe battery and electrolyser,* Energy & Environmental Science **10**, 756 (2017).

[2] B. M. H. Weninger and F. M. Mulder, *Renewable hydrogen and electricity dispatch with multiple Ni–Fe electrode storage,* ACS Energy Letters **4**, 567 (2019).

B

Efficient electricity storage with the battolyser, an integrated Ni-Fe battery and electrolyser

Electronic Supplementary Information to Chapter 2.

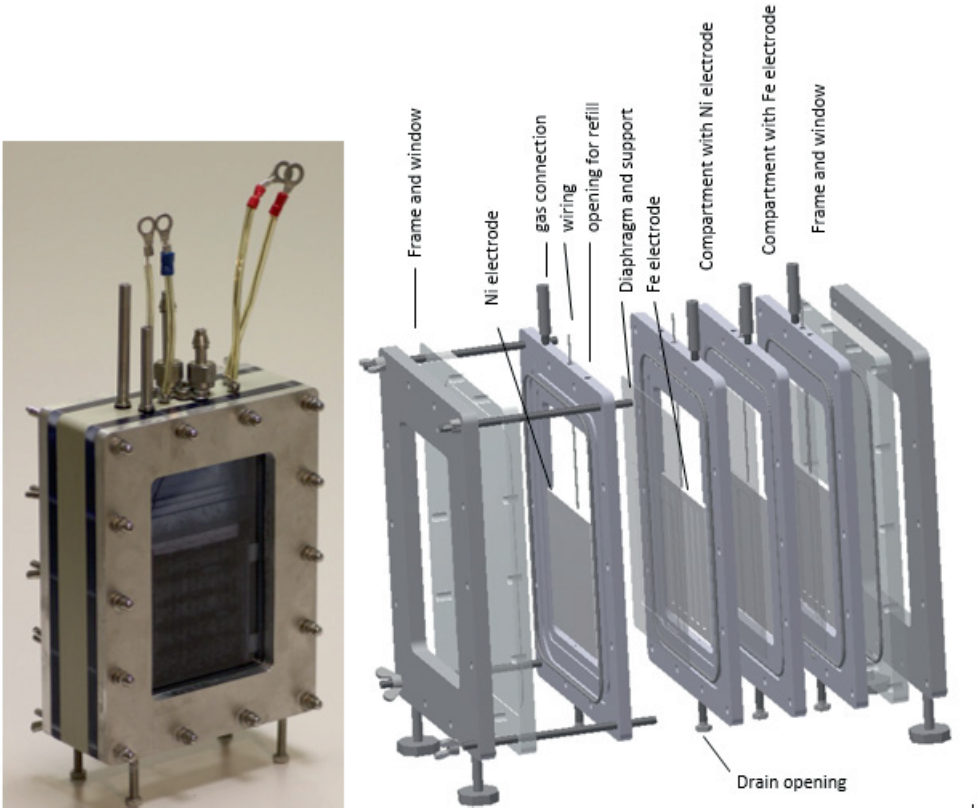

Figure B.1: Battolyser layout.

(Left) Picture of assembled battolyser with in this case two negative and two positive electrodes.

(Right) Exploded view indicating the positions of the four electrodes, four electrical wire connections, gas exhausts and electrolyte inlets, as well as three gas separation diaphragms.

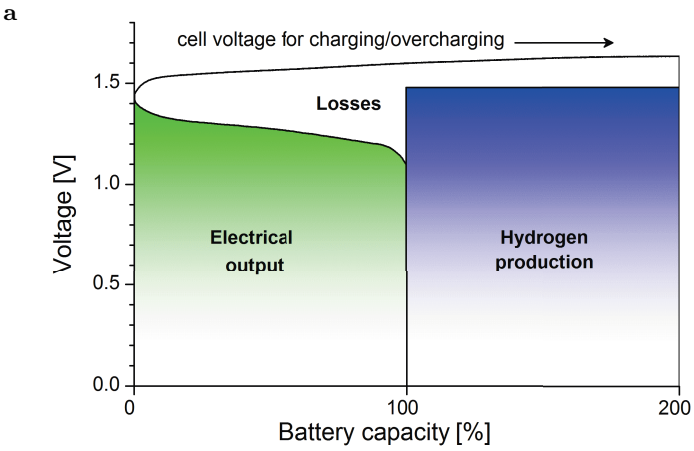

Figure B.2: Energy efficiency and charge utilisation.

(a) The total electrical energy input is given by integrating the experimental cell voltage during the charge and overcharge. The electrical energy output is given by the green area, while the hydrogen output is represented by the blue area corresponding with the thermal neutral potential times the inserted charge. The white area corresponds to the energy losses. The overall charge that is inserted comes back as either discharge of the battery or as hydrogen; as described the faradaic efficiency is 100% within the experimental accuracy of $\pm 0.5\%$. Total and partial energy efficiencies ($\eta_{battery}, \eta_{electrolyser}$) are given by dividing the relevant area's by the total inserted energy (green, blue plus white area).

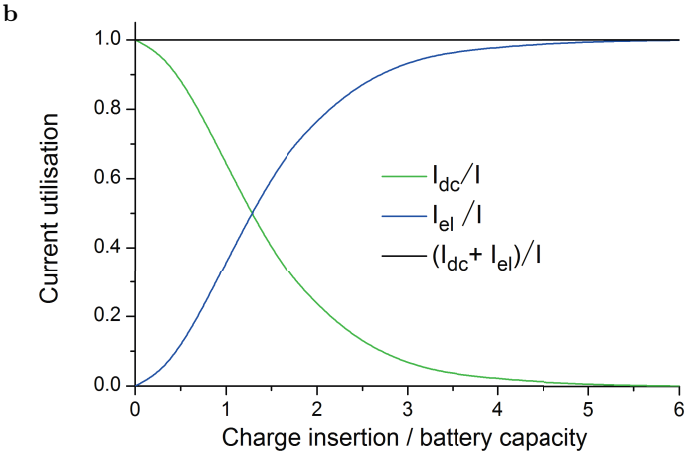

Figure B.2: Energy efficiency and charge utilisation.

(b) The utilisation of the inserted current I as represented by I_{dc}/I and I_{el}/I from equation (2.11) and (2.12) as a function of the total inserted charge. Initially all charge is used for charging the battery, but the charge for electrolysis increases from the beginning. When the inserted charge equals the nominal battery capacity (value 1 on the x-axis) the Ni-Fe electrodes already produce significant hydrogen and oxygen, which is a reason why Ni-Fe batteries historically reached low energy efficiencies of ~ 60-70% [1, 2]. In the battolyser charging can continue to many times this nominal capacity and the actual saturation in our experiments reaches $C_{cap} = 14.5\,\mathrm{A\,h}$ or 1.45 times the nominal capacity.

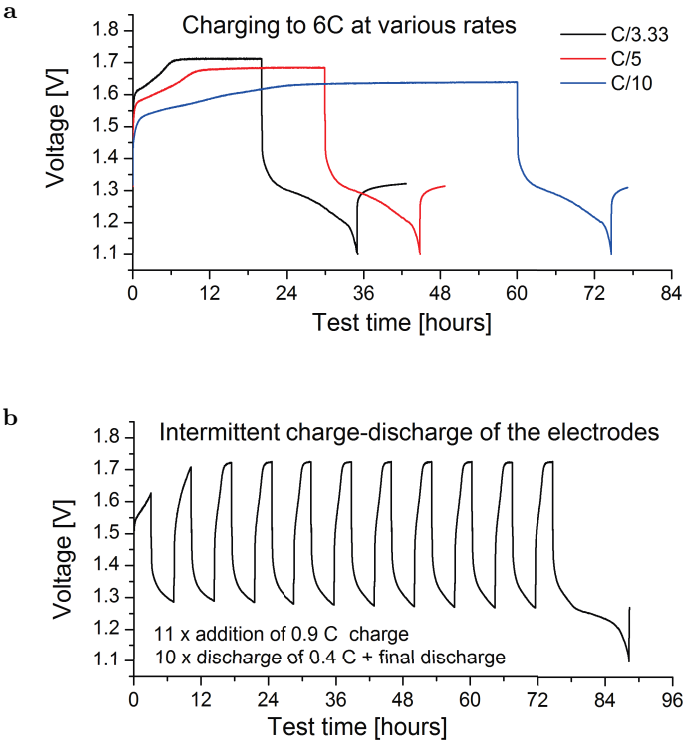

Figure B.3: Charge and switching capabilities (exemplary test cycles).

(a) Charging to 6 C (60 A h) at various charge rates; discharge at C/10 rate (this is a current of 1 A, see Experimental section)

(b) Current handling capabilities of the charged electrodes, showing charge, electrolysis and intermediate discharge capabilities, while still being able to fully discharge at the end of the cycle. Partial charge insertion of 0.9 C is followed by discharge of 0.4 C; 0.4 C of the 0.9 C is used each time to charge the battery and the remaining 0.5C part for electrolysis. Charge rate C/3.33 (or 3 A), discharge rate C/10 (or 1 A).

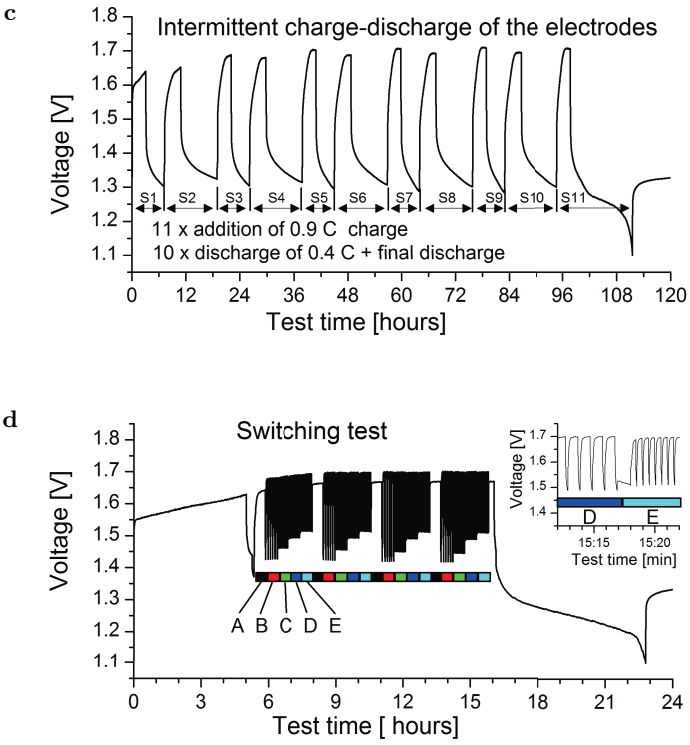

Figure B.3: Charge and switching capabilities (exemplary test cycles).

(c) Cycle with one of the highest aggregated current insertion (nr 113 in Figure 2.4 and Figure B.4).

(d) Switching test at charged electrodes: first 5 hour charge at C/3.33 rate then switching in sequences A to E. A: 30 min charging at constant rate C/3.33; B: 5 cycles 5 min charge followed by 1 min discharge; C: 2.5 min charge followed by 30 sec discharge; D: 50 sec charge followed by 10 sec discharge; E: 25 sec charge followed by 5 sec discharge; for B-E: charge rate C/2.5 and discharge rate C/5, average rate C/3.33; one minute rest between programs A-E. Note that for higher switching rate the difference in potential between charge and discharge decreases, leading to increased electrical efficiency.

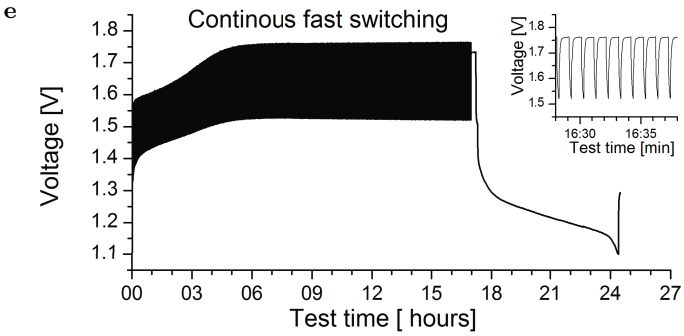

Figure B.3: Charge and switching capabilities (exemplary test cycles).

(e) Continuous fast switching test, 1000 cycles of 50 sec charge insertion (C/2.5) and 10 sec of charge withdrawal (C/5) completed by a final discharge

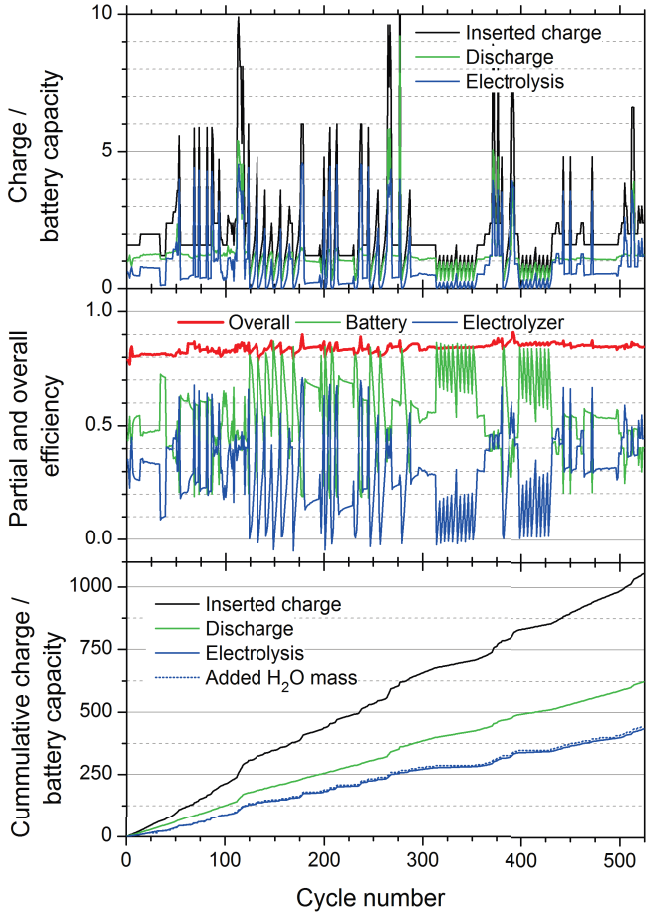

Figure B.4: Long term cycling and efficiencies.

This is an extension of Figure 2.4b, where 2.4b is now in the lower panel for convenience.

(Top) Detail information on the inserted charge for a large number of cycles of a battolyser cell. A cycle is counted from full discharge to full discharge with various full or partial (over/dis)charge programs in between (so when there are many partial discharges and recharges before a final full discharge the aggregated discharge in that cycle can be much larger than the nominal capacity. See also appendix Tables B.1-B.3). The inserted charge amounts vary strongly, from a fraction up to 10 times the nominal battery capacity insertion, and on average about two times the nominal battery capacity.

(Middle) Overall energy efficiency as sum of partial battery plus hydrogen gas

efficiency (see Experimental Section). Depending on charge insertion amounts the H_2 production is much higher or lower than the battery charge. Consistently the overall cycle energy efficiency adds up to above 80 to 91%, with the highest battery (electrolysis) contribution to the efficiency at low (high) charge insertion. Sometimes the battery appears not fully discharged (for kinetic reasons) and then additional discharge capacity can be observed in subsequent cycles, leading to apparent over capacity and efficiency for the battery and under capacity and efficiency for electrolysis. These effects cancel each other in the total capacity and efficiency.

(Bottom, the same as Figure 2.4b, shown here for convenience), Cumulative inserted charge and breakdown in battery charge and electrolysis, and the cumulative H_2O mass to replenish the electrolyte expressed with respect to the battery capacity.

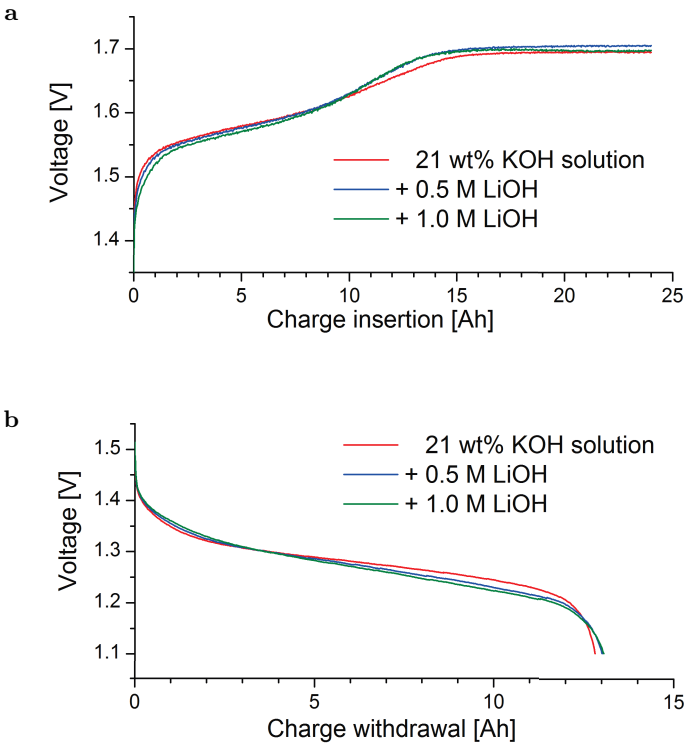

Figure B.5: Influence of LiOH addition of 21 wt% KOH electrolyte.

(a) Characteristic Charge curve using pure 21wt.% KOH electrolyte, and with the addition of 0.5 or 1.0 M/L LiOH. There is not much difference on the potentials i.e. the efficiencies, which makes that a small LiOH addition as described in [1, 3] for the battery functionality can be used.

(b) Characteristic discharge curve for the same electrolytes.

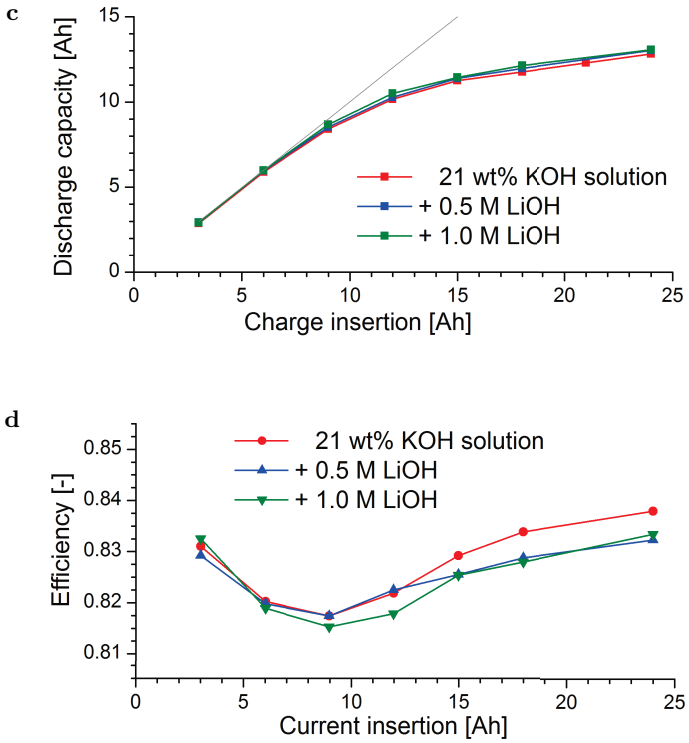

Figure B.5: Influence of LiOH addition of 21 wt% KOH electrolyte.

(c) Battery charge retention for cycles with different values of current insertion.

(d) Energy efficiency for various cycles.

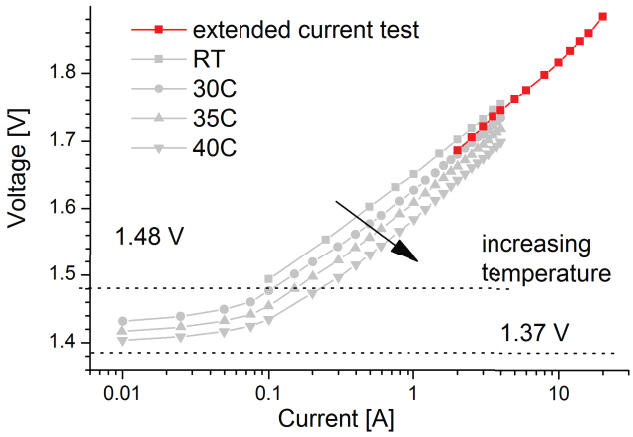

Figure B.6: Extended battolyser Current-Voltage range.

The potential reached in electrolysis mode versus the applied currents. Experiments without temperature regulation in red, plotted with data from Figure 2.6 in gray. At 20 A (corresponding to 100 mA/cm^2) the electrolysis efficiency is still close to 80% at temperatures well below 40 °C. For the nominal battery capacity of 10 A h the 20 A corresponds to a charge rate of 2 C; much higher than would be normally used for daytime charge and night time discharge, but it shows the available operational flexibility.

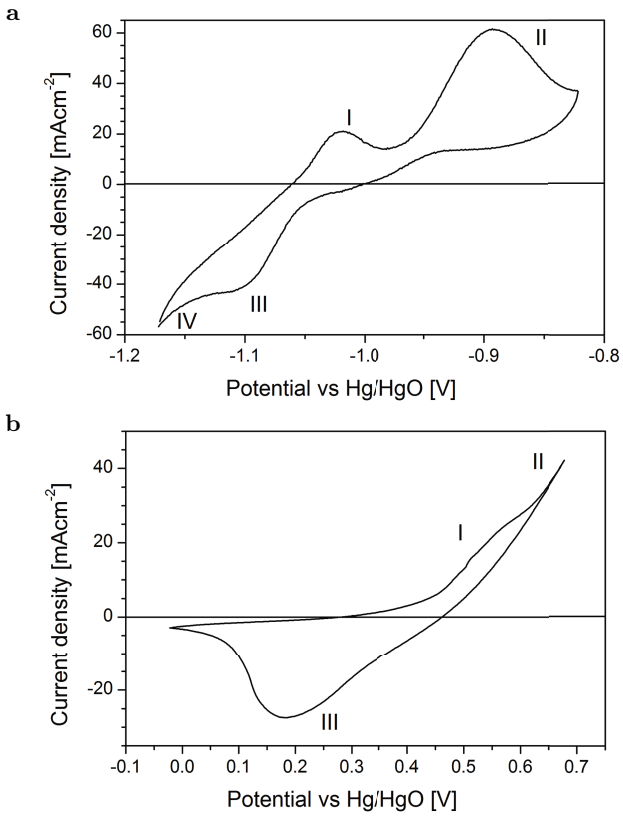

Figure B.7: Cyclic voltammograms of the electrodes.

(a) Iron electrode, current density vs. electrode potential (scan rate 1 mV/s, temperature 20 °C). The sweep is restricted to the first discharge plateau of the iron electrode. The redox-couple for the iron electrode ($Fe/Fe(OH)_2$) is indicated by the maximum peak of the anodic cycle II together with peak III of the cathodic cycle. Peak IV represents hydrogen evolution. Peak I of the anodic cycle may be attributed to the formation of initial $Fe(OH)_2$ layers or oxidation of adsorbed hydrogen atoms [4].

(b) Nickel electrode, current density vs. electrode potential (scan rate 0.025 mV/s, temperature 20 °C). The redox-couple for the nickel-electrode ($Ni(OH)_2/NiOOH$) is indicated by peak I in the anodic cycle together with peak III of the cathodic cycle [5]. Peak II in the anodic cycle represents oxygen evolution. At point II $Ni(OH)_2$ has been converted to NiOOH, the active oxygen evolution catalyst.

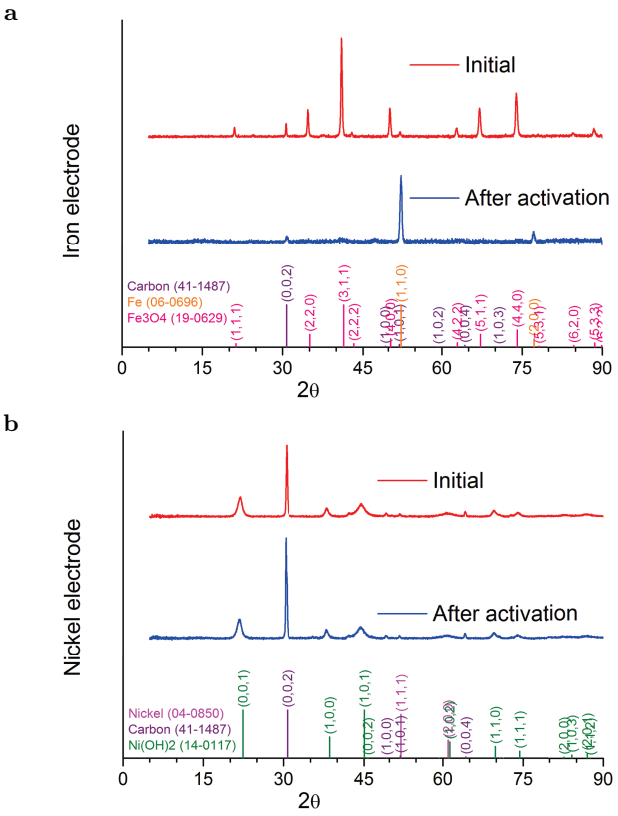

Figure B.8: XRD-data of initial and cycled electrode materials.

(X-ray source: Co K_α with wavelength of 1.788 97 Å, the vertical scale is counts [a.u.] and the background is removed.)

(a) Initial: Iron electrode material before activation; the diffraction peaks show the as prepared electrode material Fe_3O_4 with a small amount of iron and graphitic carbon. After activation in the cell the metallic Fe formed in the charged state is clearly visible, while Fe_3O_4 has almost completely been reduced.

(b) Initial: $\beta-Ni(OH)_2$ electrode material before and after activation in the cell. The large line broadening is indicating approximate crystallite sizes of ~14 nm, that remain constant after cycling. The charged NiOOH is X-ray amorphous as a result of small particle size and lattice plain defects, which has also been reported for the Ni electrode of a nickel-metal hydride battery.[6] The conductive graphitic carbon additive is recognised from the characteristic [002] diffraction peak.

Figure	Charging		Discharging		Electrolysis		Efficiency		
	Capacity [Ah]	Energy [Wh]	Capacity [Ah]	Energy [Wh]	Capacity [Ah]	Energy [Wh]	$\eta_{battery}$ [-]	$\eta_{electrolysis}$ [-]	η_{overal} [-]
5	25.89	42.61	15.86	20.29	10.03	14.85	0.476	0.348	0.825
A3a black	60.00	101.05	14.94	18.94	45.06	66.69	0.187	0.660	0.847
A3a red	60.00	99.19	14.77	18.75	45.23	66.95	0.189	0.675	0.864
A3a blue	60.00	96.41	14.53	18.44	45.47	67.30	0.191	0.698	0.889
A3b	99.00	165.35	53.50	69.71	45.50	67.35	0.422	0.407	0.829
A3c	99.00	161.66	53.70*)	71.11	45.30	67.04	0.440	0.415	0.855
A3d	48.21	80.41	16.27	21.07	31.94	47.27	0.262	0.588	0.850
A3e	56.29	97.72	19.76	25.99	36.54	54.07	0.266	0.553	0.819

*) see sub-cycle information below

Figure	Temperature [^oC]	Charge rate	Discharge rate	Observed weight loss [g]	Theoretical weight loss due to electrolysis [g]	Observed/ theoretical weight loss [-]
A3a black	30	C/3.33	C/10	15.83	15.14	1.046
A3a red	30	C/5	C/10	15.81	15.20	1.040
A3a blue	30	C/10	C/10	15.37	15.28	1.006
A3b	RT	C/3.33	C/10	15.80	15.29	1.033
A3c	Variable	Variable*)	Variable*)	15.65	15.22	1.028
A3d	40	C/3.33 & C/2.5	C/5	11.52	10.73	1.074
A3e	RT	C/2.5	C/5	12.58	12.28	1.024

*) see sub-cycle information below

Sub-cycle in Figure A3c	Rate	Charge insertion [Ah]	Energy [Wh]	Rate	Discharge capacity [Ah]	Energy [Wh]
1	C/3.33	9.00	14.46	C/10	4.00	5.35
2	C/4	9.00	14.41	C/20	4.00	5.43
3	C/3.33	9.00	14.73	C/10	4.00	5.37
4	C/4	9.00	14.58	C/20	4.00	5.41
5	C/3.33	9.00	14.85	C/10	4.00	5.35
6	C/4	9.00	14.64	C/20	4.00	5.40
7	C/3.33	9.00	14.87	C/10	4.00	5.34
8	C/4	9.00	14.67	C/20	4.00	5.39
9	C/3.33	9.00	14.90	C/10	4.00	5.33
10	C/4	9.00	14.69	C/20	4.00	5.39
11	C/3.33	9.00	14.86	C/10	13.70	17.35
Sum		99.00	161.66		53.70	71.11

Table B.1: Cycle capacities, energies, efficiencies and water losses for the cycles in Figure 2.5 and appendix Figure B.3a-B.3e.

The cycle in Figure B.3c has one of the highest aggregated current insertion in Figure 2.4 and Figure B.4 (cycle 113). The cycle from Figure B.5 is number 111. The Electrolysis Energy yield is calculated from Capacity (A h) $*$ 1.48 V (HHV of hydrogen, see Experimental section).

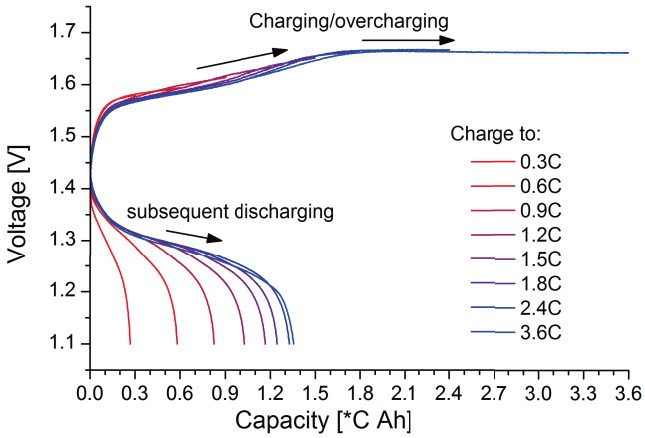

Figure B.9: Capacity vs Voltage graphs of the same cycles in Figure 2.3a.

Charge insertion to the indicated values between 0.3 C and 3.6 C with subsequent discharge to 1.1 V; charge rate C/5; discharge rate C/10; C=10 A h. Test conditions: thermally insulated cell.

Charging		Discharging		Electrolysis		Efficiency		
Capacity [Ah]	Energy [Wh]	Capacity [Ah]	Energy [Wh]	Capacity [Ah]	Energy [Wh]	$\eta_{battery}$ [-]	$\eta_{electrolysis}$ [-]	$\eta_{overall}$ [-]
3.00	4.70	2.68	3.41	0.32	0.48	0.727	0.102	0.829
6.00	9.49	5.80	7.45	0.20	0.29	0.786	0.031	0.816
9.00	14.31	8.26	10.63	0.73	1.09	0.743	0.076	0.819
12.00	19.19	10.28	13.20	1.72	2.55	0.688	0.133	0.821
15.00	24.10	11.67	14.97	3.33	4.92	0.621	0.204	0.825
18.00	29.11	12.46	15.98	5.54	8.20	0.549	0.282	0.831
24.00	39.10	13.27	17.00	10.73	15.88	0.435	0.406	0.841
36.00	59.11	13.56	17.27	22.44	33.21	0.292	0.562	0.854

Table B.2: Charge, energy and efficiency data from cycles in Figure 2.3a.

Test conditions: thermally insulated cell; charge rate C/5; discharge rate C/10.

Charging		Discharging		Electrolysis		Efficiency		
capacity [Ah]	energy [Wh]	capacity [Ah]	energy [Wh]	capacity [Ah]	energy [Wh]	$\eta_{battery}$ [-]	$\eta_{electrolysis}$ [-]	η_{overal} [-]
3.00	4.67	3.10	3.94	-0.10	-0.14	0.843	-0.031	0.812
6.00	9.50	5.81	7.49	0.19	0.28	0.788	0.029	0.818
9.00	14.39	8.11	10.47	0.89	1.31	0.728	0.091	0.819
12.00	19.35	9.98	12.87	2.02	2.99	0.665	0.155	0.820
15.00	24.33	11.30	14.56	3.70	5.47	0.598	0.225	0.823
18.00	29.37	12.03	15.42	5.97	8.83	0.525	0.301	0.826
24.00	39.90	12.96	16.54	11.04	16.34	0.415	0.409	0.824
30.00	50.00	13.63	17.44	16.37	24.23	0.349	0.485	0.833
36.00	59.87	13.88	17.74	22.12	32.74	0.296	0.547	0.843
48.00	80.38	14.55	18.51	33.45	49.50	0.230	0.616	0.846
60.00	101.05	14.94	18.94	45.06	66.69	0.187	0.660	0.847

Table B.3: Charge, energy and efficiency data for cycles used to make Figure 2.3b.

Test conditions: regulated temperature of 30 °C; charge rate C/3.33; discharge rate C/10. These cycles are corresponding to cycles 247-258 in Figure 2.4 and Figure B.4.

References

[1] S. U. Falk and A. J. Salkind, *Alkaline Storage Batteries* (John Wiley & Sons, 1969).

[2] D. Linden and T. B. Reddy, *Handbook of batteries Third Edition* (McGraw-Hill, 2001).

[3] R. Kinzelbach, *Stahlakkumulatoren* (VARTA Battery AG, 1974).

[4] M. K. Ravikumar, T. S. Balasubramanian, A. K. Shukla, and S. Venugopalan, *A cyclic voltammetric study on the electrocatalysis of alkaline iron-electrode reactions,* Journal of applied electrochemistry **26**, 1111 (1996).

[5] G. A. Snook, N. W. Duffy, and A. G. Pandolfo, *Evaluation of the effects of oxygen evolution on the capacity and cycle life of nickel hydroxide electrode materials,* Journal of power sources **168**, 513 (2007).

[6] J. J. Biendicho, M. Roberts, D. Noréus, U. Lagerqvist, R. I. Smith, G. Svensson, S. T. Norberg, S. G. Eriksson, and S. Hull, *In situ investigation of commercial $Ni(OH)_2$ and $LaNi_5$-based electrodes by neutron powder diffraction,* Journal of Materials Research **30**, 407 (2015).

C

Renewable Hydrogen and Electricity Dispatch With Multiple Ni-Fe Electrode Storage

Supporting Information to Chapter 3

C

C.1. Operation modes for hybrid hydrogen – electrical storage system

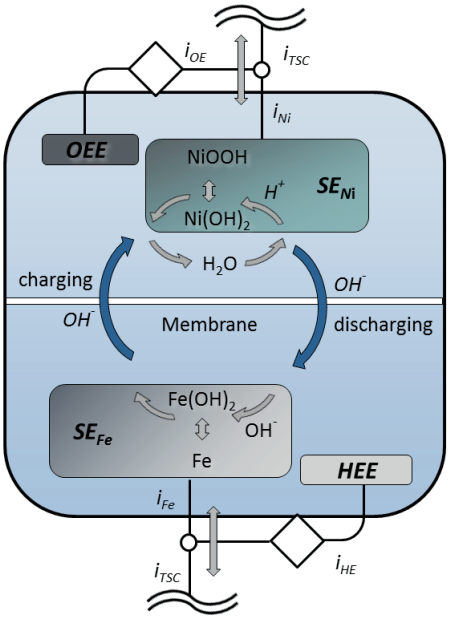

Figure C.1: Operation modes for hybrid hydrogen – electrical storage system.

Battery operation and/or charging the storage electrodes, both storage electrodes are active.

$$i_{TSC} = i_{Ni} = i_{Fe};\ (i_{HE} = i_{OH} = 0)$$

Charging:

$$\text{Cathode:} \qquad Fe(OH)_2 + 2e^- \rightarrow Fe + 2OH^- \qquad \text{(C.1)}$$

$$\text{Anode:} \qquad Ni(OH)_2 + OH^- \rightarrow NiOOH + H_2O + e^- \qquad \text{(C.2)}$$

Discharging:

$$\text{Anode:} \qquad Fe + 2OH^- \rightarrow Fe(OH)_2 + 2e^- \qquad \text{(C.3)}$$

$$\text{Cathode:} \qquad NiOOH + H_2O + e^- \rightarrow Ni(OH)_2 + OH^- \qquad \text{(C.4)}$$

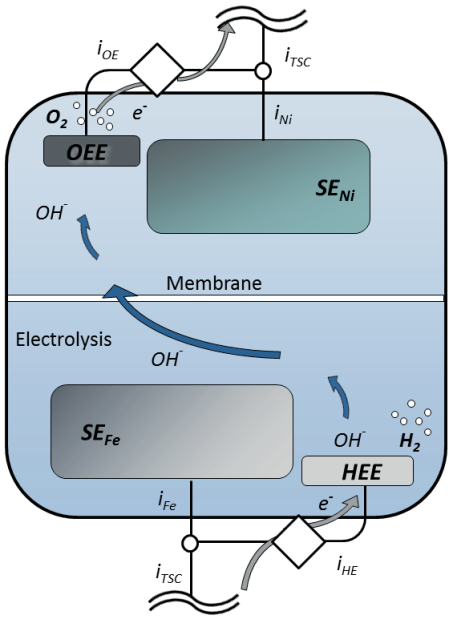

Figure C.1: Operation modes for hybrid hydrogen – electrical storage system.

Electrolysis, both gas evolution electrodes are active.

$$i_{TSC} = i_{HE} = i_{OE};\ (i_{Ni} = i_{Fe} = 0)$$

Electrolysis:

$$\text{Cathode:} \qquad 2H_2O + 2e^- \rightarrow H_2 + 2OH^- \qquad \text{(C.5)}$$

$$\text{Anode:} \qquad 4OH^- \rightarrow 2H_2O + O_2 + 4e^- \qquad \text{(C.6)}$$

Note: The positive storage electrode (nickel) stores a proton upon discharging which is released upon charging. The negative storage electrode (iron) stores a hydroxyl ion upon discharging which is released upon charging. Hence, the storage electrodes may be considered as Proton and Hydroxyl Ion storage electrode.

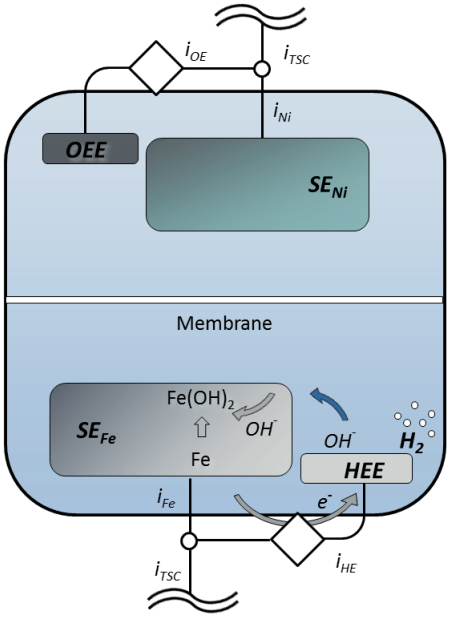

Figure C.2: Operation modes for hybrid hydrogen – electrical storage system.

Discharging the iron storage electrode in combination with hydrogen production at the HEE.

$$i_{Fe} = i_{HE};\ (i_{TSC} = i_{Ni} = i_{OE} = 0)$$

Delayed hydrogen generation:

$$\text{Cathode:} \qquad 2H_2O + 2e^- \rightarrow H_2 + 2OH^- \qquad \text{(C.5)}$$

$$\text{Anode:} \qquad Fe + 2OH^- \rightarrow Fe(OH)_2 + 2e^- \qquad \text{(C.3)}$$

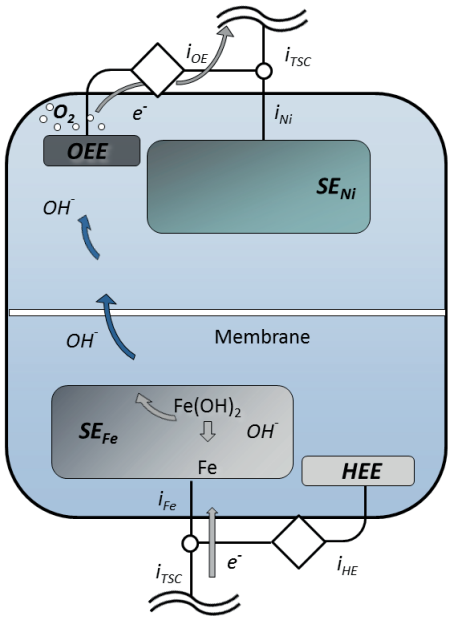

Figure C.2: Operation modes for hybrid hydrogen – electrical storage system.

Charging the iron storage electrode together with oxygen production at the OEE.

$$i_{TSC} = i_{OE} = i_{Fe};\ (i_{HE} = i_{Ni} = 0)$$

Regeneration iron storage electrode:

$$\text{Cathode:} \qquad Fe(OH)_2 + 2e^- \rightarrow Fe + 2OH^- \qquad \text{(C.1)}$$

$$\text{Anode:} \qquad 4OH^- \rightarrow 2H_2O + O_2 + 4e^- \qquad \text{(C.6)}$$

Note: Other materials such as toxic Cd may also be used as negative storage electrode.

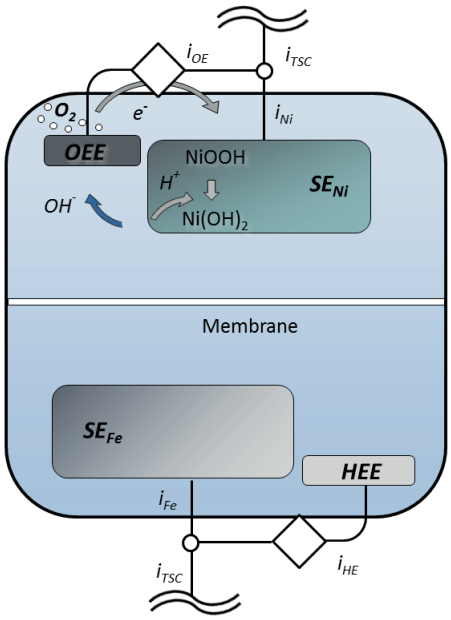

Figure C.3: Operation modes for hybrid hydrogen – electrical storage system.

Discharging the nickel storage electrode in combination with oxygen production at the OEE:

$$i_{Ni} = i_{OE};\ (i_{TSC} = i_{Fe} = i_{HE} = 0)$$

Delayed oxygen generation:

$$\text{Cathode:} \qquad NiOOH + H_2O + e^- \rightarrow Ni(OH)_2 + OH^- \qquad \text{(C.4)}$$

$$\text{Anode:} \qquad 4OH^- \rightarrow 2H_2O + O_2 + 4e^- \qquad \text{(C.6)}$$

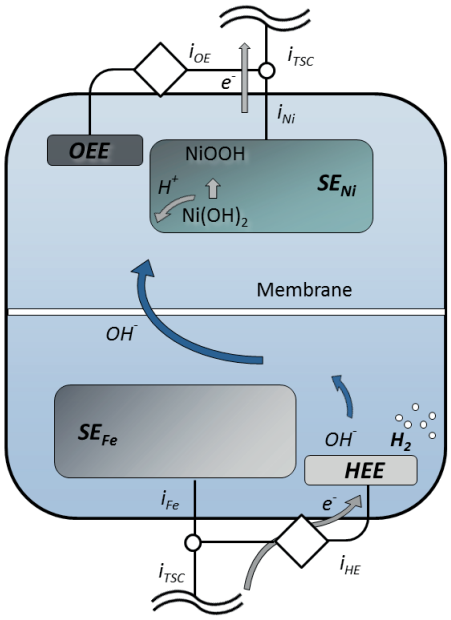

Figure C.3: Operation modes for hybrid hydrogen – electrical storage system.

Charging the nickel storage electrode together with hydrogen production at the HEE.

$$i_{TSC} = i_{HE} = i_{Ni};\ (i_{OE} = i_{Fe} = 0)$$

Regeneration nickel storage electrode:

Cathode: $$H_2O + 2e^- \rightarrow H_2 + 2OH^- \quad \text{(C.5)}$$

Anode: $$Ni(OH)_2 + OH^- \rightarrow NiOOH + H_2O + e^- \quad \text{(C.2)}$$

C.2. System integration

Figure C.4 shows integrated hydrogen storage in the battolyser and an alkaline electrolyser for the operation modes electricity sink and electricity source with electron and hydroxil ion flow.

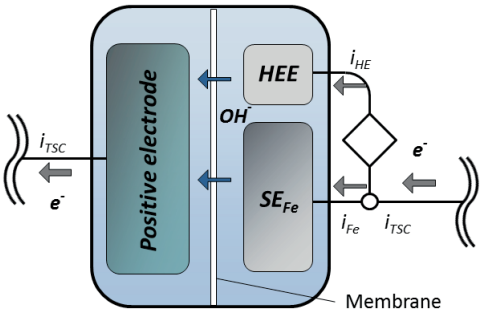

Figure C.4: Electricity sink: $i_{TSC} > i_{HE}$

The iron storage electrode operates as cathode. Hydroxyl ions flow from the negative to the positive assemblies. The iron electrode is charged. System consists of two cathodes and one anode.

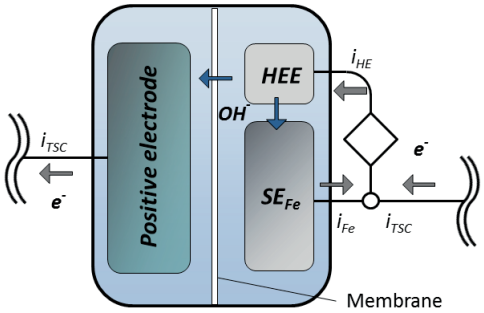

Figure C.4: Electricity sink: $i_{TSC} < i_{HE}$

The iron storage electrode operates as anode. Hydroxyl ions flow from the HEE to the positive assemblies and to the iron electrode, which is discharged. System consists of one cathode and two anodes.

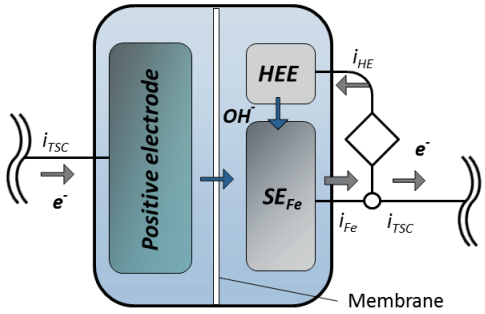

Figure C.4: Electricity source: $i_{TSC} + i_{HE} = i_{Fe}$.

The iron electrode operates as anode. Hydroxyl ions flow from the HEE and from the positive assemblies to the iron electrode. The iron electrode and the positive assembly are discharged. System consists of two cathodes and one anode.

Note: As electricity sink the positive electrode can either be charged (reaction C.2) or produce oxygen (reaction C.6): Ni based battolyser electrodes facilitate both reactions simultaneously, the distribution dependents on their SoC; Electrolyser electrodes facilitate only oxygen evolution. Hence, electrolysers cannot provide reverse operation as electricity source. The positive electrode of Iron-Air batteries provide reversible operation with oxygen. A configuration with a reversible oxygen electrode as positive electrode can therefore be used for electricity sink and electricity source operation.

Note: The average discharge potential of the battolyser at a C/10 rate is 1.25 V. The average voltage for controlled hydrogen production at this rate is 0.2 V leading to a voltage ratio of (1.25/0.2≈) 6. Electrically discharging one electron could therefore provide sufficient energy for overcoming overpotentials for 6 electrons to serve hydrogen production. A system with self-sustaining electricity for hydrogen storage would require a storage ratio of 1 to 6 for electricity to hydrogen storage in which the ratio of storage capacity of the nickel electrode to the iron electrode would be 1 to (1+6=) 7. Hence, the amount of nickel for sustained hydrogen production is reduced by 86% (6/7) for the Ni-Fe system.

C.3. Gas production from storage electrodes

Gas production was tested for simultaneous operation of the HEE and OEE at constant and equal production rates. Figure 3.2 in the main text provides the measured potentials between the storage electrodes and the gas production electrodes. The observed cell potentials include overpotentials associated with gas production and discharging of the storage electrodes. Figure C.5(a) shows the observed individual electrode voltage response vs a Hg/HgO reference electrode for a storage capacity of 0 to 80%. The potentials for oxygen evolution and hydrogen evolution are constant with proceeding test time, whereas the potentials for discharging the storage electrodes gradually decrease and increase, respectively. The bottom part of Figure C.5(b) depicts the potential differences between the gas producing electrodes and the storage electrodes, the difference may represent the potential for electrolysis and discharging. It is recognizable, that discharging the storage electrode maybe the rate limiting factor as overpotentials increase stronger with increasing rate. Figure C.6 (two pages) depict the complete test result for all rates. Comments to these results are provided after Figure C.6.

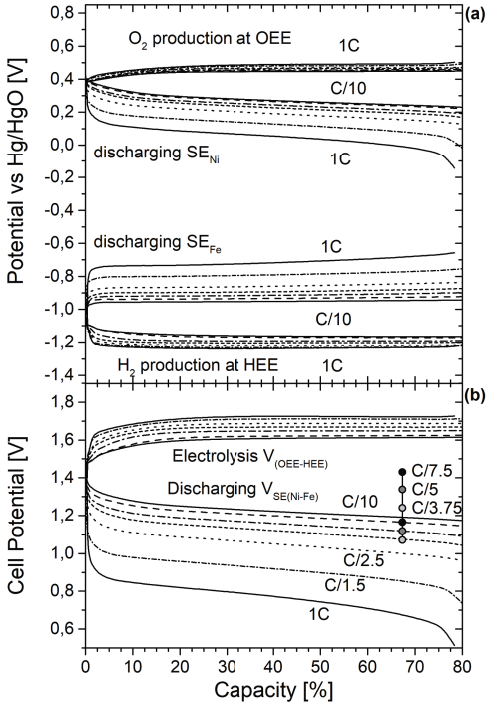

Figure C.5: Voltage response for simultaneous oxygen and hydrogen production from storage electrodes at constant and equal production rates for a storage capacity of 0 to 80%.

(a) Observed individual cell potentials plotted vs Hg/HgO reference electrode.

(b) Resulting potential for electrolysis ($V_{OEE} - V_{HEE}$) and battery discharge ($V_{Ni} - V_{Fe}$).

Note: At moderate rates (C/10) the belonging potentials at close together while they drift apart for higher rates (1C)

Figure C.6 provides the entire voltage response for all individual tested discharge rates.

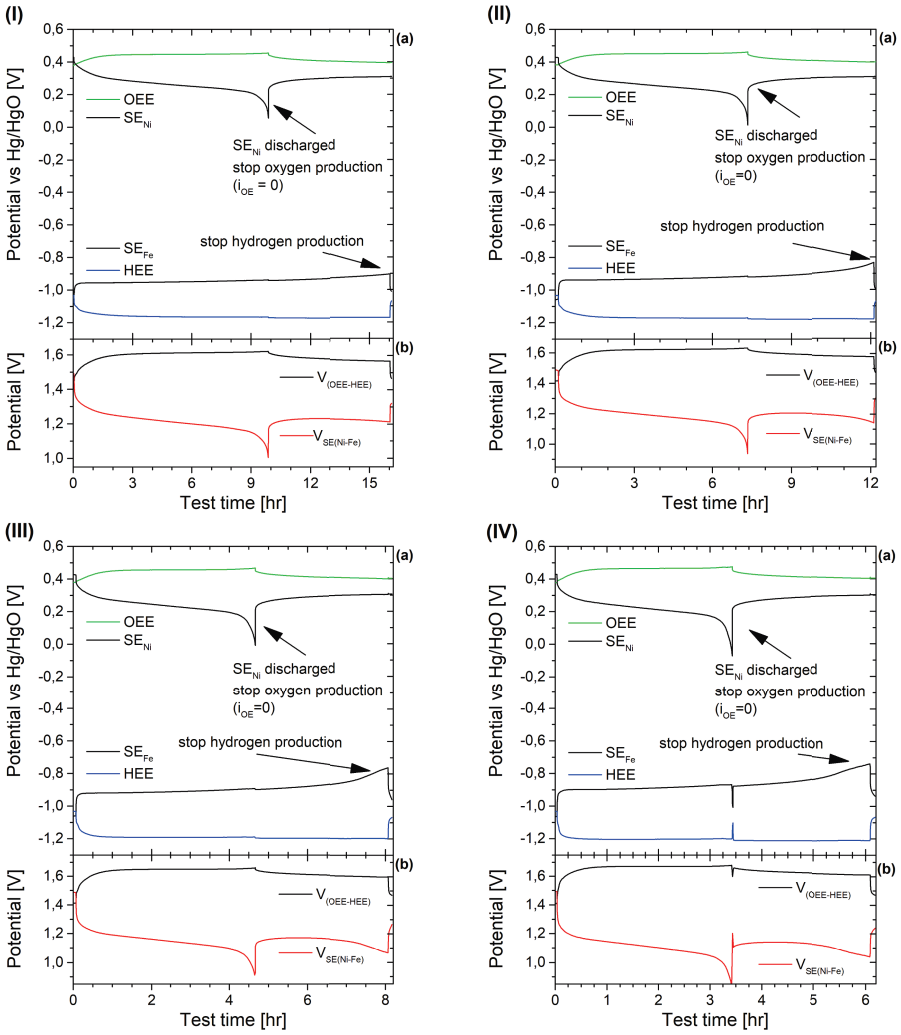

Figure C.6.: Electrode potentials for different rates.

Rates: (I) C/10, (II) C/7.5, (III) C/5 and (IV) C/3.75

Comments to Figure C.6 are added after Figure C.6 page 2.

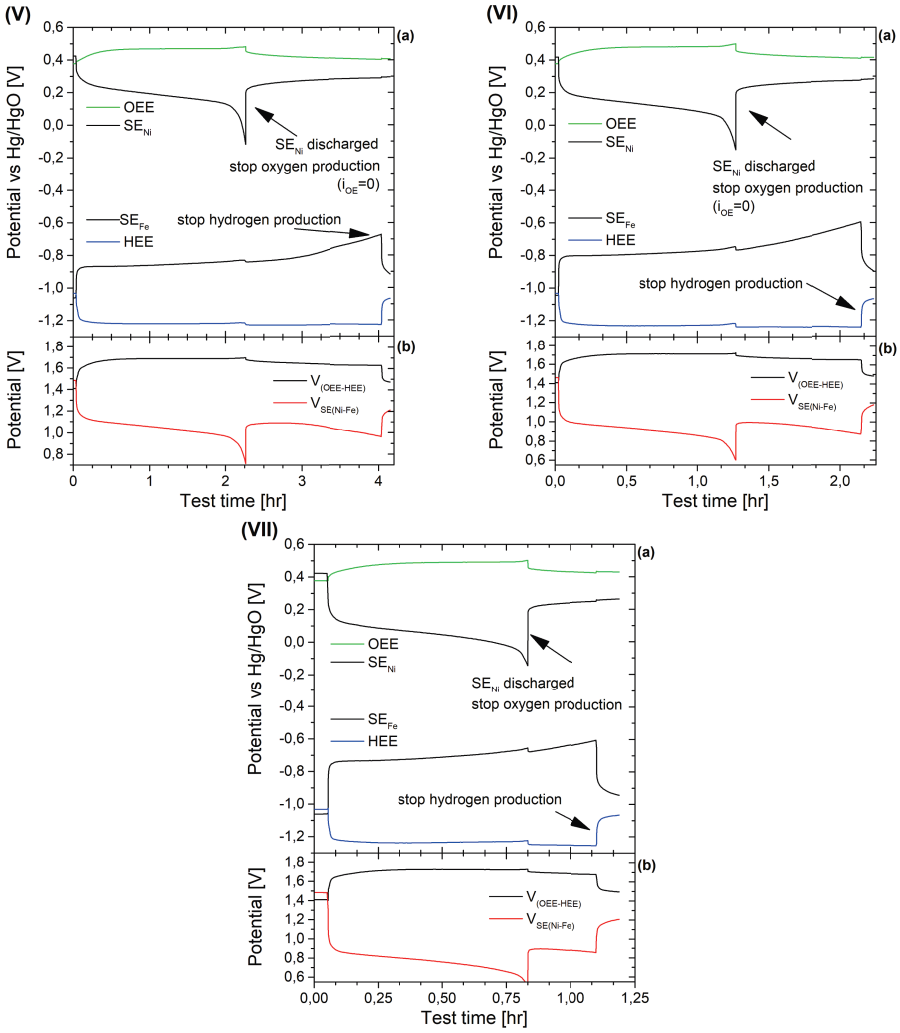

Figure C.6: Electrode potentials for different rates .

Rates: (V) C/2.5, (VI) C/1.5 and (VII) 1C

Comments to Figure C.6 see next page.

Comments to Figure C.6:

(a) Electrode potentials OEE, SE_{Ni}, SE_{Fe} and HEE vs Hg/HgO reference electrode. The green line depicts the potential for oxygen production at the oxygen evolution electrode (OEE). The top black line shows the potential of the discharging the nickel electrode. The bottom black line depicts the potential of the discharging the iron electrode. Hydrogen production at the hydrogen evolution electrode (HEE) is plotted with a blue line. All potentials are direct measurement results.

(b) Potential between gas producing electrodes ($V_{OEE-HEE}$, black line) and storage electrodes (V_{Ni-Fe}, red line). The plotted potential difference between V_{OEE} and V_{HEE} may represent the potential for electrolysis when both gas evolution electrodes are turned on at the same rate. The plotted potential difference between V_{Ni} and V_{Fe} may represent the potential for battery discharging when both electrodes are turned on and discharged at the same rate.

All electrodes are within one electrochemical cell. Stable potentials are observed for the gas producing electrodes when turned on. Turning off oxygen production does not affect hydrogen production. Hydrogen production stops independently later. Hence, the storage capacities of both storage electrodes can fully be utilised.

The reference electrode was located about 2 cm away from active electrodes. The test results indicate that the environment around the reference electrode is influenced by the operation of the electrodes. When oxygen production stops, the potentials of the iron electrode and the HEE vs Hg/HgO reference electrode show an offset. The main channel for hydrogen production (see Figure 3.2(b)) does not show any recognizable change in the cell potential indicating that the active electrodes (HEE and SE_{Fe}) were not influence by turning off oxygen production. It is likely that the environment around the reference electrode was influenced by turning off oxygen production. The resulting offset recognizable in the measurements with Hg/HgO reference electrode is hardly recognizable at low currents and scales with increasing current. (The current for oxygen evolution and hydrogen evolution is equal and constant until oxygen production stops while hydrogen production proceeds.)

Test procedure: Both storage electrodes, nickel and iron, were charged before starting the test. While the storage electrodes were charging for 12 h, HEE and OEE were at rest. For the tests the electrodes were connected as follows: OEE and SE_{Ni} were connected with one main channel, the results are plotted in Figure

3.2(a); HEE and SE_{Fe} were connected with another main channel, this results are plotted in Figure 3.2(b). The potentials of all four active electrodes vs Hg/HgO were monitored with additional channels. Both tests started simultaneously. The tests of the main channels ended by a defined current dependent cut-off voltage (meaning that the SE is discharged). Time was set as second cut-off condition. The voltage condition ended all tests executed with the SE_{Ni}, and tests with test current 1 C and C/1.5 executed with the SE_{Fe}. The time condition ended the other tests executed with the SE_{FE} at 160% of the nickel electrodes capacity.

The test channel for hydrogen production at a rate C/3.75 (Figure C.6 (IV)) stopped operation when oxygen production stopped due to a current overload of the Parstat MC operational at the current limit. The test channel was immediately restarted. This is not recognizable in Figure 3.2(b), because the main channel did not measure voltage when turned off. However, this short period (2') is recognizable in the additional voltage measurements depicted here. All other tests worked out as intended. Tests with higher test current were performed with an additional boosters.

C.4. Testing 'multi-controlled' electrochemical systems: Single-cell with simultaneous operation of four electrodes

A single-cell setup according to Figure 3.3 was assembled and tested as proof of concept. The setup utilizes battolyser electrodes, these were used as SEs, OEE and HEE.

The test program consisted of 16 sequences with varying test currents i_{TSC}, i_{HE}, and i_{OE}. i_{TSC} was turned on during the first 4 sequences and then alternately turned off and on to mimic a day-night rhythm of a solar powered system. i_{OE} and i_{HE} were both turned on in sequence 2, moreover i_{OE} was turned on from sequence 4 to 12 and i_{HE} from sequence 8 to 16. Hence, sequence 5-8 provide controlled oxygen production, sequence 9-12 controlled oxygen and hydrogen production and sequence 13-16 controlled hydrogen production. The value of i_{OE} and i_{HE} was set to 50% of i_{TSC} at sequences when i_{TSC} was turned off to provide 50% gas production at times when no excess electricity is available and to 40% of i_{TSC} when i_{TSC} was turned on to ensure that the storage electrodes were fully charged in these periods. The normalised gas production and the voltage response of the test is depicted in Figure 3.4, and Figure C.7, the energy input analysis in Figure C.8.

The test sequences depicted in Figure 3.4 demonstrate that distributing currents among the electrodes results in oxygen and hydrogen being generated independently. All controllers for current distribution can be individually turned on/off without effect on the other controllers. At night-times (main off) the additional gas-evolution electrodes provide a steady gas-output. At day-time (main on) the gas output results from continued gas-production at the gas electrodes in combination with increasing yield when recharging the SEs. Again, low potentials for gas production at gas evolution electrodes using energy stored in SEs can be observed, resulting in a low share of energy input compared to the total cycle energy input (see Figure C.8). Note that charge conservation determines that overall discharging of the SEs occurs at times when the current for gas production exceeds the total stack charge current i_{TSC} (nickel electrode: sequence 5,7,9 and 11; iron electrode: sequence 9,11,13,15). The SEs keep essentially the same SoC when the sum of both currents controlling the SEs equals zero (nickel electrode: sequence 13 and 15; Iron electrode: sequence 5 and 7).

Figure C.7 depicts the voltage response for the single-cell test setup. The top of the figure (a) shows all four electrodes with respect to the reference electrode (Hg/HgO), the bottom part of the figure (b, c and d) is identical to Figure 3.4 from the main article.

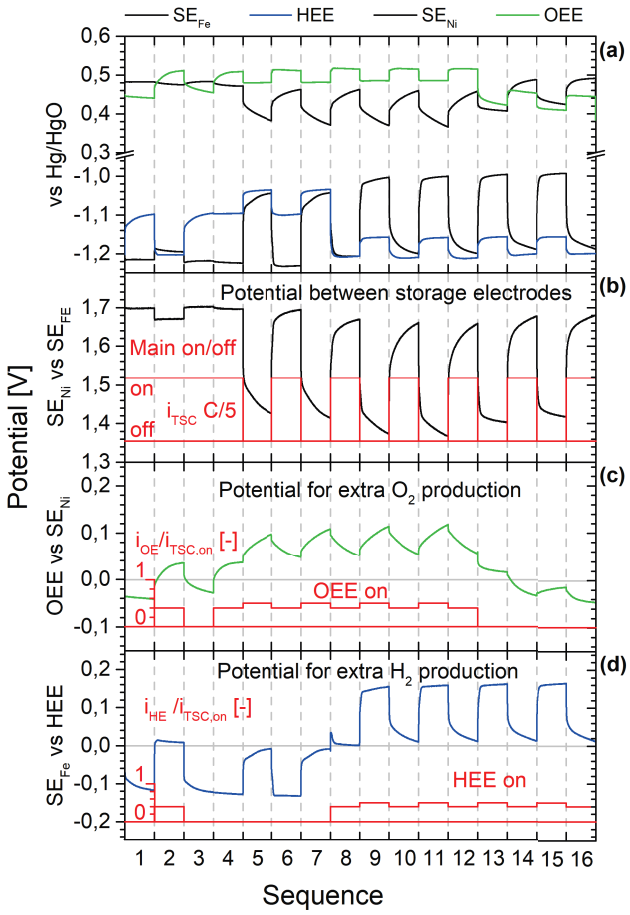

Figure C.7: Voltage response for single-cell test setup consisting of SEs, OEE, and HEE.

(a) Individual electrode potentials vs Hg/HgO reference electrode.

(b) Main channel for controlling current i_{TSC} between nickel and iron electrode with schematic operation status on/off for electrolyser operation (rate C/5 when on, red line).

(c) Channel for controlling test current i_{OE} between nickel electrode and OEE for controlled oxygen production with schematic operation status on/off (red line, ratio $i_{OE}/i_{TSC\ C/5}$).

(d) Channel for controlling test current i_{HE} between iron electrode and HEE for controlled hydrogen production with schematic operation status on/off (red line, ratio $i_{HE}/i_{TSC\ C/5}$).

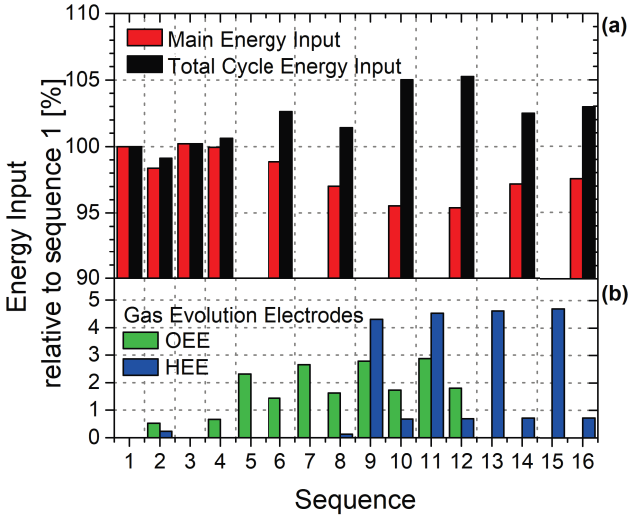

Figure C.8: Energy input for single-cell test setup consisting of SEs, OEE, and HEE, relative to sequence 1.

(a) Energy input of main channel and total cycle energy input. The total energy input is the sum of all inputs during one cycle. A cycle starts with first discharging the SEs and then charging the SEs to the same SoC. Dotted vertical lines indicate cycle steps.

(b) Additional energy input related to gas evolution electrodes OEE and HEE

Sequence	Main Stack			Oxygen evolution				Hydrogen evolution			
	status	i_{TSC} [A]	V_{main} [V]	status	i_{OE} [A]	i_{Ni} [A]	V_{OE} [V]	status	i_{HE} [A]	i_{Fe} [A]	V_{HE} [V]
1	on	1.5	1.698	off		1.5	-0.039	off		1.5	-0.106
2	on	1.5	1.670	on	0.6	0.9	0.022	on	0.6	0.9	0.010
3	on	1.5	1.702	off		1.5	-0.017	off		1.5	-0.112
4	on	1.5	1.697	on	0.6	0.9	0.028	off		1.5	-0.126
5	off		1.459	on	0.75	-0.75	0.079	off			-0.020
6	on	1.5	1.679	on	0.6	0.9	0.061	off		1.5	-0.128
7	off		1.449	on	0.75	-0.75	0.090	off			-0.021
8	on	1.5	1.647	on	0.6	0.9	0.069	on	0.6	0.9	0.005
9	off		1.404	on	0.75	-0.75	0.094	on	0.75	-0.75	0.146
10	on	1.5	1.622	on	0.6	0.9	0.074	on	0.6	0.9	0.029
11	off		1.395	on	0.75	-0.75	0.098	on	0.75	-0.75	0.154
12	on	1.5	1.620	on	0.6	0.9	0.076	on	0.6	0.9	0.029
13	off		1.415	off			0.021	on	0.75	-0.75	0.156
14	on	1.5	1.650	off		1.5	-0.019	on	0.6	0.9	0.030
15	off		1.431	off			-0.019	on	0.75	-0.75	0.160
16	on	1.5	1.657	off		1.5	-0.039	on	0.6	0.9	0.031

Table C.1: Operation status of main stack, oxygen evolution and hydrogen evolution with current distribution and average electrode potential (Data to Figure 3.4, Figure C.7 and Figure C.8.)

(V_{main} = V_{Ni}-V_{Fe}; V_{OE} = V_{OEE}-V_{Ni}; V_{HE} = V_{Fe}-V_{HEE}). Positive currents indicate charging the storage electrodes and gas evolution, negative currents indicate discharging the storage electrodes.

Sequence	Energy consumption					Deviation
	Main stack [Wh]	Oxygen evolution [Wh]	Hydrogen evolution [Wh]	Sum sequence [Wh]	Sum cycle [Wh]	from sequence 1 [%]
1	2.547			2.547	2.547	0.00%
2	2.505	0.013	0.006	2.525	2.525	-0.88%
3	2.553			2.553	2.553	0.21%
4	2.546	0.017		2.563	2.563	0.61%
5		0.059		0.059		
6	2.518	0.037		2.555	2.614	2.61%
7		0.068		0.068		
8	2.471	0.041	0.003	2.515	2.583	1.41%
9		0.071	0.109	0.180		
10	2.433	0.044	0.017	2.495	2.675	5.03%
11		0.073	0.115	0.188		
12	2.429	0.046	0.018	2.493	2.681	5.27%
13			0.117	0.117		
14	2.475		0.018	2.493	2.611	2.49%
15			0.120	0.120		
16	2.485		0.018	2.503	2.623	2.97%

Table C.2: Energy consumption for sequence 1 to 16 split up into main stack, oxygen evolution and hydrogen evolution, Data to Figure 3.4, Figure C.7 and Figure C.8.)

Sequences [5,6], [7,8], [9,10], [11,12], [13,14] and [15,16] form cycles were the storage electrode(s) are first discharged and then charged. The cycles [5,6] and [7,8] provide controlled oxygen production, cycles [9,10] and [11,12] provide controlled hydrogen and oxygen production and cycles [13,14] and [15,16] provide controlled hydrogen production.

Comments to Figure 3.4, Figure C.7, C.8, Table C.1 and C.2: Gas production, Voltage response and energy input for a single-cell test setup consisting of Ni and Fe storage electrodes, OEE and HEE.

The following characteristics can be recognized from the voltage response and the energy data from Figure 3.4, Figure C.7 and Figure C.8 and the energy input displayed in Table C.1 and C.2:

- The voltage response of the OEE and HEE show stable potentials when turned on, verifying continuous gas production.
- The voltage response of the main channel is stable from sequences 1-4, representing gas production at the storage electrodes. The effect of turning on both gas electrodes is depicted in sequence 2, the cell voltage of the main channel drops while the potentials of the auxiliary electrodes increases. The effect of turning on only OEE is visible in sequence 4, the cell voltage of the main channel drops slightly. Energetically sequence 2 saves 0.9% of input energy while sequence 4 costs 0.6% of extra energy.
- Discharging the SE benefits the subsequent charging sequence. The voltage response of previously discharge electrodes is lower, hence less energy is required to charge the SE than to produce gas at this SE's. The sequence of first discharging and then charging defines a cycle and accounts for that effect. Overcharging the SE provides that these electrodes return to the same state of charge. Peaks in the gas production at the end of sequences [6,8,10 and 12] for O_2 and [10,12,14 and 16] for H_2 indicate overcharging of the nickel and iron storage electrode, respectively (ratio inserted charge to extracted charge: $0.9/0.75 = 1,2 => 20\%$ overcharging of SEs).
- Producing hydrogen and/or oxygen at the gas evolution electrodes with SE's as counter electrode requires only a fraction of the total energy input of a cycle. Charging the SE requires most of the energy for decoupled and/or delayed electrolysis.
- Sequence [5,6] together form a cycle were only OEE is active at "night" time, this cycle for storing and delaying oxygen production result in 2.6% extra energy input.
- Sequence [11,12] together form a cycle were OEE and HEE are active, this cycle for storing and delaying oxygen and hydrogen production result in 5.3% extra energy input.

- Sequence [15,16] together form a cycle were only HEE is active, this cycle for storing and delaying hydrogen production result in 3.0% extra energy input.

- The potentials for SE_{Ni} and OEE show a stable and repetitive pattern from sequences 5 to 12 when i_{OE} is turned on. The potential difference between SE_{Ni} and OEE is about 0.1 V and increases when i_{TSC} is turned off and decreases when i_{TSC} is turned on, caused by the state of charge and operation mode of the SE. The potential of the OEE vs Hg/HgO is higher when the SE_{Ni} is charging than at times when the SE_{Ni} is discharging even when the charging rate at the OEE is lower.

- The potentials for SE_{Fe} and HEE show a stable and repetitive pattern from sequence 8 to 16 when i_{HE} is turned on. The potential difference between SE_{Fe} and HEE is about 0.1V which increases when i_{TSC} is turned off and decreases when i_{TSC} is turned on caused by the state of charge and the operation mode of the SE_{Fe}. The potential of the HEE vs Hg/HgO is lower when SE_{Fe} is charging than when the SE_{Fe} is discharging even when the charging rate at the HEE is lower.

- Comparing the voltage response of the SE_{Fe} in the charged state during charging (sequence 2 and 8) with sequences following a discharge of the SE_{Fe} (10,12,14 and 16) indicates energy savings during charging with the same rate because the voltage response is higher.

- Comparing the voltage response of the SE_{Ni} in the charged state during charging (sequence 2 and 4) with sequences following a discharge of the SE_{Ni} (6,8,10 and 12) indicates energy savings during charging with the same rate because the voltage response is lower.

- The potential of HEE at rest is higher when i_{TSC} is off compared to when i_{TSC} is on (sequence 3-7), likewise the potential of OEE at rest is lower when i_{TSC} is off compared to when i_{TSC} is on indicating a polarization effect caused by active electrodes.

C.5. Testing 'multi-controlled' electrochemical systems: Testing a two-cell system in series connection with simultaneous operation of 2x3 electrodes

A two-cell system representing a bipolar configuration consisting of one SE_{Fe}, one HEE and one SE_{Ni}, (see Figure C.9) in each cell was assembled to mimic a battolyser with controllable hydrogen production. The integrated battery functionality may balance electricity fluctuations while the added controllable hydrogen output serves the industry for e.g. synthetic H_2-based fuel production. The main power source/sink is connected to SE_{Ni1} and SE_{Fe2}, the circuit is closed with a connection between SE_{Fe1} and SE_{Ni2}. Each HEE is connected via a side-line to its SE_{Fe}.

The test setup demonstrates that the main circuit (with i_{TSC}) operates independently from the separated circuits that control the hydrogen production. Switching the main circuit on/off and reversing the main current flow including rearranging the connections of the main input is feasible without affecting the other controllers (as long as the storage electrode capacities are not depleted). Also the other controllers in this bipolar setup can be individually turned on/off without affecting the other controllers.

The voltage response to the test sequences is displayed in Figure C.10. At the start, the observed voltage is stable, all electrodes were charged prior to testing. With turning on the HEEs, first HEE_1, then HEE_2, the voltage between SE_{Fe} and HEE increases immediately while the voltage between SE_{Ni} and SE_{Fe} drops as the current is shifted from the SEs_{Fe} to the HEEs. Both of these voltage drops are recognizable in the total system voltage. The main power source has to provide less energy because it is effectively operating now to produce oxygen at the SE_{Ni} while its SE_{Fe} is effectively at rest as the current inserted to the SE_{Fe} is simultaneously redirected to the HEE ($i_{Fe} = i_{TSC}$ - $i_{HE} = 0$), so overall the state of charge of the SE_{Fe} does not change, reducing the voltage response. The additional energy to overcome the overpotentials required to produce hydrogen at the HEEs is provided by the current control units to the HEEs. Doubling i_{TSC} (sequence B) results in a voltage increase between SE_{Ni} and SE_{Fe}, as well as the system voltage. The SEs_{Fe} now do start charging while the SEs_{Ni} operate at doubled rate. The SEs_{Fe} and the HEEs operate at the same rate, therefore the potentials of these electrodes align. The main power supply provides the energy for i_{TSC} (the total current at the negative assembly) to overcome the potential difference between SE_{Ni2} and SE_{Fe2}. In sequence C the SEs_{Ni} are not operational, i_{TSC} is zero, power source and power sink are disconnected. SE_{Fe} and HEE operate at the same rate, the SE_{Fe} is discharged while hydrogen is

produced at the HEE.

Sequence D demonstrates simultaneous discharging and hydrogen production, illustrating that a storage electrode can serve two purposes at the same time. Here a LED lamp is used to simulate an electric load. In principle power electronics should therefore allow to create a self-sustaining system with the electricity storage for powering the hydrogen production. The observed voltage between SE_{Ni} and SE_{Fe} as well as the system voltage drop, all storage electrodes are now discharging. The voltage difference between SEs_{Fe} to HEEs increase further, the SEs_{Fe} are now operational at the double discharge rate. After the test sequence, first HEE_1 was turned off, then HEE_2. The voltage between SE_{Fe} and HEE decreases and the voltage between SE_{Ni} and SE_{Fe} as well as the system voltage increase, since SE_{Fe}, powered by the main input, starts operating while the extra energy inputs to power the HEEs stop. The voltage response of the test sequence in the multi-cell system follows the previously anticipated reactions, providing proof that the concept for single-cell multi-controlled electrodes holds for upscaling to multi-cell systems.

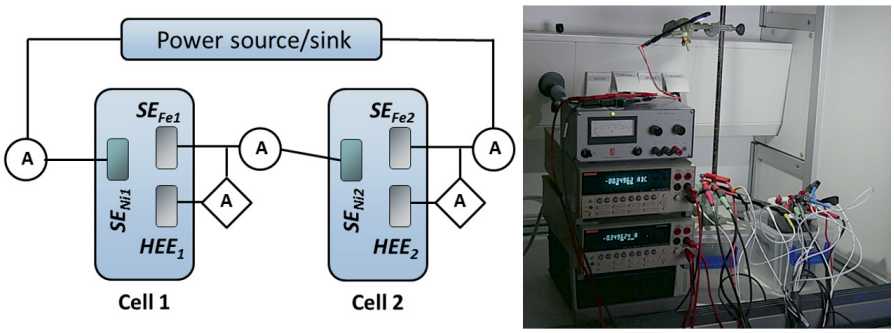

Figure C.9: Testing two cells in a series connection.

(left) Schematic drawing of the multi-cell test-assembly.

(right) Picture of the test assembly.

Note: A conventional DC power source was used to control i_{TSC}. A LED lamp was used as power sink to simulate discharging together with hydrogen production (see sequence D, Figure C.10). Both external devices were disconnected to stop current flow. We rearranged the connections of the main-line while hydrogen production via the side-lines was turned on, without influencing the current flow to the HEEs. All electrode potentials were monitored together with the current flow between the cells and from the cell to the power source/sink.

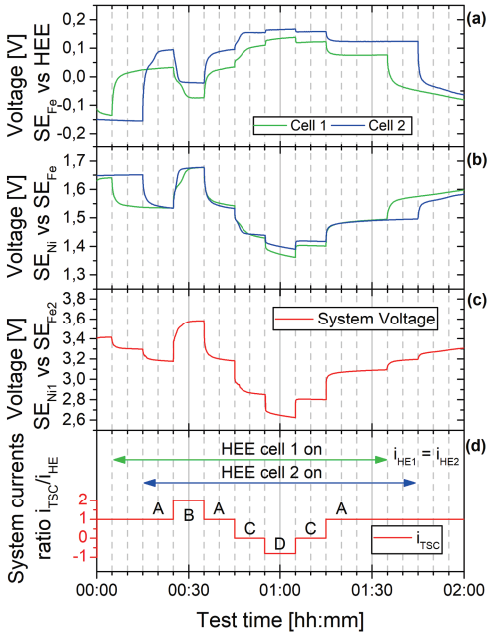

Figure C.10: Voltage response for multi-cell test using two cells in series.

(a) Monitored voltage response between SE_{Fe} and HEE.

(b) Monitored voltage response between SE_{Ni} and SE_{Fe}, the blue and green line show the individual cells.

(c) Monitored voltage response, the red line shows the system response measured between SE_{Ni1} and SE_{Fe2}.

(d) System currents

Test scheme: In the beginning and at the end only i_{TSC} is turned on. After 5' testing, HEE_1 is turned on, thereafter HEE_2. The red line displays the ratio i_{TSC} to i_{HE}. Then i_{TSC} was varied in the sequences A ($i_{TSC} = i_{HE} \Rightarrow SE_{Fe}$ inactive), B ($i_{TSC} = 2 \times i_{HE} \Rightarrow SE_{Fe}$ and HEE operate at the same rate; SE_{Ni} at double rate), C ($i_{TSC} = 0 \Rightarrow SE_{Ni}$ inactive, SE_{Fe} discharged to generate hydrogen at HEE), and D ($i_{TSC} \approx -0.8 i_{HE}$). After returning to sequence A hydrogen production at the HEEs was turned off, first HEE_1, then HEE_2.
Note: In sequence D all SEs are discharged to provide energy for the lamp (,see Figure C.9) and both SE_{FE} additionally serve as storage electrode for hydrogen

production. Hence both SEs_{Fe} simultaneously serve battery discharging and hydrogen production.

C.6. Experimental Methods

Setup:

The setup utilises battolyser-electrodes described in [1] with a 27wt% solution of potassium hydroxide as electrolyte (produced with demineralised water from a Merck Milli-Q® Advantage A10 water purification system and potassium hydroxide flakes from Alfa Aesar, 85%). Tests were performed at room temperature.

Galvanostatic testing:

Simultaneous charging and discharging experiments were programmed on a Parstat multi-channel potentiostat/galvanostat.

Energy efficiency:

The energy efficiency η_{total} for the system can be calculated with the following set of equations (in analogy to [1]). The state of charge of the electrodes is important for the round-trip efficiency of the system. It is important to return to the same state of charge so that the state of charge is equal at the beginning and at the end of one cycle. For the round-trip efficiency of the system it does not matter, whether one starts with charging or discharging. The round-trip efficiency may include many subcycles n before returning to the same state of charge:

$$\eta_{total} = \frac{E_{output}}{E_{input}} \tag{C.7}$$

$$E_{output} = E_{battery} + E_{Hydrogen} \tag{C.8}$$

$$E_{battery} = \sum_{i=1}^{n} \int_{t_{dc,n,start}}^{t_{dc,n,end}} V_{dc,system} i_{dc} dt \tag{C.9}$$

$$E_{hydrogen} = H_{el} \sum_{i=1}^{n} C_{c,n} - C_{dc,n} \tag{C.10}$$

$$E_{input} = E_{main} + E_{HEE} + E_{OEE} \tag{C.11}$$

$$E_{main} = \sum_{i=1}^{n} \int_{t_{c,n,start}}^{t_{c,n,end}} V_{c,system} i_{c} dt \tag{C.12}$$

$$E_{HEE} = \int_0^{end} (V_{SE_{Fe}-V_{HEE}}) i_{HE} dt \tag{C.13}$$

$$E_{OEE} = \int_0^{end} (V_{OEE} - V_{SE_{Ni}}) i_{OE} dt \tag{C.14}$$

Equations are provided for a system consisting of one HEE and one OEE. Multi-cell systems require summation of the energy input from all HEEs and OEEs.

V_c, i_c are the applied experimental cell voltage and current during the charge and electrolysis cycle with duration t_c. V_{dc} and i_{dc} are the experimental discharge voltage and current during the discharge time t_{dc}. I_{HE} and i_{OE} are the currents for controlled hydrogen and oxygen evolution. The energy yield for electrolysis corresponds to the thermo-neutral potential H_{el}. The H_{el} equals 1.48 V at room temperature, while $2eH_{el}$ equals the higher heating value (HHV) of hydrogen of $-286\,\mathrm{kJ\,mol^{-1}}$ H_2.

In [1] we show that the faradaic (or coulombic) efficiency equals 100% within the experimental accuracy of 0.5%. At this 100% faradaic efficiency the total charge C_c inserted in the hybrid hydrogen- electricity storage concept equals the charge used for electrolysis C_{el} plus the integrated discharge current C_{dc}:

$$C_c = \int_0^{t_c} I_c dt = \int_0^{t_c+t_{dc}} I_{el} dt + \int_{t_c}^{t_c+t_{dc}} I_{dc} dt = C_{el} + C_{dc} \tag{C.15}$$

Note that the electrolysis yield at the HEE and at the OEE are not present in the above equation (C.15). I_{HE} and i_{OE} only influence the moment when gas is produced not the gas yield itself because one considers cycles with the same initial and final charge state.

References

[1] F. M. Mulder, B. M. H. Weninger, J. Middelkoop, F. G. B. Ooms, and H. Schreuders, *Efficient electricity storage with a battolyser, an integrated Ni–Fe battery and electrolyser,* Energy & Environmental Science **10**, 756 (2017).

D

Neutron Diffraction Study of a Sintered Iron Electrode In Operando

Supporting Information to Chapter 4

D.1. Extended Experimental Section

D.1.1. Iron Characterization

Reduced metallic iron powder was produced through reduction of hematite in a flow-through reactor. A weight loss of 30% can be expected for full conversion from hematite (Fe_2O_3) to iron. The measured weight loss of 30% points indicates full conversion. The reduced powder used for the production of the electrode was characterized by neutron diffraction. Figure D.1 shows the measured diffraction pattern together with the refined data for iron. Only peaks related to iron are visible, confirming full conversion to iron.

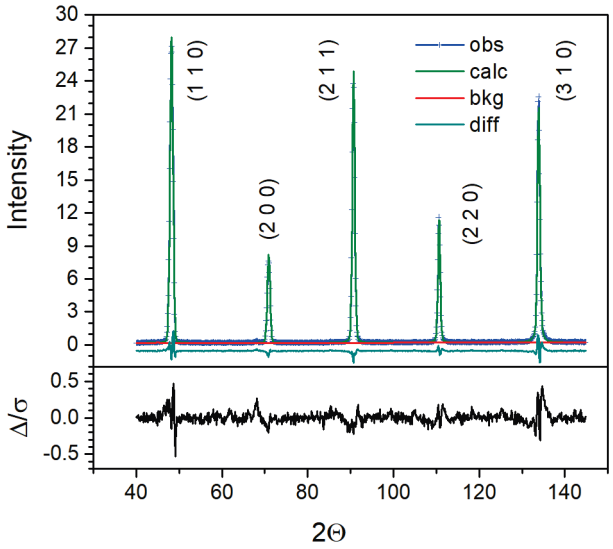

Figure D.1: Top: observed intensities for the reduced iron powder (obs), together with calculated intensities (calc), background (bkg) and difference (diff) curve. Bottom: difference curve divided by the estimated standard deviation for the data points (GSAS-II output).

D.1.2. Electrode Production

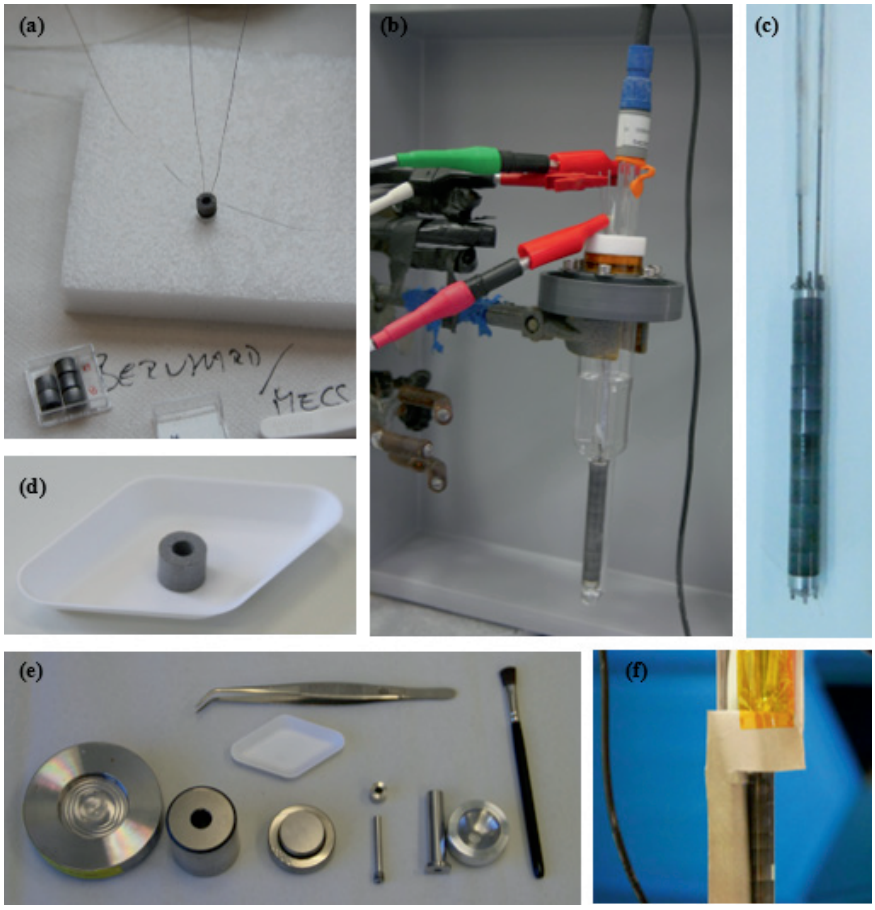

Figure D.2: Electrode production and preliminary electrode testing: (a) assembly of the tubular electrode stack. Four thin Ni-wires (0.25 mm thick) in the center hold the electrode together. They are fixed at both end elements enclosing the twelve individual electrodes. (b) Preliminary testing of the electrode. The setup comprises the tubular iron electrode, the centered nickel wire counter electrode and a Hg/HgO reference electrode which senses the headspace. A capillary at the backside connects the headspace with the bottom of the cell to provide electrolyte. (c) Assembled iron electrode after testing. (d) Tubular electrode after pressing. Inner diameter 3.5 mm, outer diameter 8.0 mm. Sintering causes the electrode to shrink to the reported inner diameters of 3.23 mm and outer diameter of 7.53 mm. (e) 8 mm die set for pressing the electrodes with an extra insert for the tubular shape. (f) Shielding of the capillary, the end elements (stainless steel) and parts of the sample holder during the measurement with Cd-foil to prevent unnecessary reflections and background.

D.1.3. Executed Electrochemical Program

This study contains four electrochemical cycles of discharging and then recharging. In the first two cycles we investigate the phase changes for the first iron discharge plateau. In the first cycle we used a moderate discharge rate of 200 mA. In the second cycle we used a 50% higher discharge rate of 300 mA. Sluggish discharge characteristics are a downside of iron electrodes. In cycles three and four we investigate the phase changes for extended discharging. Our aim is to identify the iron phase of the second iron discharge plateau. Session one (measurements 0-167) consists of: Cycle 1, Cycle 2 and Cycle 3 to a partial recharge to a capacity of 0.323 Ah/g_{Fe}. Session 2 (measurements 192-266) includes the Cycle 4 discharge from a discharge capacity of 0.156 Ah/g_{Fe} to 0.423 Ah/g_{Fe} and the partial recharge to 0.262 Ah/g_{Fe}. The third session (measurement 281-284) consists of the recharge for cycle four from 0.406 Ah/g_{Fe} to 0.454 Ah/g_{Fe}. Figure D.3 shows a timeline of the performed test together with the neutron diffraction measurements. Table D.1 provides an overview of the executed electrochemical program including all rates and capacities. All (re)charges were programmed to slightly overcharge the electrode at a rate of 300 mA. A charge rate of 300 mA is equivalent to 46.6 mA/g_{Fe} or to a current density of 46.3 mA/cm^2 at the inner circumference of the tube iron electrode. The corresponding current density at the outer circumference of the counter electrode is twice as high, 92.6 mA/cm^2.

	Discharge rate	Discharge to capacity	Charge capacity	Session
Cycle 1	200 mA	0.214 Ah/g_{Fe}	0.228 Ah/g_{Fe}	1
Cycle 2	300 mA	0.192 Ah/g_{Fe}	0.228 Ah/g_{Fe}	1
Cycle 3	200 mA	0.320 Ah/g_{Fe}	0.419 Ah/g_{Fe}	1: until a charge capacity of 0.323 Ah/g_{Fe}
	100 mA	0.335 Ah/g_{Fe}		
Cycle 4	300 mA	0.156 Ah/g_{Fe}	0.454 Ah/g_{Fe}	2: starting with discharging at discharge capacity of 0.156 Ah/g_{Fe} to charging up to a capacity of 0.262 Ah/g_{Fe}. 3: recharging from 0.406 Ah/g_{Fe} to 0.454 Ah/g_{Fe}
	200 mA	0.277 Ah/g_{Fe}		
	150 mA	0.332 Ah/g_{Fe}		
	100 mA	0.423 Ah/g_{Fe}		

Table D.1: Executed electrochemical program

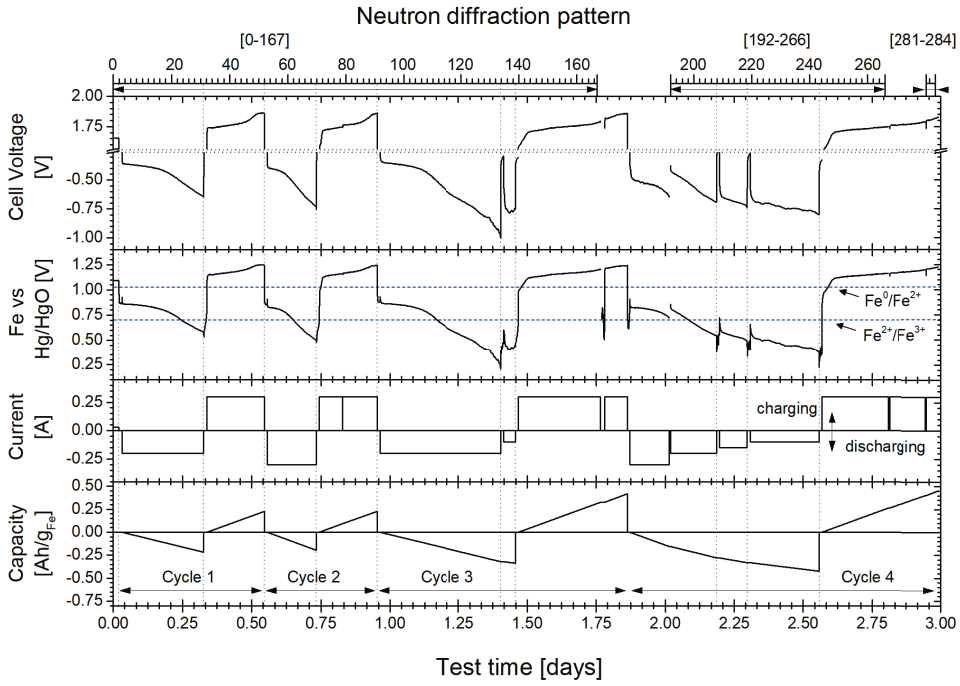

Figure D.3: Executed test program with programmed test current [A] (negative sign discharging, positive sign charging) together with observed cell voltage [V], the voltage of the iron electrode relative to a Hg/HgO reference electrode [V] with inverted sign, and the calculated (dis)charge capacity [Ah/g_{Fe}]. Top: numbering of the neutron diffraction measurements; the tick marks indicate the start of a measurement.

D.1.4. Iron Oxide/Hydroxide Simulation

Figure D.4 shows on top the observed measurement data for the most discharged sample and below simulations for various iron oxides and (oxy)hydroxides. The simulations were performed with GSAS-II [1]. Table D.2 depicts the used CIF files with their structural data used for the simulation, downloaded from the Crystallographic database [2–7]. Figure D.4 illustrates that none of the simulated iron oxides has a characteristic pattern the matches the main three peaks identified for the second iron discharge plateau.

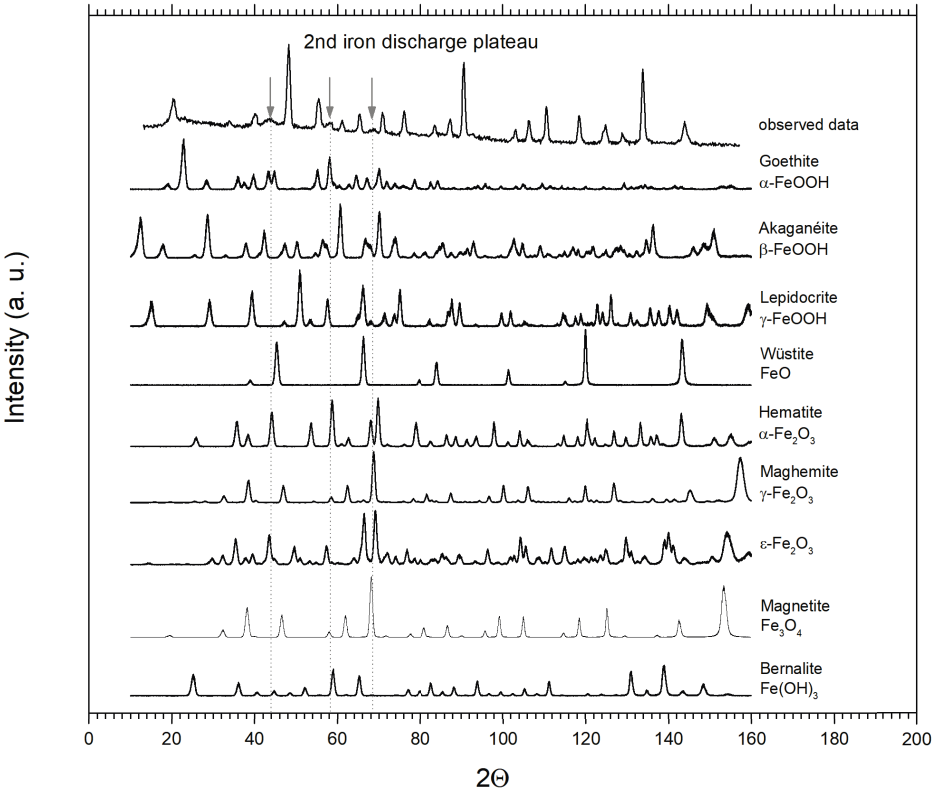

Figure D.4: Top: observed diffraction data for the most discharged state. Below: in descending order simulated neutron diffraction data for: α-, β-, γ-FeOOH, FeO, α-, γ-, ϵ-Fe_2O_3, Fe_3O_4, and $Fe(OH)_3$.

Compound	CIF file	Structure
Magnetite, Fe_3O_4	9002316	$Fd\bar{3}m$; a = 8.3965 Å;
Goethite, α-$FeOOH$	9002158	$Pnma$; a = 9.9134 Å, b = 3.0128 Å, c = 4.58 Å
Akaganéite, β-$FeOOH$	1531989	$I12/m1$; a = 10.587 Å; b = 3.0311 Å, c = 10.515 Å
Lepidocrocite, γ-$FeOOH$	9009154	$Bbmm$; a = 12.4 Å, b = 3.87 Å, c = 3.06 Å
Wüstite, FeO	1011198	$Fm\bar{3}m$; a = 4.303 Å
Hematite, α-Fe_2O_3	2101167	$R\bar{3}c$; a = 5.0355 Å; c = 13.7471 Å
Maghemite, β-Fe_2O_3	9012692	$P4_32_12$; a = b = 8.3396 Å, c = 8.322 Å
ϵ-Fe_2O_3	4002383	$Pna2_1$; a = 5.085 Å, b = 8.774 Å, c = 9.468 Å
Bernalite, $Fe(OH)_3$	9016365	$Immm$; a = 7.544 Å, b = 7.560 Å, c = 7.558 Å

Table D.2: CIF-files and structure data for simulated iron oxides and (oxy)hydroxides

D.1.5. Rietveld Refinement of the Most Discharged Stage

Figure D.5 shows on top the observed measurement data for the most discharged sample and below simulations for the identified and refined phases: iron, iron hydroxide, iron oxyhydroxide, and nickel. Table D.3 provides the refined structural parameters belonging to the Rietveld refinement. The data residuals wR result in 0.910% on 1366 observations, and $\chi^2 = 1.6$.

Compound	Iron	Iron hydroxide	Iron oxyhydroxide	Nickel
space group	$Im\bar{3}m$ no. 229	$P\bar{3}m1$ no. 164	$P\bar{3}m1$ no. 164	$Fm\bar{3}m$ no. 225
lattice parameters	a = 2.866 Å	a = 3.267 Å c = 4.601 Å	a = 2.956 Å c = 4.590 Å	a = 3.526 Å
atom site in Wyckoff notation*	Fe: 2a (0,0,0)	Fe: 1a (0,0,0) O: 2d (1/3,2/3,0.223) H: 2d (1/3,2/3,0.423)	Fe_1: 1a (0,0,0) Fe_2: 1b (0,0,1/2) O: 2d (1/3,2/3,1/4) H_1: 2d (1/3,2/3,0.46) H_2: 2d (1/3,2/3,0.04) H_3: 2d (1/3,2/3,-1/8) H_4: 2d (1/3,2/3,5/8)	Ni: 4a (0,0,0)
occupancy	Fe: 1.000	Fe: 1.000 O: 1.000 H: 0.881	Fe_1, Fe_2: 0.5 O: 1.000 H_1, H_2, H_3, H_4: 0.125	Ni: 1.000
size (μm)	0.175	0.1	0.0226	1
micostrain	821	3000	42148	2000
Unweighted phase residuals (GSAS-II output)	RF^2: 4.482% RF: 1.560%	RF^2: 4.387% RF: 1.972	RF^2: 9.232% RF: 3.571%	RF^2: 8.785 RF: 3.024

*) Wyckoff positions are retrieved from Bilbao Crystallographic server [8]

Table D.3: Structural parameters of the refined phases

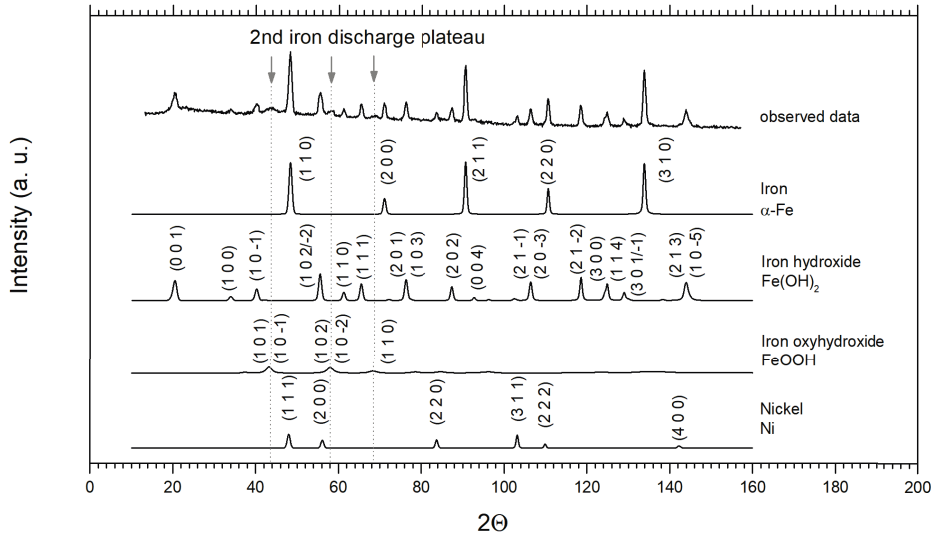

Figure D.5: Top: observed diffraction data for the most discharged state. Below: simulated diffraction pattern for the identified compounds iron, iron hydroxide, iron oxyhydroxide, and nickel of the refined structure.

D.1.6. Calculation of Volumetric Hydrogen Content.

The following section provides calculations concerning the expected hydrogen content. First the hydrogen content of compounds is calculated, see table D.4. With changing state of charge the composition changes. The composition change causes the porosity to change and with it the volume available for electrolyte.

Compound	Density $[g/cm^3]$	Molar weight $[g/mol]$	Compound content $[mol/cm^3]$	Hydrogen content* $[mol\ H/cm^3]$
Fe	7.874	55.845	0.141	-
$Fe(OH)_2$	3.4	89.859	0.0378	0.0756
H_2O at 25°	0.997	18.015	0.0553	0.111
KOH		56.106		
Electrolyte: 25 wt% KOH solution at 25°	1.234	-	H_2O: 0.0514 KOH: 0.0055	0.108

*) The volumetric hydrogen content is calculated by dividing the density by molar weight and by multiplication with the number of hydrogen atoms. Concerning electrolyte: the hydrogen content is calculated by splitting up the density to 75% Water and 25% KOH. The sum of both is depicted in the table above. Note, there is hardly any variation in hydrogen content between water and electrolyte (25wt% KOH electrolyte).

Table D.4: Calculated volumetric hydrogen densities

Table D.4 indicates that the density of iron is higher than the density of iron hydroxide. In the case of iron hydroxide 0.0378 moles are present per cm^3, in the case of iron 0.141 moles. The reduction of 1 cm^3 of iron hydroxide to iron will create a free space of 0.732 cm^3 (=1-0.0378/0.141) which will be filled with electrolyte. In the case that 100 % iron hydroxide will be converted to iron, the volume will contain 0.0756 molH/cm^3 before conversion, and will contain 0.079 molH/cm^3 (=0.732 x 0.108 molH/cm^3) after conversion to iron. Hence, the background will slightly increase with charging and decrease with discharging.

The following calculation is based on the initial porosity of 64.3%, of the sample. 35.7% of the sample volume is occupied by iron and equal to an iron fraction of 1. The volumetric ratio of iron hydroxide to iron is: 3.73 (=0.141/0.0378).

Table D.5 depicts the calculated relative hydrogen content for the transitions to charging. During the first transition (measurements 31-35) a reduction of background of 5.7% may be expected, during the second transition (measurements 70-73) a reduction of 5.4%. The transitions around measurements 148-154 and 257-264 represent the zone where the fractions of iron and iron hydroxide increase together. A reduction of background occurs here too, in the first transition around 3.3%, in the second transition around 4.7%.

Spectrum	Fraction Fe [-]	Fraction $Fe(OH)_2$ [-]	Space Fe [-]	Space $Fe(OH)_2$ [-]	Free space* [-]	Hydrogen content [-]
31	0.423	0.360	0.151	0.479	0.370	0.0762
35	0.497	0.394	0.177	0.524	0.298	0.0719
70	0.439	0.365	0.157	0.486	0.357	0.0753
73	0.490	0.413	0.175	0.550	0.275	0.0713
148	0.429	0.367	0.153	0.489	0.358	0.0756
154	0.478	0.381	0.171	0.507	0.322	0.0731
257	0.435	0.312	0.155	0.416	0.429	0.0778
264	0.485	0.352	0.173	0.469	0.358	0.0741

*) The calculation is based on the assumption that the free space is filled with electrolyte with its belonging hydrogen content.

Table D.5: Calculated relative hydrogen content for the transition to charging

Table D.6 depicts the calculated relative hydrogen content for the transitions to discharging, during the first transition (measurements 1-6) an increase of background of 2.9% may be expected, in the second transition (measurements 51-55) an increase of 3.5% and in the third transition (measurements 90-95) an increase of 3.8%.

Spectrum	Fraction Fe [-]	Fraction $Fe(OH)_2$ [-]	Space Fe [-]	Space $Fe(OH)_2$ [-]	Free space* [-]	Hydrogen content [-]
1	0.678	0.238	0.242	0.317	0.441	0.0716
6	0.617	0.243	0.220	0.323	0.456	0.0737
51	0.674	0.283	0.241	0.376	0.383	0.0698
55	0.608	0.283	0.217	0.377	0.406	0.0724
90	0.674	0.285	0.241	0.380	0.380	0.0697
95	0.602	0.285	0.215	0.379	0.406	0.0725

*) The calculation is based on the assumption that the free space is filled with electrolyte with its belonging hydrogen content.

Table D.6: Calculated relative hydrogen content for the transition to discharging

The detector counts include the reflections associated with the phase fractions and the incoherent background caused by the samples holder. The distinction in detector counts, which part counts to coherent scattering and incoherent sample holder background and which part counts to hydrogen content is not included in the calculation, hence the previously reported hydrogen related changes form an upper limit for the observed changes. The observed changes are below the calculated changes.

D.2. Results

The following results will be clustered into: (1) Start of Discharging from a Charged Electrode, (2) Steady-state Discharging at the First Plateau (3) Charging a Discharged Electrode from the First Discharge Plateau and (4) The Second Iron Discharge Plateau.

D.2.1. Start of Discharging from a Charged Electrode

The executed program contains four transitions from charging to discharging. Three of them were observed by neutron diffraction: (1) from initial floating charge to discharging at 200 mA at the start, (2) from charging at 300 mA to discharging at 300 mA around pattern 52 and (3) the transition from charging at 300 mA to discharging at 200 mA around pattern 91. Patterns 2, 52 and 91 are rest steps, before charging is programmed, thereafter discharging. Figure D.6 shows a magnification of the areas of interest. General trends described as gradients and detector count changes can also be seen in Figure 4.6 (Chapter 4).

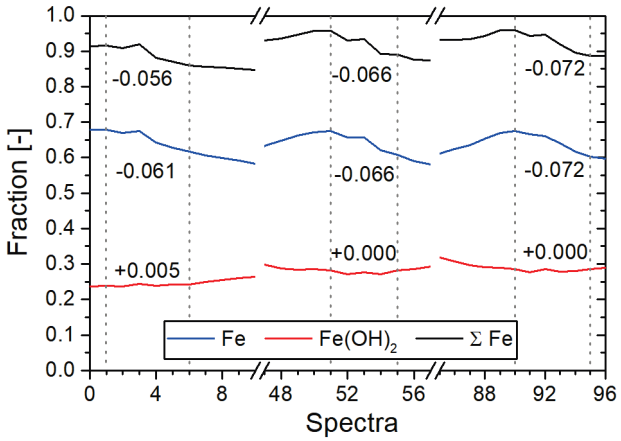

Figure D.6: Derived normalized molar fractions for the transition from charging to discharging. The change in iron fractions is evaluated between measurements [1-6], [51-55] and [90-95], starting one measurement before rest and ending when steady state rates are reached.

The measured total amount of iron decreases during these transitions between 5.6% and 7.2%, as shown. The decrease is caused by the diminishing of the iron metal fraction, which is about twice as high as expected from stoichiometric electrochemical reactions. This iron decrease is not matched by a

corresponding increase of the iron hydroxide fraction. The iron hydroxide fraction shows very little change. The transition is accompanied by an increase of detector counts of about 2%, evaluated after rest between pattern [3-6], [53-55], and [93-96].

D.2.2. Steady Gradients for the First Discharge Plateau

Steady state gradients for a discharge rate of 200 mA can be evaluated between pattern [6-29/30], [95/94-117/118] and between [192-204/202], for a discharge rate of 300 mA between pattern [54-68]. Table D.7 provides the derived gradients including the deviations from the expected values. The calculated gradients are included in Figure 4.6, see index linear fit.

Fractional change/ rate and pattern	Fe [-/h]/[%]	$Fe(OH)_2$ [-/h]/[%]
200 mA [6-30/29]	-0.0299/-5.6	0.0214/-32.3
300 mA [54-68]	-0.0486/+2.2	0.0289/-39.1
200 mA [95/94–117/118]	-0.0288/-9.2	0.0204/-35.7
200 mA [192-204/202]	-0.0231/-27.2	0.0235/-25.7

Table D.7: Evaluated fractional change for discharging the iron electrode, absolute [-/h] and relative [%] compared to a two-electron exchange process.
(Values between square brackets evaluated pattern; before hyphen: starting pattern, after: end pattern; if slash present: before slash: iron, after: iron hydroxide.)

The calculated fractional changes for iron are in good agreement with the expected charges from electrochemical calculations for a two-electron process. At a rate of 200 mA, the change is the 5.6% too slow in cycle 1 and 9.2% too slow in cycle 2. At a rate of 300 mA, the derived change is 2.2% faster than expected. The rates of iron hydroxide formation are about 35% slower than calculated for a two-electron process. The bottom row represents values with starting pattern 192, the first pattern of the second long measurement which starts with a partially discharged electrode. Here both rates are approximately equal, and both are about 25% slower than expected for a two-electron process.

D.2.3. Charging from the First Discharge Plateau

The transition from discharging to charging at the first plateau can be seen around pattern 31 and 70, with a rest period before charging. In both cases the charging current was 300 mA. The discharging current was set to 200 mA in the first cycle and to 300 mA at the second cycle. Figure D.7 shows the derived fractions for iron and iron hydroxide for this transition zone.

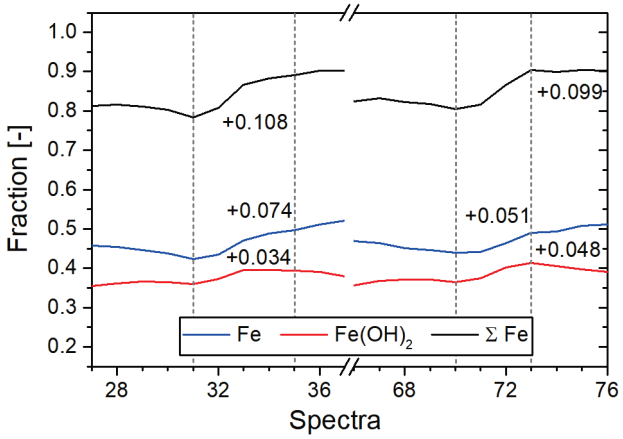

Figure D.7: Derived normalized molar fractions for the transition from discharging to charging. The change in iron fractions is evaluated between pattern [31-35], and [70-73], starting with the patterns at rest and ending were steady gradients occur.

The iron hydroxide fraction has a local maximum at patterns 29 and 68. Both measurements are before the rest period. We see a local minimum at the rest period. With charging immediately after the rest period, a significant increase of iron hydroxide is measured. In the first transition we saw +3.4%, in the second transition we saw +4.8%. This is surprising, as the fraction of iron hydroxide is expected to decrease while charging. Constant decreasing gradients can be observed later on, starting with pattern 36 and 73.

At the same time as the increase in iron hydroxide, we observe a substantial increase of the iron fraction. In the first transition the increase was +7.4%, and in the second transition it was +5.1%. In both cases, the determined change is more than twice as high as the change of about 0.8% per measurement that was expected based on the applied electrochemical rate. From pattern 34 and 73 on continuous gradients are observed.

The total amount of detected iron increases with 10.8%, and 9.9%, respectively. This substantial increase is accompanied by a decrease in detector counts of 3% during the first transition, and 4% during the second transition.

After this initial decrease in background, only linear changes in fractions were observed. Table D.8 shows the derived fractional changes for charging the iron electrode. Interestingly, two gradients concerning the iron fraction can be derived. The first gradient lags behind the expected phase change, by 5.8% and 22.9%. The second gradient, towards the end of the charging cycle, exceeds predicted values by +8.0%, and +16.4%.

Fractional change/ rate and pattern	Fe [-/h]/[%]	$Fe(OH)_2$ [-/h]/[%]
300 mA [34/36–47/49]	0.0448/-5.8	-0.0331/-30.2
300 mA [47-50]	0.0513/+8.0	
300 mA [73-82/88]	0.0366/-22.9	-0.0329/-30.8
300 mA [82-89]	0.0553/+16.4	
300 mA [281-284]	0.0507/+6.7	-0.0274/-42.4

Table D.8: . Evaluated fractional change for charging the iron storage electrode, absolute [-/h] and relative [%] compared to a two-electron exchange process.
(Values between square brackets evaluated pattern; before hyphen: starting pattern, after: end pattern; if slash present: before slash: iron, after: iron hydroxide.)

The increase in iron fraction fades out at the end of the charging process (see Figure 4.6 and 4.7). At the end of charging, the voltage reaches a stable value. This indicates that hydrogen formation has become the dominant process, see Figure D.3.

For iron hydroxide, one gradient can be derived for each charge cycle. In both cases the expected fractional change lags behind, the expected change for a two-electron process at the applied rate, by 30.2% and 30.8% respectively. The decrease of the iron hydroxide fraction nearly stops towards the end of the charging process, in both cases three pattern, pattern 49 and 88 before the rest steps, pattern 52 and 91 respectively (see Figure 4.6 and 4.7).

The final patterns, 281 to 284, show the charging process close to hydrogen evolution, however, no stable voltage is reached yet. The derived rates are in line with previous observations, the increase in iron fraction is 6.7% above expectation while iron hydroxide stays behind by 42.4%.

The voltage profile, Figure 4.6 and Figure D.3, shows a similar behaviour during the charging process. First a steep increase is seen, followed by a steady voltage increase. Towards the end of the charging process the voltage increases again, and then finally flattens out.

D.2.4. The Second Iron Discharge-Plateau

FeOOH is detected in measurements 119-149 and 203-257. Outside these boundaries, the detected fraction of FeOOH seems more like noise. It can be observed that the amount of iron remains constant while FeOOH is present, so iron is inactive/passivated at this stage. With the start of the formation of FeOOH, iron hydroxide is at the maximum of a broad peak, showing a transition zone of roughly 6 measurements or about 1.5 hours of discharge time.

During the second discharge plateau, the decrease of the iron hydroxide phase fraction is steadily increasing, see Figure 4.6. Table D.9 provides an overview of the average fractional decrease during the applied different discharge rates, as well as the rate at the beginning and at the end of each rate step.

Fractional change/ rate and pattern	Begin [-/h]/[%]	Average [-/h]/[%]	End [-/h]/[%]
200 mA [124-133]	-0.0260 / -58.9	-0.0317 / -50.0	-0.0444 / -29.9
100 mA [135-138]		-0.0189 / -40.3	
150 mA [209-218]	-0.0101 / -78.7	-0.0182 / -61.6	-0.0279 / -41.3
100 mA [220-242]	-0.0179 / -43.3	-0.0246 / -22.3	-0.0312 / -1.6

Table D.9: Evaluated fractional change for $Fe(OH)_2$ while discharging the iron storage electrode, absolute [-/h] and relative [%] compared to a one-electron exchange process. (Values between square brackets evaluated pattern; before hyphen: starting pattern, after: end pattern.)

The table above indicates that the derived rates are lower than expected. Only at the end of the last discharge step is the decrease of $Fe(OH)_2$ as fast as expected. The steady increase in curvature makes the fractional changes derived for the second discharge, at a discharge current of 100 mA, exceed the fractional changes derived for a discharge current of 150 mA. Because of this, the deviation from expectations is reduced by about 40% points.

The derived fractional changes for the formation and the reduction of FeOOH are delayed compared to the calculated values for a one-electron exchange process, see Table D.10. During the second deep discharge, the rates are in better agreement, for formation they are 30.2% too low, and for the reduction 20.4% too low. The rates for the formation of $Fe(OH)_2$ are even slower, in both cases about 60% too low.

Both phases, FeOOH and $Fe(OH)_2$ show a clear transition point when switching from discharging to charging. With additional charging FeOOH disappears and then the iron fraction starts increasing. Remarkably, both phases, Fe and $Fe(OH)_2$ increase then simultaneously, during the first deep discharge for about 5 patterns, during the second deep discharge for about 7 patterns. So conversion of Fe^{2+} to Fe and conversion of Fe^{3+} to $Fe(OH)_2$ take place. Notably, during

Fractional change/ rate and pattern	$FeOOH$ [-/h]/[%]	$Fe(OH)_2$ [-/h]/[%]
200 mA [120-134]	-0.0315/-50.3	
100 mA [135-140]	-0.0124/-61.0	
300 mA [140/141-149/148]	0.0631/-33.6	-0.0378/-60.2
100 mA [208-245]	-0.0221/-30.2	
300 mA [245-257]	0.0756/-20.4	-0.0376/-60.4

Table D.10: Evaluated fractional change during examination of the second iron discharge plateau, absolute [-/h] and relative [%] compared to a one-electron exchange process.
(Values between square brackets evaluated pattern; before hyphen: starting pattern, after: end pattern; if slash present: before slash: iron oxyhydroxide, after: iron hydroxide.)

patterns 258 and 262 we have close to perfect agreement, between measured fractional change and electrochemical charge input when assigning 66% of the charge contribute the formation of Fe in a two-electron process and 29% of the charge to the formation of $Fe(OH)_2$ in a one-electron process.

This increase in crystalline iron content can be seen in Figure 4.6, the middle of which shows the total detectable (crystalline) iron content. The iron content stays constant within the model including FeOOH during deep discharging. So the decrease in $Fe(OH)_2$ is compensated by the formation of FeOOH. On charging, the decrease of FeOOH is faster than the increase in $Fe(OH)_2$, so the total detectable iron content drops, by about 4% and 7%, respectively for the first and second deep discharge. The total detectable iron content reaches a minimum when FeOOH disappears. With further charging the measureable crystalline iron content increases by about 10% until measurement 167 after for the first deep discharge, and by about 13% until measurement 284 after the second deep discharge.

D.2.5. Correlation between Phase Precipitation and Detector Counts

The mechanism of phase precipitation and dissolution may explain the massive changes in the transition zones. At the start of the discharge period, a substantial amount of crystalline iron disappears while no detectable iron hydroxide is formed. The porosity inside the electrode increases, and with it, the amount of electrolyte inside of the electrode. The calculation indicates an increase in hydrogen content inside the sample for these three transitions of: +2.9% for pattern 1-6; +3.5% for pattern 51-55; and +3.8% for pat-tern 90-95. At the start of charging, a substantial amount of iron and iron hydroxide forms and the porosity inside the sample decreases, and with it, the amount of electrolyte

in the electrode. The calculation indicates a decrease in hydrogen content of: -5.7% for pattern 31-35; and -5.4% for pattern 70-73. A substantial decrease in counts, but with a wider spread, can be observed the two times when both iron and iron hydroxide fractions increase simultaneously, after iron oxyhydroxide has disappeared. In the first case, pattern 148-154, the calculation indicates a decrease of 3.3% of hydrogen content, in the second case, pattern 257-264, a decrease of 4.7%. Hence, it is likely that, here too, phase precipitation causes electrolyte displacement as well as a reduction of observed detector counts. The speed of change for the detector counts is correlated with the speed of phase precipitation/dissolution.

D.3. Discussion

D.3.1. Correlation Fractional Phase Changes - Detector Counts

In the regions just after the transitions from charge to discharge or discharge to charge one observes larger/lower changes than can be justified from the electrochemical conversion of solid phases. This may indicate that the screening of the sample by the incoherent scattering of hydrogen varies sufficiently to have an impact on the measured diffraction patterns. The most straightforward explanation would be that the electrolyte content inside the observed sample varies, and that the electrolyte that flows in the beam then screens part of the diffraction intensities.

We have several options to check whether varying hydrogen concentration correlates with diffraction intensities:

1. Figure 4.8 shows phase changes and detector counts during discharging. In the transition zone, the detector counts increase by about 1.5% points. During this same period, metallic iron content decreases too fast and the iron hydroxide content remains stable. This could indicate a correlation. However, on continued discharging, the detector count during C1 increases by an additional 4.5% points. Likewise, during C2 the total counts increased by an additional 3.5% points before they flattened out, without any correlation. It seems unlikely that a change of 1.5% causes correlation while a change of 4.5% does not.

2. Figure 4.9 shows phase changes and detector counts during charging. In the transition zone the detector counts decrease with 2% (C1) and 5% (C2) until they reach stable values while metallic iron and iron hydroxide increase. In the case of C1 it requires one measurement until the detector counts stabilize while it takes 4 measurements until the iron hydroxide

fraction starts declining. In the case of C2 it takes two measurements until iron hydroxide starts declining while it takes four measurements until the detector count stabilized. At the end of charging, the detector counts for C1 decease by another 2% while they hardly decrease for C2. Both charging periods show similar behavior for the metallic iron and the iron hydroxide fraction. No clear correlation between detector counts and fractional change can be determined.

3. A widely distributed decrease in counts is seen while recharging from the second iron plateau, after measurements 148 and 257. Figure 4.6 and Figure 4.10 show steady gradients for metallic iron and iron hydroxide. Both measurements show the same pattern of behavior: After FeOOH has vanished, both the iron and the iron hydroxide phases are increasing at the same time. The detector counts stabilize when iron hydroxide starts decreasing. Here it is likely that the change in porosity caused by solid phase precipitation reduces the hydrogen content. However, it is unlikely that the change in background affects the steadily changing phase fractions.

4. Figure D.8 depicts the observed intensities for patterns 71 to 73. These were the three measurements where the highest reduction of detector counts was observed. Slightly increasing intensities for iron and iron hydroxide were observed, consistent with the notion of both amorphous $Fe^{2+}(OH)_2$ and amorphous $Fe^{3+}OOH$ being reduced forming crystalline Fe and $Fe(OH)_2$ respectively, while the background - together with the two Ni reflections - substantially decreases. The insert shows the data with the background subtracted, confirming an increase of the intensities of metallic iron and iron hydroxide while the intensities for nickel remain stable.

We conclude that correlation between the changes in the phase fractions and detector counts exists when changes in the detector counts can be expected due to phase precipitation. No correlation is present when changes in detector counts occur due to gas accumulation/release. Hence, it is unlikely that changes in the background intensities affect the sample screening.

Even with correlation, the main findings of current work would not change: the high amount of iron hydroxide is already high initially, and accumulates further upon first plateau operation; the absence of substantial amounts of crystalline iron phases indicates the presence of iron in an amorphous phase; simultaneous precipitation of metallic iron and iron hydroxide occurs, indicating the presence of an amorphous iron (II) phase and an amorphous iron (III)

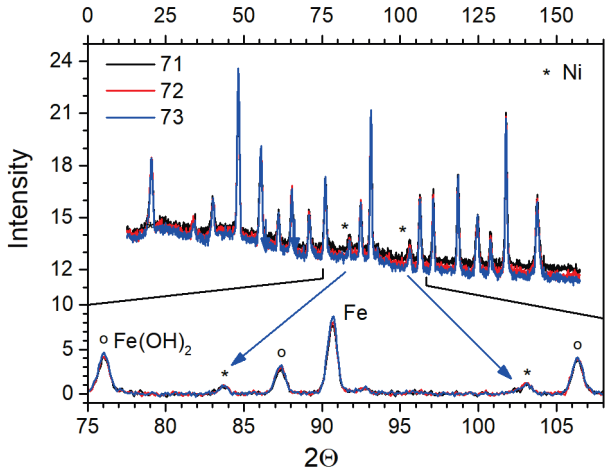

Figure D.8: Top: observed stable intensities with decreasing background for pattern 71-73 (the first three charging pattern after rest). The two Ni dominated reflections are marked with a * and shift together with the background. Bottom: magnification for a 2Θ range from 75 to 108 degrees, data with the background subtracted.

phase; and the identification of δ-FeOOH as iron phase for the second discharge plateau.

References

[1] B. H. Toby and R. B. Von Dreele, *GSAS-II: the genesis of a modern open-source all purpose crystallography software package,* Journal of Applied Crystallography **46**, 544 (2013).

[2] M. Quirós, S. Gražulis, S. Girdzijauskaitė, A. Merkys, and A. Vaitkus, *Using SMILES strings for the description of chemical connectivity in the Crystallography Open Database,* Journal of Cheminformatics **10**, 23 (2018).

[3] S. Gražulis, D. Chateigner, R. T. Downs, A. F. T. Yokochi, M. Quirós, L. Lutterotti, E. Manakova, J. Butkus, P. Moeck, and A. Le Bail, *Crystallography open database–an open-access collection of crystal structures,* Journal of applied crystallography **42**, 726 (2009).

[4] S. Gražulis, A. Daškevič, A. Merkys, D. Chateigner, L. Lutterotti, M. Quiros, N. R. Serebryanaya, P. Moeck, R. T. Downs, and A. Le Bail, *Crystallography Open Database (COD): an open-access collection of crystal structures*

and platform for world-wide collaboration, Nucleic acids research **40**, D420 (2012).

[5] S. Gražulis, A. Merkys, A. Vaitkus, and M. Okulič-Kazarinas, *Computing stoichiometric molecular composition from crystal structures,* Journal of Applied Crystallography **48**, 85 (2015).

[6] A. Merkys, A. Vaitkus, J. Butkus, M. Okulič-Kazarinas, V. Kairys, and S. Gražulis, *COD:: CIF:: Parser: an error-correcting CIF parser for the Perl language,* Journal of Applied Crystallography **49**, 292 (2016).

[7] R. T. Downs and M. Hall-Wallace, *The American Mineralogist crystal structure database,* American Mineralogist **88**, 247 (2003).

[8] M. I. Aroyo, J. M. Perez-Mato, C. Capillas, E. Kroumova, S. Ivantchev, G. Madariaga, A. Kirov, and H. Wondratschek, *Bilbao Crystallographic Server: I. Databases and crystallographic computing programs,* Zeitschrift für Kristallographie-Crystalline Materials **221**, 15 (2006).

E

Iron electrodes with Al/Zr doping for large- and small-scale energy storage and hydrogen production

Supporting Information to Chapter 5

E.1. Extended Experimental Section

E.1.1. Test setup

One test cell consist of an iron electrode and a nickel-mesh counter electrode. For some tests a H_2 reference electrode (Hydroflex® from Gaskatel) is added to the test setup. Each electrode is enclosed at the side face and the back side with a Ni-foil and placed into a 3D printed sample holder to shield the electrode and to allow electrolyte access only from the front side of the electrode, see Figure E.1. The diameter of the recess at the front of the 3D printed sample holder is designed as a support for the electrode and is printed 1 mm smaller than the diameter of the electrode. Thus, the effective exchange surface area is smaller than the reported surface area. However, all reported values refer to the electrode dimension (see table E.1. Ni-wires encapsulated with PTFE heat shrink are used as connectors and to transmit the current. An additional Ni-wire is attached through a fitting to the backside of the iron electrode to record the voltage. The Ni-mesh counter electrode is placed opposite the iron electrode with a fixed spacing of 3 mm. The Ni-mesh counter electrode was provided by the Dexmet Corporation, product code 4Ni(899L)10-125A. We use a 25wt% KOH solution without additives.

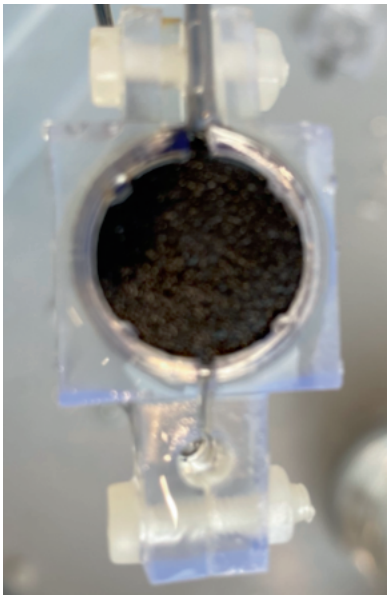

Figure E.1: Test setup. Iron electrode enclosed with Ni-foil inside a 3D printed sample holder.

Note to table 5.1, 1st plateau storage density of iron electrodes: Iron electrodes are mostly placed and tested in between counter electrodes, for instance, in between air electrodes in iron-air test cells. The current density the iron-electrode experiences is twice as high as the current density the air electrode experiences. For an explicit description of the setup we added sides to table 5.1 to report the number of accessible surfaces of evaluated electrodes and we relate the retrieved current density to the accessible surface area. (The tested NiFe pocket electrode is an exemption, here the counter electrode was placed on one side without shielding the backside. Here it may be assumed that most of the charge accesses the electrode through this side since the electrode is large and the electrolyte path around the electrode is long. This assumption rather enhances then worsens the derived capacities for the pocket electrodes.)

E.1.2. Iron electrodes

The iron electrodes we produced have a sample weight of about 0.8 g and a surface area of about 1.5 cm^2 after sintering, details see Table E.1. Table E.1 further contains the sintering temperature and the measured BET surface area of these electrodes.

	Unit	pure iron	pure iron	iron with Al	iron with Zr
Pore former		–	x	x	x
Weight	g	0.797	0.815	0.791	0.805
Thickness	cm	0.162	0.206	0.205	0.207
Surface area	cm^2	1.496	1.517	1.431	1.453
relative to 1.5	-	1	0.99	1.05	1.07
Porosity	%	58.1	66.8	65.7	65.9
Sintering temperature	°C	750	750	850	800
BET surface area	m^2/g	0.65	0.65	5.0	2.5

Table E.1: Characteristics of the iron electrodes

We used Ammonium carbonate, Puratronic®, 99.999% (metals basis) from Alfa Aesar as pore former in amount of 0.136 g pore former per gram of iron. We slightly ball-milled and sieved (-325 mesh; 42 micron particle size) the pore former before addition. Only the smaller fraction was used. Note, ball milled pore former evaporates easily. Therefore the steps mixing, electrode pressing and sintering should advance without intermediate storage.

E.1.3. Electrochemical measurements

Charging and discharging experiments were executed with a Maccor Series 4000 multifunction battery test system. Galvanostatic tests were conducted with current settings of multiples of 15 mA for charging and discharging. A current of

15 mA corresponds to approximately 10 mA/cm^2, the exact corresponding current densities can be calculated by dividing the current settings by the electrode specific surface areas. For the charging the current density is varied between 10-60 mA/cm^2 and for discharging between 10-25 mA/cm^2. To increase the readability rounded values are reported in the main document. Table E.2 shows the current settings together with approximate values for the current density and the exact values for both doped samples.

Current setting	mA	15	22.5	30	37.5	45	60	75	90
Reported current density	mA/cm^2	10	15	20	25	30	40	50	60
Current density Al-sample	mA/cm^2	10.5	15.8	21	26.3	31.5	42	52.5	63
Current density Zr-sample	mA/cm^2	10.3	15.5	20.6	25.8	30.9	41.2	51.5	61.8

Table E.2: Applied current settings and derived current densities

The same principle was used for the inserted capacities. The reported capacities of 160 mAh/cm^2 and 200 mAh/cm^2 correspond to the values of 168 mAh/cm^2 and 210 mAh/cm^2 for the Al-doped sample and to 165 mAh/cm^2 and 206 mAh/cm^2 for the Zr-doped sample. All capacities displayed in figures correspond the exact capacities.

The reported cell potentials are the cell potentials between nickel mesh and iron electrode. When applicable, an auxiliary voltage channel was assigned to the test channel to measure the voltage between the reference electrode (RHE) and the iron electrode. These measurements contain two simultaneous voltage readings. The cell temperature was measured with a thermocouple which is placed inside the electrolyte. The temperature readings were recorded simultaneously with the voltage readings. At room temperature the cell temperature was ∼23 °C, at elevated temperatures ∼40 °C. The cells were placed inside an oven for the measurements at 40 °C.

The cyclic-voltaic scans were executed with Parstat multi-channel potentiostat/galvanostat. The potential was recorded vs the H_2 reference electrode.

E.1.4. Energy efficiency

In a HSP-cell hydrogen is stored and produced. The energy yield for hydrogen production corresponds to the thermo-neutral potential H_{el}. The H_{el} equals 1.48 V at room temperature, while $2eH_{el}$ equals the higher heating value (HHV) of hydrogen of −286 kJ/mol H_2.

The inserted capacity C_c contributes to phase conversion and to water electrolysis. We confirmed a faradaic efficiency of 100% for the combined process [1] which can be represented by equation (E.1) where C_{dc} represents the discharge capacity and C_{el} the capacity contributing to electrolysis. Overall, all inserted

charge is converted into hydrogen, the amount C_{el} immediately, the amount C_{dc} delayed.

$$C_c = \int_0^{t_c} I_c dt = \int_0^{t_c+t_{dc}} I_{el} dt + \int_{t_c}^{t_c+t_{dc}} I_{dc} dt = C_{el} + C_{dc} \tag{E.1}$$

For the evaluation of the characteristic numbers – cycle efficiency, storage efficiency and electrolysis efficiency - we split up the charging process in two sections, section I - phase conversion, charging to the discharge capacity, and section II – electrolysis, overcharging. The average potentials for the entire charging process ($\overline{V_c}$) and for the two sections phase conversion ($\overline{V_{pc}}$) and electrolysis ($\overline{V_{el}}$) are calculated as defined in equations (E.2-E.4). The total energy requirement for charging equals the sum of the energy input for phase conversion and electrolysis (E.5). Note, discharging requires also energy and is calculated according to equation (E.6). The total energy input is the sum of the input during the charging process and the discharging process (E.7). The total energy output equals the inserted capacity times the thermo-neutral potential of hydrogen (E.8).

$$E_{charging} = \int_0^{C_c} V_c \, I_c \, dc = \overline{V_c} \cdot C_c \tag{E.2}$$

$$E_{phase\,conversion} = \int_0^{C_{dc}} V_c \, I_c \, dc = \overline{V_{pc}} \cdot C_{dc} \tag{E.3}$$

$$E_{electrolysis} = \int_{C_{dc}}^{C_c} V_c \, I_c \, dc = \overline{V_{el}} \cdot C_{el} \tag{E.4}$$

$$E_{charging} = E_{phase\,conversion} + E_{electrolysis} \tag{E.5}$$

$$E_{discharging} = \int_0^{C_{dc}} V_{dc} \, I_{dc} \, dc = \overline{V_{dc}} \cdot C_{dc} \tag{E.6}$$

$$E_{input} = E_{charging} + E_{discharging} \tag{E.7}$$

$$E_{output} = E_{Hydrogen} = H_{el} \cdot C_c \tag{E.8}$$

These equations form the basis for the efficiency calculations described in the main document. The cycle efficiency is the energy output divided by the energy input. The storage efficiency represents the energy requirement associated with delayed hydrogen generation and the electrolysis efficiency represents the efficiency for immediate hydrogen generation.

E.2. Material characterisation

E.2.1. Al-doped iron electrode: SEM images and mapping results

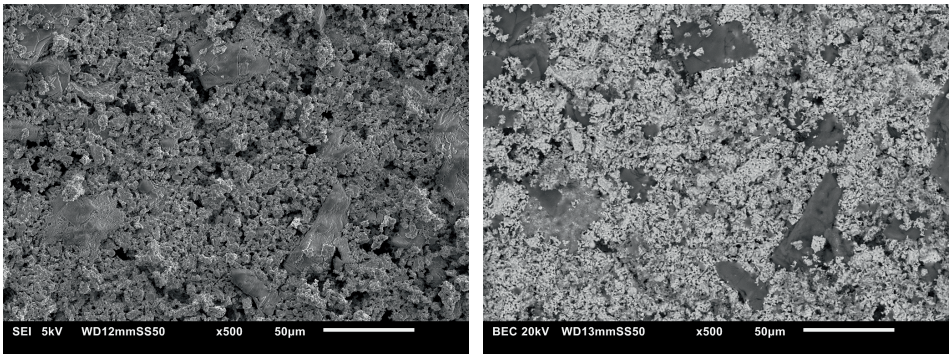

Figure E.2: Al-doped iron electrode: Magnification x500; left SEI and right BEC.

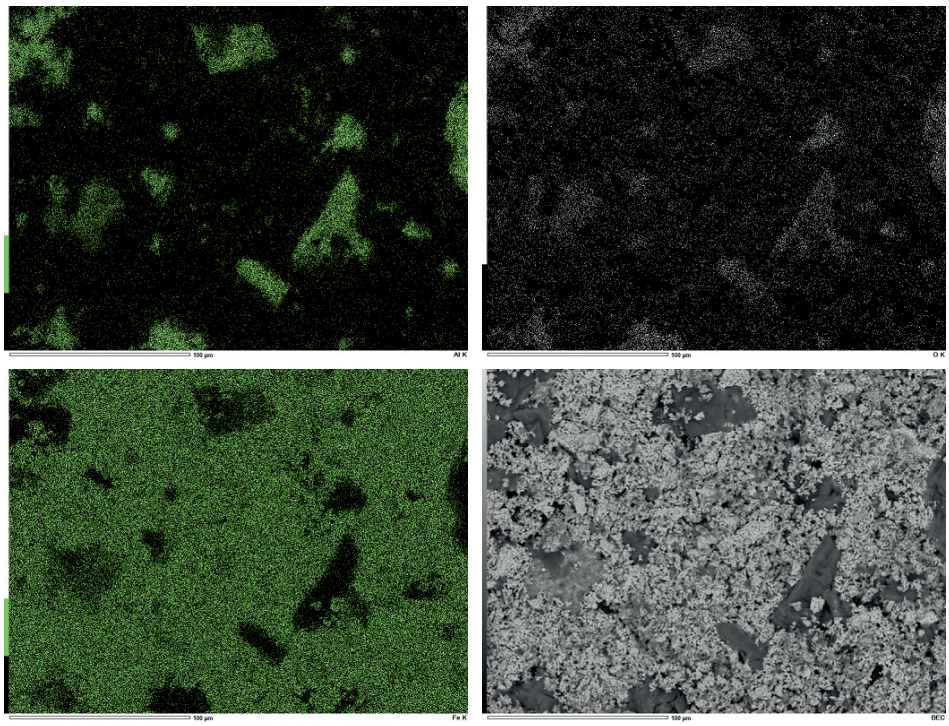

Figure E.3: Mapping images of the chemical elements of the iron electrode with Al-doping: Top left: aluminium; top right: oxygen; bottom left: iron; bottom right: BEC

E.2.2. Zr-doped iron electrode: SEM images and mapping results

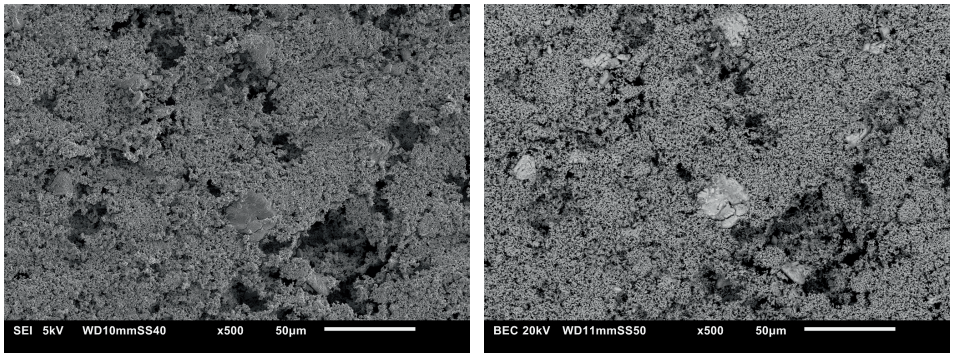

Figure E.4: Zr-doped iron electrode: Magnification x500; left SEI and right BEC.

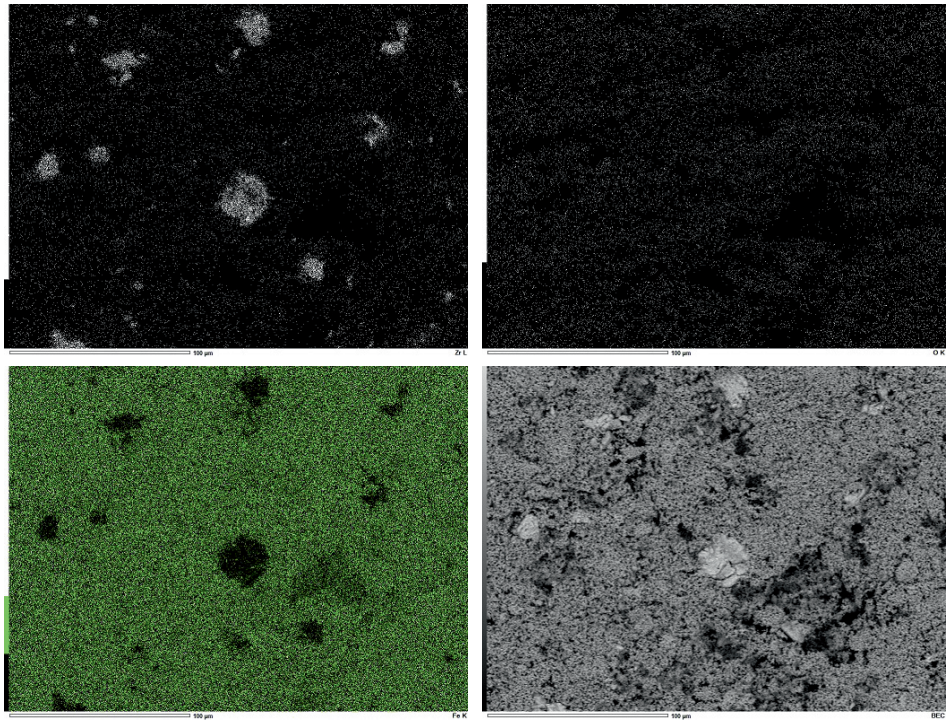

Figure E.5: Mapping images of the chemical elements of the iron electrode with Zr-doping: Top left: zirconium; top right: oxygen; bottom left: iron; bottom right: BEC

E.2.3. SEM images of the iron electrodes, magnification x2500 and x5000

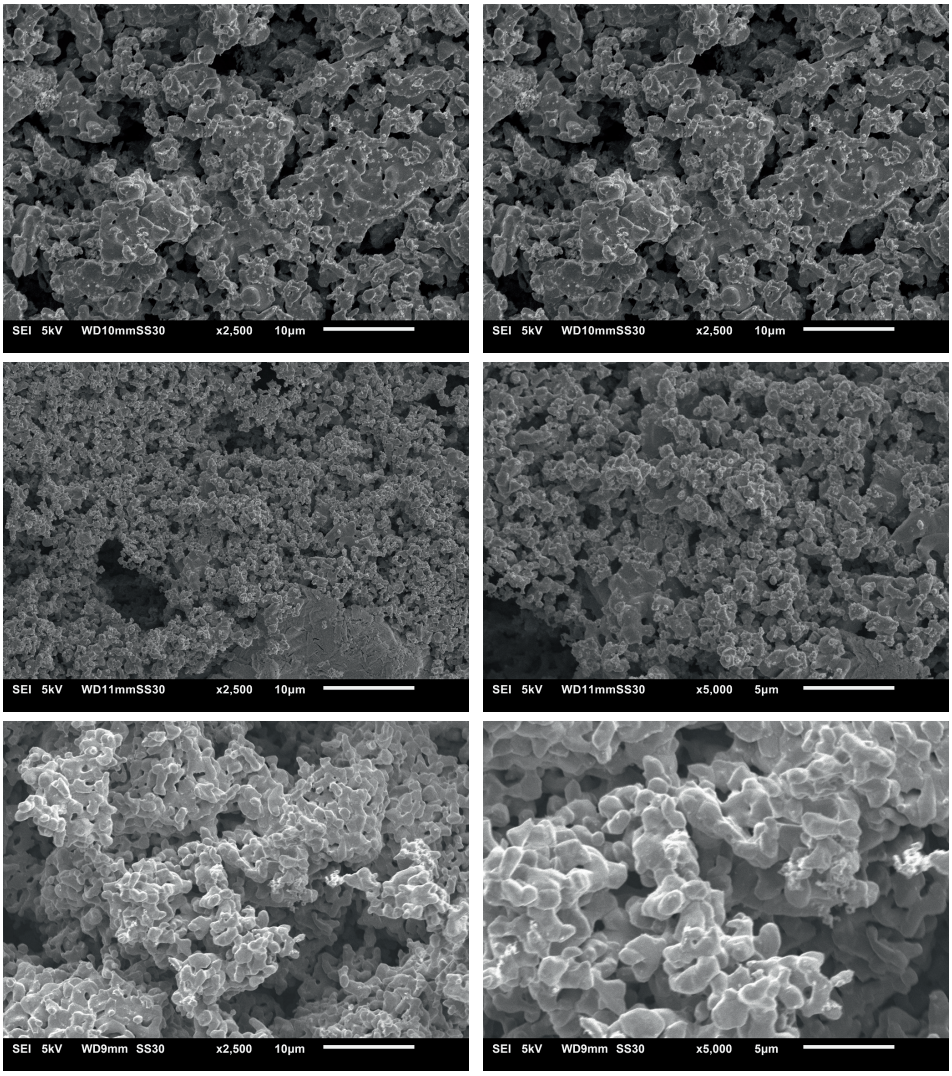

Figure E.6: Iron electrodes with magnification x2500 (left) and x5000 (right).
Top: Electrode with Al-doping; Middle: Electrode with Zr-doping; Bottom: Pure iron electrode.

E.3. Results

E.3.1. Discharge rate test

Figure E.7 shows the observed discharge voltages which form the basis of Figure 5.8 and Figure 5.13 of the main document. Figure 5.8 shows the retrieved discharge capacities and Figure 5.13 the average discharge potentials. The doped electrodes were charge to a capacity of 200 $\mathrm{mAh/cm^2}$ prior to discharging, the pure iron electrode to a capacity of 160 $\mathrm{mAh/cm^2}$. Five subsequent cycles were executed with each discharge current density before switching to the next current density. The current density was increased three times, first from 10 to 15, then to 20 and finally to 25 $\mathrm{mA/cm^2}$.

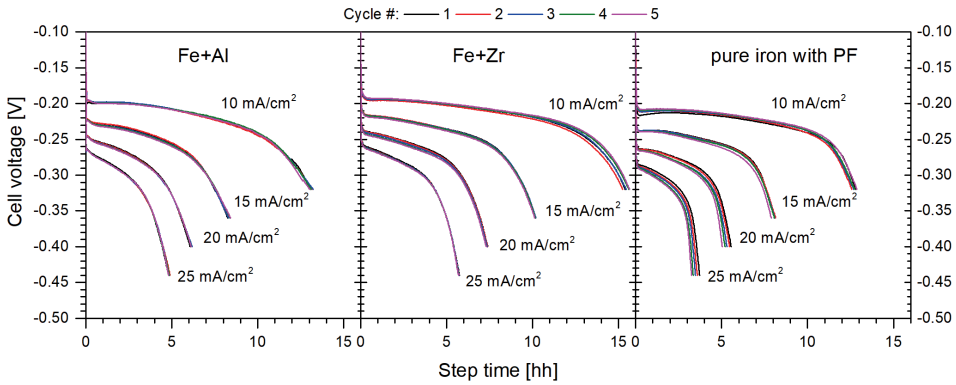

Figure E.7: Observed discharge cell voltage during the discharging rate test.
(Left) Electrode with Al-doping; (Middle) Electrode with Zr-doping; (Right) Pure iron electrode with pore former

E.3.2. Charge rate test

Figure E.8 shows the observed voltages which form the basis for Figure 5.11 and Figure 5.12 of the main document. The electrodes were charge to a capacity of 200 mAh/cm^2 at increasing rates from 10 to 60 mA/cm^2 with a subsequent discharge at a current density of 10 mA/cm^2 for room temperature measurements and at 15 mA/cm^2 for a test temperature of 40 °C.

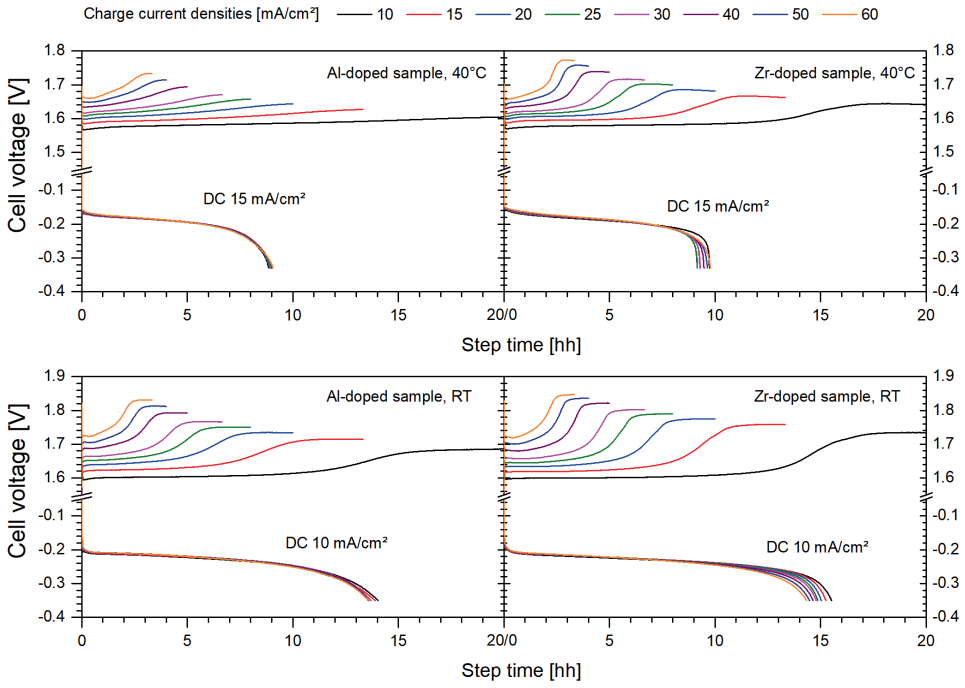

Figure E.8: Observed cell voltage during the charging rate test.
(Left) Electrode with Al-doping; (Right) Electrode with Zr-doping; (Top) Measurements at 40°C; (Bottom) Measurements at RT

E.3.3. CV Scans

Figure E.9 shows the observed CV scans vs H_2 reference electrode. This figure is equivalent to Figure 5.10, but now printed with all scans on top of each other.

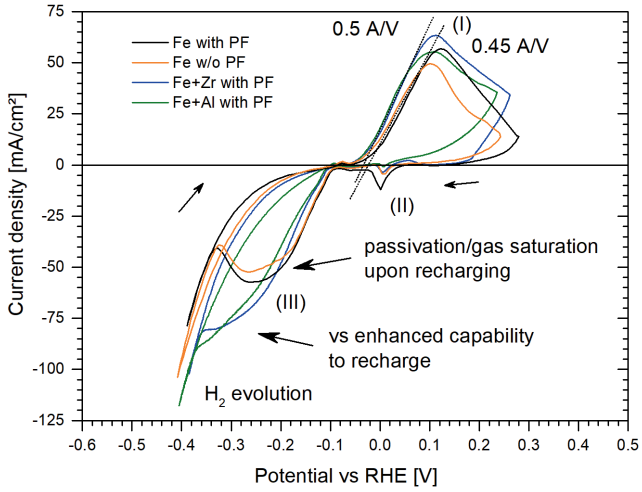

Figure E.9: CV scans vs H_2 reference electrode, scan speed 0.025 mV/s. Pure iron samples with and without pore former (orange and black line) and Al and Zr doped iron samples with pore former (blue and green line) on top of each other. Peak (I) iron oxidation and peak (III) iron reduction form together the 1st plateau transition from iron to iron hydroxide, see reaction (5.1), peak (II) 2nd plateau reaction, reduction of iron oxyhydroxide.

References

[1] F. M. Mulder, B. M. H. Weninger, J. Middelkoop, F. G. B. Ooms, and H. Schreuders, *Efficient electricity storage with a battolyser, an integrated Ni–Fe battery and electrolyser,* Energy & Environmental Science **10**, 756 (2017).

Acknowledgements

Having a PhD was never on my bucket list. It came across my path and I said yes. Doing a PhD is about learning, and about making the right choices at the right time and maybe my first choice, to say yes was a good one. But without the help of so many people around me, this thesis would not have come into being

I want to thank TU Delft for providing me the possibility to contribute to science and grow. I want to thank: Fokko Mulder for giving me the PhD position and for providing me the opportunity to do research. Ruud van Ommen who was there for me when I didn't know how to continue anymore. Lambert van Eijck and Michel Thijs for the support with the work in the reactor, and for the extra time slots in the reactor when the outcomes were promising while the time was running out before closing the reactor. Wilson Smith and Tom Burdyny for helping me swiftly and nicely with great reactions. Andreas Schmidt-Ott, Willem Haverkort, Hans Geerlings, and David Vermaas for always being open for discussions and Wim Haije and Bernard Dam for their constructive feedback. Andrea Ramirez for being open to cooperation and Pavol Bauer for providing supported with a grant application. All technicians amongst others especially Joost Middelkoop and Herman Schreuders, who always arranged what was needed. But also, many thanks to Bart Boshuizen, Ben Norder, Xiaohui Liu, Duco Bosma, Liliana Baron, Willy Rook, Ellen Meijvogel-de Koning, Wim Verwaal, Frans Ooms, Kees Goubitz, Bart van der Linden, Christiaan Schinkel, Bert Zwart and Ruben Abellón for their help. Thanks to everyone from DEMO TU Delft and especially Reinier den Oudsten-Grijzen, my contact person. I also want to thank the secretariat, Heleen van Rooijen, Noortje Fousert, Wil Stolwijk, Rajshree Madarie and Roos Roeling. Many thanks to the TUD graduate school and all their teachers who provide such a variety of courses. Also, many thanks to the people from the Innovation & Impact Center, in particular to Justin Kok, Imge Goren and Adriaan van Noord who mastered the IP-process so well. I have more than I can tell to thank Lucas van Vliet who showed leadership at crucial times and to Gabrie Meesters, Jenny Dankelman and Sandra van der Hor who were my towers of strength. And I want to thank Birgitte Peters who removed the last hurdle to cross the finish line.

I also want to thank our battolyser team, Audrey Iranzo, Andrea Mangel Raventos and Robin Möller-Gulland, my roommates Jebin James, Recep

Kas, Riccardo Zaffaroni, Sanjana Chandrashekar, Siddhartha Subramanian and Maryam Abdinejad and my peers Peter-Paul Harks, Yaolin Xu, Hugo Veldhuizen, Albert Santoso, Emma Westsson, Steffen Cornelius and all other MECSicans for the nice times and the discussions, you were a fantastic group. And also many thanks to Thomas van Dijk, who brought the topic of NiFe batteries to Delft.

To all the students (naturally including LO projects) I supervised, it was a pleasure working with you and I think I have learnt as much from you as I have tried to teach you. For the BSc and MSc projects thanks to Fleur Besteman, Ilka Kramer, Falco Vernooij, Paul Bruinen, Bob Kwakkenbos and especially Jordan Beekhuis, who stood at the basis of the battolyser development and who's supervision turned into a valued friendship and with whom interaction is always as much inspiring as it is fun.

Also, many thanks to NWO who founded the project (Project Number 15169) and to all the external project partners who supported the project. The regular user meeting were recurring highlights and here I want to especially thank Bennie Reesink for the discussions concerning materials and fabrication techniques, your input was very valuable for my project and the talks with you were inspiring. Moreover, I want to especially thank Jeff Martin and Rob Stevens for discussions concerning the hydrogen economy and the required scale necessary for the industry.

Also Sameer Sheikh thanks for your support. And many thanks to Lars Öjefors for discussing your old but still relevant papers. And many thanks to Jan Wognum for your unconditional support in crucial times.

Thanks to all my dear friends that have supported my progress, from whom I will specially mention Andreas Leibetseder, Klaus Fellner and Meindert Jansberg; thank you for your friendship and support.

Also, thanks to my family, Raimund Weninger, Dianne Nijman, Michael Mikusik, Alexander Koch and Nina Lukesch for all your support. I thank Jeroen Nijman. I always enjoy the private scientific discussions and it was great publishing an article together. And Co and Marie-Louise Nijman, thank you for all the unlimited backup. Ineke Kraus and Astrid and Julia Weninger, thank you for your mental support. I thank my father and mother for all the opportunities you have provided and for never setting any constraints on my path. And I hold my dear grandfather and grandmother in sweet memory.

Florine and Raphael, dear bright lights in my life, you are the reason for my choice to change my profession. I have done my PhD as a parttime job because of you. I am convinced that I have done a better job because I was able to spend so much time with you. All that I have done, I have done for you. My goal was to contribute to the sustainable developments to leave you a better world. With

my choices, scientifically and morally I hope to be an example. I love you. And to Katharina, Luca, Niko, Sarah and Sophie you also brighten up my life and we will have a lot of fun-hours awaiting us.

Last but not least I thank Karin Nijman-Weninger. Thanks to you I started believing I could contribute to the energy transition and left my comfort zone. Thank you for the endless evenings you have spent listening to my ideas and structuring my thoughts. You were the most challenging editor. Most of all I thank you for teaching me to stand up for myself and for your unconditional support to follow my path and believe in my ideas, even when others did not. You bring out the best in me and you make me a better person. Zusammen sind wir mehr. I love you.

Bernhard Weninger
January 2022
Alphen aan den Rijn
The Netherlands

Curriculum Vitæ

Bernhard Weninger was born on August 13th, 1977 in Mistelbach, Austria. He studied Civil Engineering at the Technical University in Vienna where he received his first master's degree in 2004. His specialization was constructional civil engineering and statics. He loves solving complex problems and challenging tasks were his favourite ones. His focus was also on energy technologies and economics. That is why he wrote his thesis on "Use and economic efficiency of geothermal heat from former producing wells for crude oil and natural gas". After graduation he worked as an engineer and lead engineer in Austria and the Netherlands. His portfolio included several buildings, as well as a water lock, which is part of the primary flood defence system of the Netherlands and a cable-stayed bridge.

Ever since his first studies the possibility to change the world on energy technologies, especially on hydrogen technologies, had interested him deeply. That is why he decided to follow his heart and to change his career to contribute to the energy transition. At the Technical University Delft, Bernhard finished the bridging-programme from civil engineering to mechanical engineering in August 2014 and his master Sustainable Energy Technology in March 2016, both cum laude. Thereafter, Bernhard work was dedicated to one of the biggest problems of our time: intermittency and energy storage. His focus was on low-cost storage solutions, based on earth abundant iron to foster the energy transition. His work introduced the following novel concepts to the community: the battolyser, electrochemical hydrogen storage, the concept of multi-controlled electrodes, the hydrogen storage and production cell and a new synthesis strategy to produce sintered iron electrodes. The research results from his work are presented in this doctoral thesis.

List of Publications

Papers

B. M. H. Weninger, *Iron electrodes with Al/Zr doping for large- and small-scale energy storage and hydrogen production*, **In Preparation**

B. M. H. Weninger, M. A. Thijs, J. A. C. Nijman, L. van Eijck, and F. M. Mulder, *Neutron diffraction study of a sintered iron electrode in operando*, The Journal of Physical Chemistry C, **125**, 16391 (2021).

B. M. H. Weninger and F. M. Mulder, *Renewable hydrogen and electricity dispatch with multiple Ni–Fe electrode storage*, ACS Energy Letters, **4**, 567 (2019).

F. M. Mulder, **B. M. H. Weninger**, J. Middelkoop, F. G. B. Ooms, and H. Schreuders, *Efficient electricity storage with a battolyser, an integrated Ni–Fe battery and electrolyser*, Energy & Environmental Science, **10**, 756 (2017).

Patents

Electrolystic cell for H_2 generation, PCT/NL2019/050881, Priority date 31-12-2018, **B. Weninger** and F. M. Mulder

Multi-Triggered electrodes in electrochemical systems, PCT/NL2018/050749, Priority date 14-11-2017, **B. Weninger**

Hybrid battery and electrolyser, PCT/NL2017/050870, Priority date 23-12-2016, F. M. Mulder and **B. Weninger**

Hybrid battery and electrolyser, PCT/NL2016/050304, Priority date 1-5-2015, F. M. Mulder and **B. Weninger**

List of Presentations

Oral Presentations

B. Weninger, *Multi-controlled electrodes in electrochemical systems, From intermittent renewable electricity input to 24/7 sustained hydrogen output*, NH3 Event Europe 2021, Rotterdam, June 4th, 2021.

B. Weninger, *Multi-controlled electrodes in electrochemical systems, From intermittent renewable electricity input to 24/7 sustained hydrogen output*, ECCM conference, The Hague, June 21st, 2019.

Poster Presentations & Demonstration

Poster Presentation, Chains, Veldhoven, December 10 & 11, 2019.

Poster Presentation & Demonstration, NWO Teknowlogy Day, Amersfort, November 7th, 2019.

Poster Presentation, NH3 Event Europe, Rotterdam, June 6 & 7, 2019.

Poster Presentation, PhD Energy Event 2017, Delft, November 2nd, 2017, 3rd price.

Poster Presentation, Renewable Energy Driven Chemistry, Differ institute, Eindhoven, April 5th, 2017.